
Numerical Study of Steady and Unsteady Canard-Wing-Body Aerodynamics

Eugene L. Tu

August 1996



National Aeronautics and
Space Administration

Numerical Study of Steady and Unsteady Canard-Wing-Body Aerodynamics

Eugene L. Tu, Ames Research Center, Moffett Field, California

August 1996



National Aeronautics and
Space Administration

Ames Research Center
Moffett Field, California 94035-1000

TABLE OF CONTENTS

	Page
Nomenclature	xv
Summary	1
Chapter 1 Introduction	3
1.1 Motivation	3
1.2 Background	4
1.3 Previous Studies	4
1.4 Objectives	6
1.5 Geometry	6
Chapter 2 Computational Modeling	9
2.1 Numerical Method	9
2.1.1 Turbulence modeling	10
2.1.2 Code performance	10
2.2 Geometry Modeling	11
2.3 Static Grid Generation	12
2.3.1 Surface grids	12
2.3.2 Flowfield grids	12
2.4 Dynamic Grid Generation	14
2.5 Boundary Conditions	14
2.6 Zonal Interfacing	15
2.7 Dynamic Stability Analysis	16
Chapter 3 Effect of Canard on Steady-State Aerodynamics	31
3.1 Experimental Validation: Coplanar Canard	31
3.1.1 Baseline grid	31
3.1.2 Refined grid	33
3.2 Aerodynamic Performance	34
3.2.1 Canard vertical position	34
3.2.2 Canard deflection angle	35

3.3	Canard-Wing Vortex Interaction	36
3.3.1	Coplanar canard	36
3.3.2	Canard vertical position	37
3.3.3	Canard deflection angle	39
3.4	Effect of Canard on Wing Vortex Breakdown	40
Chapter 4	Effect of Fixed Canard on Unsteady Aerodynamics	69
4.1	Pitch-Up Ramp Motion	70
4.1.1	Aerodynamic performance	71
4.1.2	Spatial and temporal convergence	71
4.1.3	Canard-wing vortex interaction	72
4.2	Pitch Oscillation	73
4.3	Dynamic Stability	74
4.3.1	Effect of canard	75
4.3.2	Reduced frequency	95
Chapter 5	Unsteady Aerodynamics of Moving Canards	95
5.1	Canard Pitch-Up Ramp Motion	95
5.1.1	Unsteady lift and pitching moment	96
5.1.2	Canard-wing vortex interaction	98
5.2	Canard Pitch Oscillation	98
5.2.1	Unsteady lift and pitching moment	99
5.2.2	Canard and wing vortex structures	127
Chapter 6	Conclusions	127
6.1	Validation of the Computational Method	127
6.2	Canard-Wing-Body Steady Flowfield	128
6.3	Canard-Wing-Body Unsteady Flowfield	129
6.4	Recommendations for Future Studies	135
Appendix A	Governing Equations	131
Appendix B	Numerical Algorithm	137
Appendix C	Turbulence Modeling	143
References	147

List of Tables

	Page
2.1 Surface and flowfield grid data for coplanar, vertical-offset and deflected canard configurations	18

List of Figures

		Page
1.1	Sketch of the leading-edge vortex structure of a canard or wing.....	7
1.2	Crossflow plane sketch of the leading-edge vortex.....	7
1.3	Schematic of the typical steady-state canard-wing vortex interaction for a configuration at moderate angles of attack	8
1.4	Close-coupled canard-wing-body geometry (pitch axis, moment center, and canard vertical locations shown)	8
2.1	Schematic diagram of the grid generation procedure for static canard configurations with various canard vertical positions and deflections	19
2.2	Baseline surface grid for the wing-body configuration with and without an undeflected mid-canard	20
2.3	Refined surface grid for the wing-body configuration with and without an undeflected mid-canard	20
2.4	Schematic of the procedure for generating a vertical-offset canard configuration from a baseline undeflected mid-canard configuration	21
2.5	Perspective view of the surface grid for wing-body configuration with a high-canard ($y/\bar{c} = 0.185$)	21
2.6	Schematic of the procedure for generating a deflected canard configuration from a baseline undeflected mid-canard configuration	22
2.7	Perspective view of the surface grid for wing-body configuration with a deflected canard ($\delta_c = 10$ deg)	22
2.8	Flowfield grid topology and expanded near-body grid for the undeflected mid-canard configuration.....	23
2.9	Comparison of the baseline and refined near-body flowfield grids for the undeflected mid-canard configuration.....	24
2.10	Algebraic redistribution of the flowfield grid	25
2.11	Flowfield grid at the mismatched interface surface for the high-canard configuration	26
2.12	Flowfield grid at the mismatched interface surface for the deflected canard configuration.....	26
2.13	Schematic illustrating the integration of dynamic grid generation and zonal interface computation into the time-iterative solution process	27
2.14	Types of velocity boundary conditions at the surfaces of the canard, wing and body.....	28
2.15	Schematic illustrating the interfacing of two adjacent zones	28
2.16	Example of a local search procedure for improved efficiency in dynamic zonal interface computations	29
3.1	Comparison of computed and experimental steady-state surface pressure coefficients for the baseline grid with and without mid-canard. $M_\infty = 0.90$, $\alpha \approx 4$ deg, $Re_{\bar{c}} = 1.52$ million	41

3.2	Comparison of computed and experimental force coefficients for the baseline grid with and without mid-canard. $M_\infty = 0.90$, $Re_{\bar{c}} = 1.52$ million.....	42
3.3	Comparison of component force coefficients for the baseline grid with and without mid-canard. (Lift and moment curves are given for shaded regions of the geometry). $M_\infty = 0.90$, $Re_{\bar{c}} = 1.52$ million.....	43
3.4	Comparison of baseline and refined grid surface pressure coefficients with experiment. $M_\infty = 0.90$, $\alpha = 8.21$ deg, $Re_{\bar{c}} = 1.52$ million.....	44
3.5	Comparison of baseline and refined grid surface pressure coefficients with experiment. $M_\infty = 0.90$, $\alpha = 12.38$ deg, $Re_{\bar{c}} = 1.52$ million.....	44
3.6	Comparison of baseline and refined grid force coefficients with experiment. $M_\infty = 0.90$, $Re_{\bar{c}} = 1.52$ million.....	45
3.7	Comparison of computed and experimental surface pressure coefficients for the refined grid with and without mid-canard. $M_\infty = 0.90$, $\alpha \approx 12$ deg, $Re_{\bar{c}} = 1.52$ million.....	46
3.8	Comparison of computational and experimental forces and moments for the high-, mid- and low-canard configurations. $M_\infty = 0.90$, $Re_{\bar{c}} = 1.52$ million.....	47
3.9	Comparison of component lift and pitching moment curves for the high-canard configuration. $M_\infty = 0.90$, $Re_{\bar{c}} = 1.52$ million.....	48
3.10	Effect of canard vertical position on the incremental change in lift and drag coefficients. $M_\infty = 0.90$, $Re_{\bar{c}} = 1.52$ million.....	49
3.11	Comparison of computed and experimental forces and moments for the undeflected ($\delta_c = 0.0$ deg) and deflected ($\delta_c = 10.0$ deg) canard configurations. $M_\infty = 0.85$, $Re_{\bar{c}} = 2.82$ million.....	50
3.12	Comparison of component lift and pitching moment curves for the deflected canard configuration at $\delta_c = 10.0$ deg. $M_\infty = 0.85$, $Re_{\bar{c}} = 2.82$ million.....	51
3.13	Effect of canard deflection, δ_c , on wing and canard portion lift and moment curves. $M_\infty = 0.85$, $Re_{\bar{c}} = 2.82$ million.....	52
3.14	Effect of canard deflection, δ_c , on component lifts and pitching moments. $M_\infty = 0.85$, $\alpha = 4.27$ deg, $Re_{\bar{c}} = 2.82$ million.....	53
3.15	Contour plot of computed total pitching moment with moment center at c.g. location (59.14 cm from nose). $M_\infty = 0.85$, $Re_{\bar{c}} = 2.82$ million.....	53
3.16	Computed upper surface pressure contours for the wing-body configuration with and without mid-canard. $M_\infty = 0.90$, $Re_{\bar{c}} = 1.52$ million.....	54
3.17	Computed upper surface flow patterns for the wing-body configuration with and without mid-canard. $M_\infty = 0.90$, $Re_{\bar{c}} = 1.52$ million.....	55

3.18	Crossflow plane visualization of normalized total pressure contours and scaled velocity vectors of the canard and wing leading-edge vortices. $M_\infty = 0.90$, $\alpha = 8$ deg, $Re_{\bar{c}} = 1.52$ million.....	56
3.19	Comparison of wing surface pressures for the high- and low-canard configurations. $M_\infty = 0.90$, $\alpha = 4.27$ deg and 8.55 deg, $Re_{\bar{c}} = 1.52$ million.....	57
3.20	Crossflow plane visualization of normalized total pressure contours for high- and low-canard configurations. $M_\infty = 0.90$, $\alpha = 4.27$ deg, $Re_{\bar{c}} = 1.52$ million.....	58
3.21	Crossflow plane visualization of normalized total pressure contours for the low-canard configuration. $M_\infty = 0.90$, $\alpha = 8.55$ deg, $Re_{\bar{c}} = 1.52$ million.....	59
3.22	Schematic of the canard and wing vortex trajectories for the low-canard configuration.....	60
3.23	Perspective view of normalized total pressure contours for the low-canard configuration. $M_\infty = 0.90$, $\alpha = 8.55$ deg, $Re_{\bar{c}} = 1.52$ million.....	60
3.24	Effect of canard deflection, δ_c , on surface flow patterns. $M_\infty = 0.85$, $\alpha = 4.27$ deg, $Re_{\bar{c}} = 2.82$ million.....	61
3.25	Effect of canard deflection, δ_c , on wing surface pressures. (Upper surface pressures indicated by U). $M_\infty = 0.85$, $\alpha = 4.27$ deg, $Re_{\bar{c}} = 2.82$ million.....	62
3.26	Crossflow plane visualization of normalized total pressure contours for canard deflections of $\delta_c = 5$ deg and 10 deg. $M_\infty = 0.85$, $\alpha = 4.27$ deg, $Re_{\bar{c}} = 2.82$ million.....	63
3.27	Perspective views of upper surface canard-wing vortex structure for canard deflections of $\delta_c = 5$ deg and 10 deg. $M_\infty = 0.85$, $\alpha = 4.27$ deg, $Re_{\bar{c}} = 2.82$ million.....	64
3.28	Perspective view of computed surface pressures and simulated particle traces for $\delta_c = 10$ deg. $M_\infty = 0.85$, $\alpha = 4.27$ deg, $Re_{\bar{c}} = 2.82$ million.....	64
3.29	Crossflow plane visualization of normalized total pressure contours of the wing leading-edge vortex for the canard-off case. $M_\infty = 0.90$, $Re_{\bar{c}} = 1.52$ million, $x/\bar{c} = 3.6$	65
3.30	Off-surface particle traces of the wing vortex for the canard-off case. $M_\infty = 0.90$, $Re_{\bar{c}} = 1.52$ million, $x/\bar{c} = 3.6$	66
3.31	Crossflow plane visualization of scaled axial velocity contours for the canard-off case. $M_\infty = 0.90$, $Re_{\bar{c}} = 1.52$ million, $x/\bar{c} = 3.6$	67
3.32	Off-surface particle traces of the canard and wing vortices for the canard-on case. $M_\infty = 0.90$, $\alpha = 12.38$ deg, $Re_{\bar{c}} = 1.52$ million.....	67
4.1	Schematic of unsteady pitch-up ramp motion from $\alpha_i = 0$ deg to $\alpha_f = 15$ deg.....	76

4.2	Effect of canard on unsteady aerodynamic loads during pitch-up ramp motion. $M_\infty = 0.90$, $A_p = 0.10$, $\alpha_i = 0$ deg, $\alpha_f = 15$ deg, $Re_{\bar{c}} = 1.52$ million.....	77
4.3	Drag polar of the canard-wing-body configuration undergoing pitch-up ramp motion. $M_\infty = 0.90$, $A_p = 0.10$, $\alpha_i = 0$ deg, $\alpha_f = 15$ deg, $Re_{\bar{c}} = 1.52$ million.....	78
4.4	Effect of pitch rate on canard-wing-body lift. $M_\infty = 0.90$, $\alpha_i = 0$ deg, $\alpha_f = 15$ deg, $Re_{\bar{c}} = 1.52$ million.....	78
4.5	Comparison of steady and unsteady component lift curves for the canard configuration. $M_\infty = 0.90$, $A_p = 0.05$, $\alpha_i = 0$ deg, $\alpha_f = 15$ deg, $Re_{\bar{c}} = 1.52$ million.....	79
4.6	Effect of time-step size on the unsteady component lift curves near the beginning of the ramp motion, α_i . $M_\infty = 0.90$, $A_p = 0.05$, $\alpha_i = 0$ deg, $\alpha_f = 15$ deg, $Re_{\bar{c}} = 1.52$ million.....	79
4.7	Effect of time-step size on the unsteady component lift curves near the end of the ramp motion, α_f . $M_\infty = 0.90$, $A_p = 0.05$, $\alpha_i = 0$ deg, $\alpha_f = 15$ deg, $Re_{\bar{c}} = 1.52$ million.....	80
4.8	Effect of grid refinement on the unsteady component lift curves. $M_\infty = 0.90$, $A_p = 0.05$, $\alpha_i = 0$ deg, $\alpha_f = 15$ deg, $Re_{\bar{c}} = 1.52$ million.....	81
4.9	Upper surface streamlines for the steady-state canard-wing-body configuration at various angles of attack.....	82
4.10	Upper surface instantaneous streamlines at various times for the canard-wing-body configuration undergoing unsteady ramp motion. $M_\infty = 0.90$, $A_p = 0.05$, $\alpha_i = 0$ deg, $\alpha_f = 12.83$ deg, $Re_{\bar{c}} = 1.52$ million.....	82
4.11	Upper surface pressure contours at various times for the canard-wing-body configuration undergoing unsteady ramp motion. $M_\infty = 0.90$, $A_p = 0.05$, $\alpha_i = 0$ deg, $\alpha_f = 12.83$ deg, $Re_{\bar{c}} = 1.52$ million.....	83
4.12	Comparison of crossflow total pressure contours between the steady and unsteady cases at various angles of attack. $M_\infty = 0.90$, $A_p = 0.05$, $\alpha_i = 0$ deg, $\alpha_f = 12.83$ deg, $Re_{\bar{c}} = 1.52$ million.....	84
4.13	Crossflow total pressure contours for the transient flow after the ramp motion has ended. $M_\infty = 0.90$, $A_p = 0.05$, $\alpha_i = 0$ deg, $\alpha_f = 12.83$ deg, $Re_{\bar{c}} = 1.52$ million.....	85
4.14	Effect of canard on component lift coefficients for two cycles of oscillation. $M_\infty = 0.70$, $k = 0.268$, $\alpha_m = 4.0$ deg, $A = 1.0$ deg, $Re_{\bar{c}} = 3.05$ million.....	86
4.15	Effect of canard on component pitching moment coefficients for two cycles of oscillation. $M_\infty = 0.70$, $k = 0.268$, $\alpha_m = 4.0$ deg, $A = 1.0$ deg, $Re_{\bar{c}} = 3.05$ million.....	86
4.16	Effect of canard on lift and pitching moment coefficient curves for third cycle of oscillation. $M_\infty = 0.70$, $k = 0.268$, $\alpha_m = 4.0$ deg, $A = 1.0$ deg, $Re_{\bar{c}} = 3.05$ million.....	87

4.17	Lift and pitching moment curves for the canard-off configuration (started from steady-state solutions with three cycles of oscillations shown). $M_\infty = 0.70$, $k = 0.268$, $\alpha_m = 4.0$ deg, $A = 1.0$ deg, $Re_{\bar{c}} = 3.05$ million	87
4.18	Comparisons of directly computed and Fourier-coefficient represented lift and pitching moment curves. $M_\infty = 0.70$, $k = 0.268$, $\alpha_m = 4.0$ deg, $A = 1.0$ deg, $Re_{\bar{c}} = 3.05$ million	88
4.19	Comparison of the computed and experimental longitudinal dynamic stability parameters for the canard-off configuration. $M_\infty = 0.70$, $Re_{\bar{c}} = 3.05$ million	89
4.20	Comparison of the longitudinal dynamic stability parameters for the configuration with and without the canard. $M_\infty = 0.70$, $Re_{\bar{c}} = 3.05$ million	90
4.21	Effect of the canard on pitching-moment dynamic stability parameters (differences between canard-on and canard-off values shown). $M_\infty = 0.70$, $Re_{\bar{c}} = 3.05$ million	91
4.22	Effect of reduced frequency (k) on normal force and pitching moment coefficients for the canard-on case. $M_\infty = 0.70$, $\alpha_m = 4.0$ deg, $A = 1.0$ deg, $Re_{\bar{c}} = 3.05$ million	92
4.23	Effect of reduced frequency (k) on damping-in-pitch and pitch-oscillatory stability parameters for the canard-on case. $M_\infty = 0.70$, $\alpha_m = 4.0$ deg, $Re_{\bar{c}} = 3.05$ million	93
5.1	Schematic of canard pitch-up ramp motion from $\delta_{c_i} = 0$ deg to $\delta_{c_f} = 5$ deg and 9.25 deg	100
5.2	Time history of unsteady lift and pitching-moment responses due to the canard pitch-up ramp motion for the configuration at $\alpha = 4.27$ deg. $M_\infty = 0.85$, $A_{pc} = 0.05$, $\delta_{c_i} = 0$ deg, $\delta_{c_f} = 5$ deg, $Re_{\bar{c}} = 2.82$ million	101
5.3	Effect of canard pitch rate on the time history of unsteady lift responses due to the canard pitch-up ramp motion. $M_\infty = 0.85$, $\alpha = 4.27$ deg, $\delta_{c_i} = 0$ deg, $\delta_{c_f} = 5$ deg, $Re_{\bar{c}} = 2.82$ million	102
5.4	Effect of canard pitch rate on the time history of unsteady pitching moment responses due to the canard pitch-up ramp motion. $M_\infty = 0.85$, $\alpha = 4.27$ deg, $\delta_{c_i} = 0$ deg, $\delta_{c_f} = 5$ deg, $Re_{\bar{c}} = 2.82$ million	103
5.5	Effect of time-step size on unsteady lift and moment responses due to the canard pitch-up ramp motion for $A_{pc} = 0.20$. $M_\infty = 0.85$, $\alpha = 4.27$ deg, $\delta_{c_i} = 0$ deg, $\delta_{c_f} = 5$ deg, $Re_{\bar{c}} = 2.82$ million	104
5.6	Time history of unsteady lift and pitching-moment responses due to the canard pitch-up ramp motion for the configuration at $\alpha = 8.0$ deg. $M_\infty = 0.85$, $A_{pc} = 0.05$, $\delta_{c_i} = 0$ deg, $\delta_{c_f} = 5$ deg, $Re_{\bar{c}} = 2.82$ million	105

5.7	Comparison of crossflow total pressure contours between the steady and unsteady cases at various streamwise locations for the configuration at $\alpha = 8.0$ deg and $\delta_c = 5.0$ deg (unsteady case given at the instantaneous δ_c for $t = 5.0$ deg). $M_\infty = 0.85$, $A_{pc} = 0.05$, $\delta_{c_i} = 0$ deg, $\delta_{c_f} = 5$ deg. $Re_{\bar{c}} = 2.82$ million.....	106
5.8	Time history of unsteady lift and pitching-moment responses due to the canard pitch-up ramp motion from $\delta_{c_i} = 0$ deg to $\delta_{c_f} = 9.25$ deg. $M_\infty = 0.85$, $\alpha = 4.27$ deg, $A_{pc} = 0.05$, $Re_{\bar{c}} = 2.82$ million.....	107
5.9	(Part-1) Upper and lower surface instantaneous streamlines for the canard pitch-up ramp motion from $\delta_{c_i} = 0$ deg to $\delta_{c_f} = 9.25$ deg. $M_\infty = 0.85$, $\alpha = 4.27$ deg, $A_{pc} = 0.05$, $Re_{\bar{c}} = 2.82$ million.....	108
5.9	(Part-2) Upper and lower surface instantaneous streamlines for the canard pitch-up ramp motion from $\delta_{c_i} = 0$ deg to $\delta_{c_f} = 9.25$ deg. $M_\infty = 0.85$, $\alpha = 4.27$ deg, $A_{pc} = 0.05$, $Re_{\bar{c}} = 2.82$ million.....	109
5.10	Crossflow total pressure contours over the canard ($x/\bar{c} = 2.0$) and wing ($x/\bar{c} = 3.3$) during the canard pitch-up ramp motion from $\delta_{c_i} = 0$ deg to $\delta_{c_f} = 9.25$ deg. $M_\infty = 0.85$, $\alpha = 4.27$ deg, $A_{pc} = 0.05$, $Re_{\bar{c}} = 2.82$ million.....	110
5.11	Crossflow total pressure contours over the wing ($x/\bar{c} = 3.3$) after the canard pitch-up ramp motion from $\delta_{c_i} = 0$ deg to $\delta_{c_f} = 9.25$ deg. $M_\infty = 0.85$, $\alpha = 4.27$ deg, $A_{pc} = 0.05$, $Re_{\bar{c}} = 2.82$ million.....	111
5.12	Time history of unsteady lift and pitching-moment responses due to the canard pitch oscillation motion for the configuration at $\alpha = 4.27$ deg. $M_\infty = 0.85$, $A_c = 2.0$ deg, $k_c = 1.0$, $Re_{\bar{c}} = 2.82$ million.....	112
5.13	Lift and pitching-moment curves for the configuration undergoing canard pitch oscillation motion at $\alpha = 4.27$ deg. $M_\infty = 0.85$, $A_c = 2.0$ deg, $k_c = 1.0$, $Re_{\bar{c}} = 2.82$ million.....	113
5.14	Time history of unsteady lift and pitching-moment responses due to the canard pitch oscillation motion for the configuration at $\alpha = 8.0$ deg. $M_\infty = 0.85$, $A_c = 2.0$ deg, $k_c = 1.0$, $Re_{\bar{c}} = 2.82$ million.....	114
5.15	Lift and pitching-moment curves for the configuration undergoing canard pitch oscillation motion at $\alpha = 8.0$ deg. $M_\infty = 0.85$, $A_c = 2.0$ deg, $k_c = 1.0$, $Re_{\bar{c}} = 2.82$ million.....	115
5.16	(Part-1) Crossflow total pressure contours over the canard ($x/\bar{c} = 2.0$) for the canard pitch oscillation motion at $\alpha = 4.27$ deg. $M_\infty = 0.85$, $A_c = 2.0$ deg, $k_c = 1.0$, $Re_{\bar{c}} = 2.82$ million.....	116

5.16	(Part-2) Crossflow total pressure contours over the canard ($x/\bar{c} = 2.0$) for the canard pitch oscillation motion at $\alpha = 4.27$ deg. $M_\infty = 0.85$, $A_c = 2.0$ deg, $k_c = 1.0$, $Re_{\bar{c}} = 2.82$ million.....	117
5.17	(Part-1) Crossflow total pressure contours over the wing ($x/\bar{c} = 3.5$) for the canard pitch oscillation motion at $\alpha = 4.27$ deg. $M_\infty = 0.85$, $A_c = 2.0$ deg, $k_c = 1.0$, $Re_{\bar{c}} = 2.82$ million.....	118
5.17	(Part-2) Crossflow total pressure contours over the wing ($x/\bar{c} = 3.5$) for the canard pitch oscillation motion at $\alpha = 4.27$ deg. $M_\infty = 0.85$, $A_c = 2.0$ deg, $k_c = 1.0$, $Re_{\bar{c}} = 2.82$ million.....	119
5.18	Effect of canard pitch oscillation motion on wing surface pressures at $\alpha = 4.27$ deg. $M_\infty = 0.85$, $A_c = 2.0$ deg, $k_c = 1.0$, $Re_{\bar{c}} = 2.82$ million.....	120
5.19	(Part-1) Crossflow total pressure contours over the canard ($x/\bar{c} = 2.0$) for the canard pitch oscillation motion at $\alpha = 8.0$ deg. $M_\infty = 0.85$, $A_c = 2.0$ deg, $k_c = 1.0$, $Re_{\bar{c}} = 2.82$ million.....	121
5.19	(Part-2) Crossflow total pressure contours over the canard ($x/\bar{c} = 2.0$) for the canard pitch oscillation motion at $\alpha = 8.0$ deg. $M_\infty = 0.85$, $A_c = 2.0$ deg, $k_c = 1.0$, $Re_{\bar{c}} = 2.82$ million.....	122
5.20	(Part-1) Crossflow total pressure contours over the wing ($x/\bar{c} = 3.5$) for the canard pitch oscillation motion at $\alpha = 8.0$ deg. $M_\infty = 0.85$, $A_c = 2.0$ deg, $k_c = 1.0$, $Re_{\bar{c}} = 2.82$ million.....	123
5.20	(Part-2) Crossflow total pressure contours over the wing ($x/\bar{c} = 3.5$) for the canard pitch oscillation motion at $\alpha = 8.0$ deg. $M_\infty = 0.85$, $A_c = 2.0$ deg, $k_c = 1.0$, $Re_{\bar{c}} = 2.82$ million.....	124
5.21	Effect of canard pitch oscillation motion on wing surface pressures at $\alpha = 8.0$ deg. $M_\infty = 0.85$, $A_c = 2.0$ deg, $k_c = 1.0$, $Re_{\bar{c}} = 2.82$ million.....	125

Nomenclature

A, B, C	inviscid flux Jacobians
a_0, a_1, b_1	first three Fourier coefficients
A, A_c	pitch oscillation amplitude of the entire configuration or canard
A_p	non-dimensional configuration pitch rate, $A_p = \dot{\alpha}\bar{c}/U_\infty$
A_{pc}	non-dimensional canard pitch rate, $A_p = \dot{\delta}_c\bar{c}/U_\infty$
\vec{a}_b	acceleration vector of a physical body surface point
c	speed of sound
\bar{c}	mean aerodynamic chord of the wing
c_p, c_v	specific heats at constant pressure and volume
C_p	coefficient of pressure, $\frac{p-p_\infty}{q_\infty}$
C_L	lift coefficient
C_d	drag coefficient
C_m	pitching-moment coefficient
C_N	normal force coefficient
e	total energy per unit volume
E, F, G	flux vectors
f	frequency
h	enthalpy per unit mass
J	coordinate transformation Jacobian
k	reduced frequency for the entire configuration, $k = \frac{\omega\bar{c}}{2U_\infty}$
k_c	reduced frequency for the canard, $k_c = \frac{\omega_c\bar{c}}{2U_\infty}$
L	characteristic length
M	viscous flux Jacobian
M_∞	freestream Mach number
\vec{n}	unit vector normal to the body surface
p	instantaneous static pressure
Pr	Prandtl number
q	pitch rate or dynamic pressure
q_c	canard pitch rate
Q	vector of dependent variables
R	specific gas constant
Re_c	Reynolds number based on mean aerodynamic wing chord
t, t_{deg}, t_{rad}	time (non-dimensional in degrees or radians)
t_{sec}	physical time (in seconds)
T	absolute temperature
T^{-1}, T	matrices of left and right eigenvectors or of the transformation
u, v, w	Cartesian velocity components or parametric surface coordinates
U, V, W	contravariant velocity components
u	velocity magnitude
U_∞	freestream velocity magnitude
W_p	work performed by the fluid during pitch motion
x, y, z	Cartesian physical space coordinates
$\frac{z}{\bar{c}}$	normalized canard vertical-offset distance

α	freestream angle of attack
α_{eff}	wing effective angle of attack
α_c	canard angle of attack, $\alpha_c = \alpha + \delta_c$
α_i	initial angle of attack (ramp motion)
α_f	final angle of attack (ramp motion)
α_m	mean angle of attack (pitch oscillation)
γ	ratio of specific heats
δ_c	canard deflection angle (from body centerline)
δ_{c_i}	initial canard deflection angle (ramp motion)
δ_{c_f}	final canard deflection angle (ramp motion)
δ_{cm}	mean canard deflection angle
ϵ	internal energy per unit mass
ζ	bulk coefficient of viscosity
θ	momentum thickness
κ	ratio of coefficient of thermal conductivity to the specific heat at constant volume
λ	eigenvalue or second coefficient of viscosity
Λ	diagonal matrix of eigenvalues, λ_i
μ	dynamic or first coefficient of viscosity
ξ, η, ζ	curvilinear space coordinates
ρ	density
τ	computational temporal coordinate
τ_{ij}	viscous stress tensor
ϕ	flux influence parameter
ω	angular velocity
ω_w	canard angular velocity
$\overline{(\quad)}$	mean quantity
$(\dot{\quad})$	time rate of change of quantity
$\langle \quad \rangle$	root mean square quantity
$(\quad)'$	fluctuating quantity, $f = \overline{f} + f'$
(\sim)	dimensional quantity
$(\hat{\quad})$	quantity in curvilinear coordinates

Superscripts

n time level

Subscripts

BL	Baldwin-Lomax
c	canard
i, j, k	ξ, η, ζ direction indices
i	incident
n	normal
T	total quantity
x, y, z	partial with respect to Cartesian coordinate
ξ, η, ζ	partial with respect to curvilinear coordinate
w	wing
∞	freestream quantity

NUMERICAL STUDY OF STEADY AND UNSTEADY CANARD-WING-BODY AERODYNAMICS

Eugene L. Tu
Ames Research Center

SUMMARY

The use of canards in advanced aircraft for control and improved aerodynamic performance is a topic of continued interest and research. In addition to providing maneuver control and trim, the influence of canards on wing aerodynamics can often result in increased maximum lift and decreased trim drag. In many canard-configured aircraft, the main benefits of canards are realized during maneuver or other dynamic conditions. Therefore, the detailed study and understanding of canards requires the accurate prediction of the non-linear unsteady aerodynamics of such configurations. For close-coupled canards, the unsteady aerodynamic performance associated with the canard-wing interaction is of particular interest. The presence of a canard in close proximity to the wing results in a highly coupled canard-wing aerodynamic flowfield which can include downwash/upwash effects, vortex-vortex interactions and vortex-surface interactions. For unsteady conditions, these complexities of the canard-wing flowfield are further increased.

The development and integration of advanced computational technologies provide for the time-accurate Navier-Stokes simulations of the steady and unsteady canard-wing-body flowfields. Simulations are performed for non-linear flight regimes at transonic Mach numbers and for a wide range of angles of attack. For the static configurations, the effects of canard positioning and fixed deflection angles on aerodynamic performance and canard-wing vortex interactions are considered. For non-static configurations, the analyses of the canard-wing-body flowfield includes the unsteady aerodynamics associated with pitch-up ramp and pitch oscillatory motions of the entire geometry. The unsteady flowfield associated with moving canards, which are typically used as primary control surfaces, are considered as well. The steady and unsteady effects of the canard on surface pressures, integrated forces and moments, and canard-wing vortex interaction are presented in detail, including the effects of the canard on the static and dynamic stability characteristics.

The current study provides an understanding of the steady and unsteady canard-wing-body flowfield. Emphasis is placed on the effects of the canard on aerodynamic performance as well as the detailed flow physics of the canard-wing flowfield interactions. The computational tools developed to accurately predict the time-accurate flowfield of moving canards provides for the capability of coupled fluids-controls simulations desired in the detailed design and analysis of advanced aircraft.

Chapter 1

Introduction

1.1 Motivation

Since the Wright Brothers first introduced the canard configuration almost a century ago, the benefits of canards over the now more conventional tailplane configurations have been researched and debated extensively. In particular, for the past 30 years, the use of canards in many advanced aircraft for control and improved aerodynamic performance has been the topic of continued research. The influence of canards on wing aerodynamics can often result in increased maximum lift and decreased trim drag. There are also unique dynamic performance characteristics for canard-configured aircraft coupled with the capability of present-day automatic control systems. The reduced or even negative static stability of canard configurations can lead to improved aircraft agility and maneuverability.

There are a variety of aircraft which utilize canards to enhance aerodynamic performance and controllability. Aircraft flying today can be found with canards which are fixed or movable, located at various longitudinal and vertical positions, and coincident or deflected with respect to the wing. For example, the X-31 aircraft has a “no-load” long-coupled canard which deflects between +20 and -70 deg for high angle of attack pitch recovery control (ref. 1). Otherwise, during normal flight, the X-31’s canard is “free-floating” and deflects to maintain minimal aerodynamic loads.

Close-coupled canards, by definition, have a more significant effect on the canard-wing aerodynamic interaction and, consequently, the aerodynamic performance of the aircraft. The NASA X-29, SAAB Viggen and SAAB Gripen are three examples of fully integrated close-coupled canard configurations. The X-29 has a forward-swept wing and a movable close-coupled canard which is the primary pitch control surface as well as an integral component in the active control system (ref. 2). The SAAB Viggen has a close-coupled fixed canard for high performance aerodynamics while its successor, the Gripen, utilizes movable close-coupled canards to obtain maximum lift in maneuvering, maximum lift-to-drag ratio in cruise, and even nose-down pitching moment during short-field landing roll-out (ref. 3).

Improved performance of close-coupled canard configurations is usually the direct result of the aerodynamic interaction between the canard and wing. However, depending upon geometry and flow parameters, this interaction can be either favorable or unfavorable. In many canard-configured aircraft, including some of those listed above, the main benefits of the canards are realized during maneuver or other dynamic conditions. Therefore, the detailed study of canards as aerodynamic performance or primary control surfaces requires the accurate prediction of both the steady and unsteady aerodynamics of such configurations. Proper utilization of canards requires the detailed and complete understanding of the canard’s steady and unsteady influence on the flow structure about the wing.

1.2 Background

At moderate angles of attack, for aft-swept lifting surfaces with sharp leading edges, the flow can separate at the leading edge due to the adverse pressure gradient on the leeward side. Figures 1.1 and 1.2 show a perspective and crossflow-plane schematic, respectively, of the flow structure over a typical canard or wing with leading-edge separation. A free vortex sheet is formed which rolls up over the upper surfaces of the canard or wing. If the vortex is strong enough, secondary (S_2) and, in some cases, tertiary (S_3) separations may result.

The flow structure of highly-swept or delta canard-wing configurations is characterized by a canard-downwash which modifies the wing flowfield and an interaction between the canard and wing vortex systems. A schematic of a typical canard-wing vortex interaction is given in figure 1.3. In the absence of vortex breakdown over the canard, the canard vortex convects downstream and modifies the wing flow structure through its induced flow and interaction with the wing vortex. The downwash of the canard modifies the flowfield of the wing within the canard-tip span-line by decreasing the effective angle of attack of the wing. Beyond the canard tip, upwash from the canard increases the wing's effective angle of attack. The downwash and upwash effects of the canard significantly influence the formation of the wing leading-edge vortex. The canard downwash can weaken or delay the formation of the wing vortex, thus affecting its position over the wing surface.

The effect of changing the position of the canard or deflecting the canard can drastically alter this canard-wing aerodynamic interaction. For example, a canard positioned with a vertical offset from the wing (high- or low-canard) will have varying locations of the canard wake and leading-edge vortex relative to the wing, both of which can significantly change the canard-wing flowfield from that of the coplanar canard case. For the canard with a positive deflection angle, the stronger canard downwash and modified canard trailing edge location will also change the wing flowfield relative to that of the coplanar canard case. All of these flowfield changes can potentially affect both the aerodynamic performance as well as the stability and trim characteristics of a configuration, and need to be fully understood.

Additional flow features contributing to the complex flow structure of typical canard configurations include secondary, trailing-edge, and tip vortices, as well as regions of shock-induced or boundary-layer separation. A strong primary vortex often causes the formation of a strong secondary vortex which, from the resultant induced velocities, will significantly affect the surface pressures near the canard or wing leading edge. Furthermore, trailing-edge and tip vortices can interact with the leading-edge vortex as it convects downstream. Boundary-layer separation due to high angles-of-attack or induced by a strong recovery shock is also influenced by the presence of these vortices.

In general, the characteristics of static canard configurations are adequately represented by steady-state aerodynamics. At higher angles of attack, some of the conditions which may result in unsteady aerodynamics include large regions of separated flow and vortex breakdown. For a configuration undergoing body motion with a fixed or moving canard, the unsteady effects can be quite significant. In particular, the downwash of the canard and the interaction between the canard and wing vortices can exhibit highly non-linear unsteady aerodynamic characteristics.

1.3 Previous Studies

The use of canards for improved performance has been supported by numerous experimental studies as well as some recent computational studies. An early experimental study by Behrbohm (ref. 4) indicated the potential for improved aerodynamic characteristics of short or close-coupled canard configurations

based on the canard-wing interaction. Other experimental studies by Lacey and Chorney (ref. 5), McKinney and Dollyhigh (ref. 6), and Dollyhigh (ref. 7) showed the canard's potential for obtaining increased lift and reduced drag.

Studies by Gloss and McKinney (ref. 8), and Gloss (refs. 9–11) provided further insight into the effects of canard geometry and positioning on aerodynamic loading. Experimental studies by Gloss et al. (ref. 12), and Dollyhigh (ref. 7) examined the effects of canard size, position and deflection in the subsonic and supersonic regimes, respectively. In particular, the studies by Gloss et al. (refs. 10 and 13) identified unfavorable characteristics for the low-canard configuration. Substantial loss of lift due to the interaction between the low-canard wake and the wing was experimentally measured. However, due to the nature of these studies, which only investigated aerodynamic performance parameters, insufficient data were obtained to completely describe the canard-wing flowfield.

Lacey (ref. 14) conducted an extensive four-volume experimental study on the effects of canard geometry, position and deflection on aerodynamic loads in the subsonic to supersonic regimes. Other studies (refs. 15 and 16) investigated the effects of canard and control surface deflections on more realistic canard configurations while references 7, 11, and 12 provided detailed studies on generic canard configurations with canards at various deflection angles. Recent experimental studies by Howard and Kersh (ref. 17), and Ponton et al. (ref. 18) have given extensive information on the flow structure of deflected canard geometries in the low subsonic regime and have shown encouraging results towards the optimization of such configurations.

A series of experimental studies by Gloss and Washburn (refs. 13, 19, and 20) provided detailed measurements of surface pressures as well as integrated force quantities on a variety of configurations and flow conditions near the transonic regime. Experimental studies by Er-El and Seginer (ref. 21), Calarese (ref. 22), and Oelker and Hummel (ref. 23) concentrated on the canard and wing vortex systems and provided details into the mechanisms of their interaction.

The experimental studies cited above have, in general, concentrated on steady-state aerodynamics. Considerably fewer studies have examined the unsteady aerodynamic flowfields, and more specifically, the unsteady motion of canard configurations. An earlier study by Boyden (ref. 24) investigated the dynamic stability and response characteristics of typical canard configurations and showed potential aircraft maneuverability and agility benefits with the use of canards. More recent low-speed water-tunnel studies (refs. 25–27) from the Naval Postgraduate School have examined the effects of close-coupled canards and canard oscillations on the canard-wing unsteady aerodynamic interaction. A low-speed study (ref. 28) of an actual aircraft configuration undergoing canard pitch oscillations has also been conducted.

Computational fluid dynamics (CFD) has become a valuable tool for understanding the complex three-dimensional flow physics of canard configurations. In particular, CFD has the potential to greatly expand the understanding of the unsteady canard-wing interaction. A number of previous studies based on conformal mapping, linear and non-linear vortex lattice methods, the transonic small perturbation (TSP) equation, and the Euler equations have been performed (refs. 29–39). However, limited computational work has been performed using the time-accurate Reynolds-averaged Navier–Stokes (RANS) equations. Although viscous computations are generally not required for certain leading-edge-type separations, viscous modeling is essential to capture some of the other significant features of canard-wing aerodynamics such as vortex-induced secondary separations and other boundary-layer-type separations. With the emergence of faster computers and increased memory capacities, the time-accurate RANS equations can now be utilized.

1.4 Objectives

The primary objective of this study is to develop a complete understanding of the steady and unsteady flowfield about canard-wing-body configurations in the high-subsonic and transonic flight regimes. The development and enhancement of the computational technology necessary to predict the non-linear time-accurate aerodynamics associated with close-coupled canard-wing interactions is an integral and necessary portion of this study. In this study, the time-accurate RANS equations are solved for the flow about highly-swept, close-coupled canard-wing-body configurations. The major numerical issues involved in solving the RANS equations are addressed in detail.

The accuracy of the computational techniques developed and utilized in this study is demonstrated through extensive comparisons with available experimental data. Computational results are compared with experimental lift, drag and pitching moment coefficients, as well as surface pressure data. Accuracy is further demonstrated through grid refinement studies for the steady-state computations, and through both spatial and temporal refinements for the time-accurate computations. Comparisons of the time-accurate computational results are also made with the limited unsteady experimental data which are available.

The flow physics associated with canard configurations are studied through extensive computational simulations of the steady and unsteady flowfield. The “baseline” geometry with a coplanar canard and wing is used to examine the basic steady-flow characteristics of the canard-wing aerodynamic interaction. These characteristics include the canard-wing leading-edge vortex interaction, canard downwash effects and wing vortex breakdown. The effects of the canard’s vertical position and deflection angle on the canard-wing interaction, and subsequent steady-state aerodynamic performance, are investigated. The time-accurate simulations are utilized to examine the unsteady flowfield characteristics of canard-configurations undergoing pitch-up ramp motions, pitch oscillations of the entire configuration, and independent canard oscillations. Various pitch rates are used in the study and numerical issues affecting the accurate simulation of the unsteady flowfield are addressed.

In addition to the details of the unsteady flowfield, the influence of fixed and moving canards on the dynamic stability characteristics of the configuration are studied. The results of this study not only demonstrate the suitability of RANS simulations for aerodynamic analysis and design of canard configurations, but also provide for a future direction towards utilizing high-order CFD in stability and control simulations.

1.5 Geometry

The geometry in this study is illustrated in figure 1.4 and is based on the wind-tunnel models used by Gloss et al. (refs. 9, 10, 12, 13, 19, and 20) and Boyden (ref. 24). The current geometry has also been tested at low-speeds and high angles of attack by Calarese (ref. 22) in the wind-tunnel facilities at Wright Aeronautical Labs.

The basic geometry consists of a highly-swept wing, close-coupled canard, and a fuselage with a constant cross-sectional shape aft of the nose region. The wing and canard are composed of biconvex airfoil sections which linearly vary in thickness from 6 percent to 4 percent as defined from root-to-tip. The resulting sharp leading edges of both lifting surfaces fix the primary separation locations and are conducive to generating vortices at moderate angles of attack.

For the deflected or moving canard geometries, the canard rotates about the spanwise axis (perpendicular to the symmetry plane) at the mid-canard-root location as shown in figure 1.4. For the swept

canard, static (fixed) or dynamic deflections result in pure rotation at the canard root section and a combination of translation and rotation at the canard tip.

The cross-sectional shape of the body allows for a +10 to -10 deg mid-canard deflection without a canard-root/body gap. Canard deflection angles, δ_c , are given relative to the body axis (or wing position) with positive δ_c resulting in higher canard angles of attack (α_c). The $\delta_c = 0.0$ deg mid-canard deflection represents the coplanar canard case.

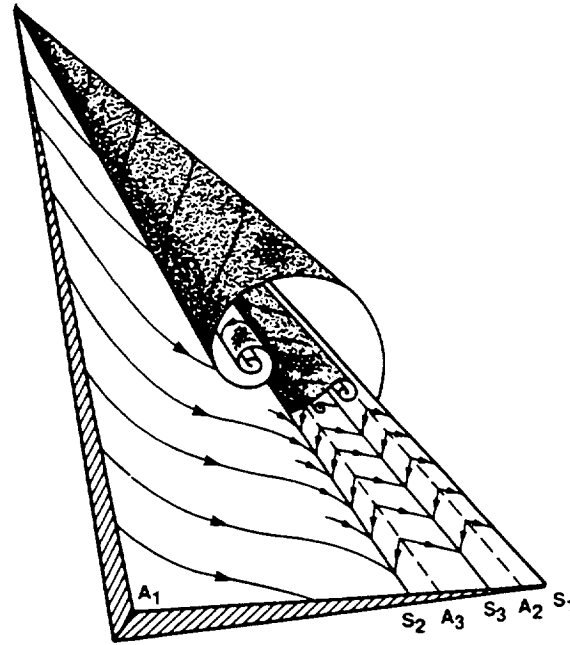


Figure 1.1. Sketch of the leading-edge vortex structure of a canard or wing.

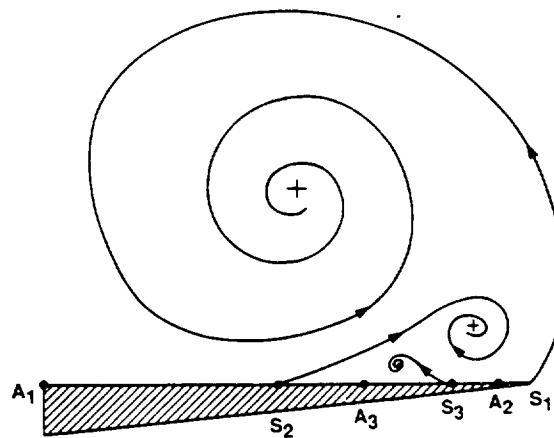


Figure 1.2. Crossflow plane sketch of the leading-edge vortex.

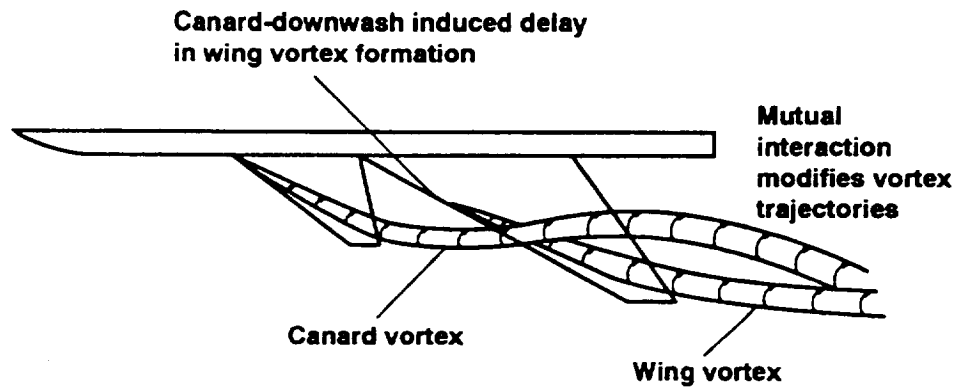


Figure 1.3. Schematic of the typical steady-state canard-wing vortex interaction for a configuration at moderate angles of attack.

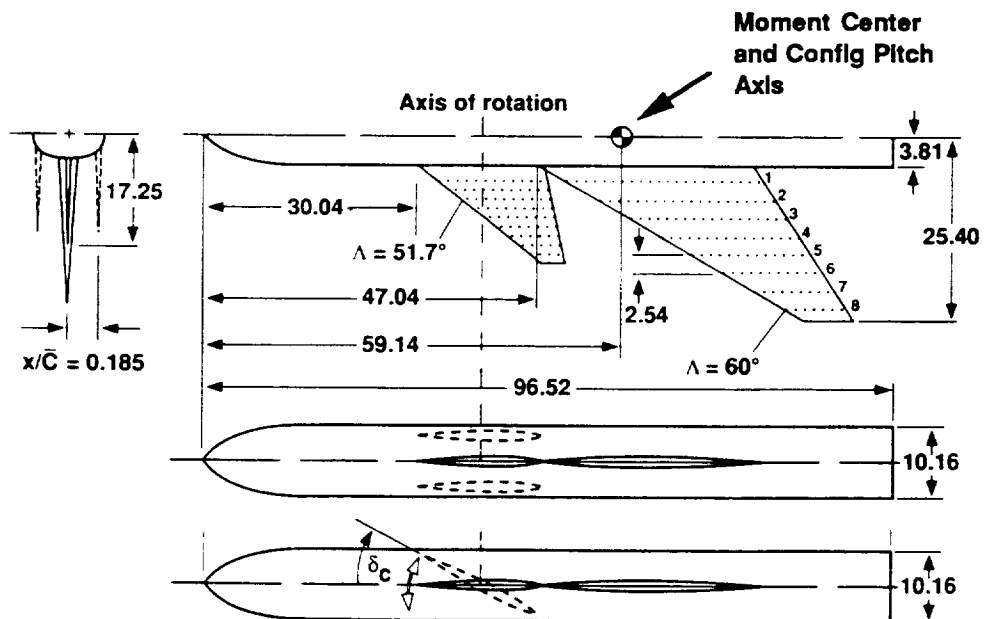


Figure 1.4. Close-coupled canard-wing-body geometry (pitch axis, moment center, and canard vertical locations shown).

Chapter 2

Computational Modeling

The ability to accurately simulate the steady and unsteady flowfield of close-coupled canard configurations is governed by the appropriate computational modeling of the relevant flow physics. Time-accurate vortical flows, transonic shocks, and viscous effects including boundary-layer separations are a few of the present features which require accurate computational modeling. In addition to the complex flowfield, geometric complexities, including moving surfaces, require advanced zonal interfacing and dynamic grid generation techniques.

The computational modeling used in this study is presented in the current Chapter. Geometry modeling, grid generation, and other case-dependent issues such as zonal interfacing and boundary conditions are discussed in detail. The methods and procedures which comprise the developed computational technology for accurately simulating canard-wing-body flowfields is described. Details on the formulation of the governing equations, numerical algorithm, and turbulence modeling are found in the Appendices.

2.1 Numerical Method

The numerical method used in this study is based on the solution of the Reynolds-averaged Navier-Stokes equations. Due to the significant potential for the presence of transonic and crossflow shocks, the strong conservation law form of the Navier-Stokes equations is utilized. As is typical for the solution of the governing equations using body-fitted structured grids, the Navier-Stokes equations are transformed to and solved in general curvilinear coordinates.

In general, for high Reynolds number flows, viscous effects are most significant in a thin region near solid surfaces. Furthermore, in order to resolve the high gradient flow features normal to the body surface, the spatial grid resolution is highest in the body-normal direction. Hence, viscous terms along the body are often neglected and the solution of the resulting “thin-layer” Navier-Stokes equations is obtained. However, it is noted that for complex configurations, the body normal directions are not always confined to one curvilinear coordinate direction. The thin-layer approximation is often made in all three directions and, as a result, only the cross-derivative viscous terms are neglected.

The algorithm employed to solve the Reynolds-averaged Navier-Stokes equations is the Beam-Warming alternating-direction-implicit (ADI) algorithm (ref. 40). The form of the Beam-Warming algorithm used in the current study is second-order accurate in space and first-order accurate in time. Higher-order time accuracy is available with minor modifications, but is generally not required due to the small stability-restricted time step sizes. For steady-state applications, the diagonal form (ref. 41) of the Beam-Warming algorithm is utilized. The diagonalization of the original block tridiagonal matrices

results in scalar pentadiagonal matrices, which have much simpler and more efficient matrix-inversion properties with the same second-order spatial accuracy (refs. 42 and 43). The use of spatially-varying (or local) time stepping in conjunction with the diagonalization procedure leads to highly efficient steady-state computations. Further details on the governing equations and numerical algorithm can be found in reference 43 and are also presented in the Appendices.

2.1.1 Turbulence modeling

For simulations of complex geometries and flowfields, practical resource considerations dictate the use of relatively large space and time scales in the computations. These scales are inadequate for direct or large-eddy simulations of turbulent fluid motions. Therefore, the RANS equations are used to simulate the flowfield. Using the RANS equations, high frequency small scale motions associated with turbulence are not resolved. However, as a result of the RANS “time-averaging” process, additional terms representing effective stresses due to turbulence can be modeled. In this study, the Baldwin-Lomax algebraic model (ref. 44) is used to provide this turbulence closure.

The Baldwin-Lomax model simulates the effects of turbulence by computing an “effective” viscosity in the stress terms of the Navier–Stokes equations. This effective viscosity is determined from a two-layer algebraic model where the inner layer is a function of density, mixing length, and vorticity magnitude. The outer layer is also based on vorticity distribution with additional parameters which are functions of wall-normal distance and maximum differences in velocity magnitudes.

Since the inner algebraic model is a function of vorticity magnitude within the boundary-layer, care must be exercised when using the model in vortex-dominated flowfields. In particular, when vortices are present near the surface boundary layer, the unmodified Baldwin-Lomax model can yield inaccurate turbulent viscosity estimates by scaling with the high vorticity values within the vortex core. For the canard and wing with sharp leading edges, these strong vortices are expected to form. Therefore, modifications as suggested by Degani and Schiff (ref. 45) are utilized in the current study. These modifications provide searching logic within the turbulence model to ensure proper boundary-layer vorticity scaling. Further details of the Baldwin-Lomax turbulence model are presented in the Appendices.

2.1.2 Code performance

Although supercomputing technology is rapidly expanding, particularly in the area of scalable parallel computing, code performance continues to be an area of major concern for large-scale complex simulations. A majority of the CFD community continues to rely on serial supercomputers running efficient highly-vectorizable flow solvers. Even though the efficiency “bottleneck” in CFD is often identified as geometry definition and grid generation, the ability to compute detailed unsteady flowfields about complex geometries is highly dependent on code performance. Memory, CPU cycle requirements and convergence or time-step characteristics for a given flow solver are key performance factors.

The general performance characteristics of the current flow solver including turbulence modeling, multi-zoned interfacing (for steady-state simulations), and the application of boundary conditions are described below. Approximately 30 words of in-core memory are required for each grid point and the typical Cray C90 single-processor performance is measured at 450 MFLOPS and 6 μ sec per iteration per grid point. It is noted that the performance estimates are dependent on maximum vector lengths which is a function of the specific computational-space dimensions. The additional “overhead” for dynamic gridding, moving interfaces and more complex boundary conditions, which are required for the moving canard cases, increases the cited computational time requirements by up to 100 percent.

A significant amount of this increase is due to interface searches and interpolations when mismatched moving interfaces are required by geometry complexities.

For steady-state computations, approximately 4,000 iterations are required to converge from free-stream conditions. Convergence is determined by a 3+ order-of-magnitude reduction in L2 Norm values as well as constant force, moment and pressure predictions. Angle of attack, Mach number or Reynolds number perturbations require an additional 1,500 iterations for re-convergence. The number of iterations for convergence increases at higher angles of attack, where vortices are stronger and the presence of vortex breakdown is possible. The number of CPU hours required for a typical steady-state simulation of the canard-wing-body configuration ranges from 5 to 20 C90 hours depending on grid size and convergence characteristics.

The number of iterations and overall computational time for unsteady cases varies widely. A typical unsteady pitch oscillation case requires up to 14,000 iterations per cycle, depending on time-step size and grid resolution. For most flow conditions, 2-3 cycles starting from a converged steady-state condition are sufficient to obtain a periodic solution. At worst, almost 150 hours of C90 CPU time may be required to obtain a periodic condition for a refined-grid simulation of a moving canard configuration. Considerably less CPU time is needed for other presented unsteady results using coarser grids, larger time steps, and higher reduced frequencies or pitch rates. In fact, key results presented in Chapter 4 show that higher pitch-oscillation frequencies can be used to significantly reduce the computational requirements for dynamic stability predictions.

2.2 Geometry Modeling

The fuselage, wing, and canard of the current geometry are analytically defined and, therefore, are computationally modeled with a high degree of geometric fidelity. However, in order to simplify the modeling, certain aspects of the geometry are approximated. In particular, differences between the computational and wind-tunnel models exist in the canard-body junction region, and near the tips of both the canard and wing. Other regions which have negligible aerodynamic effects in this study are omitted or altered as indicated.

The geometry used in this study has been tested extensively in a variety of wind tunnels as outlined in section 1.5. For these wind-tunnel models, fairings were used to facilitate a vertical-offset canard (i.e., non-coplanar) and are present for both coplanar and non-coplanar models. These fairings, which account for slight asymmetries in some of the experimental results, are omitted in the current computational modeling. The vertical tail, which is included in one of the experimental studies (ref. 24), is expected to have minimal effects on the static and dynamic longitudinal characteristics and is also omitted in the present study.

The computational modeling for the vertical-offset canard geometry (high- or low-canard) is accomplished by vertically translating the coplanar canard (mid-canard). The surfaces of the canard are then extended into the upper or lower portion of the fuselage by linear extrapolations. This extrapolation results in a thicker canard-root section for the vertical-offset canard. The 6 percent thickness, mentioned in section 1.5, applies to the canard span station located at the same span as the wing-root.

The sting used for wind-tunnel mounting is modeled by extending the body to the downstream boundary. In order to compare with the experimental data, integrated force and moment results are given for the configuration *without* the sting and the predicted drag coefficients are corrected to free-stream static pressure on the base area of the model.

2.3 Static Grid Generation

Details of the grid generation process for the static geometry simulations are presented in this section. A procedure for efficient grid generation of static canard-wing-body geometries has been developed and is outlined in figure 2.1. In general for static cases, grid generation occurs only once and can be performed as interactive pre-processing or, for sufficiently simple geometries, as an automated initialization routine within the flow solver code. It is also noted that, as opposed to dynamic geometry cases, total computational expenses involved in grid generation of the static geometries are not significant.

2.3.1 Surface grids

The baseline surface grids for the static canard-wing-body configurations are generated with algebraic techniques. Using the S3D surface geometry and grid generation code (ref. 46) developed at NASA Ames Research Center, the canard, wing and body component surface geometries are modeled from their original analytical definitions. Figures 2.2 and 2.3 show the baseline and refined surface grids, respectively, generated for the wing-body configuration with and without the fixed mid-canard. The upper surface of the half-model canard-wing-body grid contains 4,625 (baseline) and 8,790 (refined) points. To capture complex flow regions, the canard and wing surface grids are clustered near the leading edge, trailing edge, and tip. For the wing-body alone geometry, the total number of points on the half-body surface is reduced to 2,110 (baseline) and 4,320 (refined) points.

For the vertical-offset canard geometry, translation, extension and body intersection of the canard surface grids are required. These steps are shown schematically in figure 2.4. Starting with the mid-canard baseline surface grid, the canard and fore-fuselage are separated from the rest of the surface grid. The canard is translated in the vertical direction as required, and then the root section of the canard is extended towards the body centerline using linear extrapolation. Finally, surface grid intersection techniques employed in the S3D (ref. 46) program are used to produce a single, continuous, offset canard-wing-body grid. An example of the surface grid for the high-canard case is shown in figure 2.5.

Deflecting the canard is performed with an algebraic redistribution of the undeflected canard surface grid combined with cubic spline interpolation. As with the vertical-offset canard geometries, only the canard portion (canard plus forebody) of the surface grid is modified for the deflected canard cases. The generation of the deflected canard surface grid, shown schematically in figure 2.6, is outlined as follows:

1. Starting with the undeflected canard grid, the canard points are rotated about the specified axis;
 2. The upper/lower body dividing line forward of the canard is assumed to be parabolic;
 3. The axial distribution of the body cross-sections is adjusted according to the rotated canard;
- and
4. The points along each cross section are redistributed using cubic spline interpolation based on the new arc length of each section.

It is emphasized that for all deflected canard cases, the canard is actually rotated (not sheared) about the mid-canard-root spanwise axis to maintain high geometric fidelity. An example of the surface grid for the deflected canard case ($\delta_c = 10.0$ deg) is shown in figure 2.7.

2.3.2 Flowfield grids

The static flowfield grids are generated by solving the elliptic grid generation equations with orthonormal and clustering control functions near the zonal boundaries. Such techniques are readily available

in grid generation programs such as 3DGRAPE (ref. 47) and GRIDGEN (ref. 48), both of which are utilized for the current canard-wing-body geometry.

The baseline grid for the undeflected mid-canard configuration is shown in figure 2.8 and is generated as a single block, H-O topology grid with 152 axial, 32 radial, and 97 circumferential points. The H-O topology is ideal for this type of configuration because of the natural clustering of grid points in certain regions of the grid. When clustering is applied to obtain a viscous grid at the canard, wing, and body surfaces, grid clustering also results along the complex flow regions of the canard and wing wakes, and in the singularity regions along the nose radial axis and upstream of the canard. In order to resolve the viscous boundary layer near the canard, wing and body surfaces, an average value of $y^+ < 3$ for the first point away from the wall was achieved by clustering the flowfield grid to the surface (average first grid spacing is approximately $10^{-6}\bar{c}$), where y^+ is defined as (ref. 49)

$$y^+ = \frac{y\sqrt{\tau_w\rho}}{\nu_w} \quad (2.3 - 1)$$

In equation 2.3-1, y is defined as the wall-normal coordinate direction. The stretching of the grid in the wall-normal direction is also minimized (typically, stretching factor < 1.2) to reduce numerical errors.

For the refined flowfield grid, the total number of points is increased from approximately 470,000 to over 1.7 million. As shown in the expanded view of figure 2.9, refinement of the grid is emphasized in several key regions of the flowfield. In addition to an improved surface grid distribution, refinement is achieved in the interaction region between the canard and wing. The viscous regions near all of the surfaces are also refined by reducing the stretching factor while maintaining the original y^+ criteria. By reducing the amount of grid stretching, the resolution of any vortices near the canard and wing surfaces will be improved.

Earlier figures 2.5 and 2.7 showed that the generation of vertical-offset or deflected canard surface grids produces a mismatch on the body at the canard-wing junction. Furthermore, a geometric mismatch is observed between the trailing-edge root of the close-coupled canard and the leading-edge root of the wing. Consequently, to maintain the desired H-O topology grids, a mismatch is produced in the zonal interface separating the canard and wing portions of the flowfield grid.

The flowfield grids of the different canard position and deflection cases are accommodated by generating the canard and wing portions of the flowfield grid individually, with a mutual overlapping interface analytically defined. Then, as required, the flowfield grids for the vertical offset are re-generated using the elliptic solvers.

For the deflected canard cases, rather than using interactive elliptic solvers, the flowfield grids are re-generated using an algebraic redistribution of the original elliptically-generated coplanar canard-wing-body grid. Figure 2.10 illustrates the simple technique used in the algebraic redistribution. The redistribution is performed for each line in the ζ computational direction (from the surface to the outer boundary). Based on the new position of a given surface point, each off-body point is repositioned using cubic spline interpolation scaled with arc length from the outer boundary. Although this procedure does not guarantee grid quality for large surface grid motions, it produces good quality grids and is extremely fast and robust for small surface perturbations. As such, the highly efficient algebraic redistribution procedure is well suited for the unsteady moving canard cases described in the next section and Chapter 5.

By using these techniques for both the surface and flowfield grids, the grids for any canard vertical offset and deflection angle (δ_c) can be efficiently obtained. The overall H-O topology grid, with the mismatched interface, for a typical vertical-offset and deflected canard case is shown in figures 2.11 and 2.12, respectively. An expanded crossflow plane view of the mismatched interface is also shown with

the solid grid indicating the downstream boundary of the canard portion grid. The zonal interfacing techniques used to handle the mismatched interfaces are described in section 2.6.

The number of points for the resulting flowfield grids of the coplanar, vertical-offset and deflected canard configurations are summarized in table 2.1. Where needed, up to six zones stacked in the streamwise direction are used to minimize core memory requirements. Except for the canard-wing interface of the vertical-offset and deflected canard cases, one-to-one grid matching is used on all interfaces. Since the current computations are performed in the high-subsonic and transonic regimes, all of the flowfield grids are extended upstream and downstream by approximately eight wing root-chord lengths, and in the radial direction by six wing span lengths.

2.4 Dynamic Grid Generation

The generation of surface and flowfield grids for moving geometries can be a complex and time-consuming process. In particular, for motion which is not pre-determined (e.g., dynamic maneuvers, free aeroelastic responses, active control surface motions), grid generation is required to be an integral part of the time-iterative flow solution. For prescribed motions such as forced oscillation, the process can be simplified. With sufficient computational storage resources, the gridding of prescribed motions can be obtained by generating the grids as a pre-processing step to the flow solver. However, this storage requirement becomes prohibitively large for even simple cases requiring viscous analyses. Therefore, the capability to integrate efficient surface and flowfield grid generation within a flow solver is highly desirable and is often needed.

Figure 2.13 illustrates the integration of the numerical flow solver and dynamic grid generation. As each step of the time-integration is completed, the new surface geometry position is determined. For the cases presented in this study, the configuration and canard motions are based on prescribed ramp motions or forced oscillations. However, it is noted that for dynamic maneuver simulations, the equations governing the dynamics of the configuration can be easily integrated into the flow solver/grid generation process described in this study.

Based on the new geometry position, surface grids are generated accordingly. For the moving canard configuration of the current study, the steps outlined in section 2.3.1 for deflected canards are utilized. The flowfield grid is then generated based on the algebraic redistribution concept described in section 2.3.2 and illustrated in figure 2.10. By using these techniques, dynamic grid generation of the moving canard flowfield produces less than 10 percent in grid generation overhead with no additional computational storage requirements.

2.5 Boundary Conditions

The solution of the Navier–Stokes equations requires boundary conditions at each of the block boundaries. Although the finite difference scheme outlined in section 2.1 is implicit, the boundary conditions are applied explicitly in the current study. Numerous past computational studies have demonstrated the successful coupling of explicit boundary conditions with implicit flow solvers.

The boundary conditions which are required for external flow about canard-wing-body configurations can generally be categorized into two main types: 1) physical boundary conditions such as solid surfaces or outer boundaries of the solution flowfield, and 2) zonal boundaries or interfaces between adjacent (or the same) computational blocks. The first type of boundary condition is described below in this section. The implementation of the zonal boundary or interfacing is presented in section 2.6.

Physical boundary conditions are applied to the boundaries of the entire computational domain. For the current canard-wing-body study, these boundaries include the solid surfaces of the configuration (canard, wing, and body), inflow boundary, outer computational surfaces, and the outflow boundary. The solid surface boundary conditions are generally referred to as “no-slip” conditions. The components of flow velocity in physical Cartesian space are explicitly set to the physical velocity of the solid surface. The resulting types of solid surface boundary conditions for velocity are shown figure 2.14 and are outlined as follows:

Type 1) For a static configuration, the physical and contravariant velocity components at solid surfaces are set to zero;

Type 2) For a configuration with a fixed canard in rigid body motion, the surface grid remains fixed with respect to the physical surface and the physical velocity is set to the surface velocity (the contravariant velocity remains zero);

Type 3) For the moving canard configuration, the surface grid of the body (fuselage) will be moving relative to the physical surface. In this case, the surface velocity is computed separately from the grid velocity and is used to set the physical velocity components. If the entire configuration and the canard surface are in independent motion, both the physical and contravariant components of velocity will be non-zero. The additional computational step required for Type 3 boundary conditions is the separate evaluation of the surface velocity at a physical point from the evaluation of the total grid velocity.

Surface pressures and densities are determined with the aid of the normal momentum equation, perfect gas assumption, and an adiabatic wall condition. For flat surfaces, the normal momentum equation yields the familiar $\partial p / \partial n = 0$. For the more general case, terms due to wall curvature and acceleration of the moving surface yield

$$\frac{\partial p}{\partial n} = \frac{\rho \mathbf{u}^2}{R} + \rho \vec{a}_b \cdot \vec{n} \quad (2.5 - 1)$$

where R is the local wall curvature and $(\vec{a}_b \cdot \vec{n})$ represents the acceleration of the physical point on the surface in the outward normal direction. The first and second RHS terms in equation 2.5-1 represent effects due to wall curvature and wall acceleration, respectively.

However, further investigation of equation 2.5-1 reveals that differences in pressure due to both wall curvature and surface acceleration effects scale directly with the first spacing of the wall-normal grid. For viscous grids, the first spacing is small enough such that $\partial p \approx 0$ is a good assumption and zeroth-order extrapolation of pressure is reasonable. Density at the surface is determined by assuming an adiabatic wall condition which also yields a zeroth-order extrapolation of both temperature and density.

2.6 Zonal Interfacing

The close-coupled nature of the canard and wing surfaces can produce significant geometric and grid topological discontinuities for deflected or vertical-offset canard configurations. As described in section 2.3.2 and in figures 2.11 and 2.12, a mismatched interface in the flowfield grid can result between the canard and wing zones.

For the mismatched interface in this study, bilinear interpolation as formulated in references 50 and 51 is used to transfer flow quantities from one zone to the other. For general cases where the mismatched interface is not necessarily composed of coincident surfaces, trilinear interpolation may be required. Since this interpolation is non-conservative, accuracy has been determined by comparing

the solutions from a single-block (conservative) case with the multi-block mismatched-interface (non-conservative) case for the undeflected mid-canard configuration. Differences in surface and flowfield pressure contours between the two test cases were determined to be negligibly small.

As illustrated in figure 2.15, the mismatched interface between the canard and wing is overlapped by one streamwise grid cell and actually consists of two sets of “base” and “target” surfaces. The target surface represents the outer boundary of the current zone being solved, while the base surface is a subset of an adjacent zone and is used to provide flow information from that zone. The interpolation is performed by “locating” each point of the target surface within the set of base surface points. The search required to identify the four base points which comprise the “cell” containing the target point can be quite time consuming. After the target point is located, weighted coefficients (representing distances) are computed for the nearest three base points. These coefficients are then easily used to bilinearly interpolate the appropriate flow quantities to the target surface.

For static canard configurations, the interpolation described above is required only once and the weighted coefficients are stored for use throughout the solution process. However, for the moving canard cases, this mismatched interface will change for each time iteration and the interpolation is required for each iteration. Figure 2.13 provides a flow-chart diagram illustrating the integration of the zonal interface procedure within the solution process. After the new surface and flowfield grids are generated for the current zone and time iteration, the interpolation for the mismatched interface is performed and the appropriate flow quantities are transferred to adjacent zones. Since this process is required for each time iteration, local search techniques which can significantly improve the interpolation efficiency are employed.

Figure 2.16 illustrates a search procedure which, given a favorable starting position (cell #1), can significantly reduce the time required to perform the interpolation. For the current study with moving grids, a starting position based on the given target point position of the previous iteration is used. Since time steps and the corresponding grid movements are relatively small, a successful search and interpolation is usually accomplished within 10 search steps. The procedure is then repeated for each target point in the target surface. Using this technique, the time required to interpolate the interface is reduced by up to two orders of magnitude. For the moving canard cases, interface interpolation results in a 25-50 percent approximate increase in overall computer time requirements.

2.7 Dynamic Stability Analysis

In order to understand better the unsteady characteristics of the canard-wing-body configurations, dynamic stability analyses are performed on the time-accurate computational simulations. Both rigid pitch-oscillation of the entire configuration and independent canard oscillations (moving canard cases) are considered in the analyses. The effect of the presence of the canard on dynamic stability parameters, including pitch damping and oscillatory stability, are considered.

Using linear theory, the time-dependent moment coefficient due to rigid pitch oscillation of the entire configuration can be expressed as

$$C_m = \alpha C_{m_\alpha} + \frac{\dot{\alpha}\bar{c}}{2U_\infty} C_{m_{\dot{\alpha}}} + \frac{q\bar{c}}{2U_\infty} C_{m_q} + \frac{\dot{q}\bar{c}^2}{4U_\infty^2} C_{m_{\dot{q}}} + \dots \text{higher order terms (h.o.t.)} \quad (2.7 - 1)$$

where C_{m_α} , $C_{m_{\dot{\alpha}}}$, C_{m_q} , and $C_{m_{\dot{q}}}$ are the stability derivatives $(\partial C_m / \partial \alpha)_0$, $(\partial C_m / \partial (\frac{\dot{\alpha}\bar{c}}{2U_\infty}))_0$, $(\partial C_m / \partial (\frac{q\bar{c}}{2U_\infty}))_0$ and $(\partial C_m / \partial (\frac{\dot{q}\bar{c}^2}{4U_\infty^2}))_0$, respectively; q is the angular velocity of the configuration about

the pitch axis; and $C_{m_o} = 0$ (not included in eq. 2.7-1) for the symmetric configuration. The notation $(\)_0$ indicates that partial derivatives are evaluated assuming no disturbance from the other terms.

Assuming a sinusoidal motion of $\alpha = \alpha_m + A \sin \omega t$, where A is the amplitude of the oscillation, equation 2.7-1 can be expressed as

$$C_m = \alpha_m C_{m_\alpha} + (C_{m_\alpha} - k^2 C_{m_q}) A \sin \omega t + (C_{m_{\dot{\alpha}}} + C_{m_q}) A k \cos \omega t + \dots h.o.t. \quad (2.7-2)$$

The terms $(C_{m_\alpha} - k^2 C_{m_q})$ and $(C_{m_{\dot{\alpha}}} + C_{m_q})$ in equation 2.7-2 represent the oscillatory stability and damping-in-pitch parameters, respectively.

For the oscillating canard cases, the sinusoidal canard deflection as a function of time is given as $\delta_c = \delta_{cm} + A_c \sin \omega_c t$, where A_c is now the amplitude of the canard oscillation. In this case, the time-dependent moment coefficient due to canard oscillations is written as

$$C_m = \delta_{cm} C_{m_{\delta_c}} + \frac{\dot{\delta}_c \bar{c}}{2U_\infty} C_{m_{\dot{\delta}_c}} + \frac{q_c \bar{c}}{2U_\infty} C_{m_{q_c}} + \frac{\dot{q}_c \bar{c}^2}{4U_\infty^2} C_{m_{\dot{q}_c}} + \dots h.o.t. \quad (2.7-3)$$

where $C_{m_{\delta_c}}$, $C_{m_{\dot{\delta}_c}}$, $C_{m_{q_c}}$, and $C_{m_{\dot{q}_c}}$ are the stability derivatives $(\partial C_m / \partial \delta_c)_0$, $(\partial C_m / \partial (\frac{\dot{\delta}_c \bar{c}}{2U_\infty}))_0$, $(\partial C_m / \partial (\frac{q_c \bar{c}}{2U_\infty}))_0$ and $(\partial C_m / \partial (\frac{\dot{q}_c \bar{c}^2}{4U_\infty^2}))_0$, respectively; q_c is the angular velocity of the canard about its pitch axis.

Again, the resulting dynamic stability parameters are derived from

$$C_m = \delta_{c0} C_{m_{\delta_c}} + (C_{m_{\delta_c}} - k_c^2 C_{m_{\dot{q}_c}}) A_c \sin \omega_c t + (C_{m_{\dot{\delta}_c}} + C_{m_{q_c}}) A_c k_c \cos \omega_c t + \dots h.o.t. \quad (2.7-4)$$

where the stability terms are now expressed as $(C_{m_{\delta_c}} - k_c^2 C_{m_{\dot{q}_c}})$ and $(C_{m_{\dot{\delta}_c}} + C_{m_{q_c}})$ representing the oscillatory stability and damping-in-pitch parameters, respectively, for canard oscillations.

Similar analyses of the normal force coefficient given by

$$C_N = \alpha C_{N_\alpha} + \frac{\dot{\alpha} \bar{c}}{2U_\infty} C_{N_{\dot{\alpha}}} + \frac{q \bar{c}}{2U_\infty} C_{N_q} + \frac{\dot{q} \bar{c}^2}{4U_\infty^2} C_{N_{\dot{q}}} + \dots h.o.t. \quad (2.7-5)$$

or

$$C_N = \delta_c C_{N_{\delta_c}} + \frac{\dot{\delta}_c \bar{c}}{2U_\infty} C_{N_{\dot{\delta}_c}} + \frac{q_c \bar{c}}{2U_\infty} C_{N_{q_c}} + \frac{\dot{q}_c \bar{c}^2}{4U_\infty^2} C_{N_{\dot{q}_c}} + \dots h.o.t. \quad (2.7-6)$$

will yield the pitch displacement and pitch rate terms given by $(C_{N_\alpha} - k^2 C_{N_q})$ and $(C_{N_{\dot{\alpha}}} + C_{N_q})$ from eq. 2.7-5; or $(C_{N_{\delta_c}} - k_c^2 C_{N_{\dot{q}_c}})$ and $(C_{N_{\dot{\delta}_c}} + C_{N_{q_c}})$ from eq. 2.7-6.

The dynamic stability parameters for the canard configurations are predicted from the Fourier analysis of the computed time histories of normal force and pitching moment coefficients. For example, the time-history of computed pitching moments can be expressed as

$$C_m(t) = \frac{a_0}{2} + a_1 \sin \omega t + b_1 \cos \omega t + \dots h.o.t. \quad (2.7-7)$$

where the Fourier coefficients are given by

$$a_n = \frac{2}{T_o} \int_{-T_o/2}^{T_o/2} C_m(t) \cos(n\omega t) dt; \quad n = 0, 1, \dots$$

and

$$b_n = \frac{2}{T_o} \int_{-T_o/2}^{T_o/2} C_m(t) \sin(n\omega t) dt; \quad n = 1, 2, \dots$$

In most cases of forced sinusoidal oscillations of the canard or the entire configuration, the normal force and pitching moment responses are adequately represented by the first three Fourier coefficient terms (a_0 , a_1 , and b_1). This assumption is easily verified by direct comparisons of the original predicted responses and the Fourier analysis using only these terms.

A direct comparison of equation 2.7-7 with equations 2.7-2 or 2.7-4 yields the result

$$(C_{m_\alpha} - k^2 C_{m_q}) \text{ or } (C_{m_{\delta_c}} - k^2 C_{m_{q_c}}) = \left(\frac{a_1}{Ak}\right) \text{ or } \left(\frac{a_1}{A_c k_c}\right)$$

for pitch damping, and

$$(C_{m_\alpha} + C_{m_q}) \text{ or } (C_{m_{\delta_c}} + C_{m_{q_c}}) = \left(\frac{b_1}{A}\right) \text{ or } \left(\frac{b_1}{A_c}\right)$$

for pitch oscillatory-stability parameters. Similar analyses of the normal force responses will produce predicted values for the pitch displacement and pitch rate parameters.

Table 2.1. Surface and flowfield grid data for coplanar, vertical-offset and deflected canard configurations

Configuration	Surface points (half-body)	Flowfield grid dimension (j,k,l-normal)(zone)	Total number of grid points
Baseline canard-off	4,220	99 × 79 × 32	250,000
Refined canard-off	8,640	136 × 119 × 58	940,000
Baseline mid-canard	9,250	152 × 97 × 32	470,000
Refined mid-canard	17,580	250 × 119 × 58	1,700,000
Low- or high-canard	11,000	89 × 128 × 40 (canard) 70 × 97 × 40 (wing)	725,000
Deflect canard	9,250	84 × 97 × 40 (canard) 70 × 97 × 40 (wing)	600,000
Unsteady fixed canard ramp or pitch (baseline)	9,250	152 × 97 × 32	470,000
Unsteady fixed canard ramp or pitch (refined)	17,580	250 × 119 × 58	1,700,000
Unsteady moving canard	9,250	84 × 97 × 40 (canard) 70 × 97 × 40 (wing)	600,000

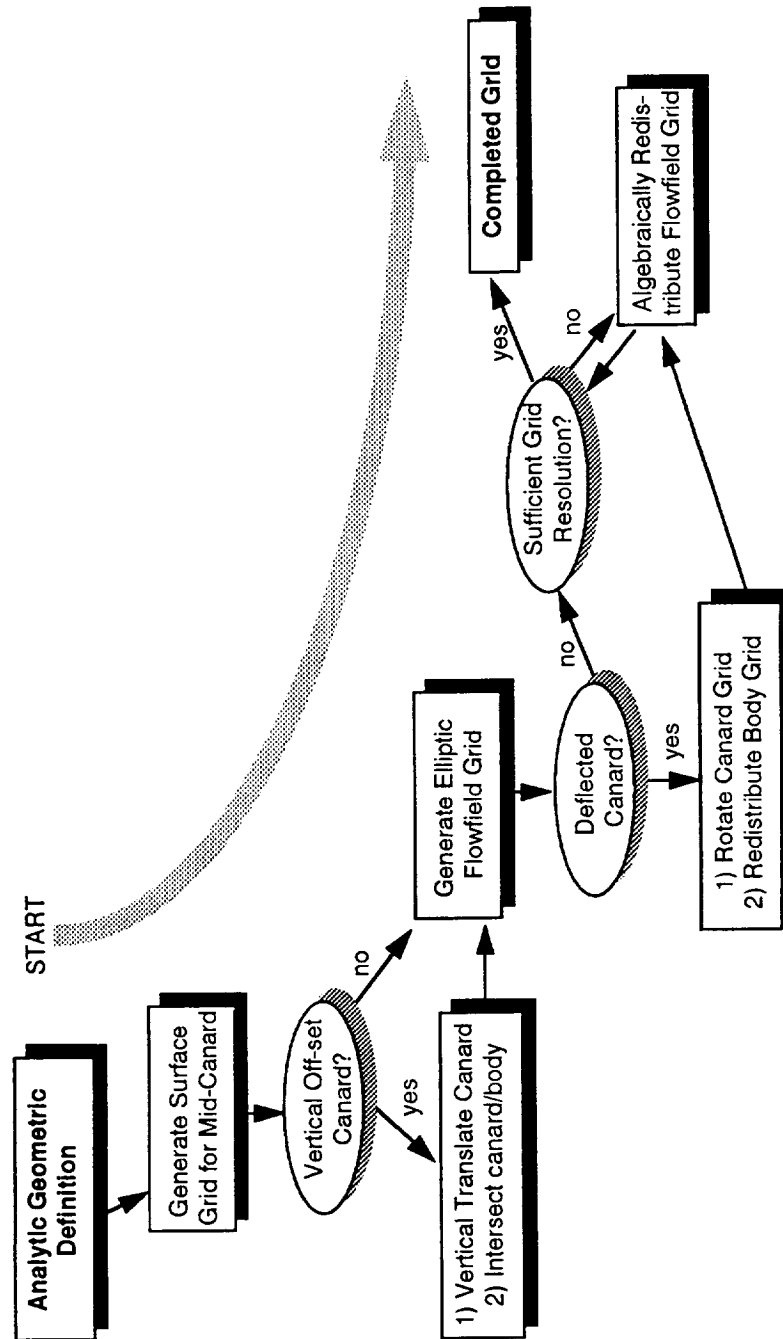


Figure 2.1. Schematic diagram of the grid generation procedure for static canard configurations with various canard vertical positions and deflections.

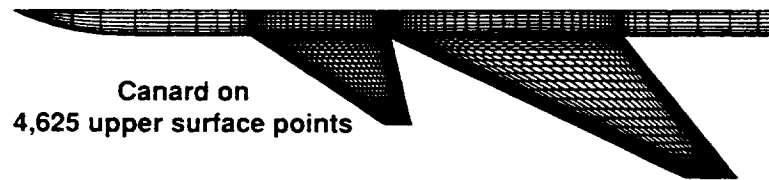


Figure 2.2. Baseline surface grid for the wing-body configuration with and without an undeflected mid-canard.

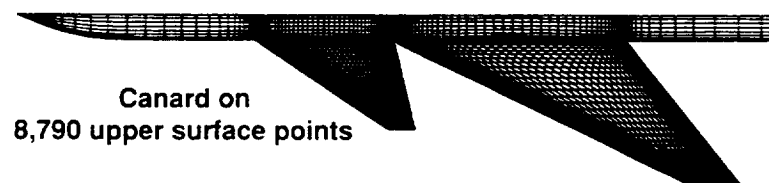


Figure 2.3. Refined surface grid for the wing-body configuration with and without an undeflected mid-canard.

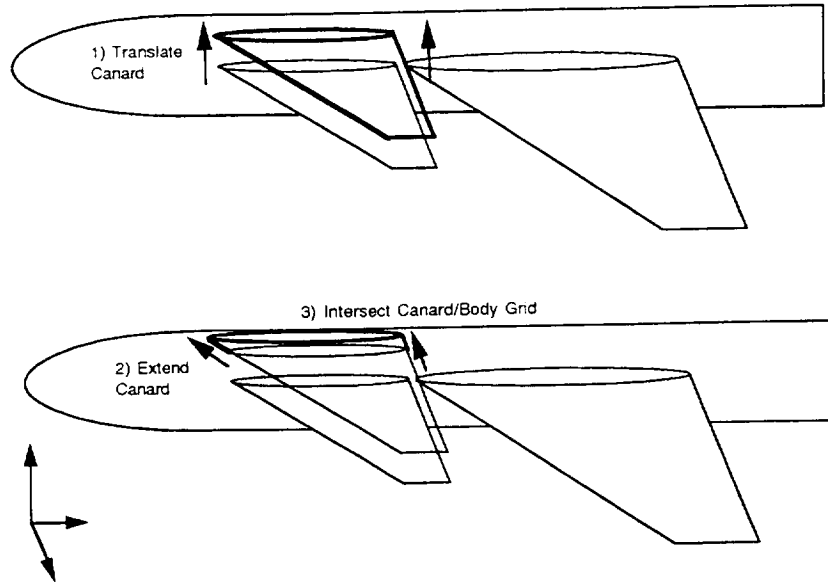


Figure 2.4. Schematic of the procedure for generating a vertical-offset canard configuration from a baseline undeflected mid-canard configuration.

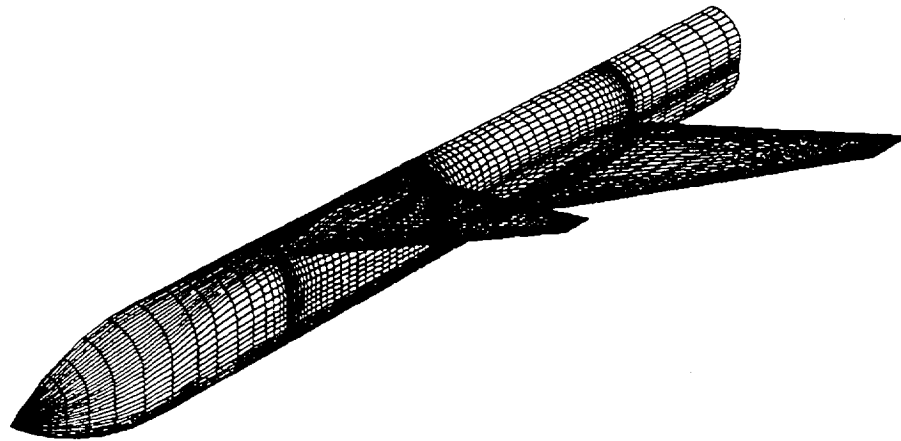


Figure 2.5. Perspective view of the surface grid for wing-body configuration with a high-canard.

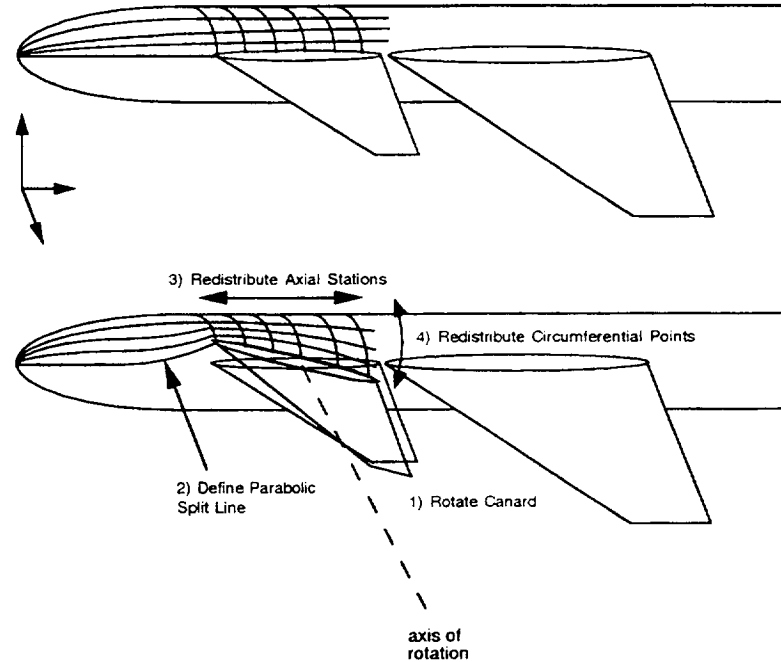


Figure 2.6. Schematic of the procedure for generating a deflected canard configuration from a baseline undeflected mid-canard configuration.

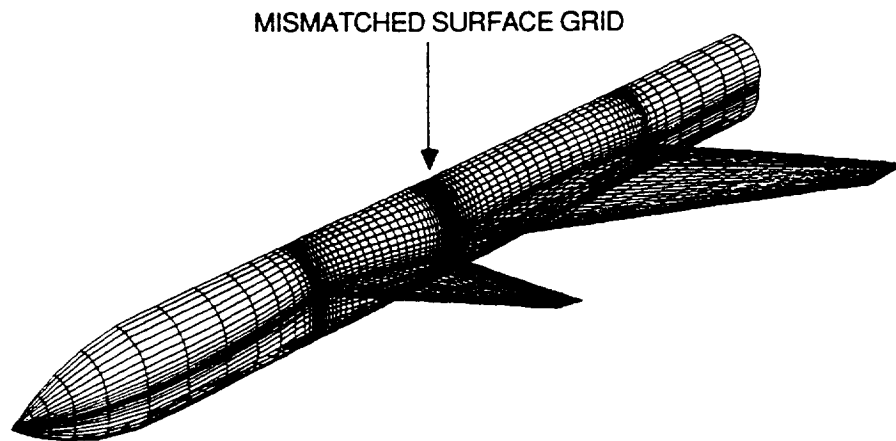


Figure 2.7. Perspective view of the surface grid for wing-body configuration with a deflected canard ($\delta_c = 10^\circ$).

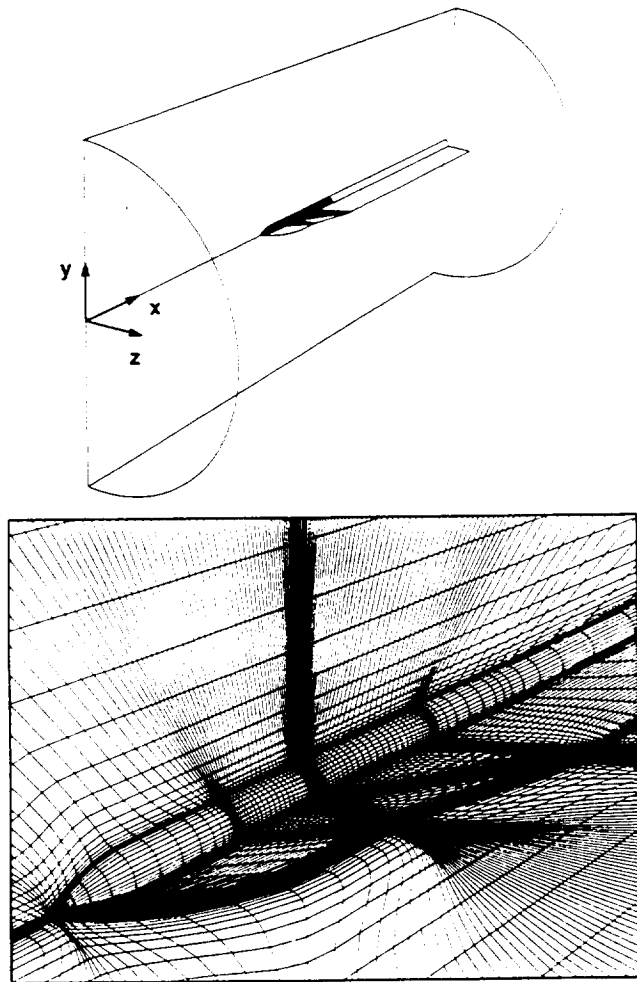
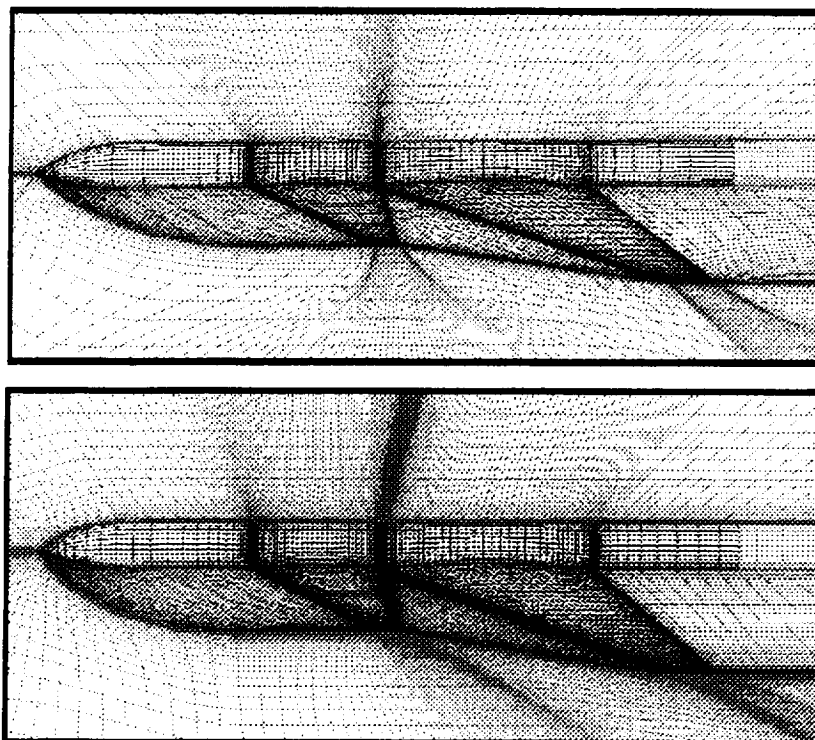


Figure 2.8. Flowfield grid topology and expanded near-body grid for the undeflected mid-canard configuration.



BASELINE GRID
152 X 32 X 97

REFINED GRID
250 X 58 X 119

Figure 2.9. Comparison of the baseline and refined near-body flowfield grids for the undeflected mid-canard configuration.

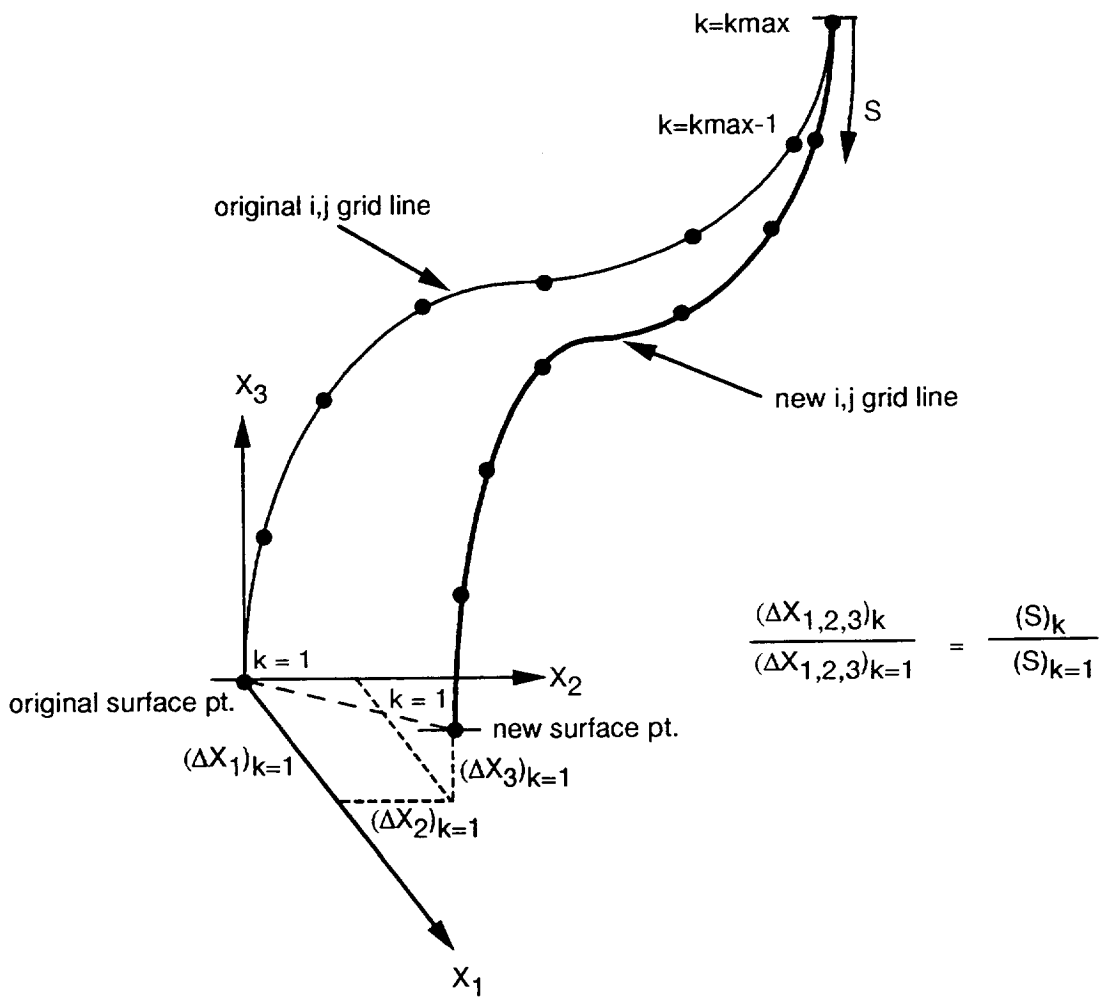


Figure 2.10. Algebraic redistribution of the flowfield grid.

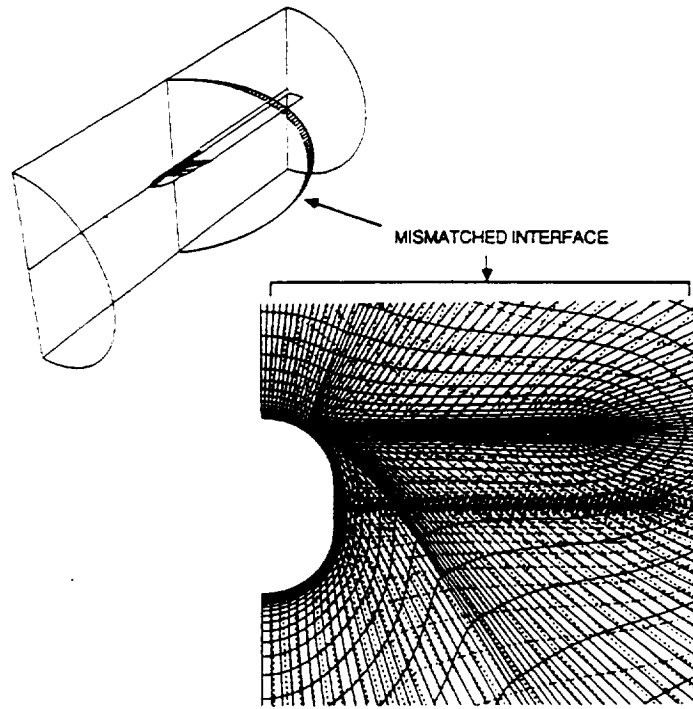


Figure 2.11. Flowfield grid at the mismatched interface surface for the high-canard configuration.

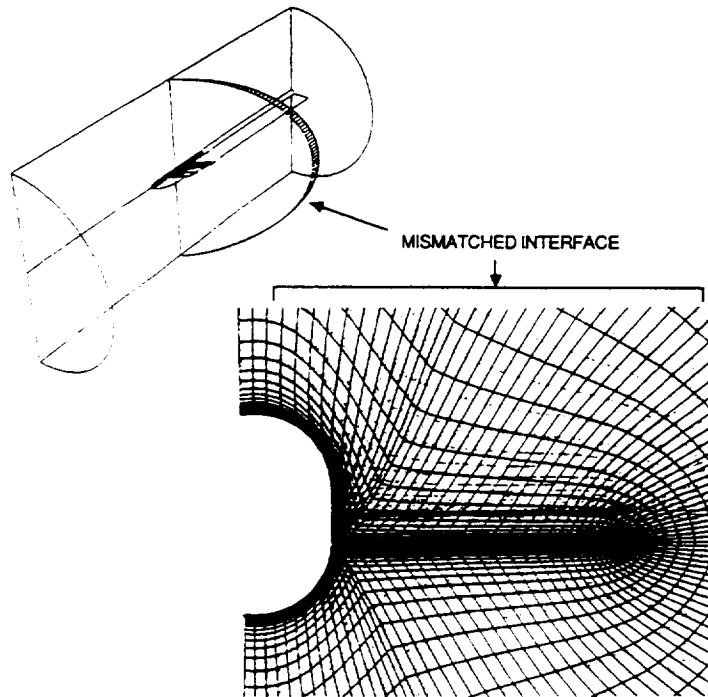


Figure 2.12. Flowfield grid at the mismatched interface surface for the deflected canard configuration.

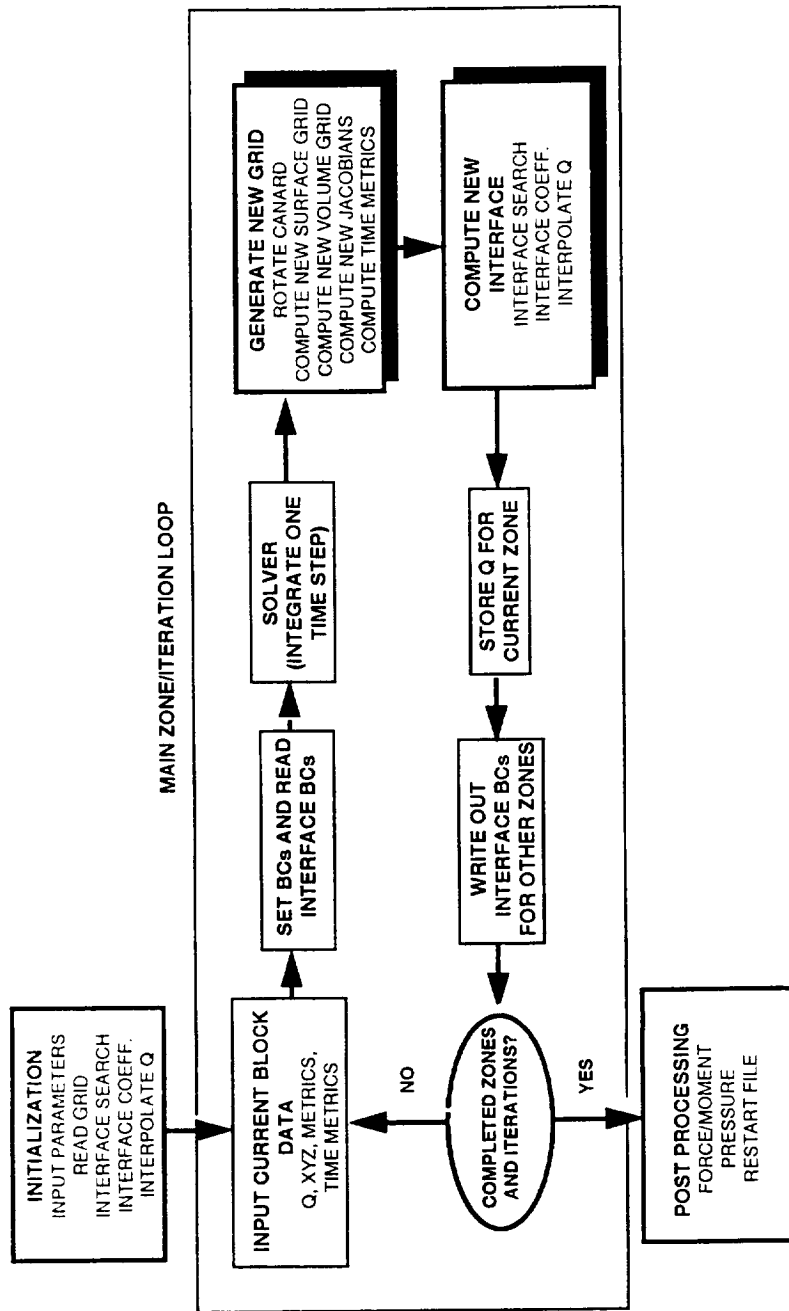
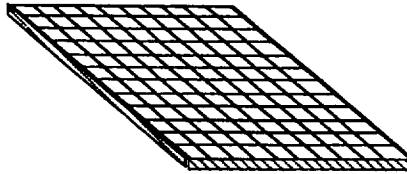


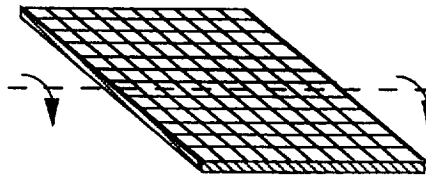
Figure 2.13. Schematic illustrating the integration of dynamic grid generation and zonal interface computation into the time-iterative solution process.

TYPE 1
 NON-MOVING WALL
 NON-MOVING GRID
 PHYSICAL VELOCITY = 0
 CONTRAVARIANT VELOCITY = 0



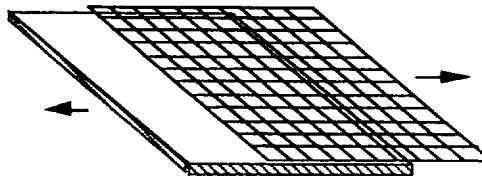
a) Fixed canard steady-state case

TYPE 2
 MOVING WALL
 GRID MOVING WITH WALL
 PHYSICAL VELOCITY $\neq 0$
 CONTRAVARIANT VELOCITY = 0



b) Fixed canard unsteady case

TYPE 3
 STATIC/MOVING WALL
 MOVING GRID INDEP. OF WALL
 PHYSICAL VELOCITY = 0 or $\neq 0$
 CONTRAVARIANT VELOCITY $\neq 0$



c) Moving canard unsteady case

Figure 2.14. Types of velocity boundary conditions at the surfaces of the canard, wing and body.

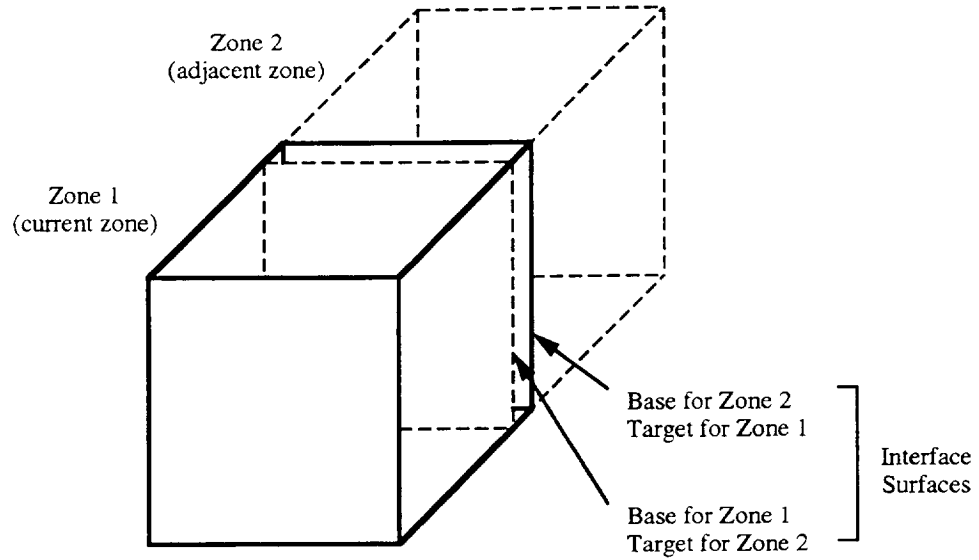


Figure 2.15. Schematic illustrating the interfacing of two adjacent zones.

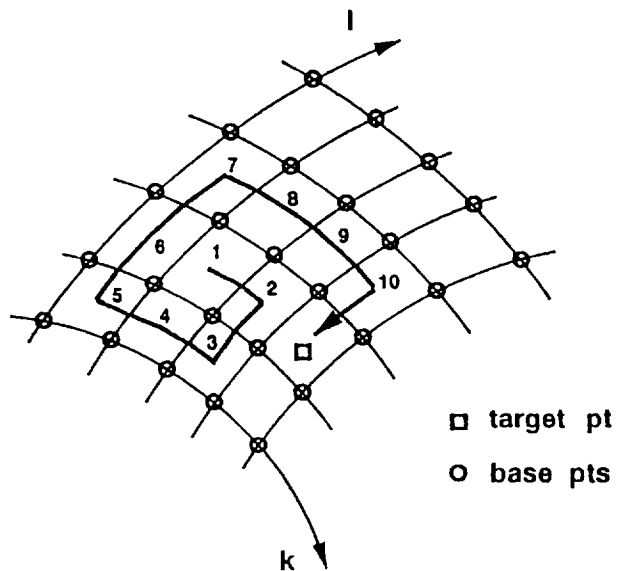


Figure 2.16. Example of a local search procedure for improved efficiency in dynamic zonal interface computations.

Chapter 3

Effect of Canard on Steady-State Aerodynamics

The influence of canards on the steady-state aerodynamics of the wing-body geometry is studied through a series of computational simulations. Computations are conducted for the configuration with and without the canard, with the canard at various vertical positions, and with the canard at specified deflection angles. The accuracy of the steady-state computations is assessed with experimental comparisons and a grid refinement study. The effect of the canard is characterized through analyses of the aerodynamic performance (e.g., lift, drag, and pitching moments), and with the detailed investigation of the canard-wing flow structure.

3.1 Experimental Validation: Coplanar Canard

To assess the accuracy of the computational modeling given in Chapter 2 for steady-state predictions, computations are conducted on the wing-body geometry with and without a coplanar canard. All computational results in this section are for a transonic Mach number (M_∞) of 0.90, a Reynolds number based on mean wing aerodynamic chord ($Re_{\bar{c}}$) of 1.52 million, and nominal angles of attack (α) ranging from 0 to 12 deg. Based on transition strips used in the experimental studies, boundary-layer transition for the computations is assumed to occur at the canard and wing leading edges and at the nose of the body. Comparisons between the computed results and the force balance and wing surface pressure measurements are made for both the baseline and refined grids.

3.1.1 Baseline grid

The first set of results is for computations performed on the baseline grids which were generated from the surface grids of figure 2.2. A comparison of computed wing surface pressure coefficients (C_p) with experimental data (ref. 13) at $\alpha \approx 4$ deg is illustrated in figure 3.1. The precise angles of attack are reported in reference 13 and are shown in the figure. It is noted that no angle-of-attack or Mach number corrections to calibrate the code were made for any computations in this study. Comparisons with the experimental data are given at wing semispan-stations of 25, 35, 45, 65, and 85 percent as measured from the symmetry plane. The first three span-stations on the wing are within the canard-span region.

For the canard-off case, the leading-edge vortex, as indicated by the suction peak in the C_p distribution, moves aft with increasing wing span. At the relatively low incidence of approximately 4 deg, the major canard influence on wing surface pressures is the canard downwash effect. Within the span

of the canard, a significant difference in wing surface pressure between the canard-on and canard-off cases is observed. The effective local angle of attack (α_{eff}) of the wing is reduced and the formation of the wing leading-edge vortex is inhibited. At wing span-stations beyond the canard tip, the wing is no longer influenced by the canard downwash and the leading-edge vortex forms. In fact, outboard of the canard tip the canard upwash increases the α_{eff} of the wing. This normally would be expected to increase the lift of the wing-tip region. However, the upwash effect is minimized due to the high sweep of the wing, which results in a relatively large distance between the canard-tip and wing-tip regions.

The discrepancies between the computed and measured data towards the wing tip are due to both computational modeling of the tip geometry and grid resolution. A previous study by Srinivasan et al. (ref. 52) found that, especially for separated and vortex-dominated flows, the modeling of the tip geometry has a considerable effect on the accuracy of the numerical results near the tip. Since detailed geometric data were unavailable for the canard and wing tips of the wind-tunnel model, the tips are computationally modeled as rounded.

In addition to the tip modeling, grid resolution has a significant effect on the accuracy of the computations. Difficulty in capturing the leading-edge vortex increases towards the canard and wing tips. As the vortex is convected downstream and away from the leading edge, computational accuracy becomes increasingly sensitive to the degrading grid resolution. This effect becomes more acute at higher angles of attack where the vortex trajectory is further above the wing surface. An effort to improve the computational accuracy by increasing the grid resolution is performed and presented later in this study.

Although detailed comparisons of flow quantities such as surface pressure are better measures of the computational accuracy, integrated quantities such as lift, drag, and moments are often used to assess the overall aerodynamic performance characteristics of a given configuration. Figure 3.2 presents the comparison of canard-on and canard-off integrated force and moment quantities for the coplanar canard-wing-body configuration. The canard-on computations are also compared with the appropriate experimental data (ref. 10). Figure 3.2 shows that the nonlinearity of the lift coefficient curve for the canard-on case is captured well by the computations. For angles of attack less than 6 deg, the computed lift coefficients for the canard-off and canard-on cases are comparable. At these low angles of attack, the reduction in wing lift due to the canard downwash is balanced by the additional canard lift. As the angle of attack is increased, the canard-on lift curve exhibits significant nonlinearity.

The drag polar in figure 3.2 indicates comparable levels of drag coefficient for both the canard-on and canard-off cases. The “cross-over” of the two drag curves shows the potential of the canard configuration for reduced drag at a given lift. At low angles of attack, the canard-on drag is higher due to the additional viscous drag of the canard surface area. At higher angles of attack, the computed additional lift due to the canard and the canard’s influence on the wing aerodynamics results in a higher lift-to-drag (L/D) ratio for the canard-on case.

Due to the relative location of the canard and the moment-center (fig. 1.4), the pitching moment curve in figure 3.2 illustrates the typical nose-up pitching moment which is characteristic of many canard configurations. At higher angles of attack, the computations overpredict the pitch-up moment of the canard-on case. This overprediction is further studied by examining the lift and moment curves of the canard and wing regions separately.

The lift and pitching moment coefficient curves for different regions of the canard-wing-body configuration are given in figure 3.3. The forward and aft regions including the body (henceforth designated as the canard and wing regions, respectively) are chosen to correspond with regions measured in the experiment (ref. 10). The significant decrease in the wing-region lift for the canard-on case in comparison

with the canard-off case is due to the canard downwash. In figure 3.3, the lift coefficient of the complete canard-on configuration is being supplemented by the canard region lift. Favorable experimental comparisons of the canard and wing region lift curves confirm that the computed lift is accurately distributed between these two regions. The pitching moment curves show that the canard's influence on the wing region pitching moment is nominal. The nose-up pitching moment of the canard-on configuration is almost entirely due to the canard region. Again, good comparisons with experimental data indicate accurate distribution of pitching moment in the computed results. Figure 3.3 also shows that the overpredicted pitch-up moment for the complete configuration, noted in figure 3.2, is approximately evenly distributed between the canard and wing regions.

3.1.2 Refined grid

At higher angles of attack, the canard and wing leading-edge vortex trajectories move above and away from the highly-clustered grid region of the canard and wing surfaces. In addition, separated regions on the wing become more prominent, recovery shock strength increases and the potential for leading-edge vortex burst exists. Accurate computational modeling of these and other relevant flow features requires improved surface and flowfield grid resolution.

To improve the accuracy of the computed results in this study, refined surface and flowfield grids were generated for the coplanar canard-on and canard-off cases. The refined surface grids were shown earlier in figure 2.3. Refinement of the wing and canard surface grids, as well as the body surface grid near the canard-wing junction, was emphasized. For the current topology, the body surface grid at the junction directly determines the grid resolution between the canard and the wing, and therefore affects the computational accuracy of capturing the canard's influence on the wing. The resulting canard-off and canard-on flowfield grids generated from the refined surface grids contain over 900,000 and 1.7 million points, respectively.

Since the wing, in the absence of the canard, exhibits a higher α_{eff} and a more pronounced leading-edge vortex, the canard-off configuration was chosen to verify the anticipated improvement in computational accuracy with the refined grid. Figures 3.4 and 3.5 illustrate computed surface pressure coefficients for the baseline and refined grids of the canard-off configuration at $\alpha = 8.21$ deg and $\alpha = 12.38$ deg, respectively. In both figures, the comparisons with the experimental data show considerable improvement for the refined grid solution over the baseline grid solution. Figure 3.6 illustrates the computed force quantities using the refined canard-off grid. Note that since the computations were performed at three angles of attack only, the refined grid results in figure 3.6 are indicated as solid square symbols. Improvements in lift, drag and pitching moment comparisons with experimental data are also observed.

A comparison between canard-on and canard-off wing surface pressure coefficients at $\alpha \approx 12$ deg is shown in figure 3.7. Good agreement between the computed and experimental data (ref. 13) shows the suitability of both the canard-on and canard-off refined grids for angles of attack up to at least 12 deg. A strong secondary vortex is evident from the sustained low pressure region between the suction peak of the primary vortex and the wing leading edge. In comparing the results of figure 3.7 with figure 3.1, one observes that for the canard-on case at higher angles of attack, the wing leading-edge vortex is no longer inhibited at the inboard wing span-stations. The vortex forms at the wing apex and remains near the leading-edge up to the wing location corresponding to the canard-tip span-line.

3.2 Aerodynamic Performance

The highly interactive flowfield of a close-coupled canard results in aerodynamic performance which is extremely sensitive to changes in canard geometry, position and deflection angle. These changes, in turn, have pronounced effects on the lift, drag and pitching moment performance of the wing and the entire configuration. In order to determine the potential aerodynamic performance benefits of utilizing canards, the effects of canard position and deflection on aerodynamic performance are investigated in this section.

Comparisons between the computed results and the available experimental data (refs. 9, 10, 12, 13, 19, and 20) are made to validate the current method for accurately predicting the steady flowfield of the vertical-offset and deflected canard cases. Computations for these cases are at transonic Mach numbers (M_∞) of 0.85 and 0.90, angles of attack (α) ranging from -4 to $+12$ deg, canard vertical positions of $z/\bar{c} = -0.185, 0.0$ and $+0.185$ (henceforth referred to as low-, mid- and high-canard, respectively), and canard deflection angles (δ_c) for the mid-canard cases from -10 to $+10$ deg. To match experimental conditions, at $M_\infty = 0.85$ and 0.90 , the Reynolds number based on the mean aerodynamic chord of the wing ($Re_{\bar{c}}$) is 2.82 million and 1.52 million, respectively. As with the earlier coplanar (or undeflected mid-canard) cases, transition strips were used in the experiments at the body nose and leading edges of the canard and wing. Therefore, the computations are performed assuming fully turbulent flow.

3.2.1 Canard vertical position

Comparisons of the lift, drag and pitching moment curves with experimental data (ref. 10) are given in figure 3.8 for the low-, mid-, and high-canard cases. Figure 3.8(a) shows the nonlinearities in the high- and mid-canard lift curves. At $\alpha > 4$ deg, significant differences are noted in the lift curves for the three canard positions. Although the absolute values of lift are slightly underpredicted by the computations, the relative differences are captured. Further investigation of the incremental changes due to canard vertical position is presented later in this section.

Figures 3.8(b) and (c) show computed drag and pitching moment coefficient comparisons with experimental measurements. At the higher angles of attack, the low-canard configuration exhibits lower drag at a given α . Figure 3.8(c) shows an overprediction of pitching moment by the computations at the higher angles of attack. This overprediction is of the same order-of-magnitude as shown earlier and discussed in figure 3.2. However, as in the lift and drag curves of figures 3.8(a) and (b), the overall pitching moment comparisons are favorable.

Figures 3.9(a) and (b) illustrate lift and moment curves, respectively, for the two component regions of the high-canard configuration. As with the coplanar canard studies, the canard region consists of the canard and the body forward of the wing leading-edge root location (fore-body). The wing region consists of the wing and the remaining aft-body (not including the sting).

The wing portion lift curve slope of figure 3.9(a) is influenced by the effect of the canard downwash on reducing wing lift. The total lift is augmented by the canard portion lift. Figure 3.9(a) also shows that the slight underprediction in total lift is primarily due to the computed wing portion lift. The pitching moment curves in figure 3.9(b) show that the wing, in the presence of the canard, exhibits statically stable characteristics while the canard pitching moment causes the total configuration to be approximately neutrally stable. Such characteristics are often typical of canard-configured aircraft and were also evident in the mid-canard configurations shown earlier. Favorable comparisons in figures 3.9(a) and (b) between computations and experimental data indicate that the distribution of lift and moment between the component regions is captured well by the computations.

In order to predict the potential benefits of placing the canard in a non-coplanar (either high- or low-canard) configuration, a more detailed analysis of the lift and drag results is required. Polynomial curve fits through the computational and experimental results are used to determine the incremental lift and drag differences due to vertical positioning of the canard.

Figure 3.10(a) shows the effect of canard vertical position on the incremental change in lift coefficient (ΔC_L) at different angles of attack. The reference line ($\Delta C_L = 0.0$) is the C_L corresponding to either computations or experiment for the mid-canard configuration. Although the absolute ΔC_L values are not exactly predicted by the computations, it is noted that relatively small values are being compared. The qualitative trends indicating the relative effects of canard vertical position are captured well by the computations. Both the computations and experiment show increased lift at higher angles of attack for the high-canard case. However, the low-canard ΔC_L curves show significant loss of lift as α is increased.

The incremental changes in drag coefficients (ΔC_d) given in figure 3.10(b) show that the high-canard configuration exhibits the best overall drag characteristics. At a higher C_L , the high-canard case has a lower C_d than both the mid- and low-canard cases. The results in figure 3.10 show clear evidence of an unfavorable canard-wing interaction for the low-canard configuration.

3.2.2 Canard deflection angle

Comparisons of the computed lift, drag and pitching moment curves with experimental data (ref. 12) are given in figure 3.11 for mid-canard deflections (δ_c) of 0 and 10 deg. Figure 3.11(a) shows the nonlinearity in the lift curves. Note that the subtle differences in the experimental $\delta_c = 0$ deg and $\delta_c = 10$ deg lift curves are captured well by the computations. The drag polar curves in figure 3.11(b) show that the undeflected mid-canard ($\delta_c = 0$ deg) exhibits a lower overall drag coefficient. The drag polars also show that minimum C_d for the 10 deg case occurs at a negative lift coefficient. Figure 3.11(c) shows that increasing mid-canard deflection increases overall pitching moment for all computed angles of attack. Significant nonlinearities due to the canard-wing interaction are also noted in the pitching moment curves.

Similar to the vertical-offset studies, the lift and pitching moment curves are separated into two configuration component regions in order to examine the effects of mid-canard deflections in more detail. Figures 3.12(a) and (b) illustrate lifts and moments, respectively, for the $\delta_c = 10$ deg case. The wing portion lift curve of figure 3.12(a) shows the effect of the canard downwash on reducing wing lift. For example, at $\alpha = 0$ deg, the additional canard lift (due to its deflection) is mostly cancelled by the negative lift generated by the wing (due to the canard downwash). The pitching moment curves in figure 3.12(b) show that the wing, in the presence of the canard, exhibits statically stable characteristics while the canard pitching moment causes the total configuration to be statically unstable. Such characteristics are often typical of canard-configured aircraft. Favorable comparisons in figures 3.12(a) and (b) between computations and experimental data indicate that the distribution of lift and moment between the component regions of the mid-canard deflection cases are captured well by the computations.

An analysis of the effect of canard deflection on lift, pitching moment, and, particularly, trimmed conditions is of interest. For long-coupled canard configurations, the effect on aerodynamic performance is usually limited to the lift of the canard itself and the total pitching moment. However, the close-coupled canard has significant influences on wing performance as well.

Figure 3.13 shows lift and moment curves for the canard and wing portions at various canard deflection angles (δ_c) ranging from -10 to $+10$ deg. While the canard portion lift curve (fig. 3.13(a)) exhibits increasing lift for increasing δ_c at a given α , the wing portion lift curve (fig. 3.13(b)) decreases

for increasing δ_c . As δ_c is increased, the canard generates greater lift and, consequently, greater downwash in the canard wake. The resulting effective wing angle of attack (α_{eff}) on the inboard portion of the wing decreases with increasing δ_c . Vortex visualization results presented later in this study will show that, for certain α and δ_c values, α_{eff} can be negative in the inboard wing while freestream α is positive.

The canard and wing portion pitching moment curves for various canard deflection angles are given in figures 3.13(c) and (d), respectively. The canard portion pitching moment increases as δ_c is increased while the wing portion pitching moment is relatively insensitive to δ_c . The strong δ_c coupling with wing portion lift (fig. 3.13(b)) and the weak coupling with wing moment (fig. 3.13(d)) indicate a significant shift in wing center-of-pressure as a function of δ_c . Due to the canard downwash effect of “unloading” the inboard portion of the wing, the aft-swept wing’s center-of-pressure location moves outboard and aft for increasing canard deflections.

Figure 3.14 illustrates lift and moment as a function of δ_c at a representative α of 4.27 deg. The lift curves in figure 3.14(a) are given for the total configuration, canard portion and wing portion. For increasing δ_c , the cancellation of the lift between the canard and wing portions is clearly observed. At this moderate angle of attack, the total lift is minimally affected by the deflection of the canard. The moment curves in figure 3.14(b) show that the canard portion moment is the major contributor to changes in the total configuration moment. At this condition ($M_\infty = 0.85, \alpha = 4.27$ deg), the configuration is trimmed about the moment center (69.17 cm from the nose) at $\delta_c \approx -4$ deg.

For a realistic aircraft configuration, the determination of trimmed lift and drag is critical in assessing aerodynamic performance. A contour plot of pitching moment about the model center-of-gravity location (c.g. = 59.14 cm from the nose) is given in figure 3.15. The trimmed ($C_m = 0.0$) pitching moment curve is highlighted and indicates that relatively small, negative canard deflections are required to trim this configuration at moderate angles of attack.

3.3 Canard-Wing Vortex Interaction

For the configurations in this study, many of the complex non-linear effects of the various canards on aerodynamic performance can be directly attributed to the canard and wing vortical flowfields and, in particular, the canard-wing vortex interaction. The current configuration flowfield is characterized by strong leading-edge vortices from the canard and the wing. As vortex strength increases, secondary separation induced by adverse pressure gradients can result in strong secondary vortices. The presence of secondary vortices will also serve to alter the position and trajectory of the primary canard and/or wing vortex. In cases of high vortex strength, tertiary separations can be observed as well.

One of the primary mechanisms for the canard-wing interaction is the canard’s influence on the wing leading-edge vortex. Both the canard downwash and the canard leading-edge vortex have pronounced effects on the formation and subsequent trajectory of the wing vortex. The canard vortex influences the surface pressures on the wing directly and, to a greater extent, indirectly through its influences on the wing vortex. Furthermore, the effect of the canard vortex on the wing is highly sensitive to vortex strength and relative location, which are both significantly modified by variations in the canard position and deflection angles.

3.3.1 Coplanar canard

A baseline analysis of the canard-wing vortex interaction is performed for the undeflected mid-canard (coplanar) configuration at $M_\infty = 0.90$, $Re_{\bar{c}} = 1.52$ million, and various angles of attack. Comparisons

are made between canard-on and canard-off cases to determine the effects of the canard on the structure of the wing flowfield.

Figure 3.16 illustrates a comparison between the upper-surface pressure contours of the canard-off and canard-on configurations at three angles of attack. These contours show a significant canard influence on the body as well as the influence of the canard and wing vortices on surface pressures. The vortex-induced low pressure region (L) gives a qualitative estimate of the vortex trajectory over the upper surface. As angle of attack increases, these low pressure regions move inboard. Note that, since the canard sweep angle is lower, and because there is an absence of a downwash field upstream of the canard, the recovery shock is strongest and most easily observed on the canard at the higher angles of attack.

Although evident in the surface pressure contours of figure 3.16, the canard's effect on the formation of the wing vortex is more clearly observed in the computed surface flow patterns given in figure 3.17. The secondary separation line (S_2) due to the wing leading-edge vortex is observed for both the canard-on and canard-off cases. As the angle of attack is increased, the secondary separation and primary attachment lines move inboard and are indicative of the upward and inward movement of the wing primary vortex. The surface flow patterns for the canard-on cases show the modified wing flowfield including the delay in wing primary vortex formation. At $\alpha \approx 4$ deg, no evidence of a leading-edge vortex is detected on the inboard portion of the wing. At $\alpha \approx 8$ deg and 12 deg, the corresponding inboard surface flow patterns are influenced by a small leading-edge vortex which is comparable to a leading-edge vortex formed for the canard-off case at lower angles of attack. These observations correlate with the surface pressure distributions which were given earlier in figures 3.1 and 3.7.

The dominating effect of the canard downwash on the wing, inboard of the canard-tip span-line, has already been illustrated. Outboard of the canard-tip span-line, the canard leading-edge vortex is the primary mechanism for the canard's influence on the wing flowfield. Crossflow-plane vortex visualizations in the form of normalized total pressure contours and velocity vectors at two constant streamwise stations are given in figure 3.18, and show the effect of the canard-vortex induced flow on the wing. The approximate total pressure loss at each canard or wing primary vortex core is also given in figure 3.18 and is an indication of the instantaneous vortex strength. Although the computed canard vortex (fig. 3.18(a)) is considerably weaker than the corresponding wing vortex, its influence on the wing flowfield is still significant. For the two co-rotating vortices, each with a counter-clockwise rotation and position as shown in figure 3.18(a), the wing vortex flowfield induces a relative downward and inward motion of the canard vortex while the canard vortex induces an upward and outward movement of the wing vortex. In the absence of such interaction, the canard and wing vortex trajectories would be expected to follow an upward and outward path which would be dependent on the angle of attack and respective sweep angles.

In addition to the canard-wing vortex interaction, the flowfield is further complicated by the presence of a counter-rotating secondary vortex. The secondary vortex for the canard-off case is clearly visible in both total pressure contours and velocity vectors of figure 3.18(b). The smaller wing vortex for the canard-on case renders the corresponding secondary wing vortex undetectable in the scale of figure 3.18(a). However, computed surface flow patterns given earlier in figure 3.17 clearly show the existence of secondary separation for both the canard-on as well as the canard-off cases. Evidence of a tertiary wing or canard vortex is not observed.

3.3.2 Canard vertical position

For the same flow conditions as the mid-canard cases given in the previous section (3.3.1), the differences in wing surface pressures between the high- and low-canard configurations are shown in figures 3.19(a)

and (b) for $\alpha = 4.27$ deg and 8.55 deg, respectively. The upper and lower surface pressure distributions are given at three wing span stations for each angle of attack. All three stations are inboard of the canard-tip span line and, therefore, are directly influenced by the high- or low-canard downwash. Results in figure 3.19 show that the relative canard and wing positions have a large effect on the level of canard-wing interaction.

At $\alpha = 4.27$ deg (fig. 3.19(a)), small differences in wing surface pressures are observed. For the high-canard case, lower pressures on the upper surface near the wing leading edge indicate the possible formation of a leading-edge vortex. In the low-canard case, formation of the wing leading-edge vortex is inhibited due to the canard downwash and the relative positions of the canard and wing.

In figure 3.19(b), the wing leading-edge vortex is clearly visible and contributes substantially to the lift of the high-canard configuration. However, even at this higher angle of attack, the low-canard results do not show evidence of a strong vortex on the inboard wing. In addition to inhibiting the formation of this vortex, the low-canard case also shows a substantial low pressure region on the wing lower surface. Both of these factors (absence of the wing vortex and low pressure on the wing lower surface) contribute to the loss of lift for the low-canard case observed in figures 3.8(a) and 3.10(a).

Further insight into the unfavorable nature of the low-canard configuration can be gained by examining the canard-wing flowfield structure. Figure 3.20 illustrates crossflow contours of stagnation pressures for the high- and low-canard configurations at $\alpha = 4.27$ deg. For each configuration, five streamwise stations are chosen to illustrate the development and convection of the canard and wing vortices. The high-canard results (fig. 3.20(a)) show the formation of the canard vortex and its subsequent trajectory *over* the wing surface. At $x/\bar{c} = 3.2$ and 3.6, formation of the wing leading-edge vortex is observed. Although the vortex positions differ, the high-canard-wing vortex interaction has similar characteristics to that of the mid-canard configuration shown in section 3.3.1.

The low-canard case given in figure 3.20(b) shows a significantly different flowfield structure. Like the high-canard case, the low-canard vortex forms as visualized at $x/\bar{c} = 2.0$. However, due to the relative position of the low-canard to the wing and the canard-wing aerodynamic interaction, the subsequent canard vortex is convected *under* the wing surface. The low-canard vortex can therefore induce an unfavorable low pressure region on the wing lower surface. The formation of the wing vortex on the upper surface is again observed in figure 3.20(b) at $x/\bar{c} = 3.6$.

Figure 3.21 shows that at the higher angle of attack of 8.55 deg, the low-canard vortex interacts directly with the wing. The original low-canard vortex ($x/\bar{c} = 2.0$) splits into two (upper and lower canard) vortices upon impact with the wing leading edge ($x/\bar{c} = 2.8$). Further downstream at $x/\bar{c} > 3.2$, the split canard vortices continue to have the same rotational structure, but now exhibit independent trajectories. The canard lower vortex (C1L), with its counter-clockwise rotational sense as viewed in the figure, tends to move inboard due to its proximity to the wing lower surface. The canard upper vortex (C1U), also with a counter-clockwise rotation, is additionally influenced and moved inward by the formation of the wing vortex (W1) on the wing upper surface ($x/\bar{c} = 3.2$ and 3.6).

To visualize the results in figure 3.21 more clearly, a qualitative schematic of the canard-wing vortex trajectories for the low-canard case is given in figure 3.22. The low-canard vortex impacts the wing leading-edge and is split into the upper and lower vortices. The wing vortex forms on the wing upper surface and interacts with the canard upper vortex.

A perspective view of the low-canard vortex interaction with the wing is given in figure 3.23 for $\alpha = 8.55$ deg. Crossflow contours of stagnation pressures show the formation of the canard vortex, the splitting of the canard vortex by the wing, and the formation of the wing vortex on the outboard wing. The effect of this wing vortex on the canard upper-vortex trajectory is also clearly visible.

3.3.3 Canard deflection angle

In addition to those canard influences due to changing vertical position, the additional freedom-of-motion of mid-canard deflections allows for further variations in the types of canard-wing vortex structures. Changing δ_c affects the strength of the canard downwash and vortex, the location of the canard trailing-edge relative to the wing, and the subsequent canard vortex trajectory in the wing flowfield.

Results given in section 3.2.2 illustrated the effect of canard deflections on lift, drag and pitching moments for the entire configuration and the separate canard and wing component regions. The aerodynamic performance characteristics from that section are better understood with further analyses of the canard-wing vortex interactions. The differences in surface flow patterns for $\delta_c = 0$ deg, 5 deg and 10 deg are illustrated in figure 3.24. As for the undeflected mid-canard case, the secondary separation lines from the canard and wing primary vortices are indicated (S2) for each case and show that viscous effects are significant to the overall flow structure. As canard deflection is increased, the secondary separation line on the canard moves inward reflecting the upward and inward shift of the canard vortex. In all three cases, the secondary separation line forms near the apex of the canard while its formation on the wing inboard is inhibited. At this angle of attack, the formation of the wing vortex is delayed until outboard of the canard-tip span location.

Figure 3.25 illustrates the effect of canard deflection on wing surface pressure at 35, 55 and 75 percent semispan. For clarity, the upper surface pressure curves are indicated (U). As canard deflection is increased from 0 to 10 deg, the near-leading-edge lower surface pressure at 35 percent span transitions from positive to negative values. At $\delta_c = 10$ deg, a strong suction peak exists on the lower surface, indicating the possibility of a wing vortex on the wing lower surface. Furthermore, high upper surface pressures at 35 percent span are clearly indicative of a decrease in local angle of attack for the inboard wing with increasing canard deflection angle. The loss of wing lift due to these pressure changes was shown previously in figure 3.13(b). Towards the outboard stations, figure 3.25 shows that the effect of canard deflection on surface pressure is minimal.

To visualize the effect of canard deflection on the canard-wing vortex interaction, crossflow contours of total stagnation pressures are given in figure 3.26 for $\delta_c = 5$ deg and 10 deg. The crossflow contours are shown at $x/\bar{c} = 2.0, 2.8$ and 3.5 as measured from the fuselage nose. The relative primary vortex strengths are indicated in the figure by the approximate total pressure loss in the vortex core. For $\delta_c = 5$ deg (fig. 3.26(a)), there are canard primary (C1), canard secondary (C2), and wing primary (W1U) vortices over the upper surfaces of the canard and wing. The distortion of the canard primary vortex at $x/\bar{c} = 2.8$ is due, in part, to the canard secondary vortex.

At $\delta_c = 10$ deg (fig. 3.26(b)), an additional wing primary vortex (W1L) forms and is visible on the wing lower surface ($x/\bar{c} = 2.8$). This vortex causes the suction peak on the lower surface of the wing observed earlier in figure 3.25 and would generally be considered an unfavorable effect. At these flow conditions, there is a transition from negative to positive effective wing angle of attack, α_{eff} , from the wing-root to wing-tip locations. At the last station, $x/\bar{c} = 3.5$, the wing flowfield structure for the $\delta_c = 10$ deg case includes two wing primary vortices (upper and lower) as well as the canard primary vortex.

The mutual interaction between these vortices is an important factor in wing performance and is complex in nature. A comparison of the relative position of the canard vortex between $x/\bar{c} = 2.8$ and 3.5 in figure 3.26 shows that the trajectory of the canard vortex is influenced by the wing upper-surface vortex. For two co-rotating vortices (canard and wing primary), each with a position and counter-clockwise rotation as shown in the figure, the wing vortex induces a relative inward motion of the canard vortex.

The influence of the wing vortex on the canard vortex trajectory is more clearly visualized in figure 3.27, which illustrates the upper surface canard and wing vortex systems for $\delta_c = 5$ deg and 10 deg. Crossflow contours of total stagnation pressure are shown at selected streamwise stations. As shown earlier in figures 3.24 to 3.26 for both $\delta_c = 5$ deg and 10 deg, the formation of the wing vortex on the wing upper surface is inhibited by the canard downwash until outboard of the canard-tip span location. The difference in the canard primary and secondary vortex strengths between the two δ_c cases is qualitatively observed. In each case, as the canard primary vortex is convected over the wing upper surface, the wing primary vortex in the outboard region clearly modifies the canard vortex trajectory inward.

Figure 3.28 shows a perspective view of the overall flowfield for the configuration at $\alpha = 4.27$ deg and $\delta_c = 10$ deg. The darker region over the canard upper surface indicates low pressure induced by the canard vortex. The particle traces released near the wing root and towards the wing tip show the formation of the leading-edge vortices on both the upper and lower surfaces.

3.4 Effect of Canard on Wing Vortex Breakdown

The potential for a canard to delay or eliminate wing vortex breakdown is of significant interest and has been the topic of numerous experimental studies (refs. 19, 21, 53, and 54) and a recent numerical study (ref. 55). By comparing vortex lift theory with experimental results, Gloss and Washburn (ref. 19) found that wing vortex burst occurs at $\alpha \approx 13$ deg for the current canard-off case. For the undeflected mid-canard case, their study indicated no evidence of wing vortex burst for angles of attack up to at least 20 deg.

Figure 3.29 shows a crossflow-plane visualization of the predicted wing vortex for the canard-off case at three angles of attack. At the higher angles of attack, the resulting increased vortex strength and relative shift of the core location is observed in the normalized total pressure contours. The development of the secondary vortex is also noted. The corresponding off-surface particle traces for the canard-off cases are shown in figure 3.30. Evidence of vortex burst in the computational simulation is observed at $\alpha = 12.38$ deg. Crossflow-plane visualization of scaled axial velocity contours in figure 3.31 serves to confirm the presence of predicted vortex breakdown over the wing for the canard-off case. Reversed axial flow in the core of the primary vortex is identified (ref. 56) as a qualitative indication of vortex breakdown, and is observed in figure 3.31. From figure 3.30, the wing vortex burst location appears to be near the trailing edge of the wing and indicates that the computed angle of attack for vortex burst is approximately 12 deg, which is within reasonable agreement with the experimental observations (ref. 19).

Computed particle traces for the undeflected mid-canard case at $\alpha = 12.38$ deg are given in figure 3.32. The lower leading-edge sweep-angle of the canard results in a canard vortex burst further upstream of the canard trailing edge compared to the wing vortex burst relative to its trailing edge shown earlier. Figure 3.32 shows a stable wing vortex with no evidence of wing vortex breakdown in the presence of the undeflected mid-canard. Although not computed directly for this study, the results shown in Secs. 3.2 and 3.3 indicate that wing vortex breakdown is quite possible given certain canard vertical positions and deflection angles.

The good comparisons with the experimental data for both the canard-on and canard-off cases at $\alpha \approx 12$ deg and the corresponding canard-off vortex burst location near the wing trailing edge show that the computed relative effects on vortex breakdown location and behavior in the presence of the canard are accurate. However, it is noted that vortex breakdown is generally an unsteady phenomenon and steady-state computations downstream of the burst location may be suspect. To perform a detailed

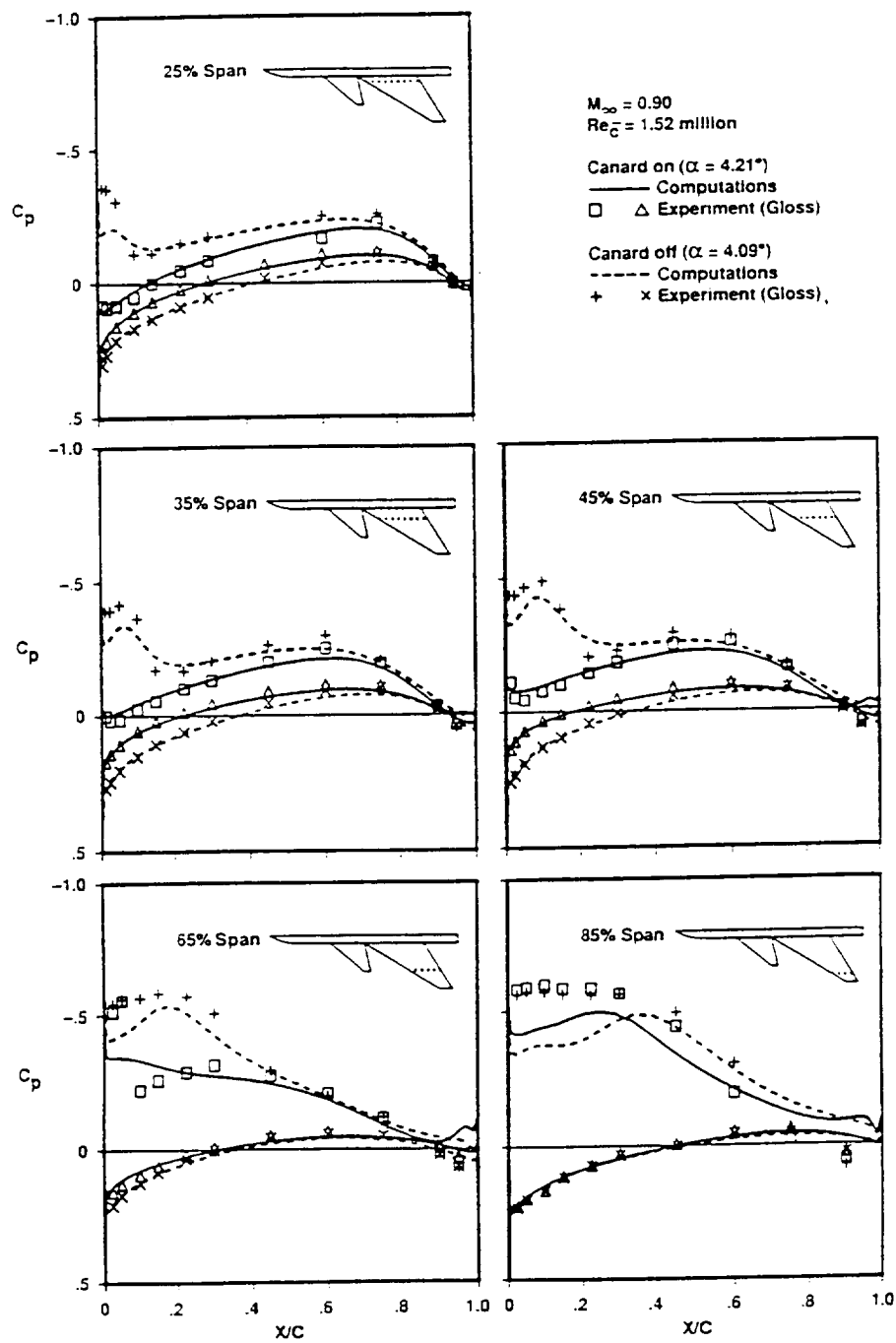


Figure 3.1. Comparison of computed and experimental steady-state surface pressure coefficients for the baseline grid with and without mid-canard. $M_\infty = 0.90$, $\alpha \approx 4^\circ$, $Re_{\bar{c}} = 1.52$ million.

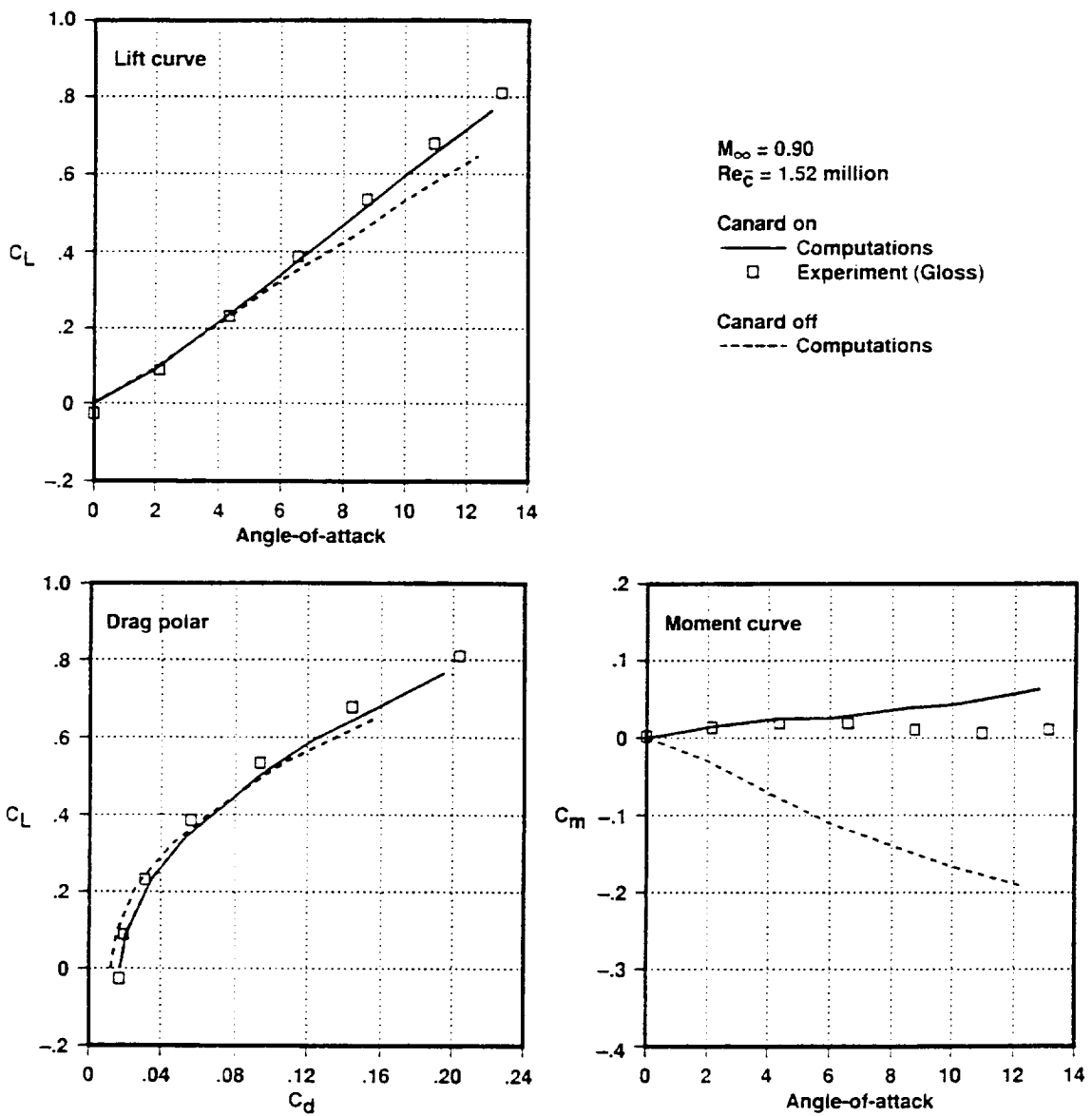


Figure 3.2. Comparison of computed and experimental force coefficients for the baseline grid with and without mid-canard. $M_\infty = 0.90$, $Re_{\bar{c}} = 1.52 \text{ million}$.

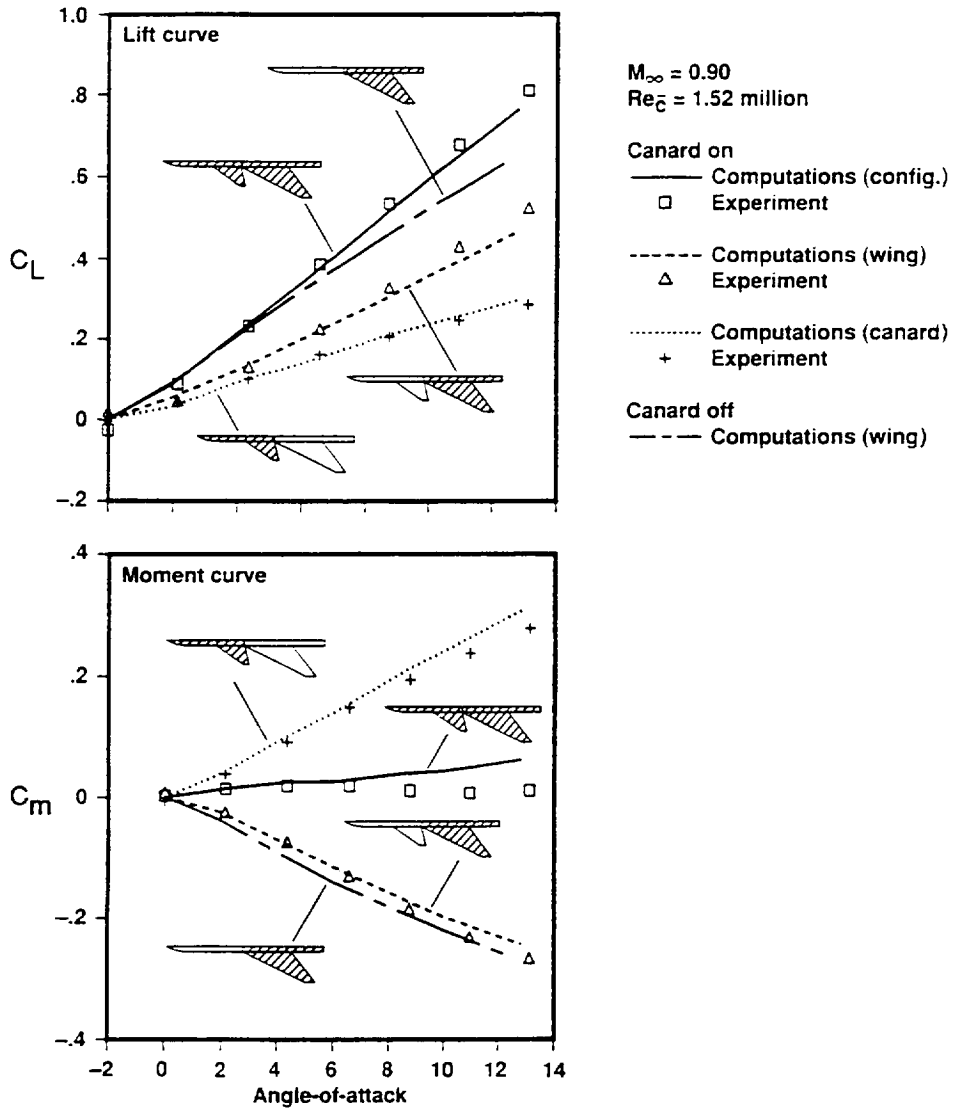


Figure 3.3. Comparison of component force coefficients for the baseline grid with and without mid-canard. (Lift and moment curves are given for shaded regions of the geometry). $M_\infty = 0.90$, $Re_{\bar{c}} = 1.52$ million.

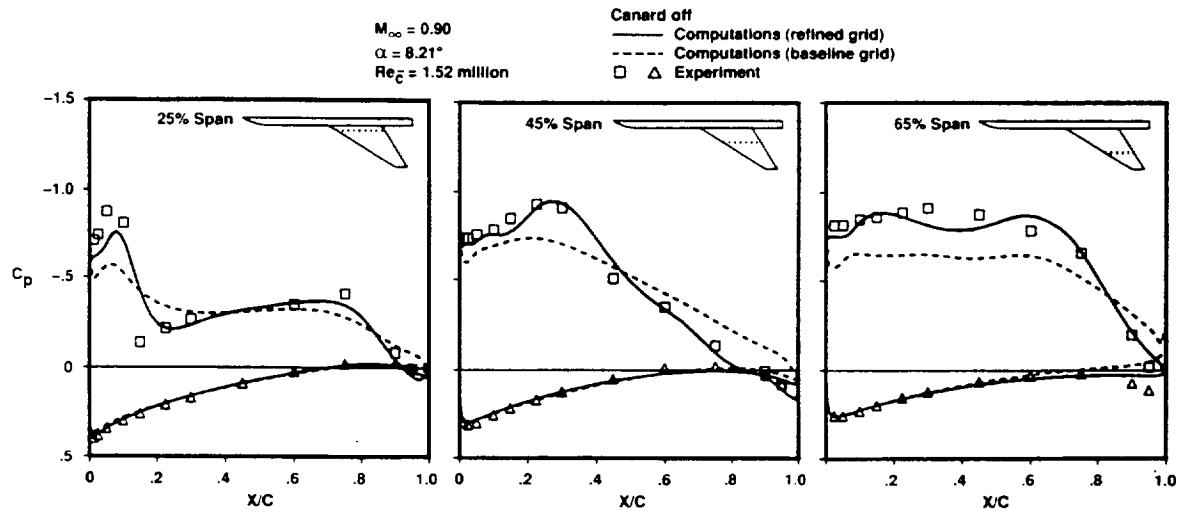


Figure 3.4. Comparison of baseline and refined grid surface pressure coefficients with experiment. $M_\infty = 0.90$, $\alpha = 8.21^\circ$, $Re_{\bar{c}} = 1.52$ million.

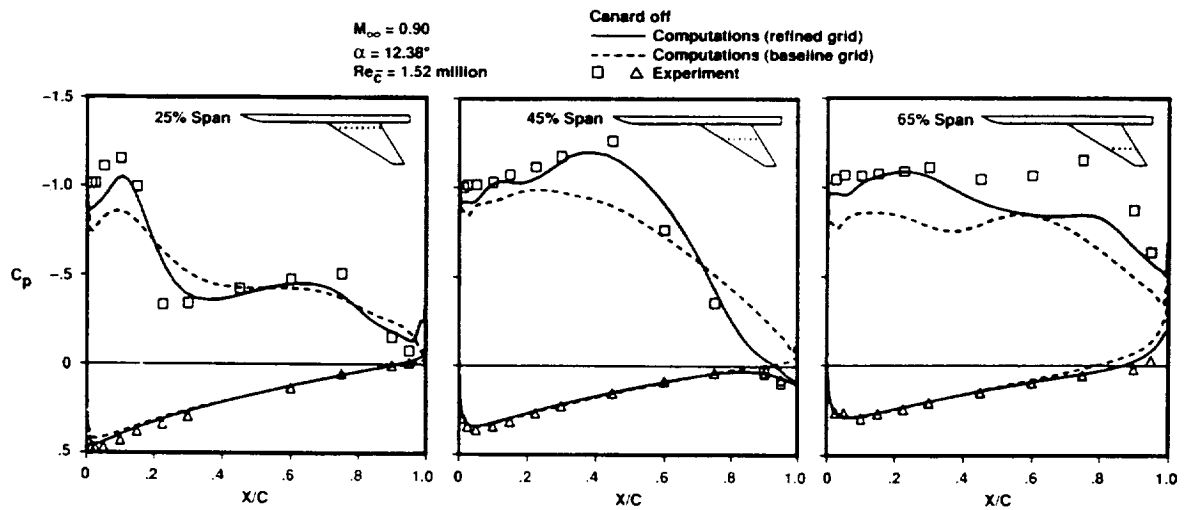


Figure 3.5. Comparison of baseline and refined grid surface pressure coefficients with experiment. $M_\infty = 0.90$, $\alpha = 12.38^\circ$, $Re_{\bar{c}} = 1.52$ million.

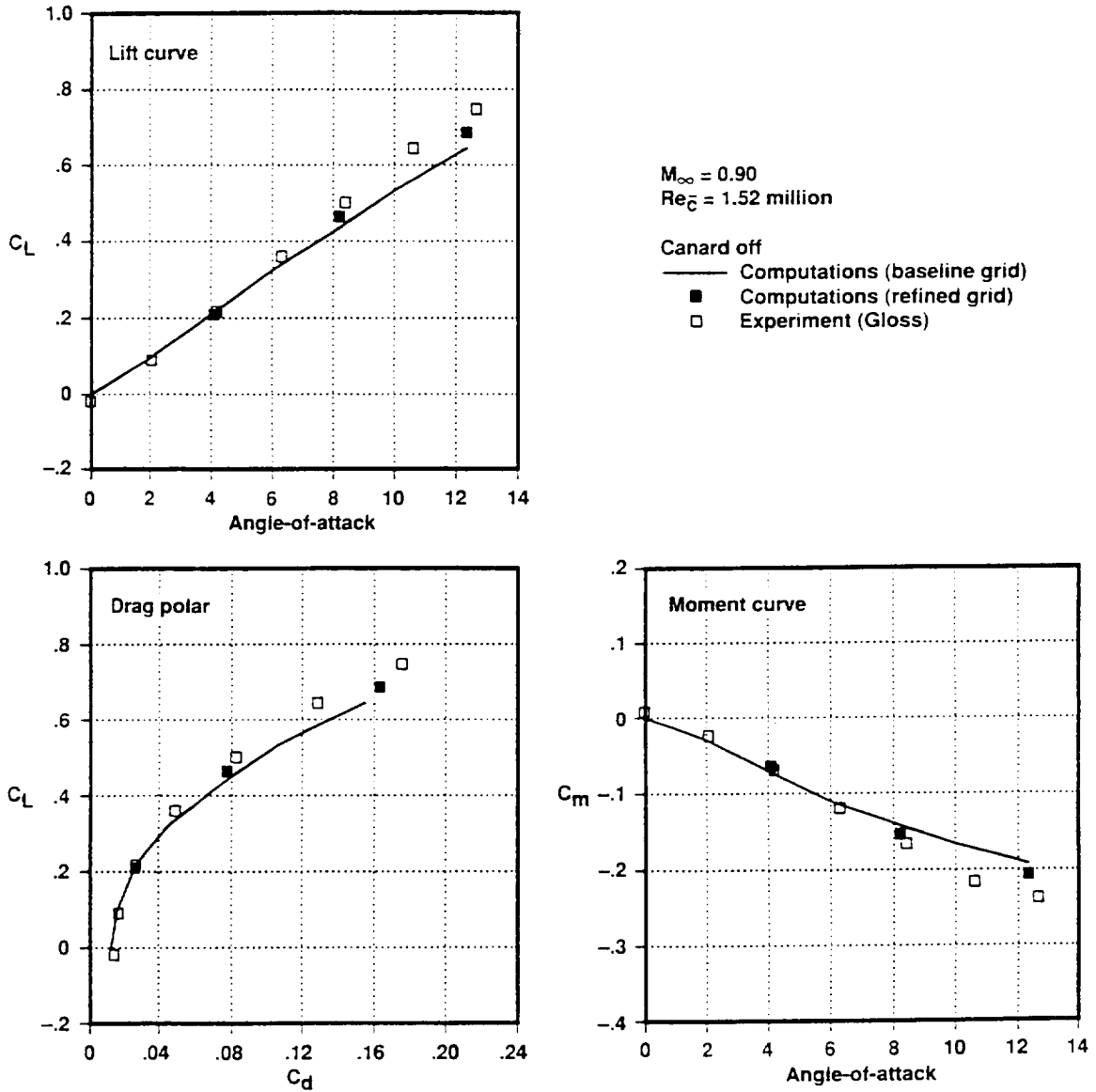


Figure 3.6. Comparison of baseline and refined grid force coefficients with experiment. $M_\infty = 0.90$, $Re_{\bar{c}} = 1.52 \text{ million}$.

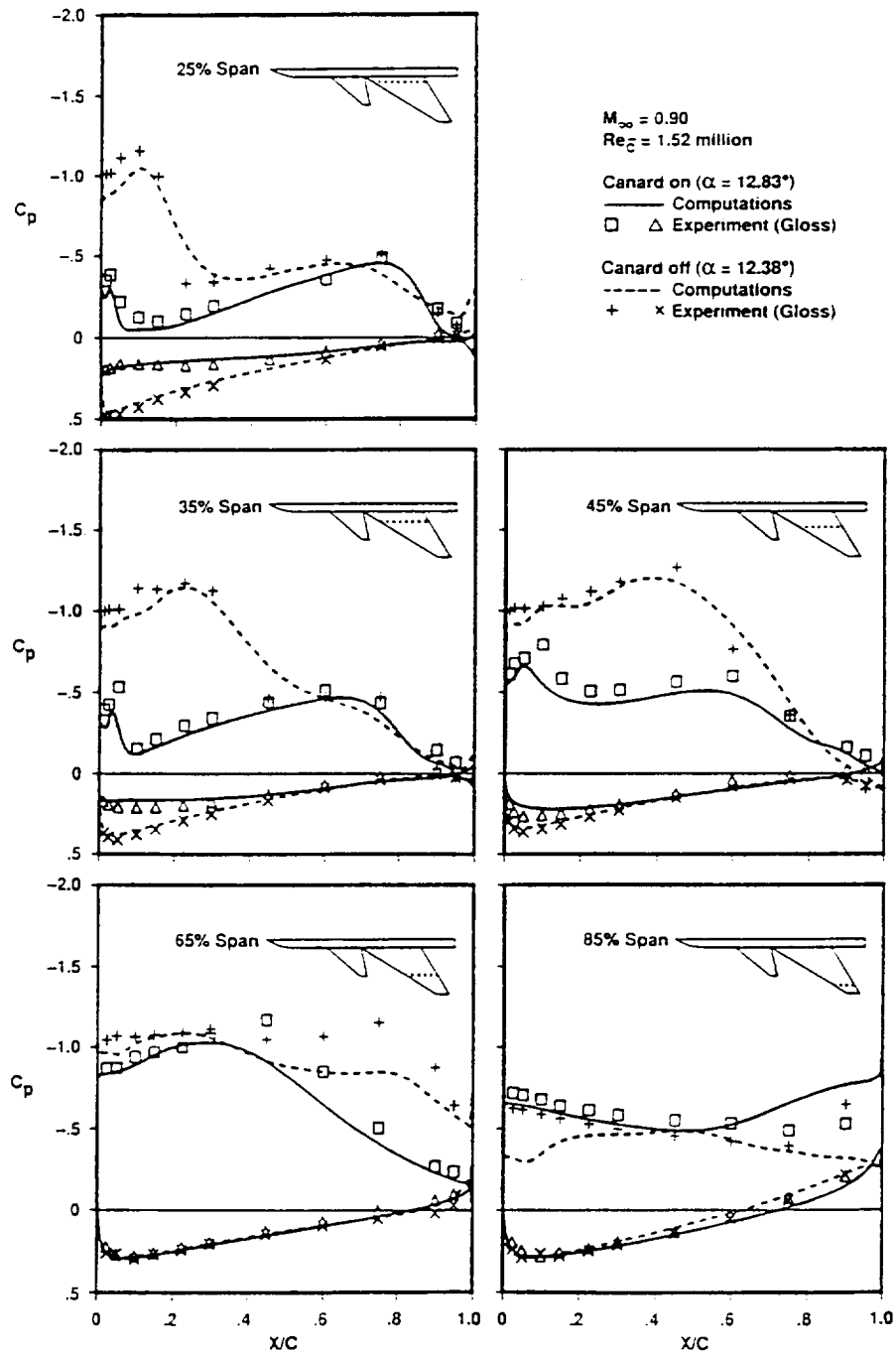


Figure 3.7. Comparison of computed and experimental surface pressure coefficients for the refined grid with and without mid-canard. $M_\infty = 0.90$, $\alpha \approx 12^\circ$, $Re_c = 1.52$ million.

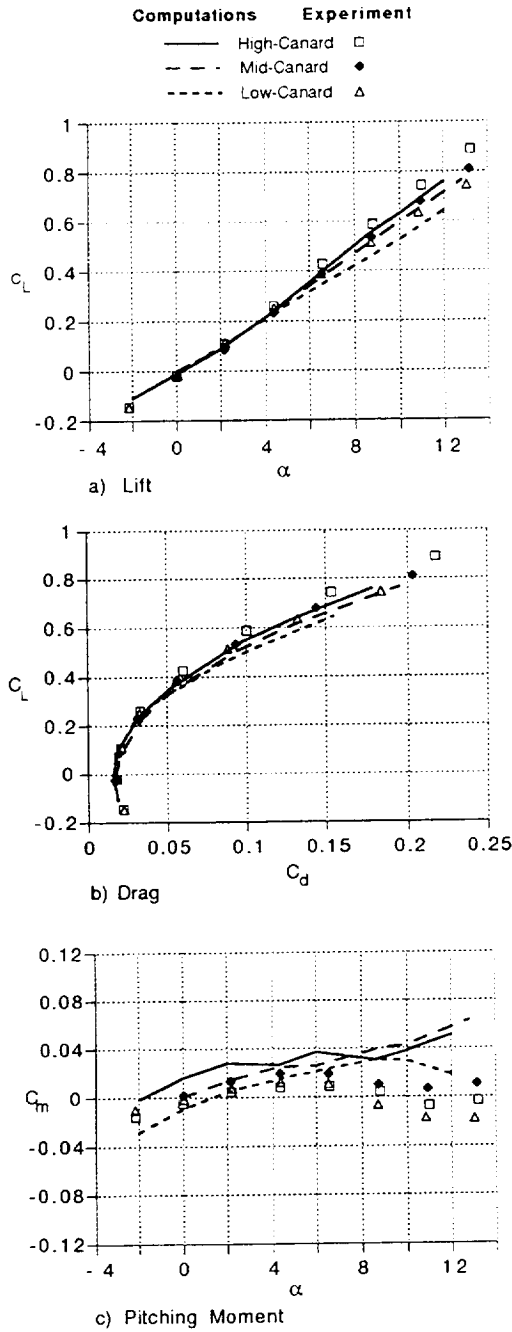


Figure 3.8. Comparison of computational and experimental forces and moments for the high-, mid- and low-canard configurations. $M_\infty = 0.90$, $Re_{\bar{c}} = 1.52$ million.

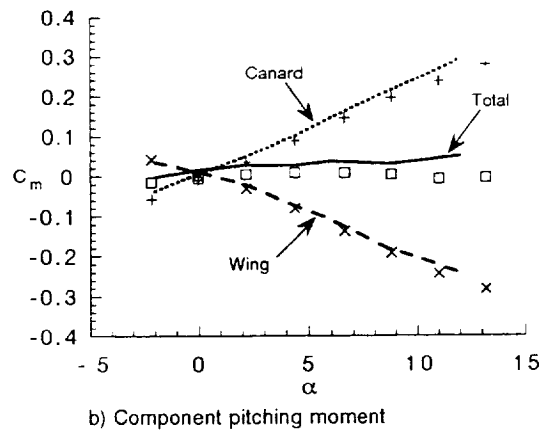
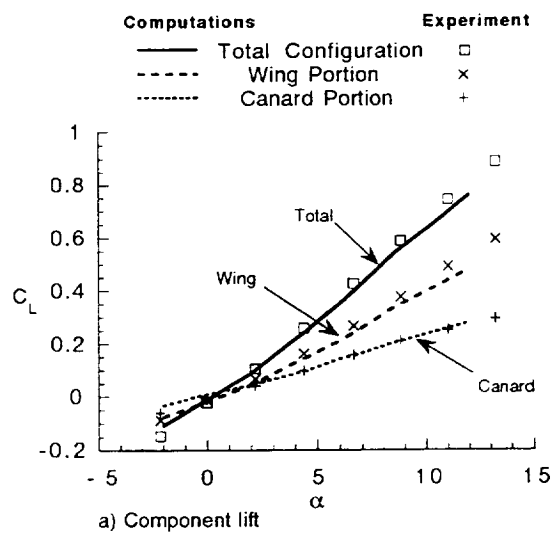
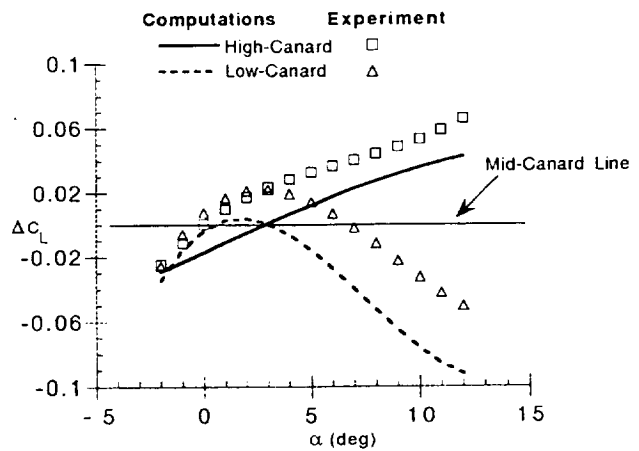
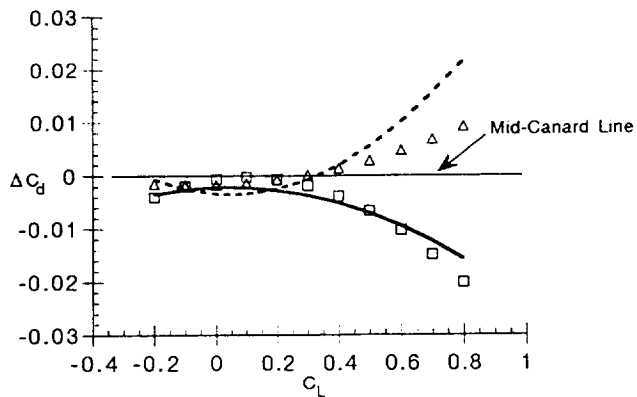


Figure 3.9. Comparison of component lift and pitching moment curves for the high-canard configuration. $M_\infty = 0.90$, $Re_{\bar{c}} = 1.52$ million.



a) Lift



b) Drag

Figure 3.10. Effect of canard vertical position on the incremental change in lift and drag coefficients. $M_\infty = 0.90$, $Re_{\epsilon} = 1.52$ million.

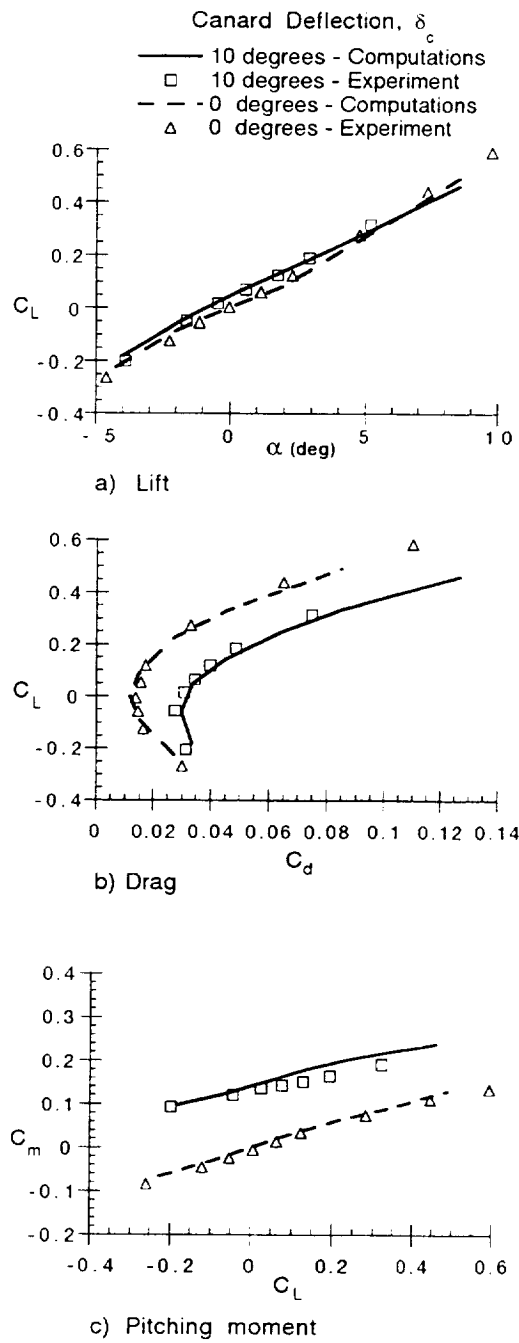


Figure 3.11. Comparison of computed and experimental forces and moments for the undeflected ($\delta_c = 0.0^\circ$) and deflected ($\delta_c = 10.0^\circ$) canard configurations. $M_\infty = 0.85$, $Re_{\bar{c}} = 2.82$ million.

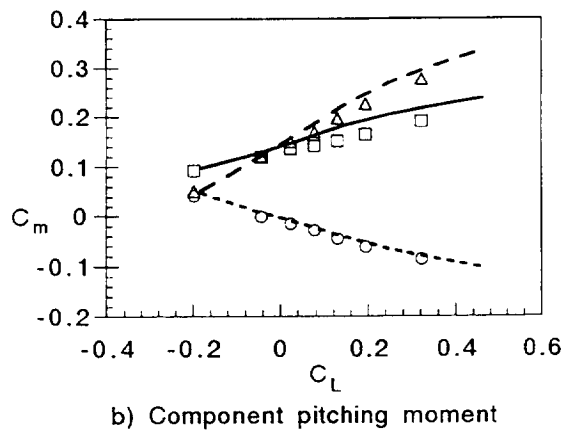
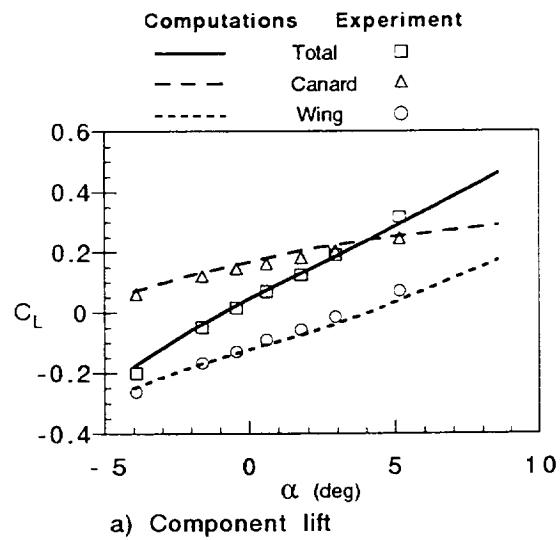


Figure 3.12. Comparison of component lift and pitching moment curves for the deflected canard configuration at $\delta_c = 10.0^\circ$. $M_\infty = 0.85$, $Re_c = 2.82$ million.

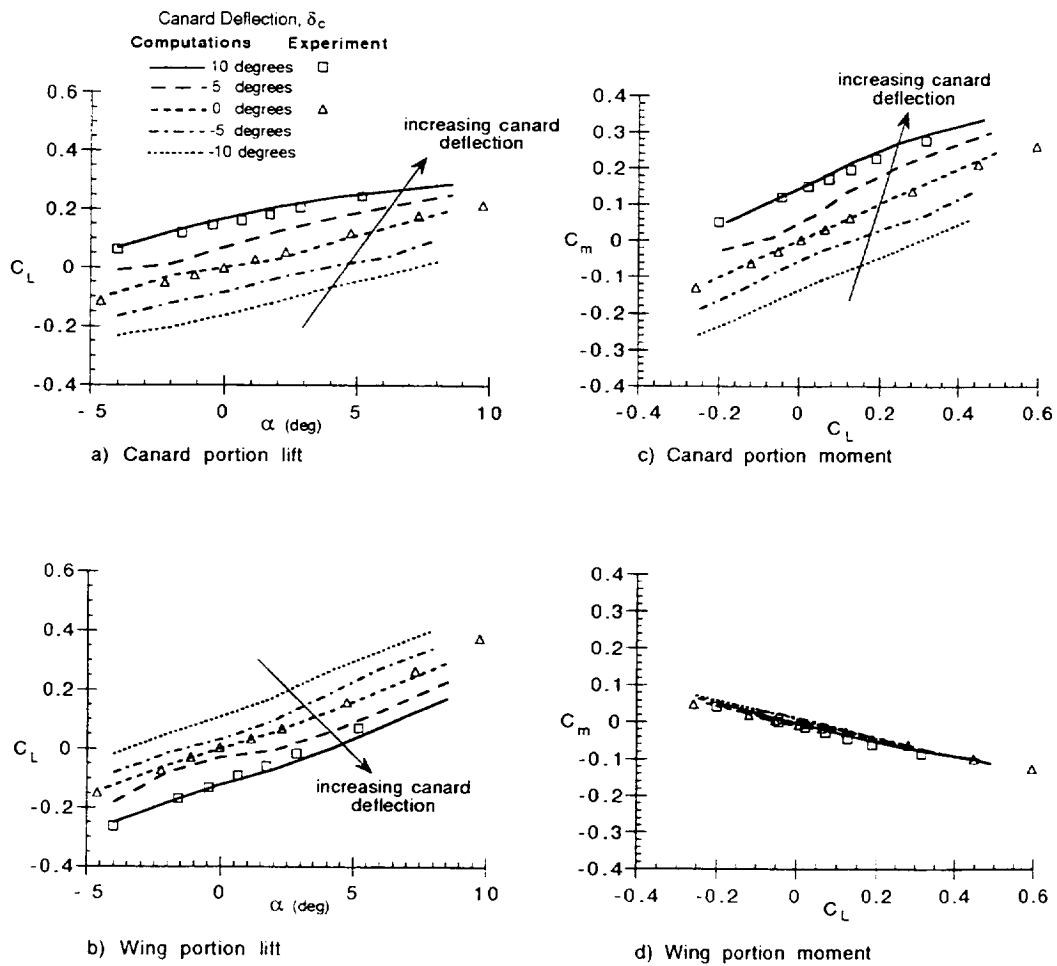


Figure 3.13. Effect of canard deflection, δ_c , on wing and canard portion lift and moment curves. $M_\infty = 0.85$, $Re_{\bar{c}} = 2.82$ million.

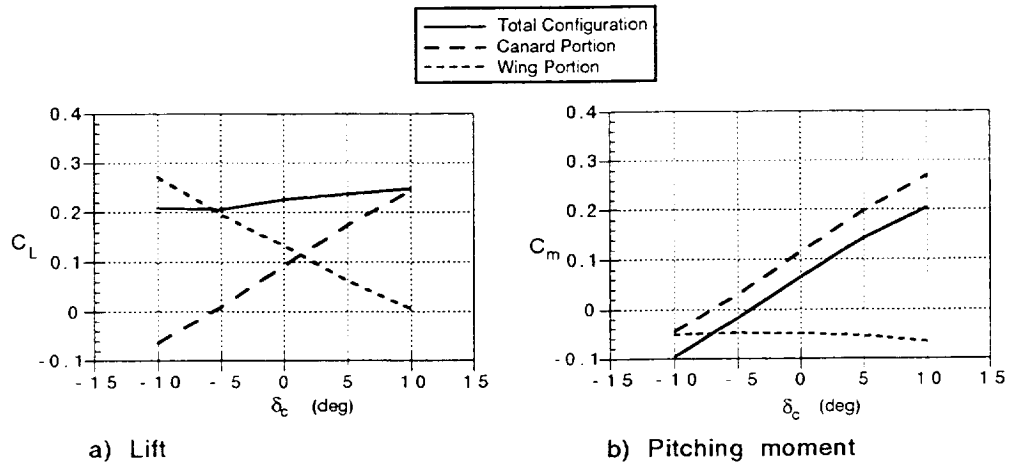


Figure 3.14. Effect of canard deflection, δ_c , on component lifts and pitching moments. $M_\infty = 0.85$, $\alpha = 4.27^\circ$, $Re_{\bar{c}} = 2.82$ million.

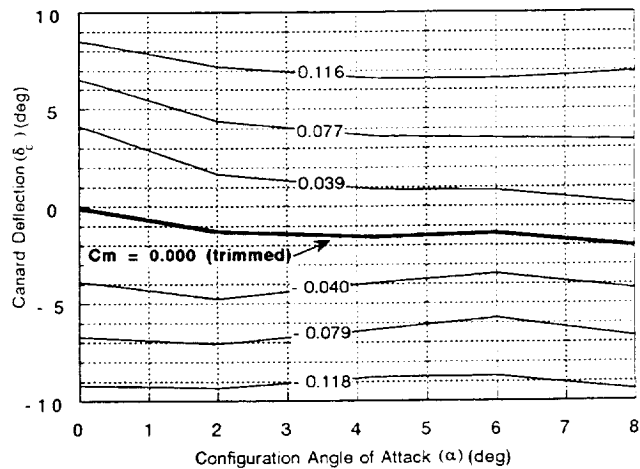


Figure 3.15. Contour plot of computed total pitching moment with moment center at c.g. location (59.14 cm from nose). $M_\infty = 0.85$, $Re_{\bar{c}} = 2.82$ million.

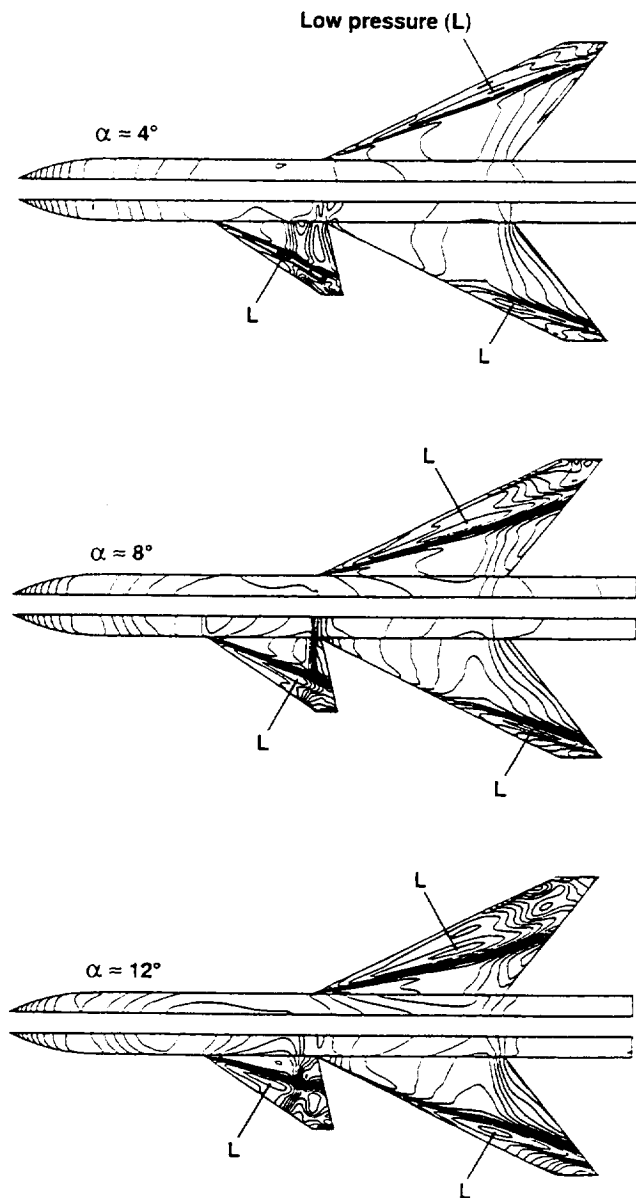


Figure 3.16. Computed upper surface pressure contours for the wing-body configuration with and without mid-canard. $M_\infty = 0.90$, $Re_\varepsilon = 1.52$ million.

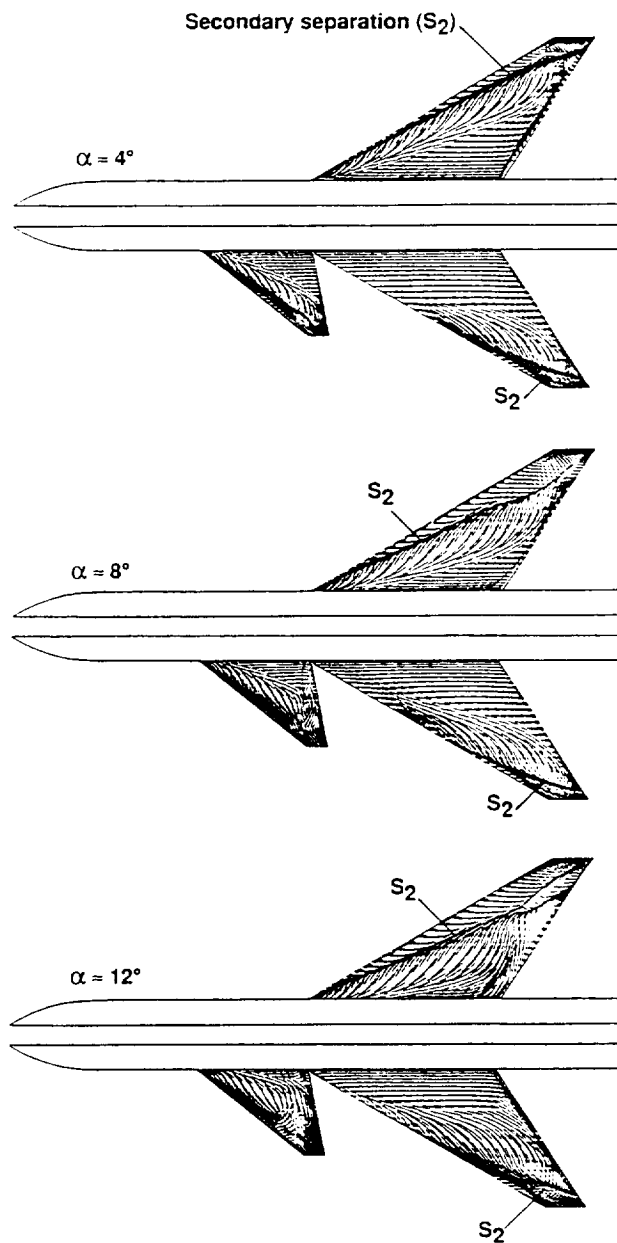


Figure 3.17. Computed upper surface flow patterns for the wing-body configuration with and without mid-canard. $M_\infty = 0.90$, $Re_\varepsilon = 1.52$ million.

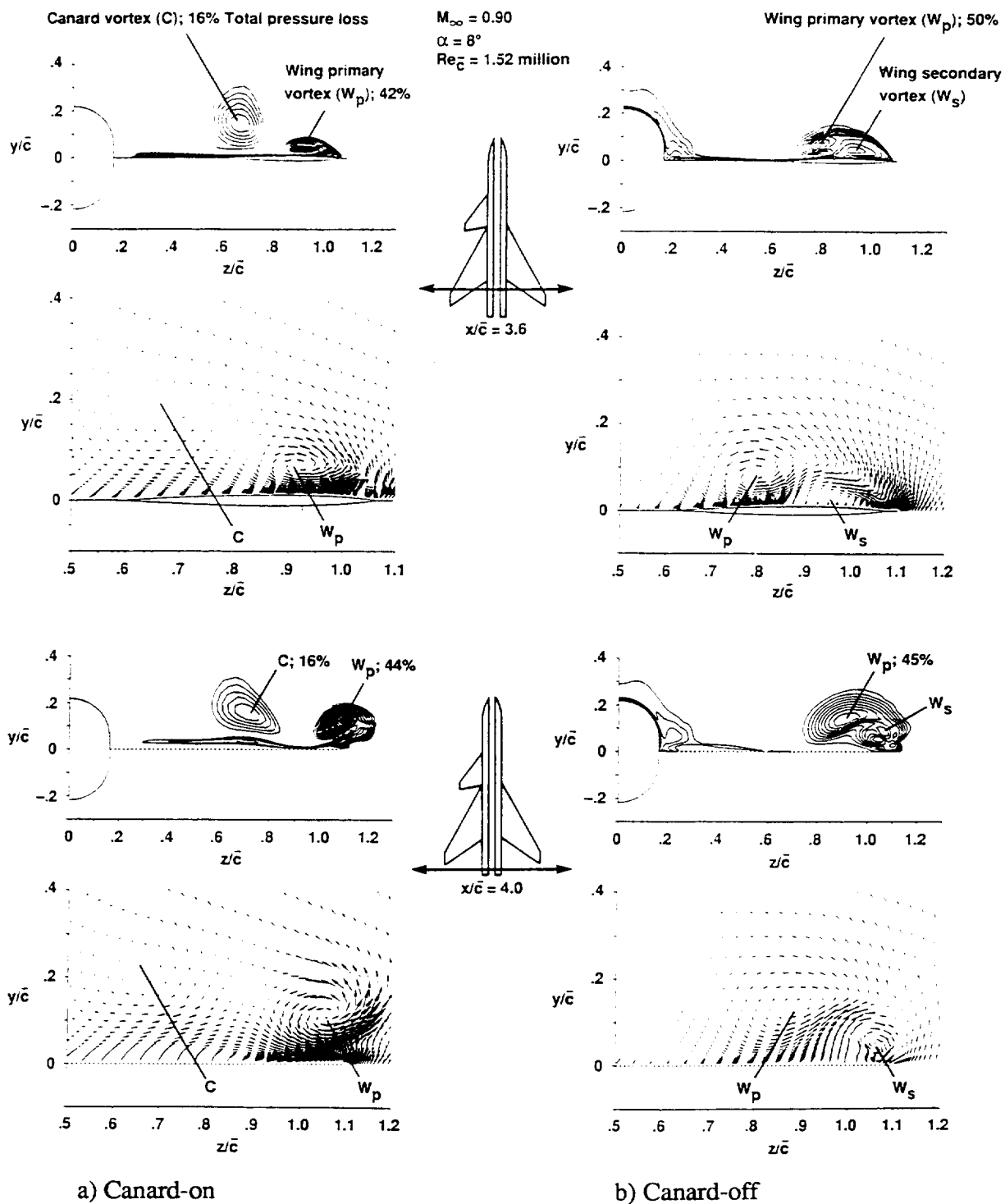


Figure 3.18. Crossflow plane visualization of normalized total pressure contours and scaled velocity vectors of the canard and wing leading-edge vortices. $M_\infty = 0.90$, $\alpha = 8^\circ$, $Re_{\bar{c}} = 1.52 \text{ million}$.

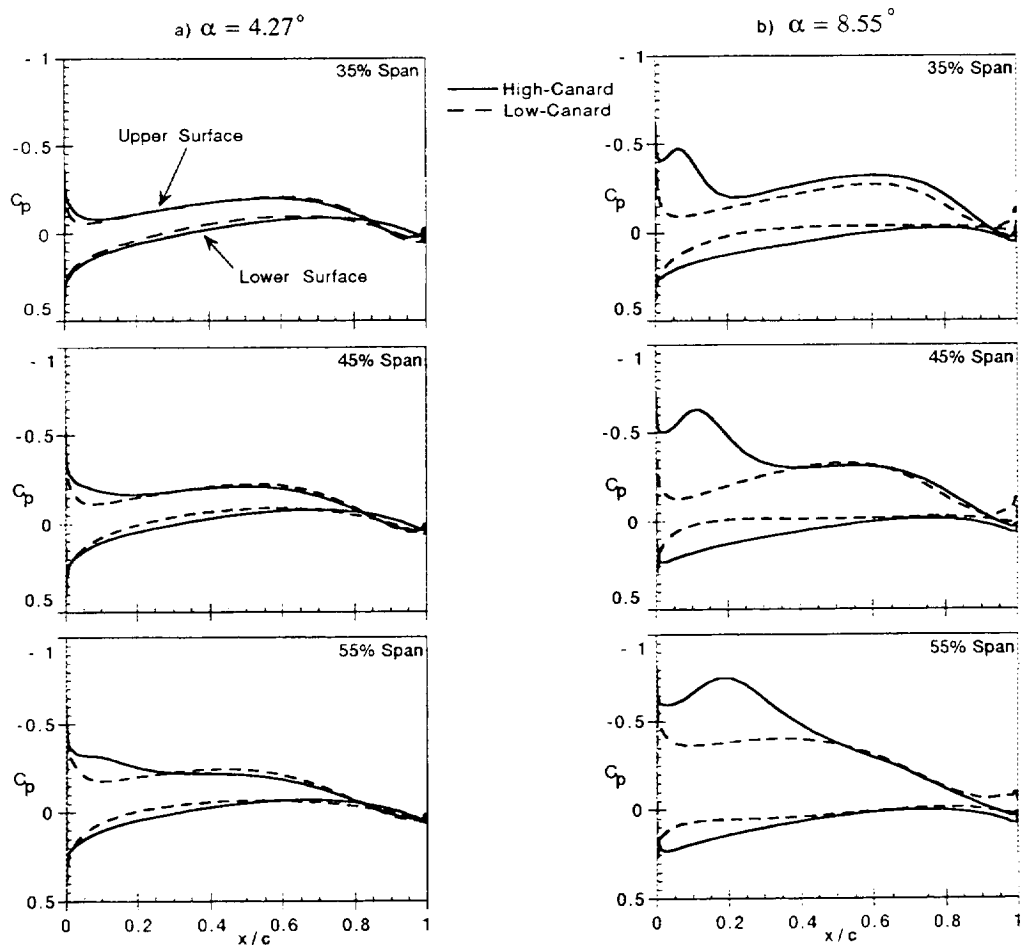


Figure 3.19. Comparison of wing surface pressures for the high- and low-canard configurations. $M_\infty = 0.90$, $\alpha = 4.27^\circ$ and 8.55° , $Re_{\bar{c}} = 1.52$ million.

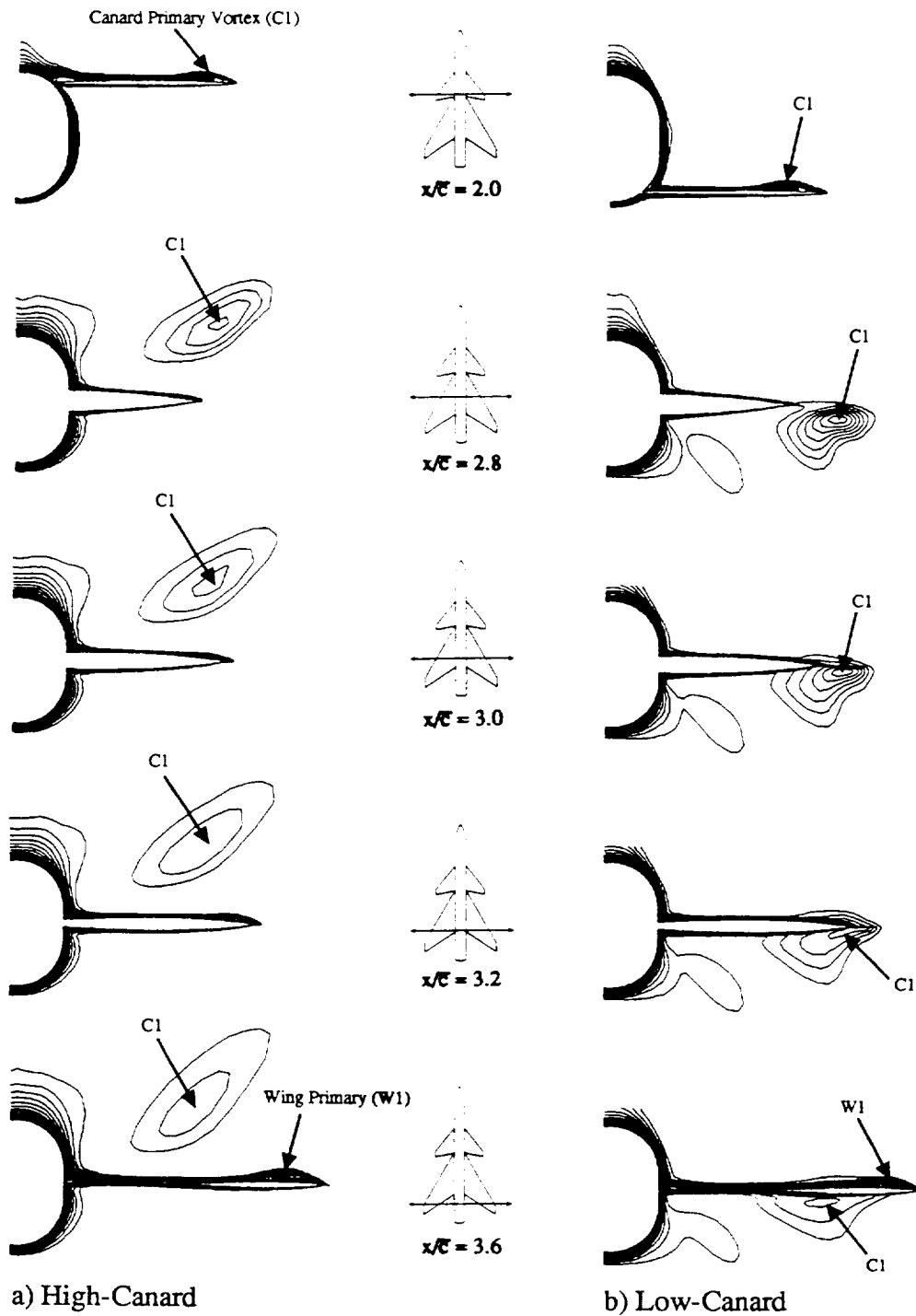


Figure 3.20. Crossflow plane visualization of normalized total pressure contours for high- and low-canard configurations. $M_\infty = 0.90$, $\alpha = 4.27^\circ$, $Re_\varepsilon = 1.52$ million.

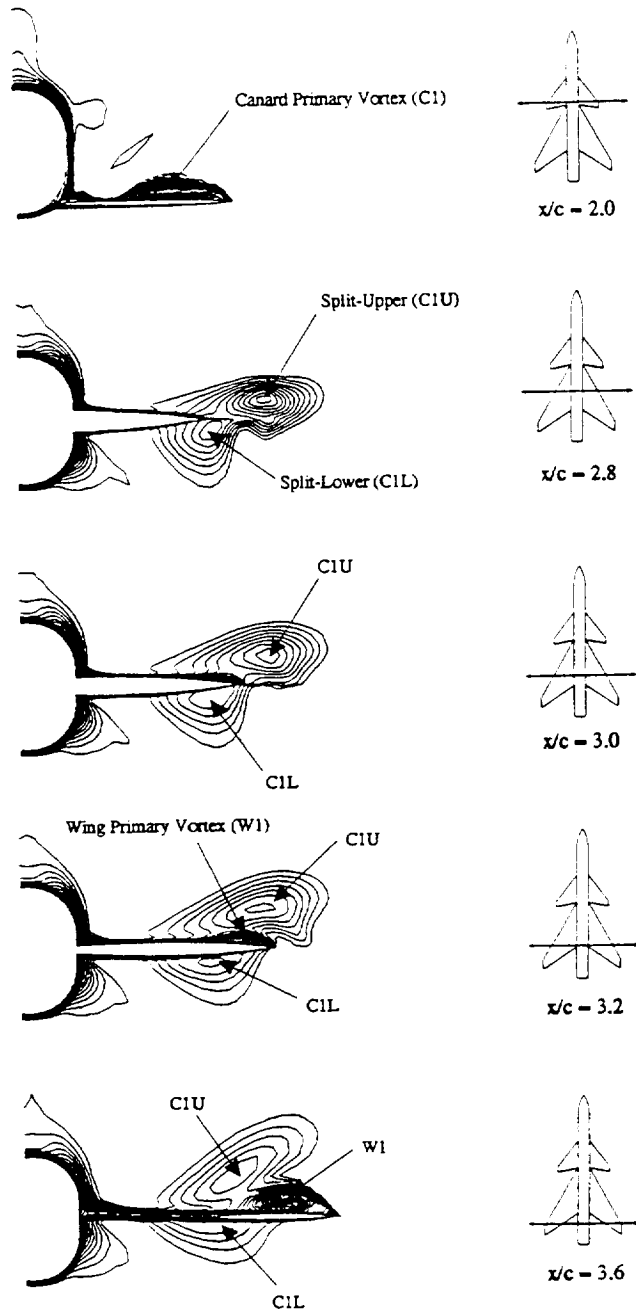


Figure 3.21. Crossflow plane visualization of normalized total pressure contours for the low-canard configuration. $M_\infty = 0.90$, $\alpha = 8.55^\circ$, $Re_\xi = 1.52$ million.

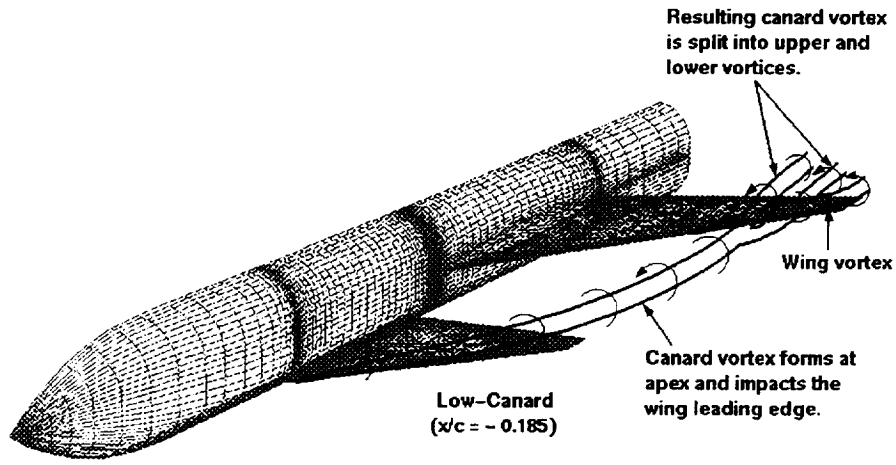


Figure 3.22. Schematic of the canard and wing vortex trajectories for the low-canard configuration.

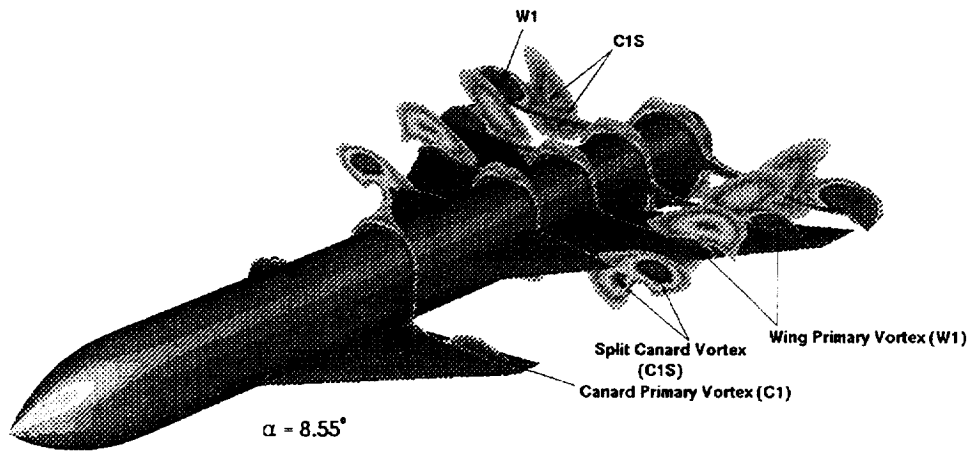


Figure 3.23. Perspective view of normalized total pressure contours for the low-canard configuration. $M_\infty = 0.90$, $\alpha = 8.55^\circ$, $Re_{\bar{c}} = 1.52$ million.

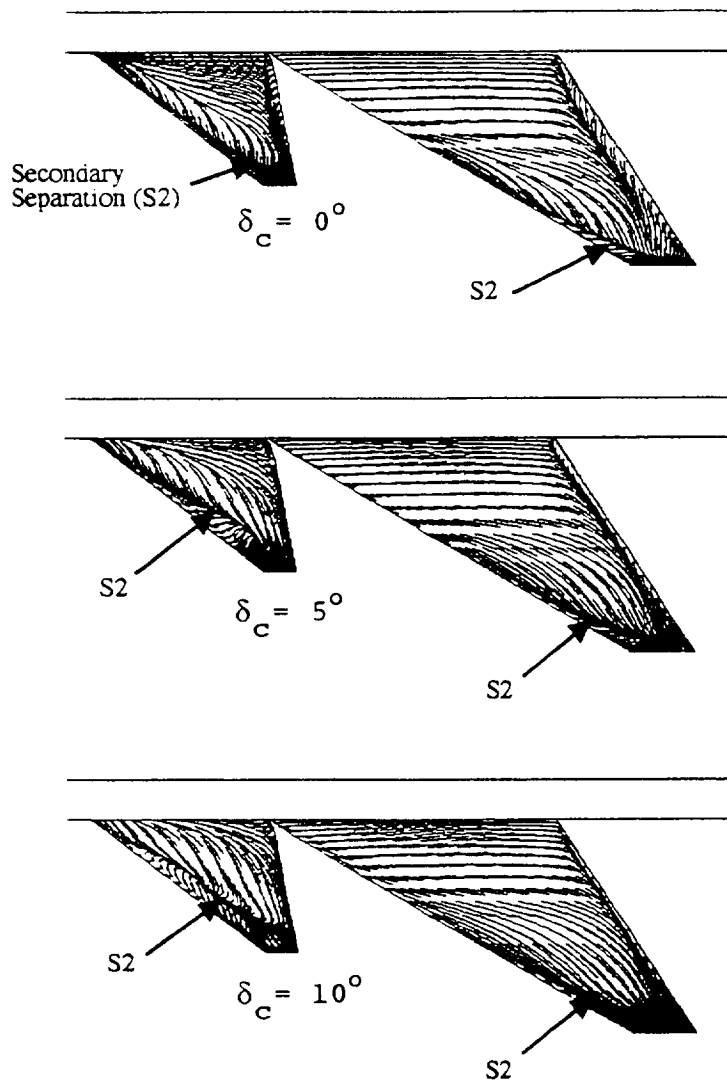


Figure 3.24. Effect of canard deflection, δ_c , on surface flow patterns. $M_\infty = 0.85$, $\alpha = 4.27^\circ$, $Re_{\bar{c}} = 2.82$ million.

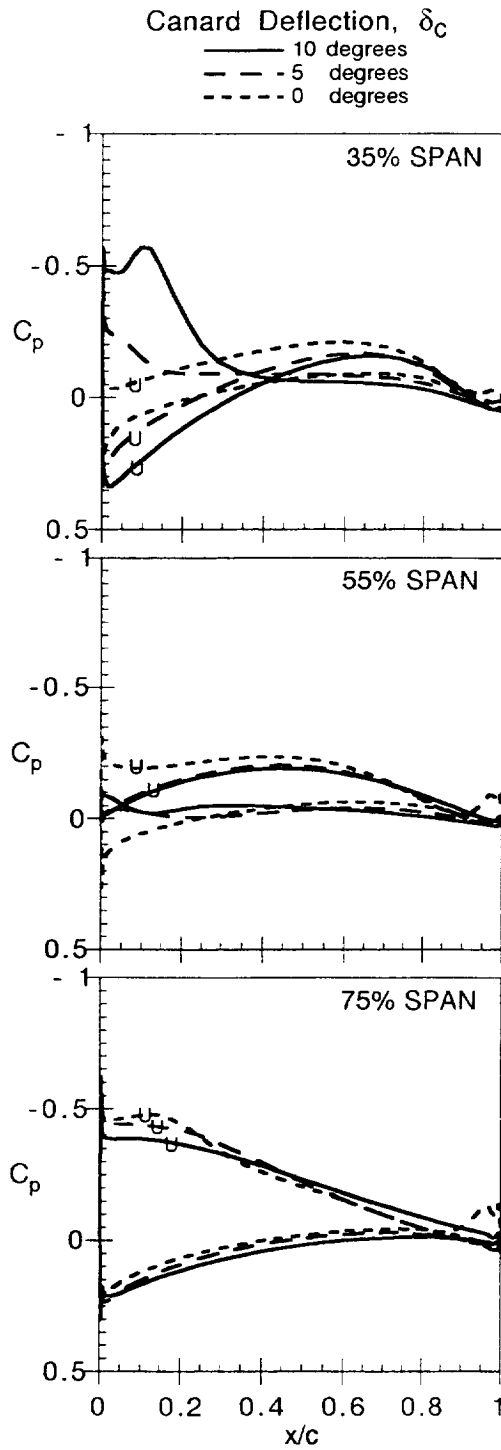


Figure 3.25. Effect of canard deflection, δ_c , on wing surface pressures. (Upper surface pressures indicated by U). $M_\infty = 0.85$, $\alpha = 4.27^\circ$, $Re_{\bar{c}} = 2.82$ million.

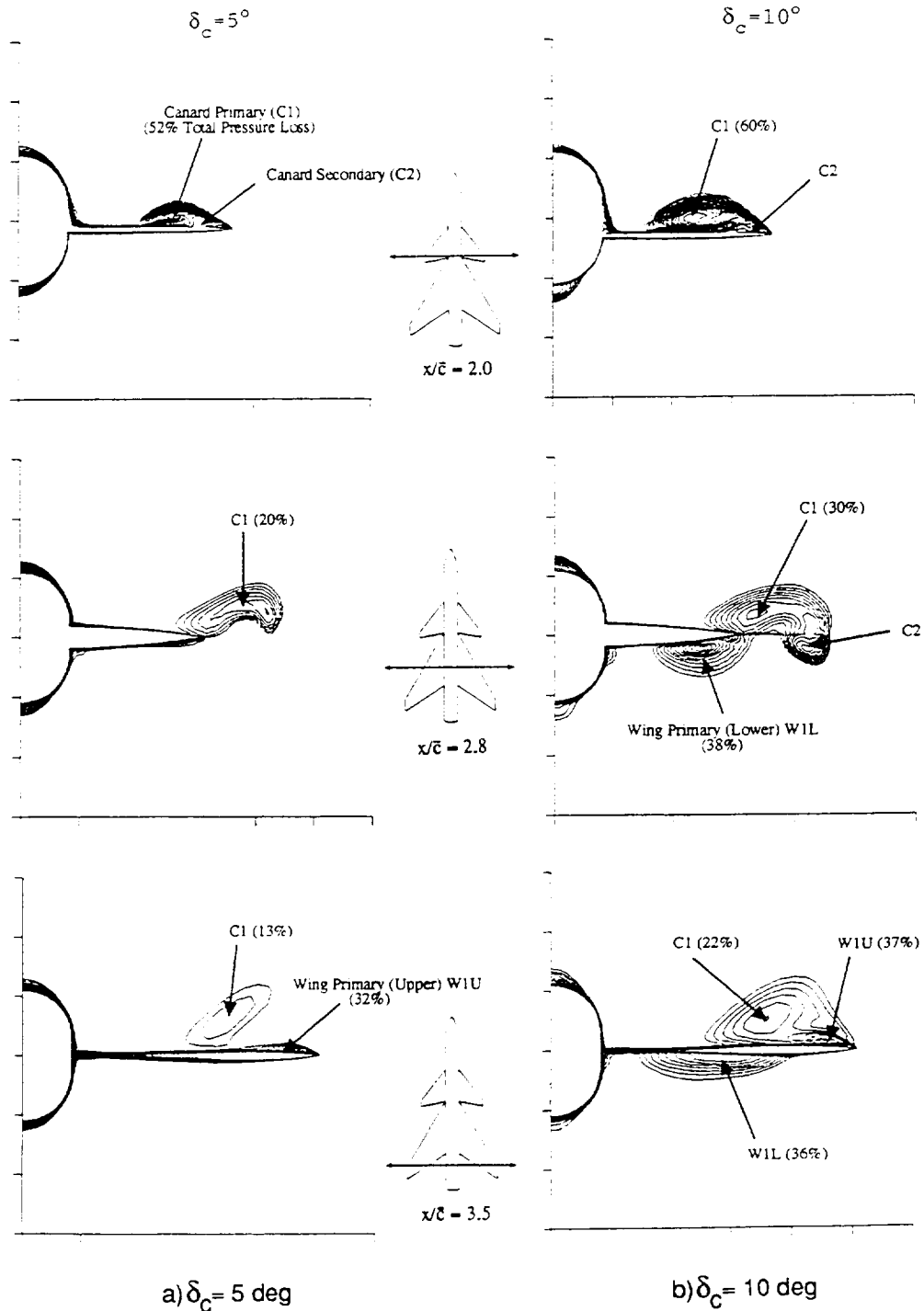


Figure 3.26. Crossflow plane visualization of normalized total pressure contours for canard deflections of $\delta_c = 5^\circ$ and 10° . $M_\infty = 0.85$, $\alpha = 4.27^\circ$, $Re_{\bar{c}} = 2.82$ million.

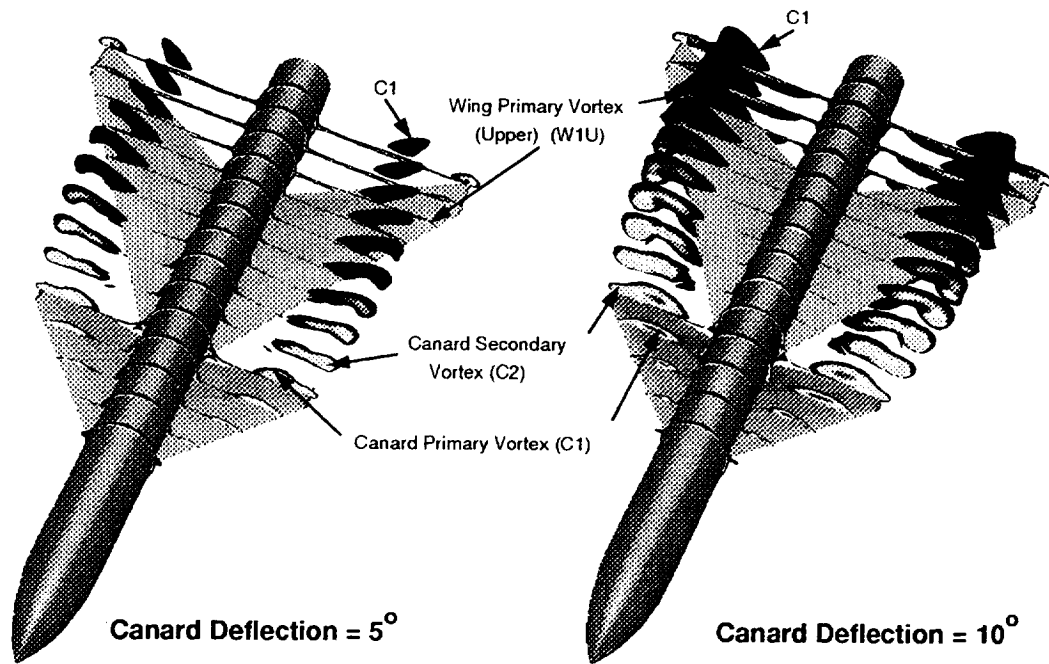


Figure 3.27. Perspective views of upper surface canard-wing vortex structure for canard deflections of $\delta_c = 5^\circ$ and 10° . $M_\infty = 0.85$, $\alpha = 4.27^\circ$, $Re_\epsilon = 2.82$ million.

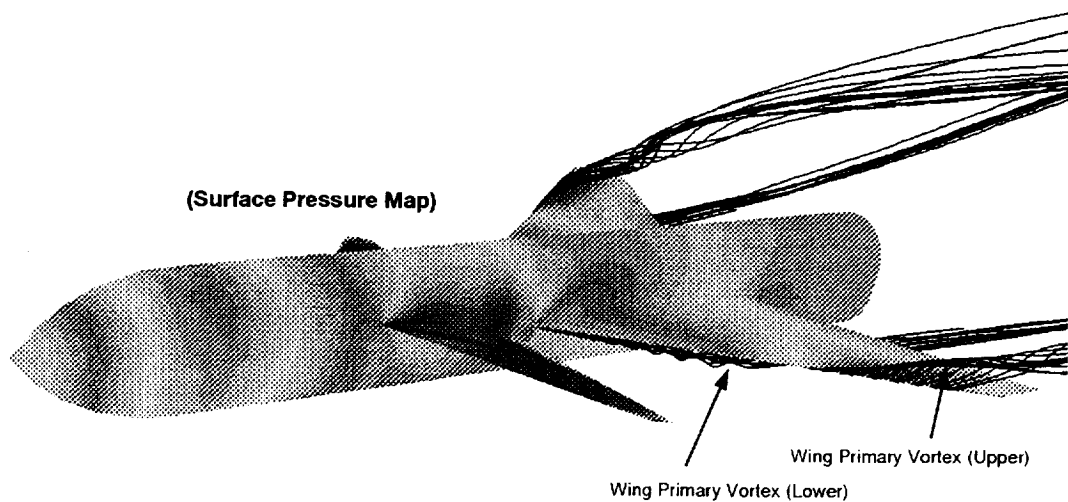


Figure 3.28. Perspective view of computed surface pressures and simulated particle traces for $\delta_c = 10^\circ$. $M_\infty = 0.85$, $\alpha = 4.27^\circ$, $Re_\epsilon = 2.82$ million.

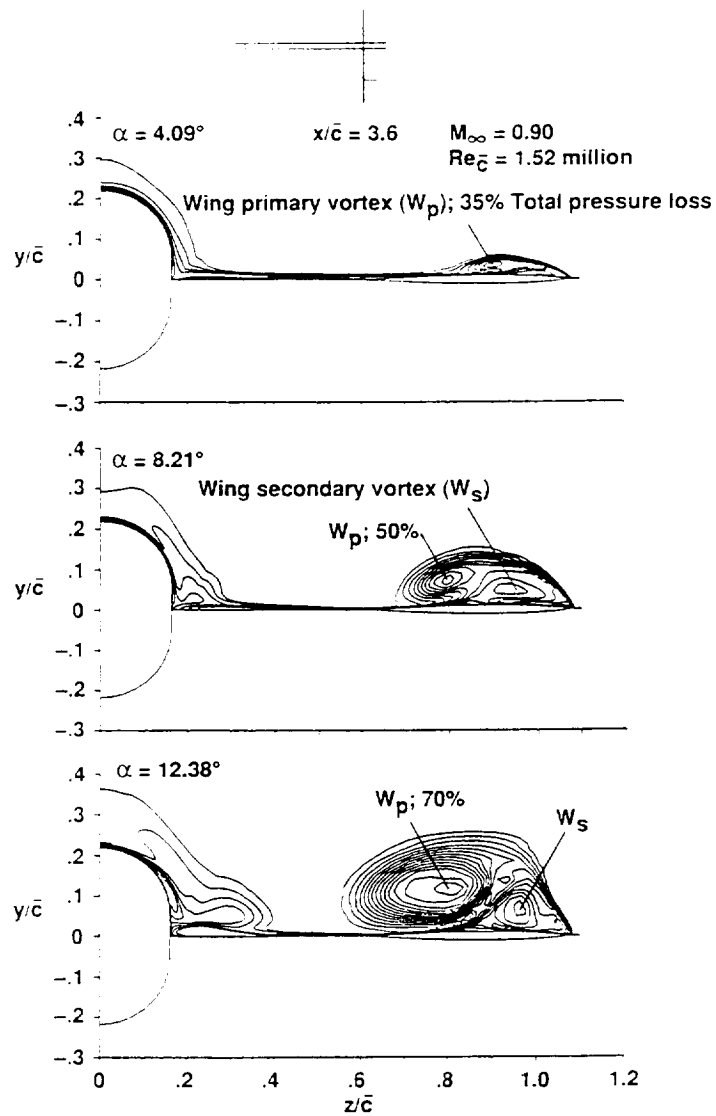


Figure 3.29. Crossflow plane visualization of normalized total pressure contours of the wing leading-edge vortex for the canard-off case. $M_\infty = 0.90$, $Re_{\bar{c}} = 1.52$ million, $x/\bar{c} = 3.6$.

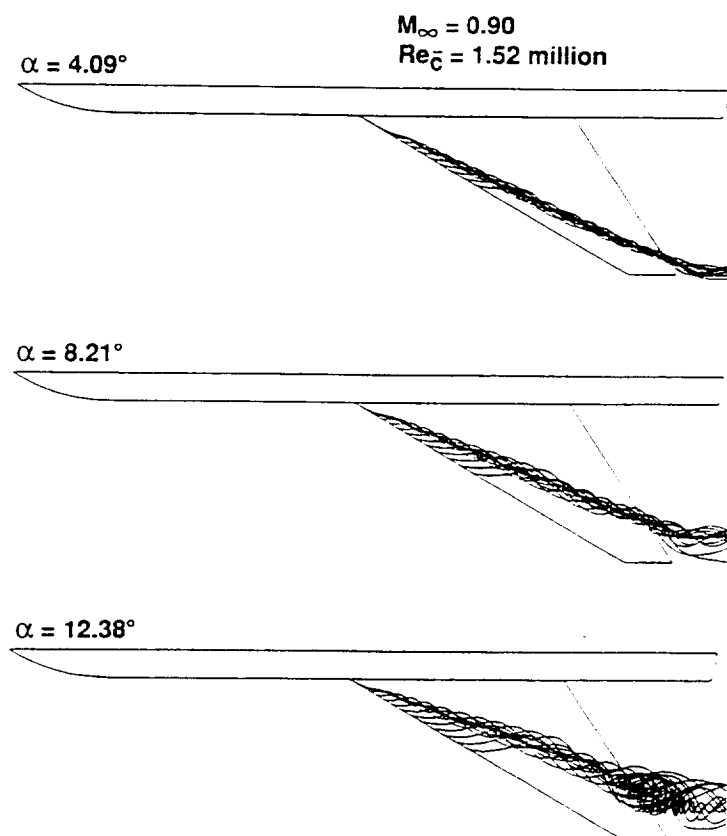


Figure 3.30. Off-surface particle traces of the wing vortex for the canard-off case. $M_\infty = 0.90$, $Re_{\bar{c}} = 1.52 \text{ million}$, $x/\bar{c} = 3.6$.

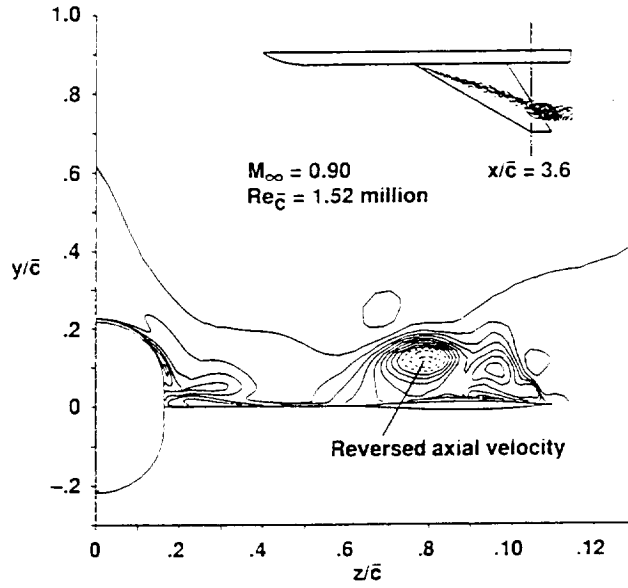


Figure 3.31. Crossflow plane visualization of scaled axial velocity contours for the canard-off case. $M_\infty = 0.90$, $Re_{\bar{c}} = 1.52$ million, $x/\bar{c} = 3.6$.

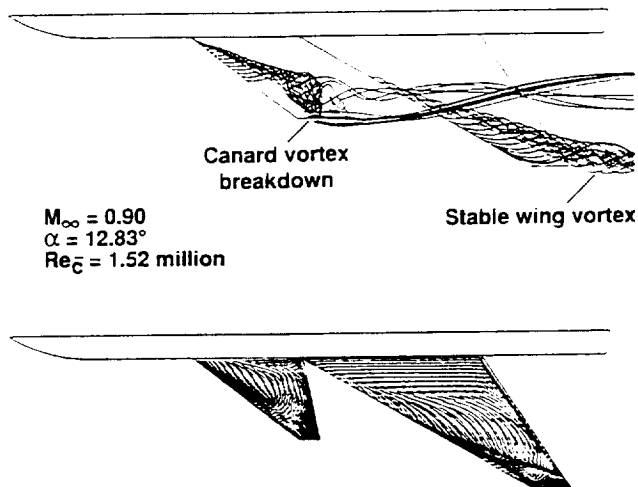


Figure 3.32. Off-surface particle traces of the canard and wing vortices for the canard-on case. $M_\infty = 0.90$, $\alpha = 12.38^\circ$, $Re_{\bar{c}} = 1.52$ million.

Chapter 4

Effect of Fixed Canard on Unsteady Aerodynamics

The effects of fixed canards on the unsteady longitudinal aerodynamics of the canard-wing-body configuration are presented in this section. As outlined earlier in the Introduction, many benefits of canards are realized during maneuver and other dynamic conditions which result in highly unsteady aerodynamics. In such conditions, the fixed canard has a pronounced influence on the unsteady forces, moments, and ultimately the performance and stability of the configuration.

Computational simulations solving the time-accurate Reynolds-averaged Navier–Stokes equations are used to study the effects of the canard on the pitch-up ramp motion and pitch oscillations of the canard-wing-body configuration. All fixed canard simulations in this section are performed for the undeflected mid-canard configuration. Comparisons are made with available experimental data (ref. 24), and numerical convergence is demonstrated through spatial and temporal refinement studies.

The results of the simulations are used to study the unsteady forces and moments due to the canard, and the unsteady canard-wing vortical flowfield. Ultimately, in section 4.3, the capability of utilizing high-order CFD for configuration stability evaluation is demonstrated through a dynamic stability analysis (derived in sec. 2.7) of the time-accurate pitch-oscillation predictions.

4.1 Pitch-Up Ramp Motion

Results are presented to provide the analyses of the unsteady canard-wing-body flowfield associated with pitch-up ramp motions. All unsteady results in this section are computed at $M_\infty = 0.90$ and a Reynolds number based on the mean aerodynamic chord of the wing (Re_c) of 1.52 million. Convergence of the unsteady flowfield is verified using both spatial and time-step refinement studies.

All unsteady canard-wing-body results are computed for α from 0 deg to either 12.83 deg or 15 deg and for non-dimensional pitch rates (defined by $A_p = \dot{\alpha}\bar{c}/U_\infty$) of 0.05 and 0.10. Ramp motions are started from converged steady-state solutions at an initial angle of attack (α_i) and held at the final angle (α_f) for a fixed length of time. The pitch axis of the ramp motion and the pitching moment results are taken from the model c.g. location shown in figure 1.4.

A typical ramp motion from $\alpha_i = 0$ deg to $\alpha_f = 15$ deg is illustrated in figure 4.1. In order to directly compare unsteady results at different pitch rates and steady-state results, time (t) is given in degrees. During the ramp motion ($0 \text{ deg} \leq t \leq 15 \text{ deg}$) α and t are equal ($\alpha = t$). However, for $t > 15 \text{ deg}$, α is held constant at 15 deg ($\alpha = 15 \text{ deg}$ or α_f). It is noted that during the ramp motion, α increases linearly as a function of time. Consequently, the ramp motion has an impulsive start and

stop which significantly influences the unsteady results. (Note that the conversion to physical time can be easily obtained using the definition $A_p = \dot{\alpha}\bar{c}/U_\infty$ and replacing $\dot{\alpha}$ with $\Delta t_{rad}/\Delta t_{sec}$.)

4.1.1 Aerodynamic performance

Computed time histories of lift, drag and pitching moment for the configuration, with and without canard, undergoing a ramp motion (pitch rate, $A_p = 0.10$) are illustrated in figure 4.2. Computational and experimental steady-state results are also given for the corresponding angles of attack. The lift curves of figure 4.2 show a significant lift increase for the unsteady canard-on case. Early in the motion ($t < 4$ deg), the unsteady canard-on lift is slightly lower than the canard-off lift due to the pitch-rate effects of the configuration. Since the entire canard is forward of the pitch axis, there is an initial loss of lift on the canard at the start of the ramp motion ($t = 0$ deg). As the ramp motion continues, the canard-on case exhibits increased lift over both the canard-off and steady-state canard-on cases.

The time histories of drag coefficient show that at a given instantaneous angle of attack, there is higher drag for the canard-on case. However, by replotting the drag results of figure 4.2 in drag polar form, figure 4.3 shows that the unsteady canard-on case exhibits improved dynamic lift-to-drag performance at the higher angles of attack.

The pitching moments given in figure 4.2 also illustrate the significant influence of the fluid virtual (or apparent (ref. 57)) mass at the beginning ($t = 0$ deg) and end ($t = 15$ deg) of the ramp motion. The virtual mass acts to counter the acceleration of the body and, therefore, causes a rapid nose-down pitching moment at $t = 0$ deg and a nose-up moment at $t = 15$ deg. Beyond $t = 15$ deg, the lift, drag and pitching moment values converge toward the steady-state $\alpha = 15$ deg result.

The effect of pitch rate on lift for the canard-on case is given in figure 4.4 for $A_p = 0.10$ and 0.05. Note that since comparisons are made at instantaneous angles of attack during the ramp motion (t in deg), the physical time (t_{sec}) between the two pitch rates differ by a factor of two. Figure 4.4 shows that the lift of the canard configuration is increased at the higher pitch rate throughout the ramp motion. Further into the ramp motion ($t > 10$ deg), the pitch rate and total lift are approximately proportional at given angles of attack.

Better insight into the dynamic loads produced by the ramp motion can be attained by examining the separate component regions of the geometry. Similar to the steady-state component results given earlier, the canard region consists of the canard and the body forward of the wing leading-edge root location (fore-body). The wing region consists of the wing and the remaining aft-body (not including the sting).

Time histories of the canard and wing region lift contributions for the $A_p = 0.05$ ramp motion are illustrated in figure 4.5. Computed steady-state lift coefficients are also given for reference. By definition, the total configuration lift is the sum of the canard and wing region lift. The effects of the fluid virtual mass are evident at both $\alpha_i = 0$ deg and $\alpha_f = 15$ deg. Due to the relative locations of the canard and wing to the pitch axis, there is an initial increase in wing region lift and a decrease in canard region lift at $\alpha_i = 0$ deg. These trends are then reversed at $\alpha_f = 15$ deg.

Figure 4.5 shows that, in comparison to the steady-state results, there is a net loss of lift for the canard throughout the ramp motion. The increased lift for the total configuration during the ramp motion is due to the large increase in the lift of the wing. Although the canard-wing flowfield is highly non-linear and complex in nature, it can be quite useful to qualitatively describe the effects of the unsteady motion in terms of simplified linear theory. In linear theory, the lift of the wing or canard can be written as the sum of the static lift ($C_{L_\alpha}\alpha$), the lift due to pitch or quasi-static lift ($C_{L_q}q$), and the unsteady lift ($C_{L_\dot{\alpha}}\dot{\alpha}$). The terms C_{L_α} , C_{L_q} , and $C_{L_\dot{\alpha}}$ are the stability derivatives $(\partial C_L/\partial\alpha)_0$, $(\partial C_L/\partial q)_0$ and $(\partial C_L/\partial\dot{\alpha})_0$, respectively; q is the angular velocity of the configuration about the pitch axis. The

notation $()_0$ indicates that partial derivatives are evaluated assuming the disturbance quantities are zero. Note that for the ramp motion, $q = \dot{\alpha}$.

For the canard or wing, the lift contribution due to pitch is represented in the C_{L_q} and $C_{L_{\dot{\alpha}}}$ terms. The loss of canard lift is primarily due to the canard location forward of the pitch axis which, if described by linear stability theory, causes a large negative contribution to $C_{L_{canard}}$ from the $C_{L_q}q$ term for high pitch rates. The directions of the induced velocities due to pitch are given schematically in figure 4.5 as well. After the ramp motion stops ($t > 15$ deg), the wing region lift contribution converges to the steady-state result much more slowly than the canard region lift. Results shown in section 4.1.3 indicate that the canard-wing vortex interaction is a significant factor in this phenomenon.

4.1.2 Spatial and temporal convergence

To confirm the convergence and accuracy of the pitch-up ramp motion computations, time-step and grid refinements are performed for the $A_p = 0.05$ ramp case presented earlier in figure 4.5. Figures 4.6 and 4.7 show the effect of time-step size (Δt in deg) on the unsteady lift curves near $t = 0$ deg and $t = 15$ deg, respectively, for the component regions of the geometry. In the previous computations presented in this section, $\Delta t = 0.0025$ deg was used.

From figure 4.6, it is clear that with decreasing time-step size, the time-accurate solutions converge quickly. In fact, even when using a larger step size, the lift curves compare favorably for $t > 0.1$ deg. Figure 4.7 shows that, after the ramp motion has stopped, the transient solution is adequately converged in time using $\Delta t = 0.0025$ deg.

Spatial accuracy is demonstrated in figure 4.8 by the favorable comparison between baseline and refined grid solutions of component lift curves. The refined grid contains over 1.7 million points in the flowfield and was used extensively in Chapter 3 for the steady-state study. Figure 4.8 shows that, with the refined grid, slightly higher lift coefficients are predicted due to the improved resolution of the canard and wing leading-edge vortices. The remaining analyses of the unsteady canard-wing vortex interaction are performed using the refined grid.

4.1.3 Canard-wing vortex interaction

An analysis of the canard-wing vortex interaction provides further understanding of the complex flowfield that produces the unsteady load characteristics of the ramp motions shown earlier. Computations are performed for the canard-wing-body configuration undergoing a ramp motion of $\alpha_i = 0.00$ deg to $\alpha_f = 12.83$ deg and at a pitch rate of $A_p = 0.05$. Comparisons are also made with the corresponding steady-state results.

The steady and unsteady ramp motion results are summarized in figures 4.9 and 4.10, respectively, which show instantaneous streamlines released on the upper surfaces of the canard and wing. Positions $A_s, B_s,$ and $C_s,$ as indicated in figure 4.9, correspond to steady-state $\alpha = 4.21$ deg, 8.55 deg, and 12.83 deg, respectively. Similarly, during the ramp motion (fig. 4.10), positions $A, B,$ and C correspond to instantaneous $\alpha = 4.21$ deg, 8.55 deg, and 12.83 deg. The ramp motion stops at $\alpha_f = 12.83$ deg and the configuration is held fixed for all remaining time ($t > 12.83$ deg). Time-accurate transient results are given for $t > 12.83$ deg at instances D, E, and F. The α vs. time plot given in figure 4.10 illustrates the relative time instances of the ramp motion ($A-F$). Corresponding upper surface pressure contours for the steady and unsteady cases are given in figure 4.11 for the same instances during the ramp motion as in figures 4.9 and 4.10 ($A_s - C_s$ and $A - C,$ respectively).

A comparison between the steady and unsteady results shows significant differences in the characteristics of the canard and wing vortices during the early portion of the ramp motion. Steady and

unsteady case total pressure contours at a crossflow plane of $x/\bar{c} = 3.6$, as measured from the body nose, are given in figure 4.12 for these same angles of attack. As observed in figures 4.10, 4.11, and 4.12(b), a delay in canard vortex formation occurs for the unsteady case which correlates with the loss of canard lift due to the pitching motion (fig. 4.5). For the steady case, figure 4.12(a) shows the presence of the convected canard vortex, even at the lower angles of attack. Differences between the steady and unsteady wing vortices are also noted in figure 4.12. During the ramp motion, the increased strength of the wing vortex (fig. 4.12(b)) contributes to the increased lift of the wing portion observed earlier in figure 4.5.

For the current ramp motion, as the configuration reaches α_f , the motion stops. Figure 4.10 shows the formation of the canard vortex and, at later times, evidence of canard vortex breakdown. Total pressure contours in figure 4.13 illustrate the transient vortical flowfield of the canard ($x/\bar{c} = 2.0$) and wing ($x/\bar{c} = 3.6$) once the ramp motion has stopped. The development of the canard vortex, which was inhibited during the early portion of the ramp motion, is clearly observed. The canard vortex convects downstream and the changes in canard lift and downwash influence the characteristics of the wing vortex. As time increases from instances D to F (fig. 4.13), the canard-wing flowfield approaches the steady-state results illustrated earlier in figure 4.12(a).

Although the canard vortex forms rapidly once the ramp motion has stopped, figure 4.13 shows that the increasing strength of the canard vortex, its subsequent convection downstream, and its interaction with the wing vortex occur more slowly. As also observed earlier in figure 4.5, it is evident that the time scale is considerably larger for the wing than the canard to reach a relatively steady-state condition. Although some unsteadiness remains in the flow due to the breakdown of the canard vortex, the time-accurate results indicate a relatively stable flowfield for large time ($t \gg 12.83$ deg).

4.2 Pitch Oscillation

Results of pitch-oscillation simulations are presented to understand the unsteady flowfield, provide analyses of the canard-wing-body dynamic stability characteristics and to evaluate CFD accuracy and efficiency issues in predicting stability parameters. In order to match experimental test conditions (ref. 24) for the dynamic stability analysis, unsteady results are computed at $M_\infty = 0.70$ with the Reynolds number based on the mean aerodynamic chord of the wing ($Re_{\bar{c}}$) of 3.05 million.

Unsteady computations are performed for the mid-canard configuration undergoing pitch oscillations about the pitch axis (shown earlier in fig. 1.4). Computations are made at mean angles of attack, α_m , of 0 to 16 deg and a pitch amplitude, A , of 1.0 deg. A reduced frequency, as defined by $k = \frac{\omega \bar{c}}{2U_\infty}$, of 0.236 radians is used in the majority of the computations.

The computed time histories for the lift and moment coefficients are given in figures 4.14 and 4.15, respectively, as a function of non-dimensional time, ωt . Each case was computed for three full cycles of oscillation about a mean angle of attack of 4 deg, with the time histories of the latter two cycles shown in the figures. The angle of attack, with the appropriate scale on the right vertical axis, is given in each figure for reference.

A comparison of the lift time histories in figure 4.14(a) shows that the canard-on and canard-off cases exhibit similar trends. The amplitude of the oscillation in lift is slightly higher and the average lift coefficient is slightly lower for the canard-on case. Figure 4.14(a) also shows no significant phase shift for the total lift due to the canard. A breakdown of the lift time histories into component regions is given in figure 4.14(b) for the canard-on case. As with the pitch-up ramp cases given earlier, the canard and wing regions include the fore- and aft-body portions, respectively. Figure 4.14(b) shows that significant phase differences exist between the canard and wing lift curves. In fact, the wing

lift is shown to lead the pitch motion while the canard lift appears to lag. Previous results given in section 4.1 demonstrated that the lead and lag in wing and canard lift curves is primarily caused by the induced velocities due to the rapid pitch motion. A comparison of figures 4.14(a) (canard-off) and 4.14(b) (wing lift) also shows that the presence of the canard causes a phase shift in the wing region lift curve. The resulting total lift for the canard-on case slightly leads the pitch oscillation.

The time histories of canard-on/off total and canard-on component pitching moments are given in figures 4.15(a) and (b), respectively. Figure 4.15(a) shows that the canard-on case exhibits a higher average nose-up moment. In contrast to the total lift curves of figure 4.14(a), a more significant phase shift between canard-on and canard-off total moment curves is also noted. The breakdown into components of the moment contributions (fig. 4.15(b)) illustrates the large phase differences between the canard and wing region moments. Due to the forward position of the canard, the nose-up pitching moment of the canard results in a significant nose-up shift of the total moment curve.

In order to isolate the effects of the canard on the amplitude and phase of the lift/moment curves, a plot of the change in lift/moment as a function of the change in angle of attack is given in figure 4.16. In both the lift (fig. 4.16(a)) and moment (fig. 4.16(b)) curves, the change in lift/moment is taken from the average lift/moment coefficients for the respective canard-on or canard-off cases. The direction of the curves are also indicated in the figure. From figure 4.16(a), the larger oscillation amplitude and the minimal phase change of lift coefficient for the canard-on case is more clearly observed. Figure 4.16(b) shows the significant phase shift in moment coefficient for the canard-on case.

Further insight into the energy balance related to the motion of the configuration can be gained by integrating the pitching moment curves of figure 4.16. For the co-located moment center and pitch axis, an evaluation of

$$W_p = \oint C_m(\alpha)d\alpha \quad (4.2 - 1)$$

for a single cycle represents the amount of nondimensional work done by the fluid due to the motion of the configuration. A similar analysis for roll oscillations of delta wings has been performed in a previous computational study (ref. 58). For the pitching moment curves of figure 4.16(b), which have a counter-clockwise sense, an evaluation of equation 4.2-1 yields $W_p < 0$ indicating that work (or energy) is imparted to the fluid by the pitch oscillation of the configuration. Therefore, the configuration is expected to be positively damped in pitch. Furthermore, the apparent increased area contained within the canard-on moment curve (fig. 4.16(b)) indicates that more work is imparted to the fluid for the canard-on case, leading to a higher damped condition.

The periodicity of the oscillatory motion is demonstrated with the plot of lift and moment as a function of instantaneous angle of attack given in figure 4.17. The time-accurate computations are started from converged steady-state solutions at α_m . Figure 4.17 shows that lift and moment time histories reach a periodic oscillatory response within 2-3 cycles. A Fourier analysis was also performed on the second and third cycles of the oscillatory motion and the results showed less than 0.5 percent difference between the cycles in computed Fourier coefficients. Therefore, for the current configuration and flow conditions, the second cycle of oscillation is sufficiently accurate to perform the detailed dynamic stability analysis.

4.3 Dynamic Stability

A comparison between the lift/moment curves and the appropriate Fourier series using the first three Fourier coefficients (commonly referred to as a_0 , a_1 , and b_1) is given in figure 4.18 for the canard-on configuration. The coefficients were determined from a Fourier analysis of the computed second cycle

and the excellent agreement confirms that the higher-order terms can be neglected. These coefficients are then scaled with A and Ak as described in section 2.7 to obtain the corresponding dynamic stability parameters.

Figure 4.19 shows a generally favorable comparison between the computed and experimental (ref. 24) dynamic stability parameters for the canard-off case at various mean angles of attack (α_m) and an amplitude, $A = 1.0$ deg. The stability parameters based on normal force are given in figures 4.19(a) and (b) as the pitch rate and pitch displacement parameters, respectively. Damping-in-pitch and pitch-oscillatory stability, which are based on pitching moment coefficients, are given in figures 4.19(c) and (d), respectively. In addition, results from fine grid computations at two different α_m are given in figure 4.19 and show improvement in the damping-in-pitch parameter (fig. 4.19(c)) at $\alpha_m \approx 16$ deg. For moderate angles of attack ($\alpha < 10$ deg), both computations and experiment predict positive damping, $(C_{m_\alpha} + C_{m_q}) < 0$ in figure 4.19(c), and positive oscillatory stability, $(C_{m_\alpha} - k^2 C_{m_q}) < 0$ in figure 4.19(d), for the canard-off configuration.

4.3.1 Effect of canard

The canard is expected to have a pronounced effect on the dynamic stability of the wing-body configuration. Results from Chapters 3 and 4 on this configuration have shown that the close-coupled canard has a large influence on both the steady-state and unsteady wing aerodynamics. The effect of the mid-canard on longitudinal dynamic stability parameters is summarized in figure 4.20. Each data point on the curves represents the predictions at a mean angle of attack of α_m and an amplitude, $A = 1.0$ deg.

Figure 4.20 shows that the presence of the canard significantly changes the dynamic stability characteristics of the configuration. In particular, the pitch-rate parameter in figure 4.20(a) shows an increase throughout the mean angle-of-attack range, while the pitch-displacement parameter (fig. 4.20(b)) shows a dependence on angle of attack for the effect of the canard. For the pitching moment based parameters (figs. 4.20(c) and (d)), the computations show an increase in damping and a decrease in longitudinal stability with the canard.

The changes in damping-in-pitch and oscillatory stability due to the presence of the mid-canard is of particular interest and is again summarized in figure 4.21. Differences between canard-on and canard-off stability parameters are shown in figure 4.21 with the “zero-line” representing the canard-off case. As with figure 4.20 earlier, figure 4.21 also illustrates that the canard increases the damping-in-pitch of the configuration while reducing the oscillatory stability. The increase in damping with the canard correlates with the earlier analysis of the fluid “work” (eq. 4.2-1) described in section 4.2 and shown in figure 4.16(b).

For reference, the experimental data for the high-canard configuration is shown in figure 4.21. Since there is a difference in the canard vertical positions between the computation (mid-canard) and experiment (high-canard), the comparison with the experimental measurements is intended as a qualitative confirmation of the computational findings. However, it is noted that the agreement with experiment is quite favorable, except at $\alpha_m = 0$ deg, where the wake of the mid-canard in the computational model directly interacts with the co-planar wing.

The results given above are based on the computations of the canard-off and canard-on configurations undergoing pitch oscillations at a reduced frequency, $k = 0.268$. On the other hand, the experiment (ref. 24) was conducted at a one-order-of-magnitude lower reduced frequency, $k = 0.0268$. The implications of this difference and, in general, the effect of reduced frequency on predicting dynamic stability parameters is a topic of considerable interest and is discussed in the following section.

4.3.2 Reduced frequency

Time-accurate Navier–Stokes computations are generally restricted to small time-step sizes by accuracy and numerical stability constraints. As a result, simulations of low reduced-frequency cases, which are typical of small-scale wind-tunnel tests, can require extensive amounts of computer resources. The number of iterations required for each cycle of oscillation becomes inversely proportional to reduced frequency. Therefore, in order to improve computational efficiency, it is highly desirable to evaluate the effects of reduced frequency on the accuracy of the dynamic stability parameter predictions.

In particular, such an evaluation can provide guidance on the highest reduced frequencies which can be used in computational simulations for a given configuration and flow condition. When the simulated reduced frequencies become too high, the higher-order terms of equations 2.7-1 and 2.7-7 become significant and can no longer be neglected. Furthermore, the classical assumption of linear aerodynamic theory, from which equation 2.7-1 is based, can no longer be taken.

Figure 4.22 illustrates the effect of reduced frequency (k) on the normal force and pitching moment coefficients as a function of angle of attack for the canard-on configuration. The mean angle of attack is 4 deg and reduced frequency varies from $k = 0.268$ to 1.072. The increase in amplitude and shift in phase due to increasing k is observed in figures 4.22(a) and (b) for both the normal force and pitching moment coefficients, respectively.

From the dynamic stability analysis, the effect of k on the damping-in-pitch and pitch oscillatory stability parameters is given in figure 4.23 for the canard-on case. For clarity, the reduced frequency (horizontal axis) is plotted as the inverse of k ($1/k$) on a log scale. The experimental values are given at the actual reduced frequencies (k) reported in the wind-tunnel tests. Figure 4.23 shows that the dynamic stability parameters are accurately computed for a wide range of reduced frequencies. In fact, for damping-in-pitch, a computed reduced frequency which is up to 1.5 orders-of-magnitude higher than the experimental value continues to yield accurate stability parameter predictions. In the present study, a reduced frequency of $k = 0.268$ is utilized and allows for an order-of-magnitude reduction in the required computational time. For dynamic stability evaluations in general, a similar study on the sensitivities to reduced frequency has the potential to reduce computational expenses by orders of magnitude.

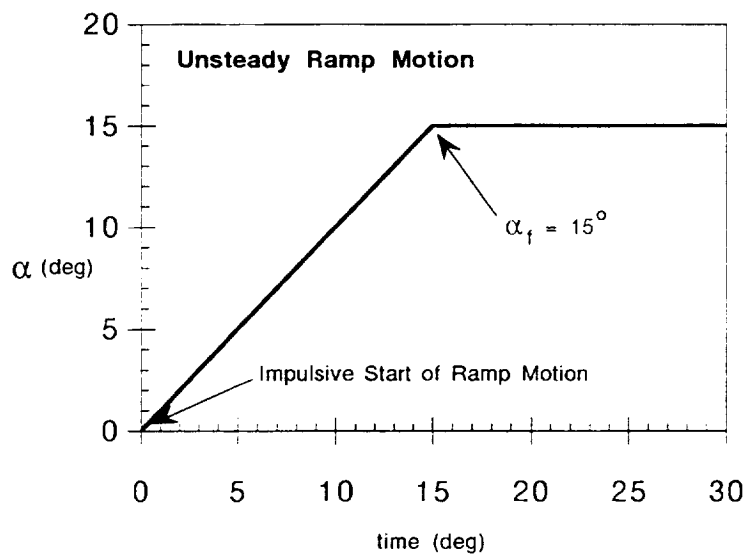


Figure 4.1. Schematic of unsteady pitch-up ramp motion from $\alpha_i = 0^\circ$ to $\alpha_f = 15^\circ$.

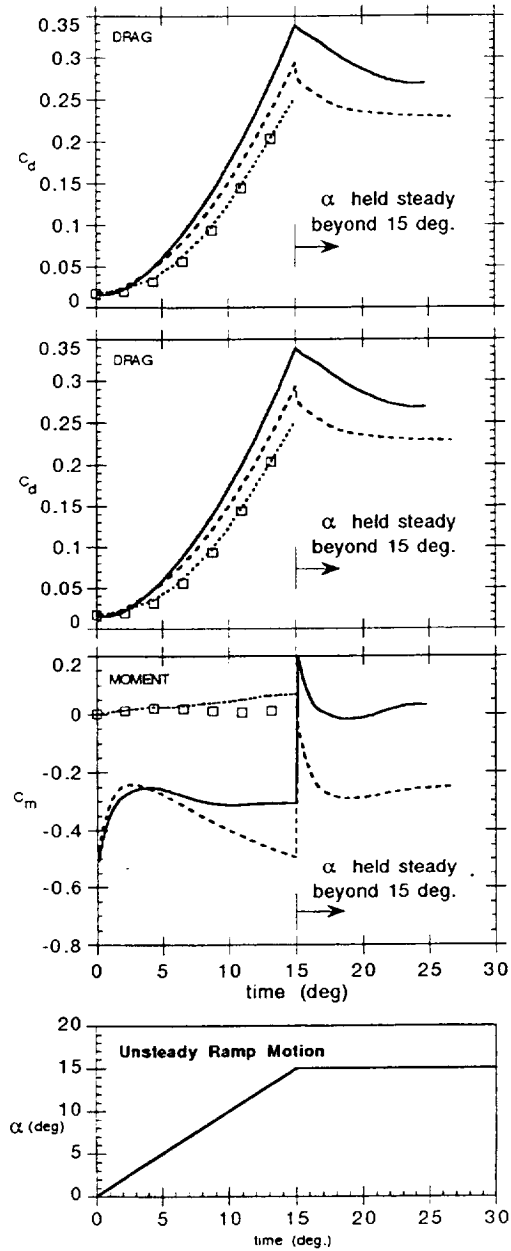


Figure 4.2. Effect of canard on unsteady aerodynamic loads during pitch-up ramp motion. $M_\infty = 0.90$, $A_p = 0.10$, $\alpha_i = 0^\circ$, $\alpha_f = 15^\circ$, $Re_{\bar{c}} = 1.52$ million.

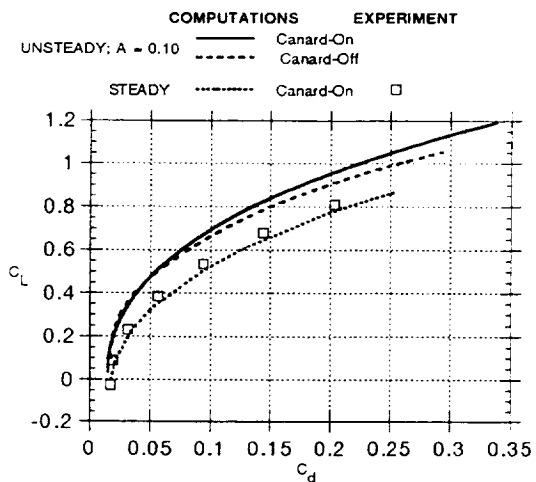


Figure 4.3. Drag polar of the canard-wing-body configuration undergoing pitch-up ramp motion. $M_\infty = 0.90$, $A_p = 0.10$, $\alpha_i = 0^\circ$, $\alpha_f = 15^\circ$, $Re_{\bar{c}} = 1.52$ million.

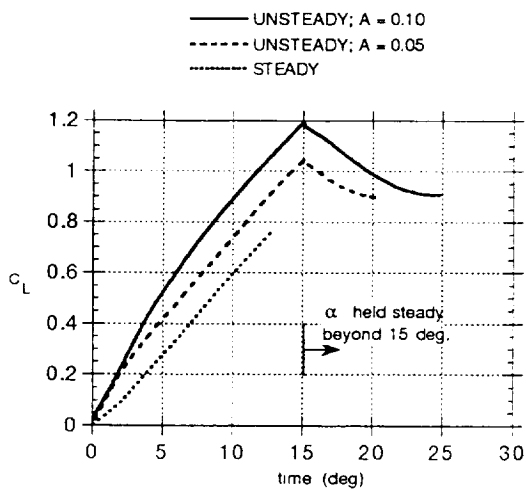


Figure 4.4. Effect of pitch rate on canard-wing-body lift. $M_\infty = 0.90$, $\alpha_i = 0^\circ$, $\alpha_f = 15^\circ$, $Re_{\bar{c}} = 1.52$ million.

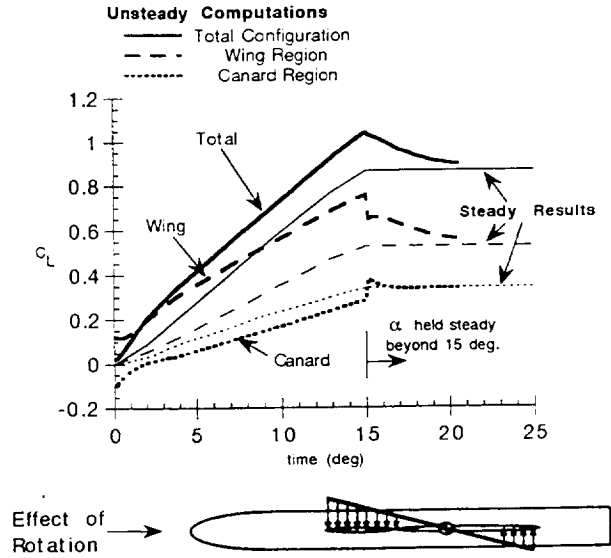


Figure 4.5. Comparison of steady and unsteady component lift curves for the canard configuration. $M_\infty = 0.90$, $A_p = 0.05$, $\alpha_i = 0^\circ$, $\alpha_f = 15^\circ$, $Re_{\bar{c}} = 1.52$ million.

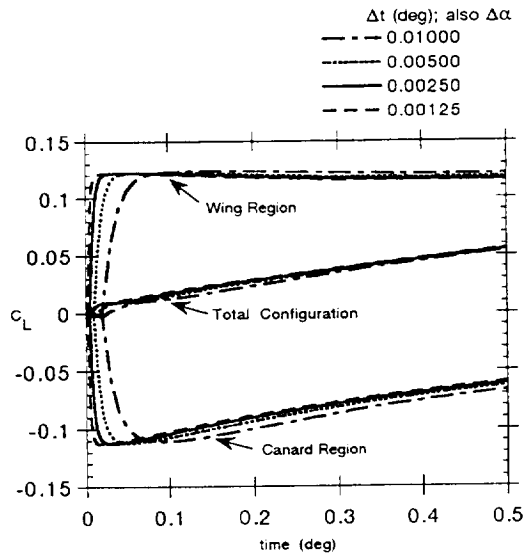


Figure 4.6. Effect of time-step size on the unsteady component lift curves near the beginning of the ramp motion, α_i . $M_\infty = 0.90$, $A_p = 0.05$, $\alpha_i = 0^\circ$, $\alpha_f = 15^\circ$, $Re_{\bar{c}} = 1.52$ million.

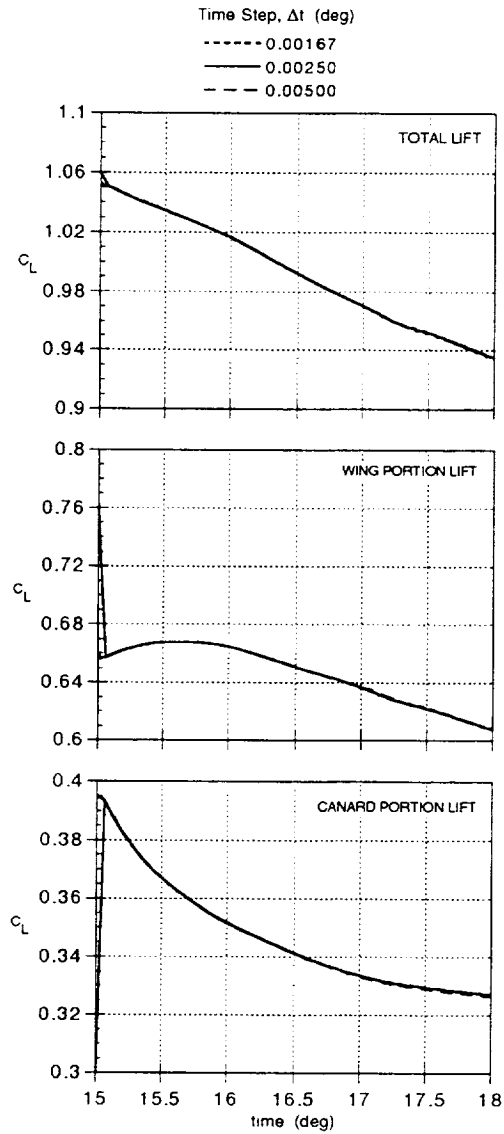


Figure 4.7. Effect of time-step size on the unsteady component lift curves near the end of the ramp motion, α_f . $M_\infty = 0.90$, $A_p = 0.05$, $\alpha_i = 0^\circ$, $\alpha_f = 15^\circ$, $Re_{\bar{c}} = 1.52$ million.

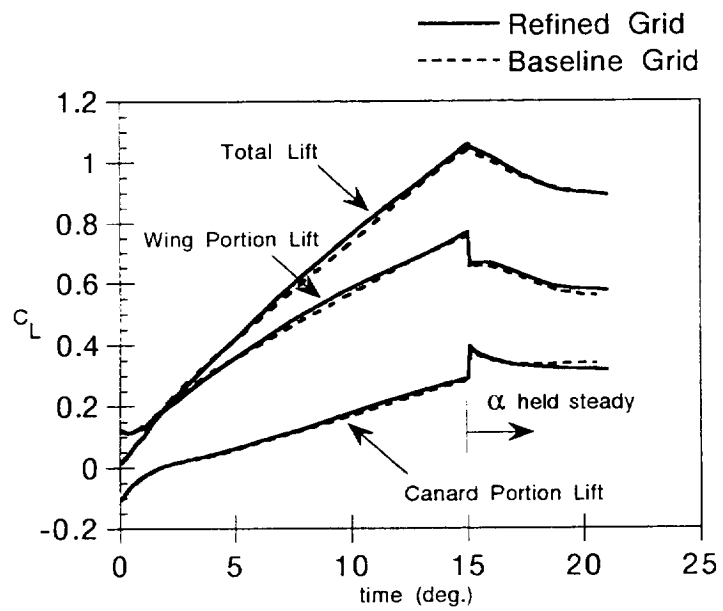


Figure 4.8. Effect of grid refinement on the unsteady component lift curves. $M_\infty = 0.90$, $A_p = 0.05$, $\alpha_i = 0^\circ$, $\alpha_f = 15^\circ$, $Re_{\bar{c}} = 1.52$ million.

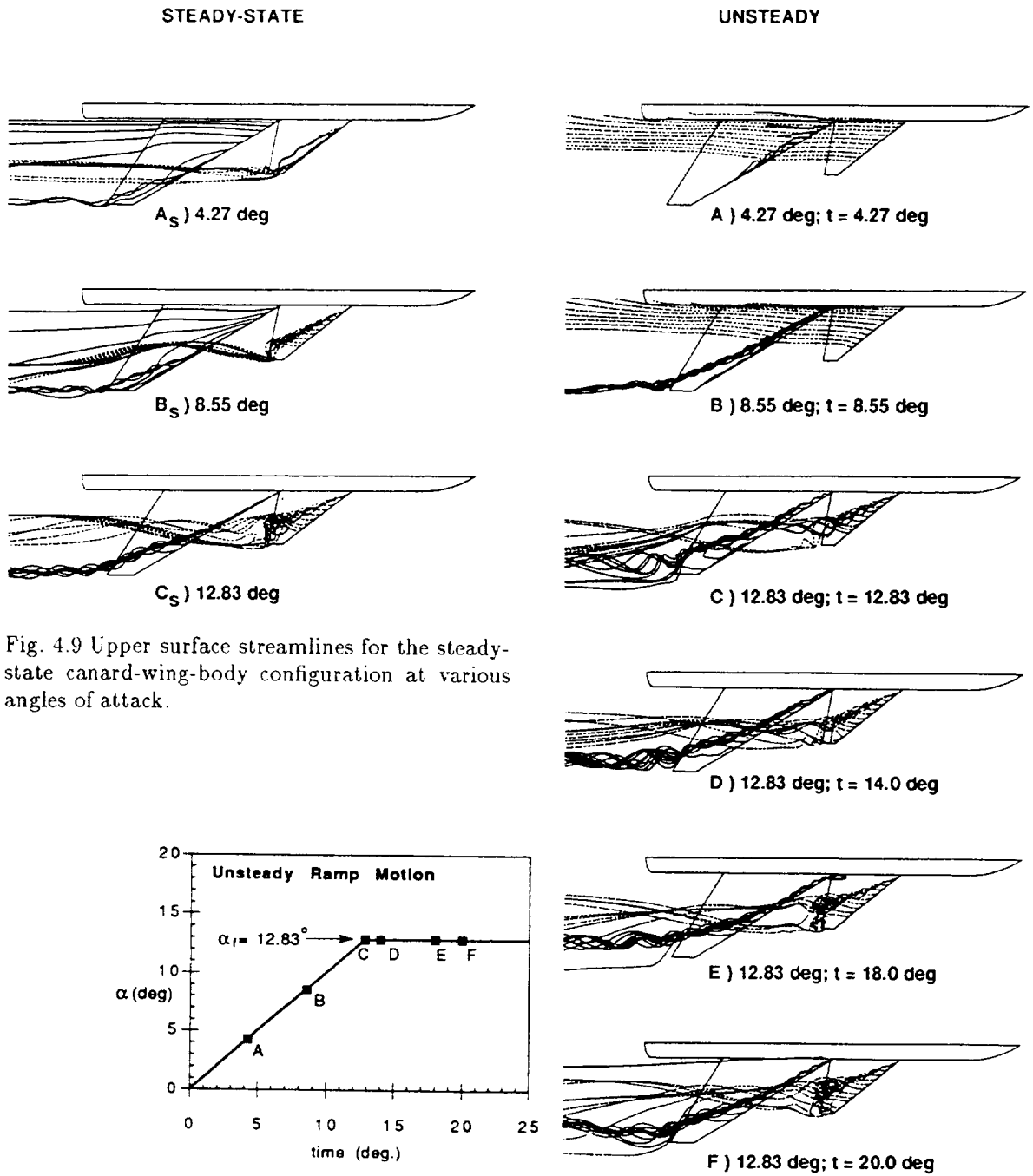


Fig. 4.9 Upper surface streamlines for the steady-state canard-wing-body configuration at various angles of attack.

Figure 4.10. Upper surface instantaneous streamlines at various times for the canard-wing-body configuration undergoing unsteady ramp motion. $M_\infty = 0.90$, $A_p = 0.05$, $\alpha_i = 0^\circ$, $\alpha_f = 12.83^\circ$, $Re_\varepsilon = 1.52$ million.

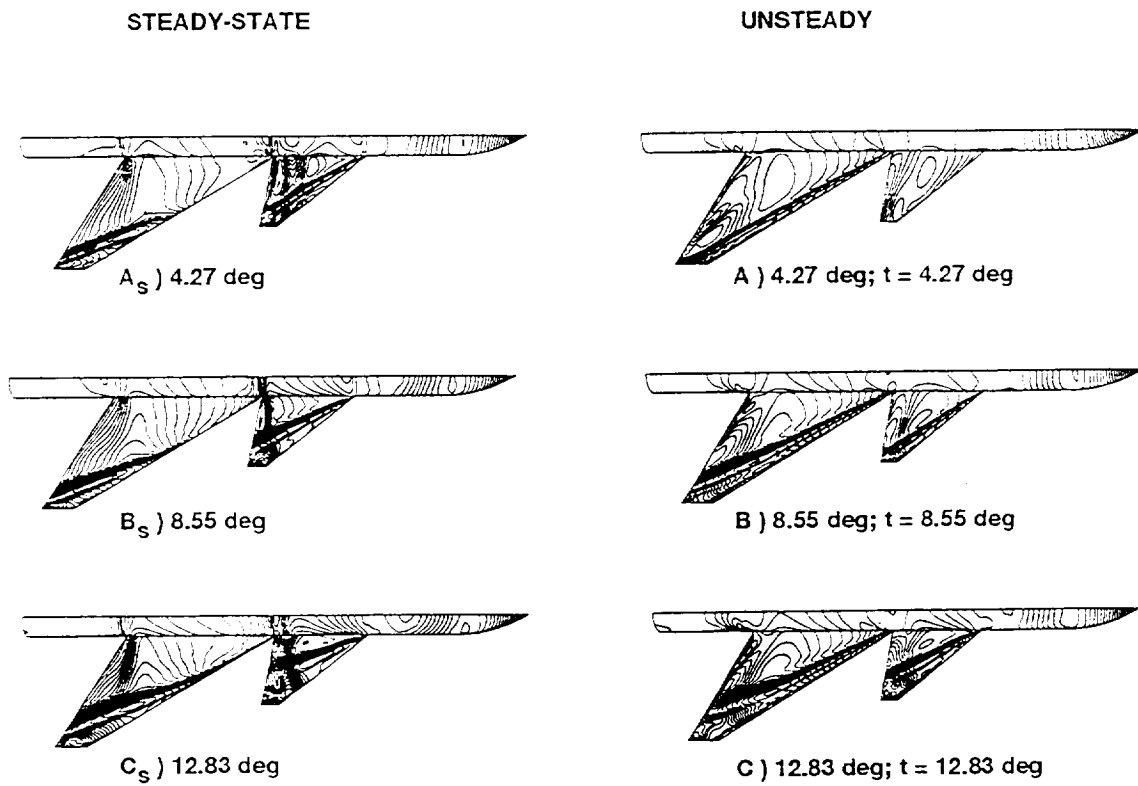


Figure 4.11. Upper surface pressure contours at various times for the canard-wing-body configuration undergoing unsteady ramp motion. $M_\infty = 0.90$, $A_p = 0.05$, $\alpha_i = 0^\circ$, $\alpha_f = 12.83^\circ$, $Re_{\bar{c}} = 1.52$ million.

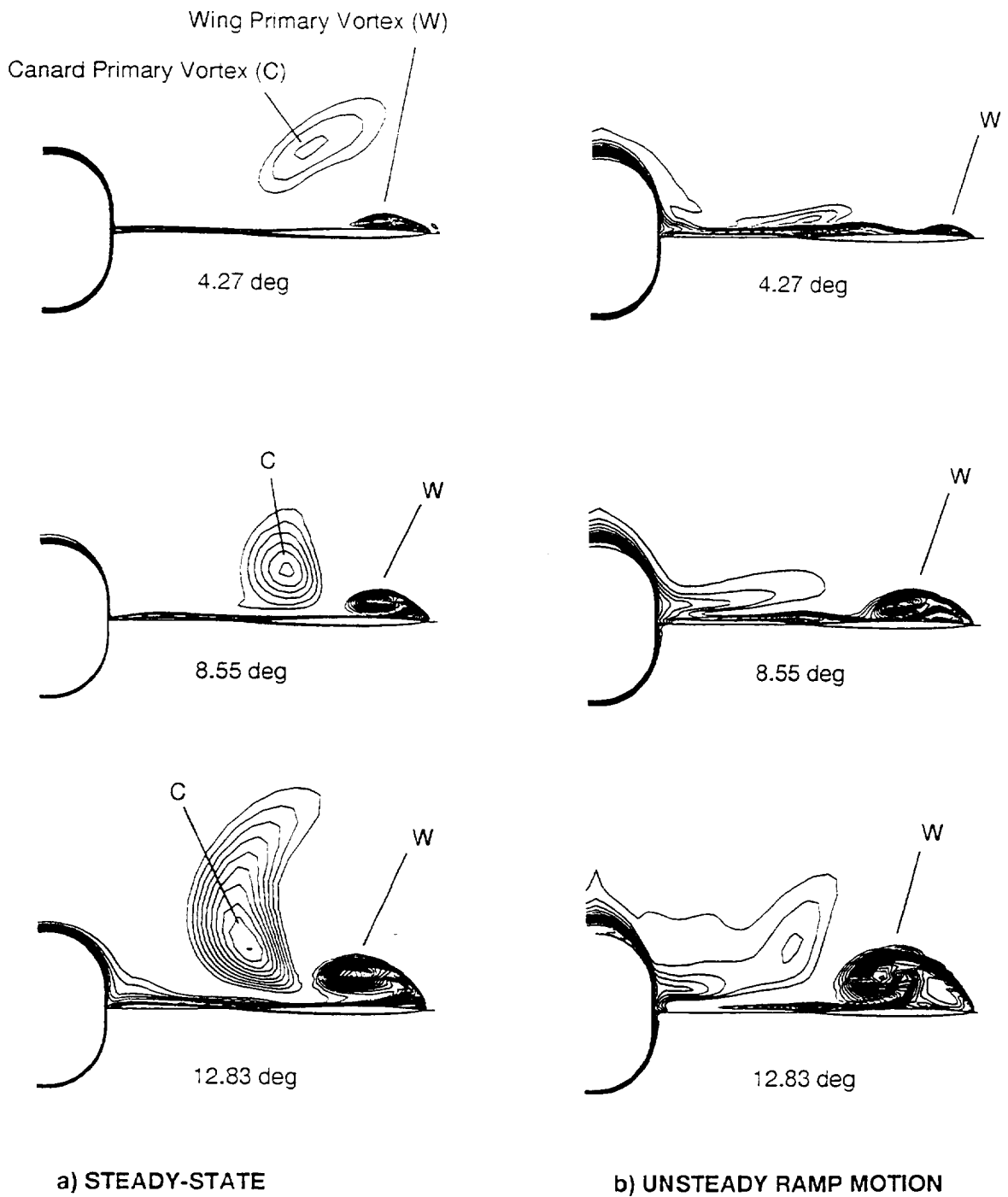


Figure 4.12. Comparison of crossflow total pressure contours between the steady and unsteady cases at various angles of attack. $M_\infty = 0.90$, $A_p = 0.05$, $\alpha_i = 0^\circ$, $\alpha_f = 12.83^\circ$, $Re_{\bar{c}} = 1.52$ million.

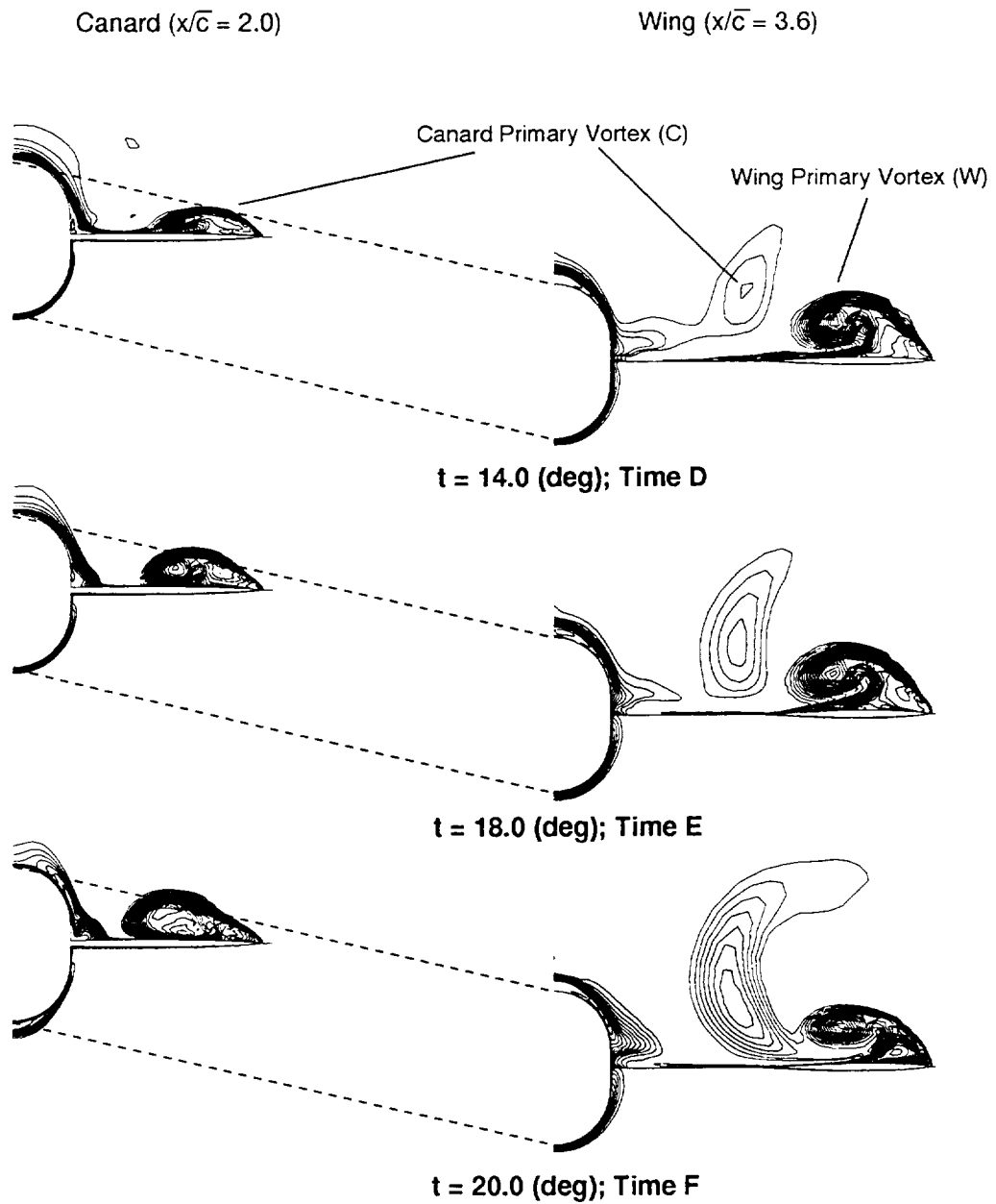


Figure 4.13. Crossflow total pressure contours for the transient flow after the ramp motion has ended. $M_\infty = 0.90$, $A_p = 0.05$, $\alpha_i = 0^\circ$, $\alpha_f = 12.83^\circ$, $Re_{\bar{c}} = 1.52$ million.

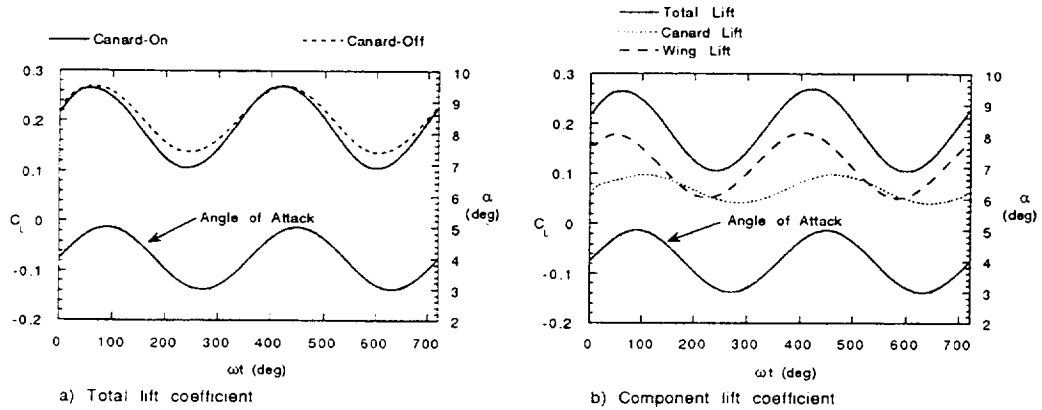


Figure 4.14. Effect of canard on component lift coefficients for two cycles of oscillation. $M_\infty = 0.70$, $k = 0.268$, $\alpha_m = 4.0^\circ$, $A = 1.0^\circ$, $Re_{\bar{c}} = 3.05$ million.

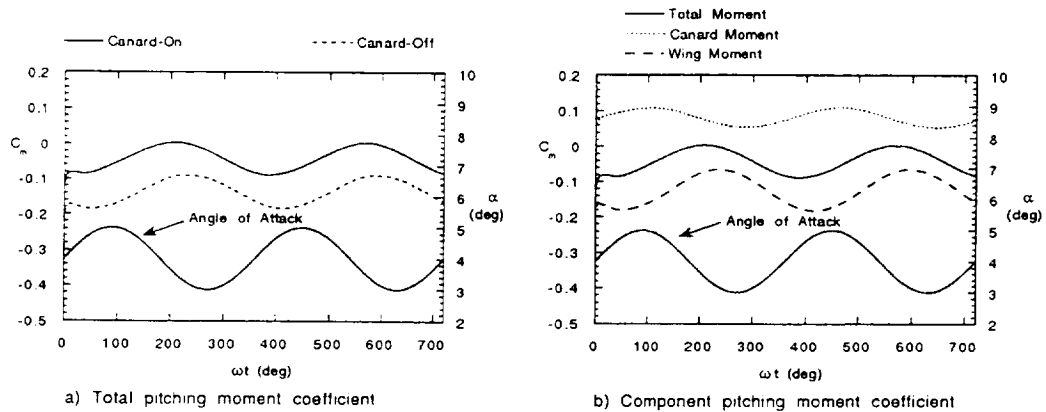


Figure 4.15. Effect of canard on component pitching moment coefficients for two cycles of oscillation. $M_\infty = 0.70$, $k = 0.268$, $\alpha_m = 4.0^\circ$, $A = 1.0^\circ$, $Re_{\bar{c}} = 3.05$ million.

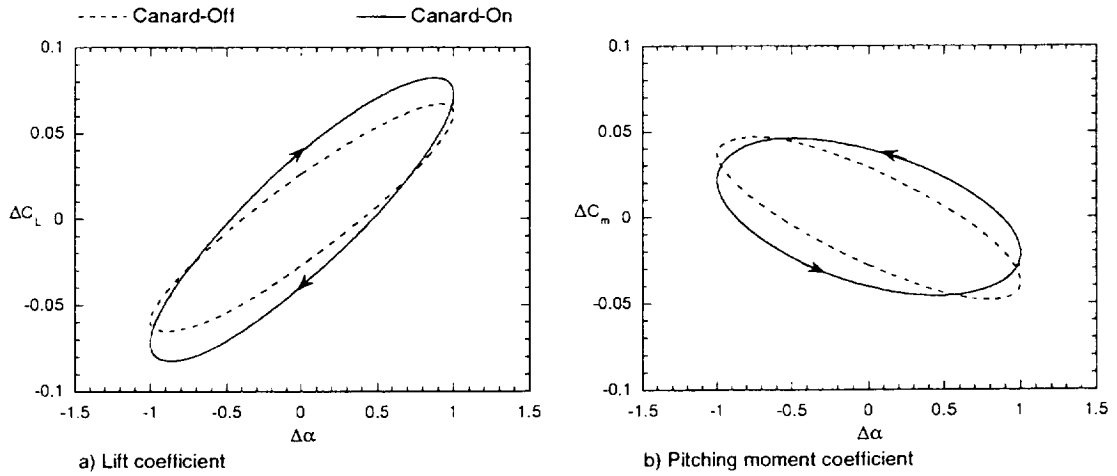


Figure 4.16. Effect of canard on lift and pitching moment coefficient curves for third cycle of oscillation. $M_\infty = 0.70$, $k = 0.268$, $\alpha_m = 4.0^\circ$, $A = 1.0^\circ$, $Re_{\bar{c}} = 3.05$ million.

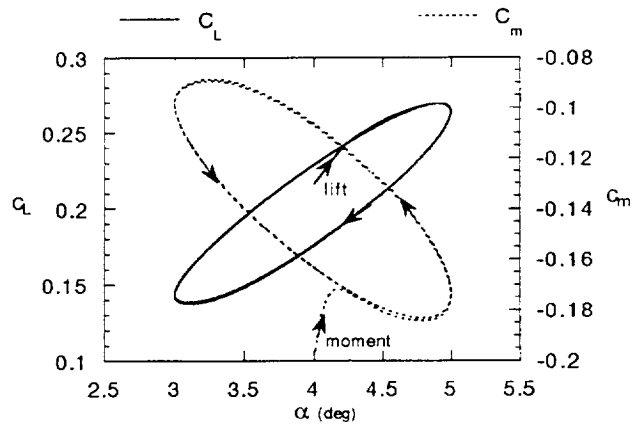


Figure 4.17. Lift and pitching moment curves for the canard-off configuration (started from steady-state solutions with three cycles of oscillations shown). $M_\infty = 0.70$, $k = 0.268$, $\alpha_m = 4.0^\circ$, $A = 1.0^\circ$, $Re_{\bar{c}} = 3.05$ million.

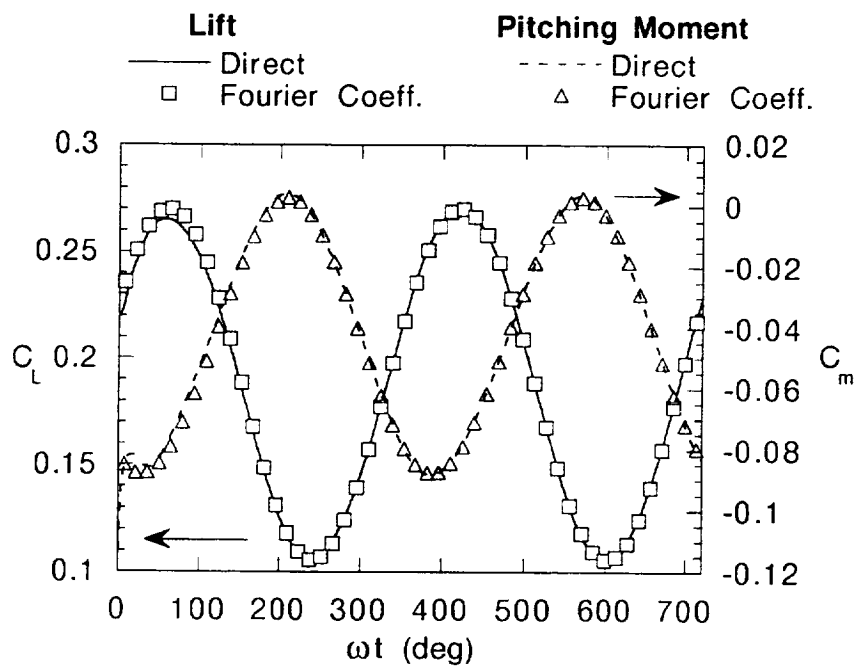


Figure 4.18. Comparisons of directly computed and Fourier-coefficient represented lift and pitching moment curves. $M_\infty = 0.70$, $k = 0.268$, $\alpha_m = 4.0^\circ$, $A = 1.0^\circ$, $Re_{\bar{c}} = 3.05$ million.

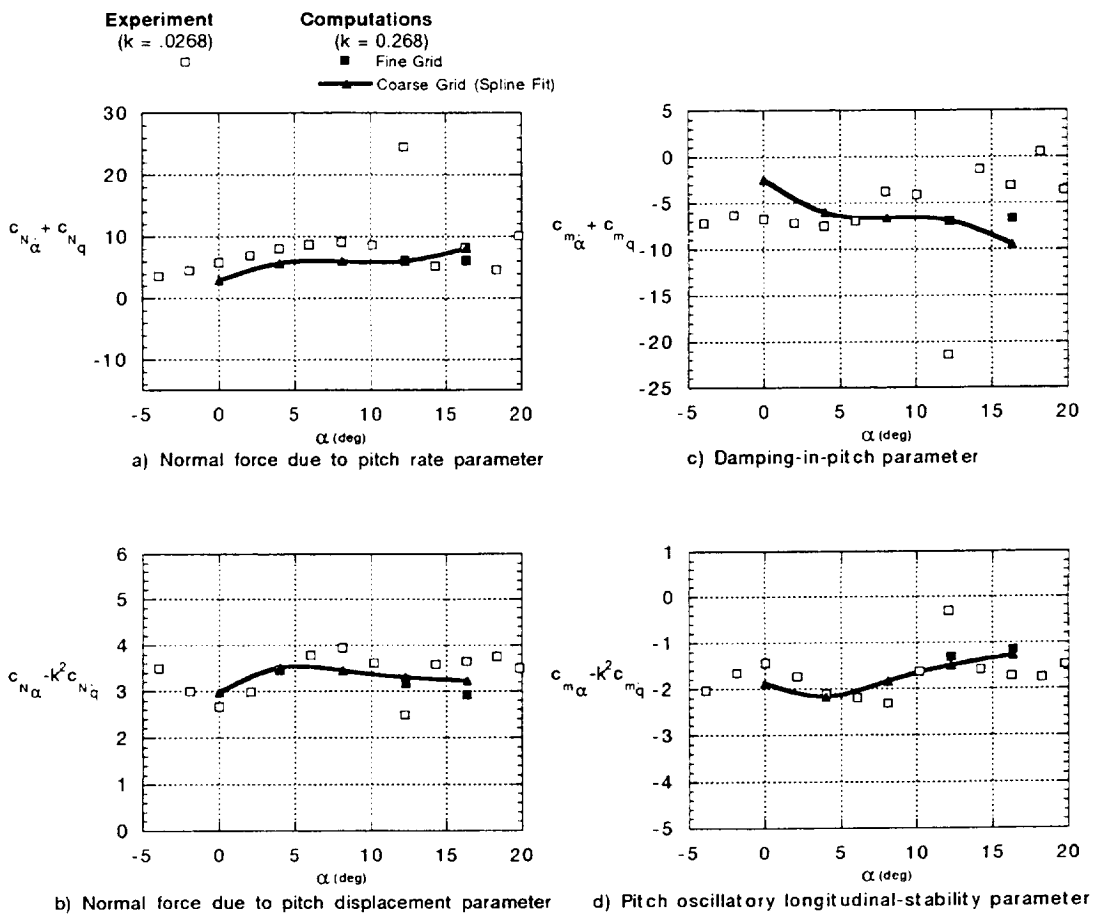


Figure 4.19. Comparison of the computed and experimental longitudinal dynamic stability parameters for the canard-off configuration. $M_{\infty} = 0.70$, $Re_{\bar{c}} = 3.05$ million.

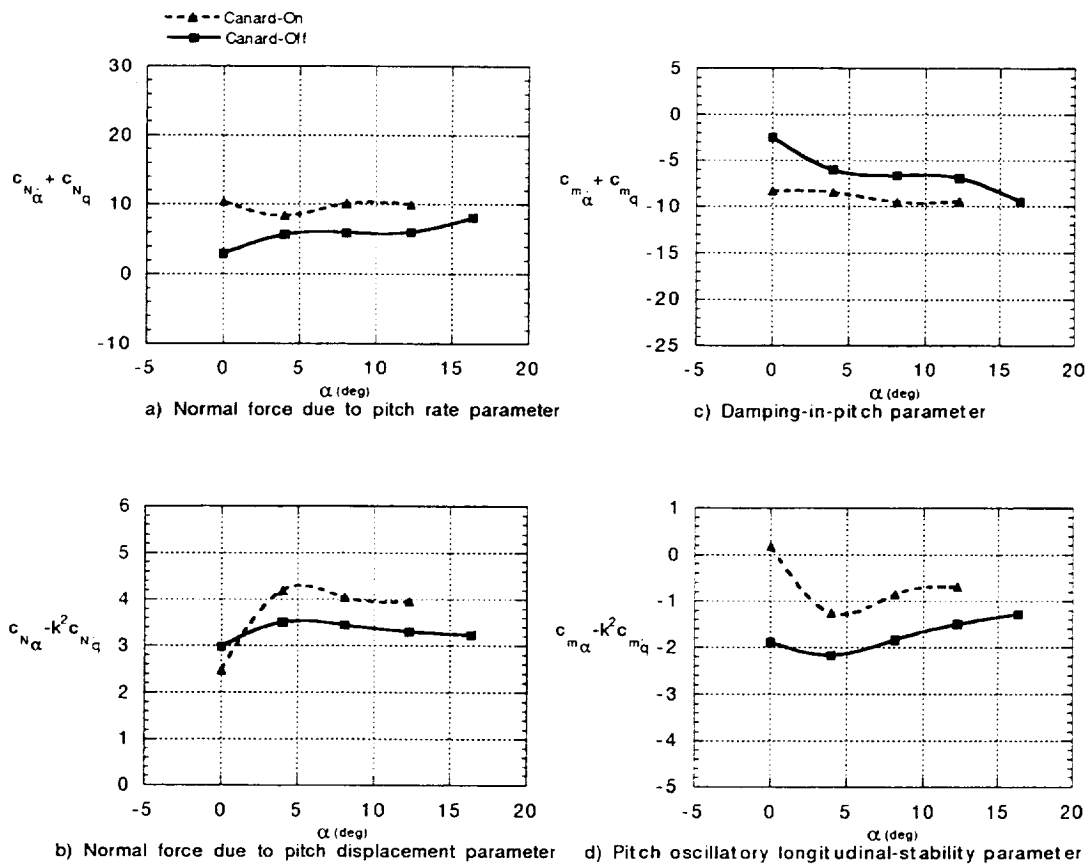


Figure 4.20. Comparison of the longitudinal dynamic stability parameters for the configuration with and without the canard. $M_{\infty} = 0.70$, $Re_{\bar{c}} = 3.05$ million.

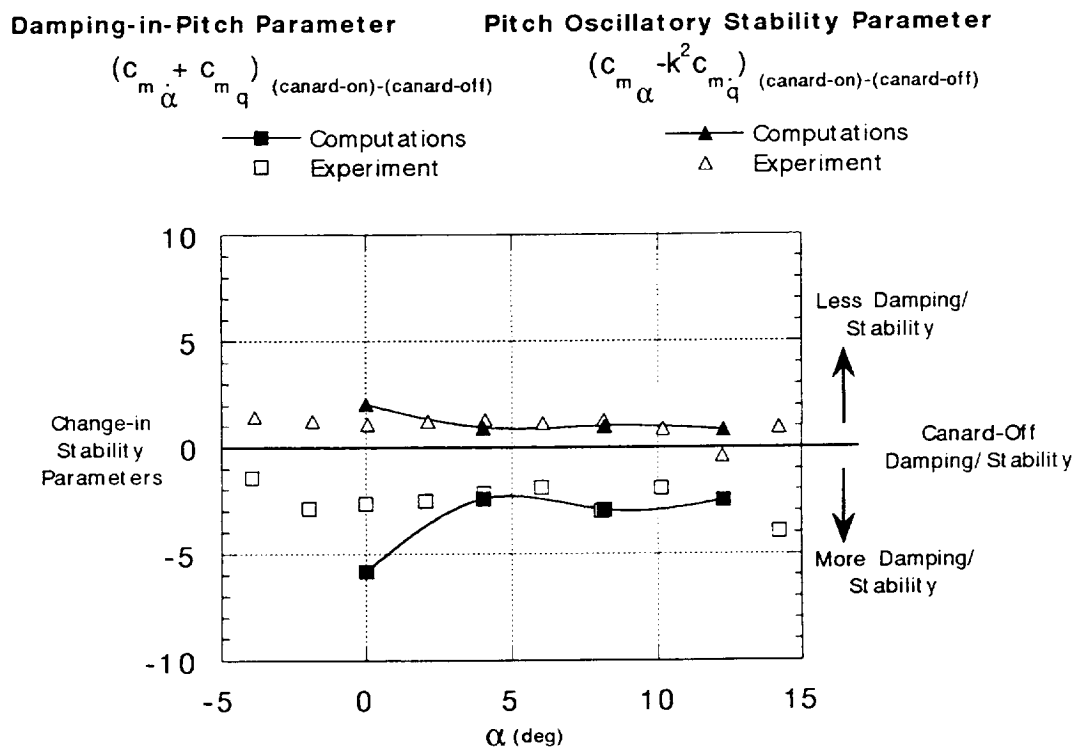
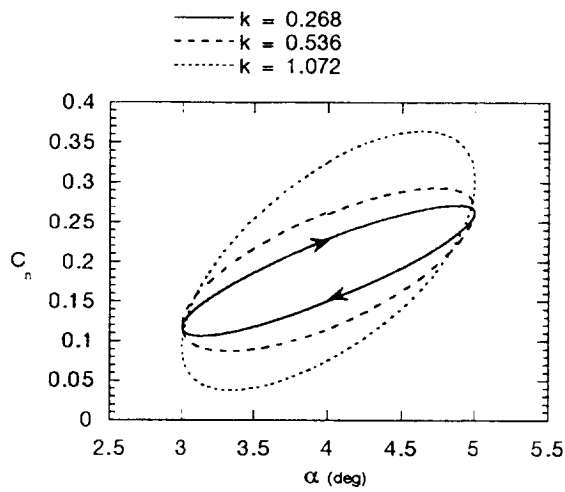
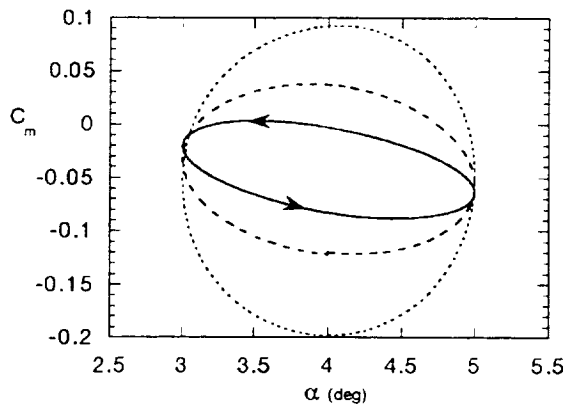


Figure 4.21. Effect of the canard on pitching-moment dynamic stability parameters (differences between canard-on and canard-off values shown). $M_\infty = 0.70$, $Re_{\bar{z}} = 3.05$ million.



a) Normal Force Coefficient



b) Pitching Moment Coefficient

Figure 4.22. Effect of reduced frequency (k) on normal force and pitching moment coefficients for the canard-on case. $M_\infty = 0.70$, $\alpha_m = 4.0^\circ$, $A = 1.0^\circ$, $Re_{\bar{c}} = 3.05$ million.

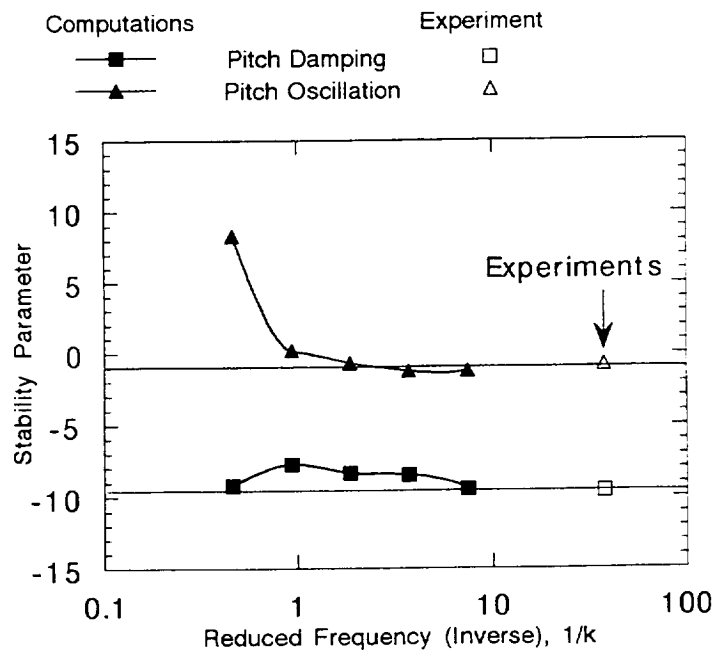


Figure 4.23. Effect of reduced frequency (k) on damping-in-pitch and pitch-oscillatory stability parameters for the canard-on case. $M_\infty = 0.70$, $\alpha_m = 4.0^\circ$, $Re_{\bar{c}} = 3.05$ million.

Chapter 5

Unsteady Aerodynamics of Moving Canards

Many canard-configured aircraft, including several mentioned in Chapter 1, utilize moving canards for longitudinal stability, pitch control and aerodynamic performance. In order to understand the influence of moving canards and to demonstrate the current capability to predict the resulting unsteady flowfield, time-accurate Navier–Stokes simulations are solved for the configuration undergoing pitch-up and oscillatory canard motions. Details of the grid generation, boundary conditions and zonal interfaces for the moving canard cases are found in sections 2.4, 2.5, and 2.6, respectively. The freestream flowfield conditions used in the canard motion studies are $M_\infty = 0.85$ and a Reynolds number based on the mean aerodynamic chord of the wing ($Re_{\bar{c}}$) of 2.82 million. These conditions match those used for the steady-state canard deflection studies (secs. 3.2.2 and 3.3.3), thereby allowing for the direct comparisons and observations between fixed and moving canard results.

5.1 Canard Pitch-Up Ramp Motion

The deflections of the canard during the pitch-up ramp motions are illustrated in figure 5.1. All canard pitch-up cases begin with an initial canard deflection (δ_{c_i}) of 0.0 deg, and final canard deflections (δ_{c_f}) of 5.0 and 9.25 deg. As with the pitch-up motions of the entire fixed-canard configuration (sec. 4.1), the canard motions begin and end instantaneously. Various canard pitch rates (A_{pc}) are simulated in this section. The time histories of force and moment are again given in non-dimensional time ($t_{rad} = \frac{t_{sec} A_{pc} U_\infty}{c}$). Note that during the portion when the canard is moving, $\delta_c = t$.

5.1.1 Unsteady lift and pitching moment

The time histories of lift and pitching moment coefficients are given in figure 5.2 for the canard configuration at $\alpha = 4.27$ deg. Canard deflection angles as a function of non-dimensional time (t) are also indicated in the figure. Starting from a steady-state condition at $\delta_c = 0.0$ deg, the canard begins to pitch up at time, $t = 0$ deg with a pitch rate of $A_{pc} = 0.05$. The lift curve for $\alpha = 4.27$ deg (fig. 5.2(a)) shows that an increase in total lift is purely transitory during the unsteady aerodynamic portion of the canard motion. In fact, the initial total lift at $t = 0$ deg ($\delta_c = 0.0$ deg) and the final total lift for $t > 8$ deg ($\delta_c = 5.0$ deg) are basically unchanged. This result is consistent with the steady-state computations at various fixed canard deflections shown earlier (fig. 3.14), which illustrated an increase in canard lift and a decrease in wing lift as a function of increasing canard deflection angles.

Figure 5.2(b) shows the effects of the canard motion on the pitching moment coefficients for the configuration. Steady-state results of section 3.2 found that the wing portion pitching moment is relatively insensitive to the various fixed canard deflection angles. The results in these two figures indicate that this effect is extended to unsteady canard ramp motions as well. For the configuration in this study, the pitching moments for the entire configuration at $\alpha = 4.27$ deg (fig. 5.2(b)) is purely dependent on the canard portion contributions.

Although the pitching moments of the configuration undergoing canard pitch-up motion are very similar to the corresponding steady-state characteristics, the unsteady nature of the lift curve is of particular interest. Figure 5.2(a) also shows that although the canard portion lift responds almost immediately to the canard pitch-up motion, a significant delay is observed before the wing portion lift responds to the effects of the canard motion. This delay is due to the time required to convect the effects of the canard downstream to the wing. The length of the delay observed in the figure, which is on the order of $\Delta t \approx 3$ deg (or 0.05 rad.), correlates well with the pitch rate of $A_{pc} = 0.05$ for this angle-of-attack case. In essence, for $A_{pc} = 0.05$, $\Delta t = 0.05$ rad. is the length of time for a freestream fluid particle to travel the distance \bar{c} , which also represents the approximate average distance between the canard and the wing. The transient increase in total lift is primarily due to this delay in the wing's response to the increase in canard lift.

The transient nature of the configuration lift curve and, specifically, the delay observed in the wing response is a direct function of the canard pitch rate. Figures 5.3 and 5.4 show the effects of canard pitch rate, A_{pc} , on lift and moment coefficients, respectively, for the configuration at $\alpha = 4.27$ deg. As pitch rate is increased, both the magnitudes of the canard lift and the non-dimensional time delay in the wing response increase (figs. 5.3(b) and (c)). The combination of these two effects produces a higher peak lift coefficient for the entire configuration (fig. 5.3(a)). The results of figure 5.4 illustrate that canard pitch-rate effects on pitching moment are considerably less significant than for lift.

For the higher pitch rate cases given in figures 5.3 and 5.4, a constant physical time-step size results in a higher non-dimensional time step. However, refining the step sizes can be used to demonstrate temporal convergence. Figure 5.5 shows the effect of time-step size on the lift and pitching moment predictions of the computations performed for $A_{pc} = 0.20$. The excellent comparison between the computational simulations at various step sizes, particularly during the transient period after the canard motion has stopped ($t \geq 5$ deg), confirms the adequate time-step resolution for the canard pitch-up ramp cases.

5.1.2 Canard-wing vortex interaction

The results given in the preceding section can be further understood by examining the canard-wing vortex interaction during the canard pitch-up maneuver. For easier visualization of stronger vortices, a canard pitch-up simulation is performed for the configuration at the higher angle of attack of $\alpha = 8.0$ deg. Figure 5.6 illustrates the time histories of lift and pitching moment coefficients for this case. Similar to the lower angle-of-attack case given earlier in figure 5.2, the current case at $\alpha = 8.0$ deg shows a transitory increase in total lift which is due to the delay in wing lift response. Figure 5.6(b) also shows that pitching moment characteristics during the canard motion are similar to the lower angle-of-attack case.

Comparisons of total pressure contours at constant streamwise locations are given in figure 5.7 for the instant when the canard is deflected at $\delta_c = 5.0$ deg during the canard pitch-up motion ($A_{pc} = 0.05$). The steady-state results of the static canard at the corresponding freestream condition and canard deflection angles are also shown in the figure. The crossflow total pressure contours illustrate a slightly weaker canard vortex formation for the unsteady cases ($x/\bar{c} = 2.0$) in comparison to the

steady cases. The weaker canard vortex at a given deflection angle is primarily due to the induced velocities at the canard leading edge from the canard rotation about its pitch axis. Further downstream at the same instant in time, the weaker canard vortex and the effects from convection of the canard's influences produce a less developed canard vortex over the wing surface ($x/\bar{c} = 2.8$ and 3.5). After the canard motions stops, the effects of the canard vortex on the wing flowfield will approach the steady-state results.

To better visualize the effects of the wing flowfield development, the time scales and canard effects are increased by starting with the lower angle of attack case ($\alpha = 4.27$ deg) and continuing the canard pitch-up motion to a higher deflection angle. Figure 5.8 shows the lift and pitching moment curves for the configuration undergoing a canard pitch-up from $\delta_{c_i} = 0$ deg to $\delta_{c_f} = 9.25$ deg with a non-dimensional pitch rate of $A_{pc} = 0.05$. The increase in total lift and the delay in wing response are both clearly evident in figure 5.8(a). For the canard pitching to $\delta_c = 9.25$ deg, the downwash of the canard causes the wing to generate very little lift at the positive α of 4.27 deg. This effect was also observed in the deflected static canard cases of section 3.2.2, which showed steady-state vortices on both the wing upper and lower surfaces.

Traces representing instantaneous streamlines at seven different times are given in figure 5.9 for the $\delta_{c_f} = 9.25$ deg canard pitch-up case. As illustrated in the legend of figure 5.9, the first four instances (A-D) are during the canard motion ($\delta_c \leq \delta_{c_f}$), and the last three instances (E-G) are during the transient phase as the flowfield approaches a steady-state condition. Visualization of the canard and wing vortices is performed by starting the traces near the upper- and lower-surface leading edges of the wing, and the upper-surface leading edge of the canard.

As the canard deflection begins to increase, minimal initial influence of the canard on the wing vortex structure is shown (time positions A and B). As the canard deflection approaches $\delta_c \approx 7$ deg, time position C shows the initial formation of a leading edge vortex on the wing lower surface. Just before the canard motion stops at time position D, the wing lower surface vortex becomes more organized, and the canard leading-edge vortex shows evidence of vortex breakdown. Time positions E-G show the completion of the vortex structure development while the canard deflection is fixed at $\delta_c = \delta_{c_f} = 9.25$ deg. The formations of the lower surface vortex on the inboard of the wing and the upper surface vortex on the outboard wing portion are clearly evident.

Crossflow visualizations of total pressure contours are given in figure 5.10 for the canard and wing regions. Figures 5.10(a)–(c) correspond to time instances A–C from figures 5.9(a)–(c) during the canard ramp motion. In figure 5.10, the development of the canard vortex and its convection over the wing surface is observed. Furthermore, the initial formation of the wing lower surface vortex is noted in figure 5.10(c) (wing region) and correlates with the instantaneous streamlines of figure 5.9(c).

In order to more clearly visualize the development of the wing vortex structure, crossflow total pressure contours are given in figure 5.11 at the same $x/\bar{c} = 3.3$ for five time positions starting with just prior to when the canard deflection angle has reached δ_{c_f} . As time increases, the development of the canard vortex over the wing and the wing leading-edge vortices on the upper and lower surfaces are observed. Since the contour levels of total pressure are evenly distributed, the relative strengths of these vortices are indicated in figure 5.11 as an approximate loss in total pressure at the vortex cores. Although at slightly different conditions, a qualitative comparison can also be made with the static canard deflection cases given in figure 3.26, where the canard, wing upper surface and wing lower surface vortices were also observed in the wing flowfield. As illustrated earlier in figures 5.2 and 5.6 of section 5.1.1, and currently in figures 5.9 and 5.11, the time required for the full development of the wing flowfield and vortex structure allows for the transient increases observed in the total lift of the configuration.

5.2 Canard Pitch Oscillation

The investigation of the unsteady aerodynamics of canard pitch oscillations can lead to an evaluation of the dynamic stability characteristics of the moving canard control surface. Furthermore, previous studies (refs. 26–28) have experimentally examined the potential of using canard oscillations to promote wing performance in extreme maneuver conditions. Specifically, these studies explored the potential of using high frequency canard oscillations as an active control method of delaying wing stall. Although unsteady experiments may be able to evaluate the effectiveness of such techniques, computational simulations are required to fully understand the physics of such unsteady flow phenomenon and, more importantly, to optimize the use of the oscillating canard. This section will present the results of canard pitch oscillations at the pre-stall conditions of interest in this study.

Canard pitch oscillation simulations are performed at a pitch amplitude (A_c) of 2 deg, and reduced frequencies (k_c) of 1.0. Mean angles of attack for the configuration of 4.27 deg and 8.00 deg are presented. As with the rigid-body oscillation studies of sections 4.2 and 4.3, high values of reduced frequencies are simulated to minimize computational expense.

5.2.1 Unsteady lift and pitching moment

The effects of the oscillating canard on the configuration lift and pitching moment characteristics are given in figures 5.12(a) and (b), respectively, as a function of non-dimensional time ($\omega_c t$) for the configuration at $\alpha = 4.27$ deg. The canard deflection angles with respect to $\omega_c t$ are also indicated in the figure. From figure 5.12, it is evident that the time histories of the canard lift and moment are closely in-phase with the canard oscillation. On the other hand, the wing contributions to both lift and moment exhibit significant shifts in phase and appear to be the primary contributor to the phase differences between the canard motion and the total lifts and moments. These effects of the oscillating canard on the canard and wing contributions are consistent with the earlier findings of the canard pitch-up ramp motion studies (sec. 5.1), which also found almost instantaneous canard response to changes in deflection angle δ_c .

Figure 5.13 shows that a periodic time response is achieved within two cycles of canard oscillations in spite of the fact that the wing responses are due to the canard motions rather than direct wing motions. Note also that the significant contributions of the wing responses to the overall phase differences in both lift and moment are observed in figures 5.13(a) and (b), respectively. In fact, figure 5.13(b) shows that the phase differences between the overall pitching moment and the canard deflections are almost entirely due to the wing response. Furthermore, it is significant to observe that the relatively small amplitude oscillations of the canard produce relatively large wing responses in pitching moment. The amplitude of wing responses due to the pitch oscillations are comparable to those resulting from the much larger canard deflections of the canard ramp motion cases (fig. 5.8). Correspondingly, the wing lift response due to the canard oscillations in figure 5.13(a) also exhibits a relatively high amplitude for the small canard deflection angles. These results indicate that the high frequency nature of the canard oscillations has a significant influence on the wing response characteristics, even at relatively small pitch amplitudes.

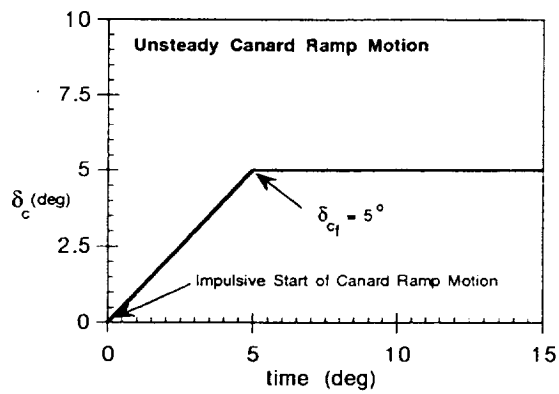
Similar trends are observed for the lift and moment characteristics of the configuration at $\alpha = 8.0$ deg. Figures 5.14 and 5.15 show that the canard oscillation produces nearly in-phase responses for the canard region and significant phase shifts for the wing responses in both lift and pitching moment. Amplitudes of the total configuration as well as the canard and wing region responses are comparable to the lower angle-of-attack case.

5.2.2 Canard and wing vortex structures

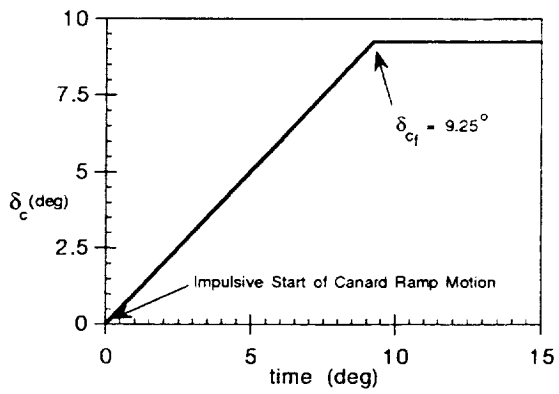
Visualizations of the canard and wing vortex structures are given in figures 5.16 and 5.17, respectively, for the canard oscillation case of $\alpha = 4.27$ deg. For both figures, crossflow visualization of normalized total pressure contours are shown at different $\omega_c t$ values, as indicated in the legend at the end of each figure. Figure 5.16 shows that the strength and location of the canard leading-edge vortex changes throughout the cycle. Early in the cycle (a-c), the canard vortex appears weaker and is increasing in strength. Near the middle to the end of the cycle (d-i), the canard vortex appears to move inward towards the root of the canard and then begins to weaken again. The effect on the wing of these changes in the canard vortex characteristics is shown in figure 5.17. Over the stationary wing surface, the convected canard vortex changes in strength, location and structure throughout the oscillation cycle. It is noted from figure 5.17 that the wing vortex strength and location appear to be relatively unchanged. However, further analysis of the wing surface pressures shows that the characteristics of the wing vortex are indeed affected by the oscillating canard.

Figure 5.18 illustrates the effect of the oscillating canard on the wing surface pressures at the 55 percent and 75 percent semispan stations. Each streamwise pressure distribution curve represents the instantaneous pressure on the wing at the same corresponding time instance (A, C, E, G, and I) indicated earlier in figures 5.16(a)–5.17(i). On the inboard portion of the wing, the canard oscillation clearly affects the formation of the wing leading-edge vortex. The effect on the lower-surface pressure distribution near the leading edge indicates that the local effective angle of attack of the wing is changing as well. Further outboard, figure 5.18 shows that there are significant changes in the upper-surface pressure peaks which are generated by the wing vortex. Starting from the beginning of the cycle, the suction peak weakens and appears to move aft (from A–C). Later in the same cycle, the peak moves forward towards the leading edge as suction again increases near the end of the cycle (E–I). Although the wing upper surface at 75 percent semispan shows considerable change, the local effective angle of attack at this station is observed to be relatively constant from the nearly constant lower surface leading-edge pressures.

The effects of the canard oscillation on vortex structures are given in figures 5.19 and 5.20 for the configuration at $\alpha = 8.0$ deg. At these conditions, the amplitude of the canard oscillations is a smaller fraction of the mean angle of attack. Therefore, over the canard region (fig. 5.19), the changes in the canard vortex characteristics appear to be more subtle than for the earlier $\alpha = 4.27$ deg case. However, results over the wing in figure 5.20 show that the convected canard vortex does indeed change in strength and structure throughout the canard oscillation cycle. Similar to the earlier $\alpha = 4.27$ deg case, figure 5.21 shows that the wing vortex at $\alpha = 8.0$ deg, as characterized through surface pressures, is also affected by the canard oscillations. The local effective angle of attack of the wing is again most influenced in the inboard portion of the wing.

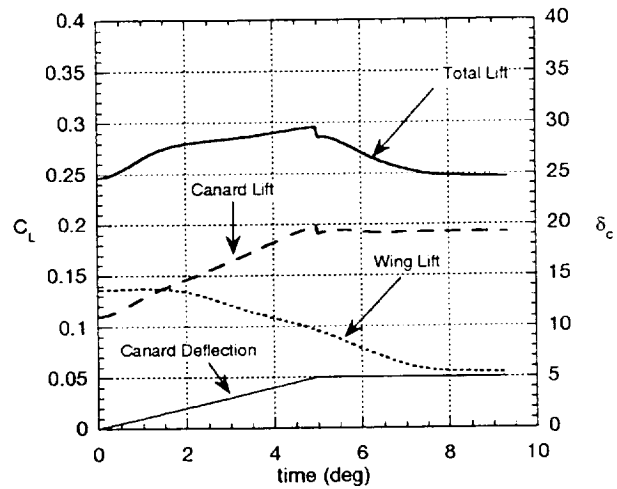


a) Canard ramp to 5.00 deg.

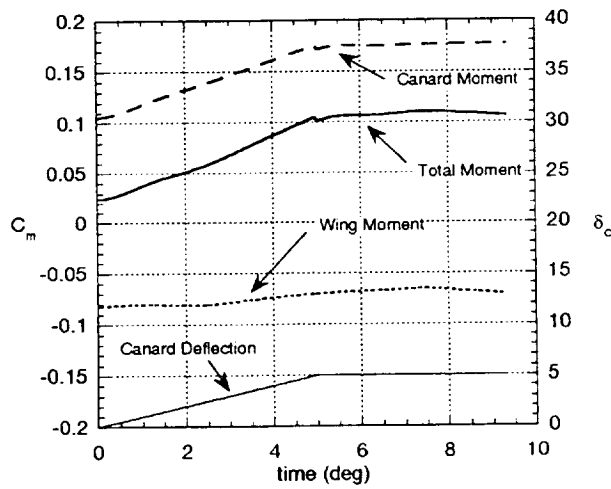


b) Canard ramp to 9.25 deg.

Figure 5.1. Schematic of canard pitch-up ramp motion from $\delta_{c_i} = 0^\circ$ to $\delta_{c_f} = 5^\circ$ and 9.25° .

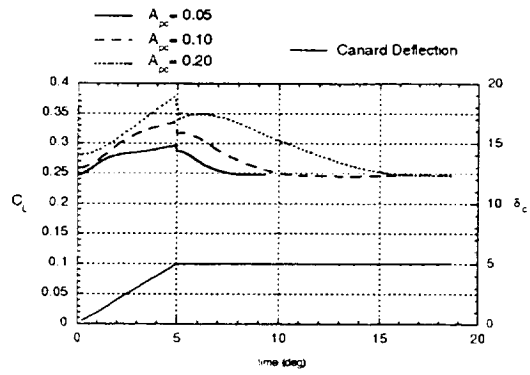


a) Lift coefficient

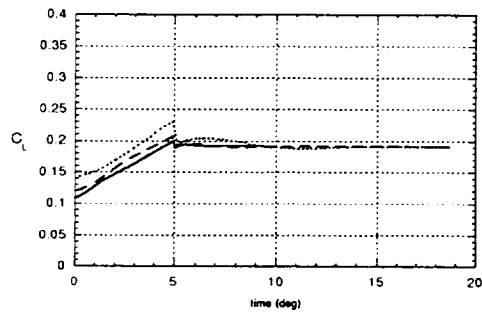


b) Pitching moment coefficient

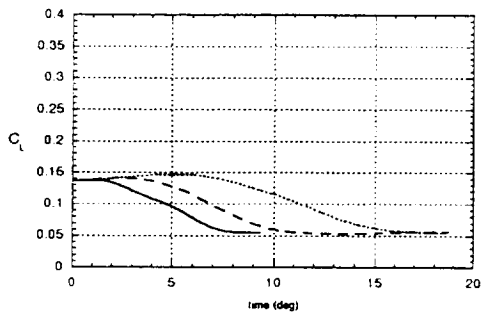
Figure 5.2. Time history of unsteady lift and pitching-moment responses due to the canard pitch-up ramp motion for the configuration at $\alpha = 4.27^\circ$. $M_\infty = 0.85$, $A_{pc} = 0.05$, $\delta_{c_i} = 0^\circ$, $\delta_{c_f} = 5^\circ$, $Re_{\bar{c}} = 2.82$ million.



a) Total lift coefficient

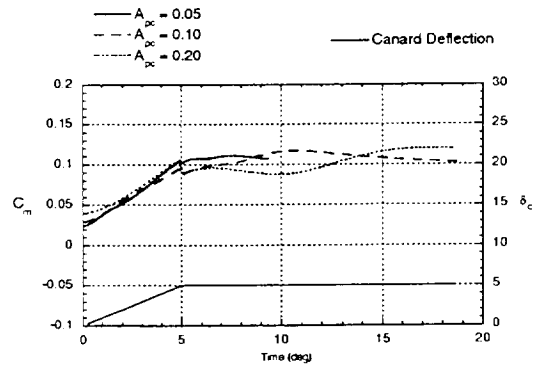


b) Canard lift coefficient

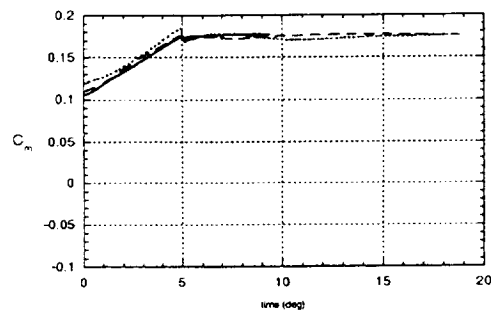


c) Wing lift coefficient

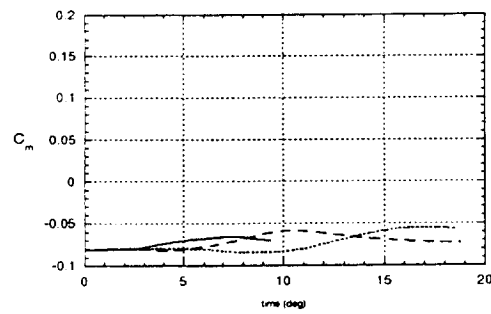
Figure 5.3. Effect of canard pitch rate on the time history of unsteady lift responses due to the canard pitch-up ramp motion. $M_\infty = 0.85$, $\alpha = 4.27^\circ$, $\delta_{c_i} = 0^\circ$, $\delta_{c_f} = 5^\circ$, $Re_{\bar{c}} = 2.82$ million.



a) Total pitching moment coefficient

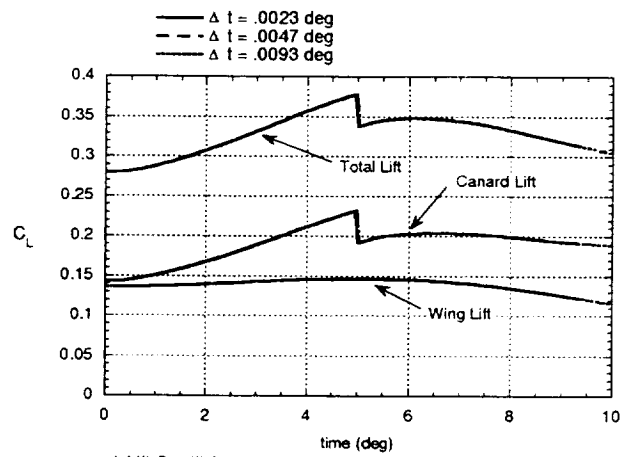


b) Canard pitching moment coefficient

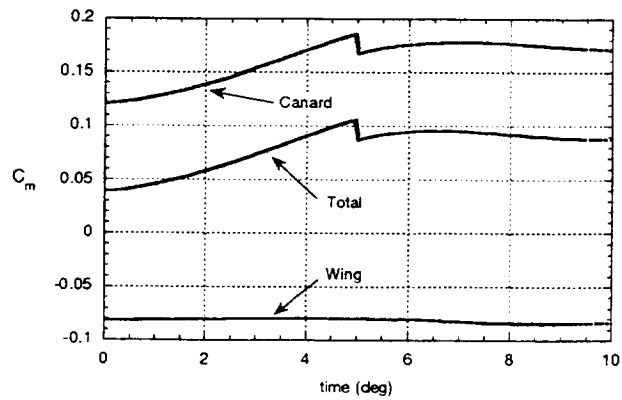


c) Wing pitching moment coefficient

Figure 5.4. Effect of canard pitch rate on the time history of unsteady pitching moment responses due to the canard pitch-up ramp motion. $M_{\infty} = 0.85$, $\alpha = 4.27^\circ$, $\delta_{c_i} = 0^\circ$, $\delta_{c_f} = 5^\circ$, $Re_{\bar{z}} = 2.82$ million.

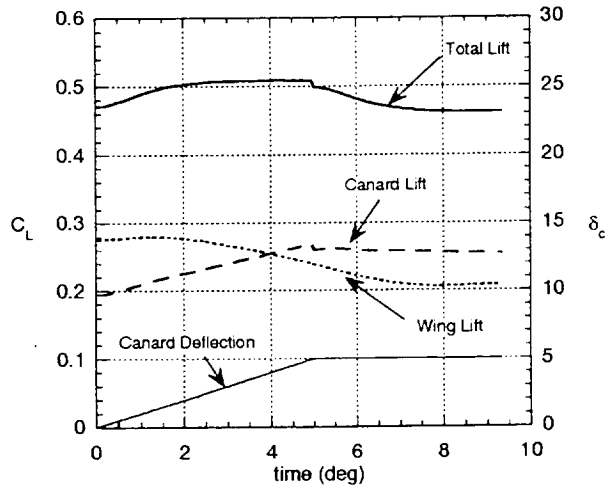


a) Lift Coefficient

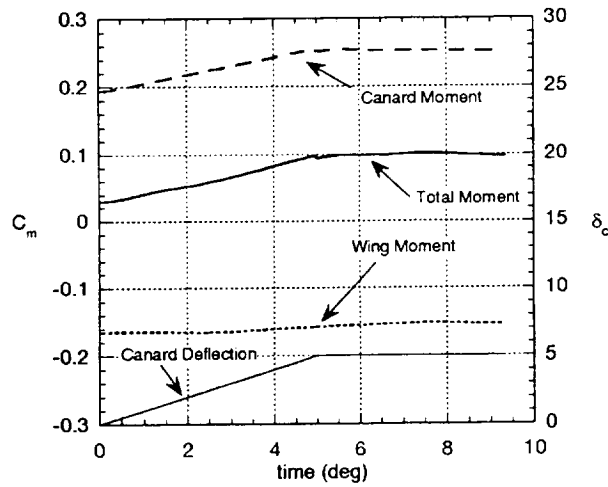


b) Pitching Moment Coefficient

Figure 5.5. Effect of time-step size on unsteady lift and moment responses due to the canard pitch-up ramp motion for $A_{pc} = 0.20$. $M_\infty = 0.85$, $\alpha = 4.27^\circ$, $\delta_{c_i} = 0^\circ$, $\delta_{c_f} = 5^\circ$, $Re_{\bar{c}} = 2.82$ million.



a) Lift Coefficient



b) Pitching Moment Coefficient

Figure 5.6. Time history of unsteady lift and pitching-moment responses due to the canard pitch-up ramp motion for the configuration at $\alpha = 8.0^\circ$. $M_\infty = 0.85$, $A_{pc} = 0.05$, $\delta_{c_i} = 0^\circ$, $\delta_{c_f} = 5^\circ$, $Re_{\bar{c}} = 2.82$ million.

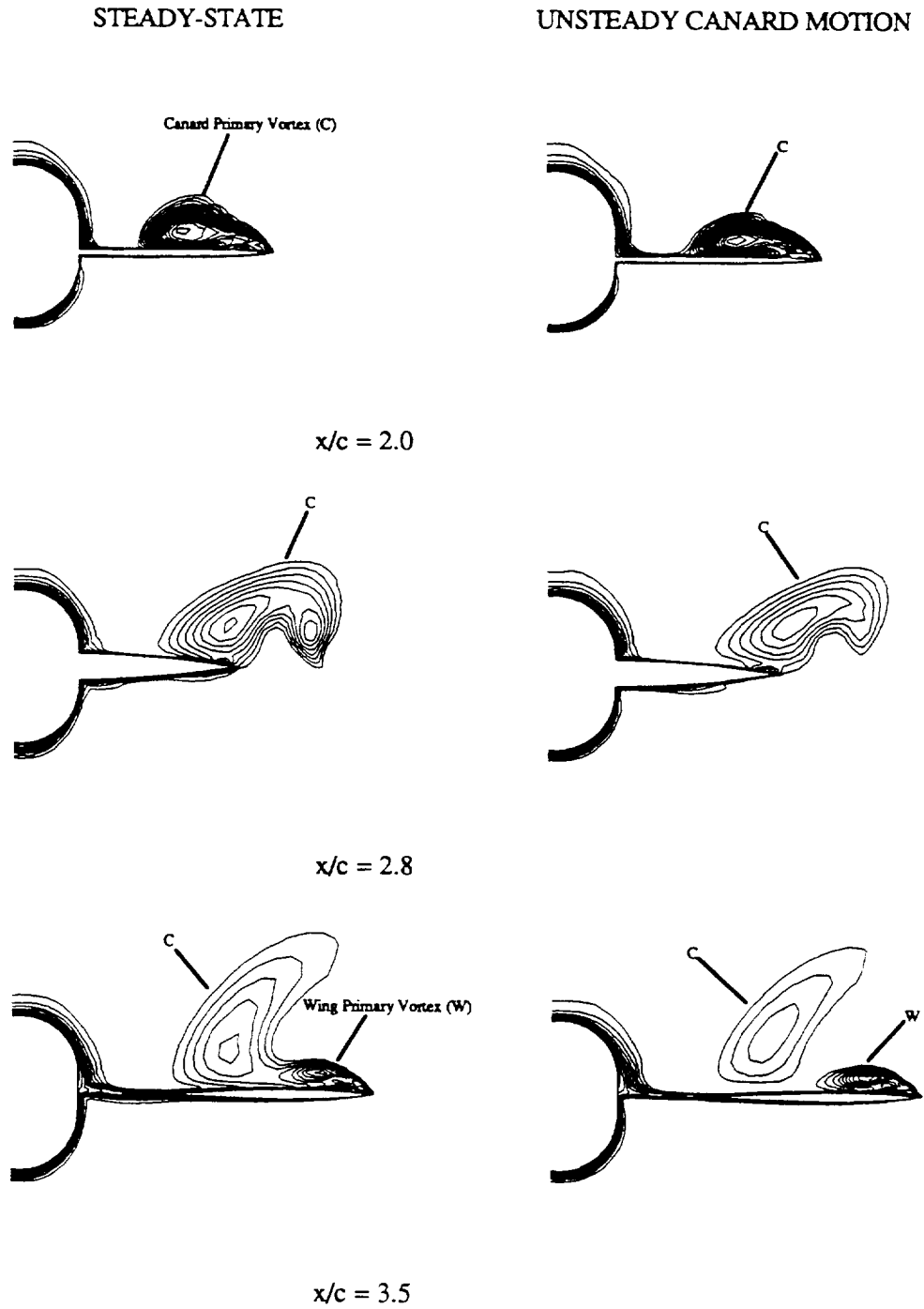
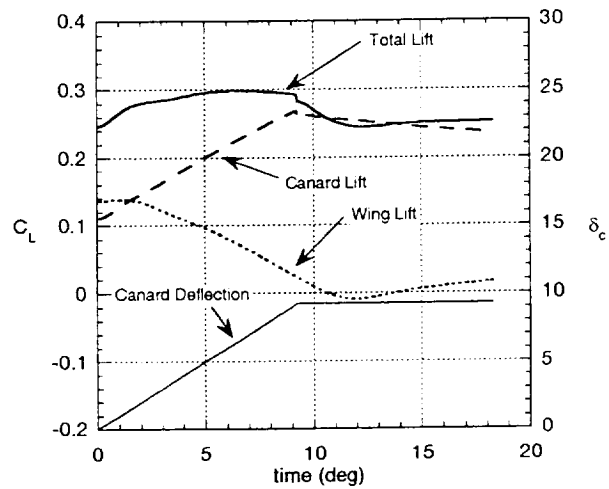
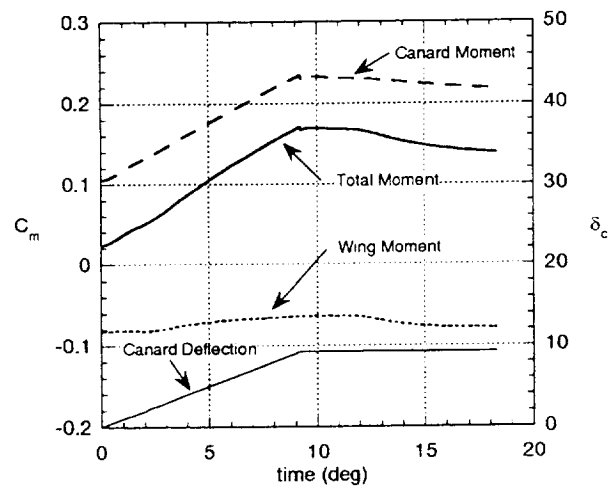


Figure 5.7. Comparison of crossflow total pressure contours between the steady and unsteady cases at various streamwise locations for the configuration at $\alpha = 8.0^\circ$ and $\delta_c = 5.0^\circ$ (unsteady case given at the instantaneous δ_c for $t = 5.0^\circ$). $M_\infty = 0.85$, $A_{pc} = 0.05$, $\delta_{ci} = 0^\circ$, $\delta_{cf} = 5^\circ$, $Re_{\bar{\epsilon}} = 2.82$ million.



a) Lift Coefficient



b) Pitching Moment Coefficient

Figure 5.8. Time history of unsteady lift and pitching-moment responses due to the canard pitch-up ramp motion from $\delta_{c_i} = 0^\circ$ to $\delta_{c_f} = 9.25^\circ$. $M_\infty = 0.85$, $\alpha = 4.27^\circ$, $A_{pc} = 0.05$, $Re_{\bar{c}} = 2.82$ million.

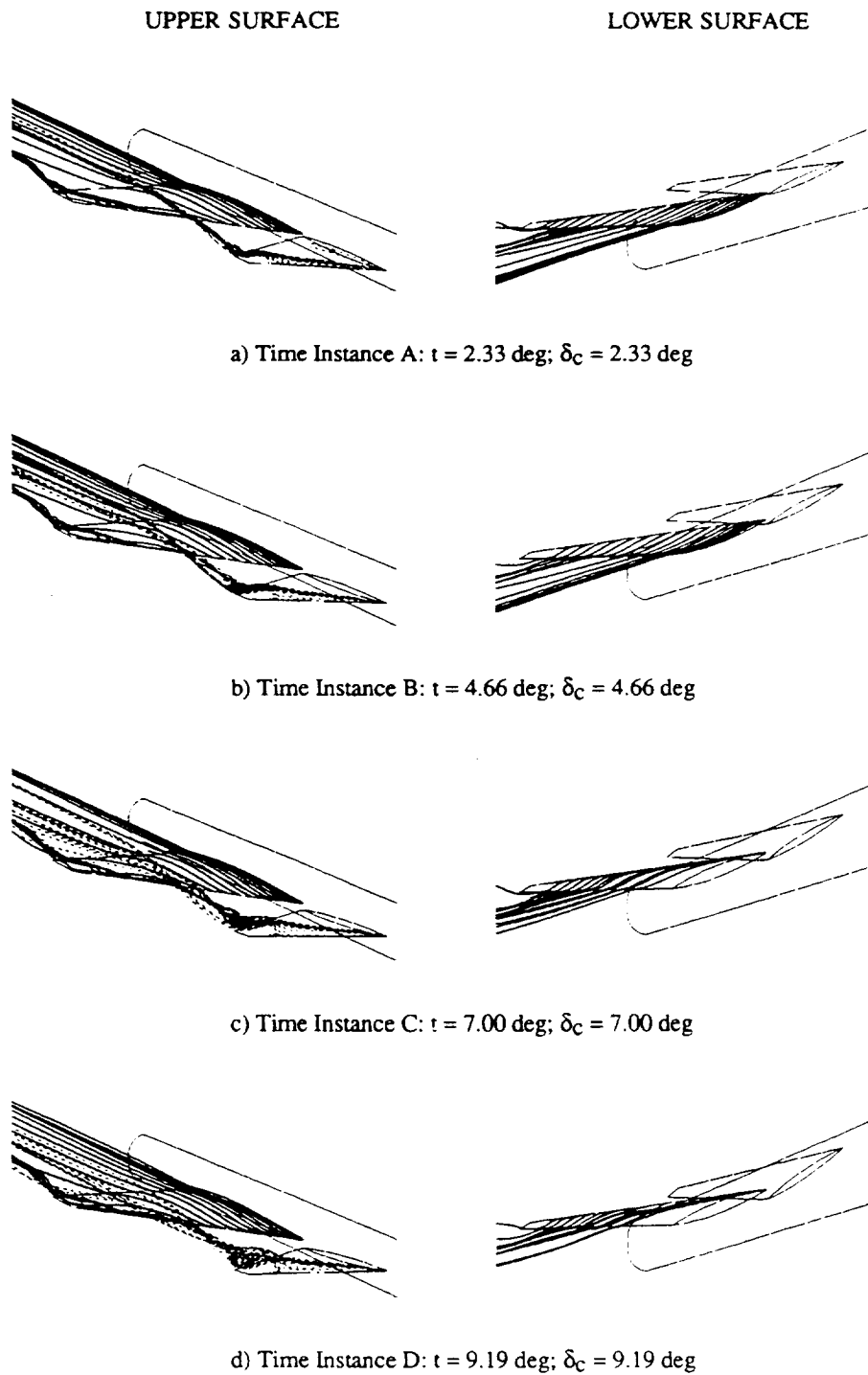
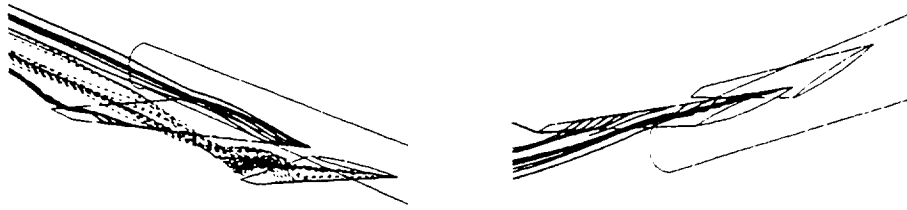
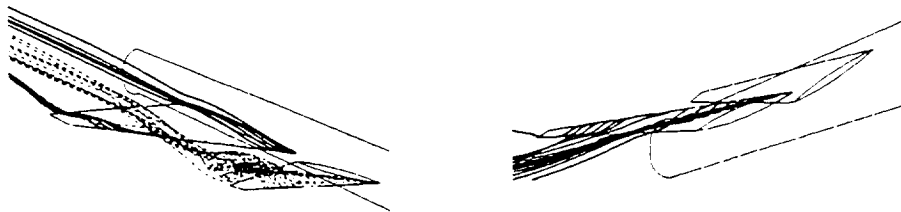


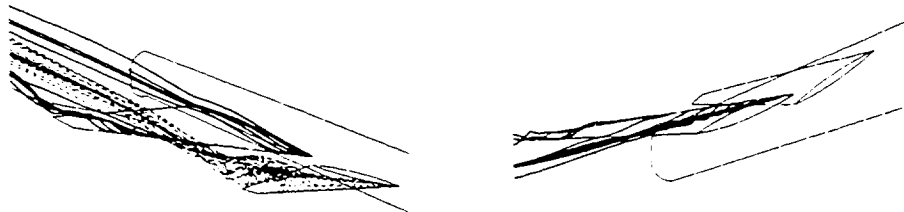
Figure 5.9. (Part-1) Upper and lower surface instantaneous streamlines for the canard pitch-up ramp motion from $\delta_{c_i} = 0^\circ$ to $\delta_{c_f} = 9.25^\circ$. $M_\infty = 0.85$, $\alpha = 4.27^\circ$, $A_{pc} = 0.05$, $Re_{\bar{c}} = 2.82$ million.



e) Time Instance E: $t = 12.00$ deg; $\delta_c = 9.25$ deg



f) Time Instance F: $t = 13.67$ deg; $\delta_c = 9.25$ deg



g) Time Instance G: $t = 18.33$ deg; $\delta_c = 9.25$ deg

LEGEND

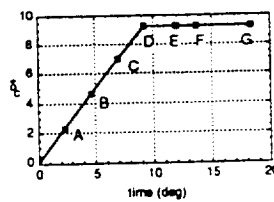
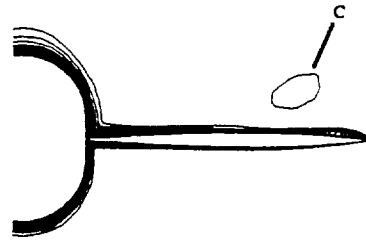
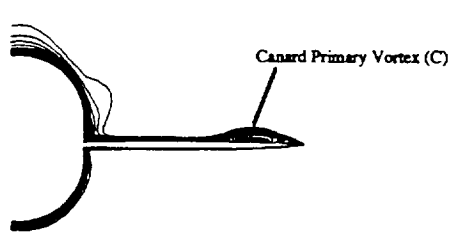


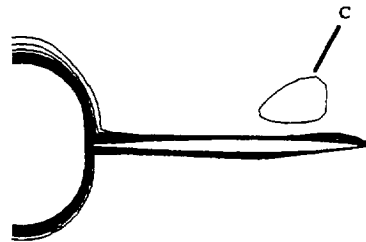
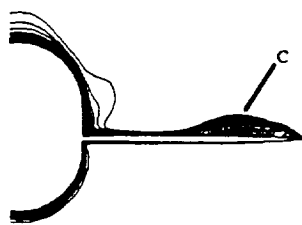
Figure 5.9. (Part-2) Upper and lower surface instantaneous streamlines for the canard pitch-up ramp motion from $\delta_{c_i} = 0^\circ$ to $\delta_{c_f} = 9.25^\circ$. $M_\infty = 0.85$, $\alpha = 4.27^\circ$, $A_{pc} = 0.05$, $Re_{\bar{c}} = 2.82$ million.

CANARD REGION ($x/c = 2.0$)

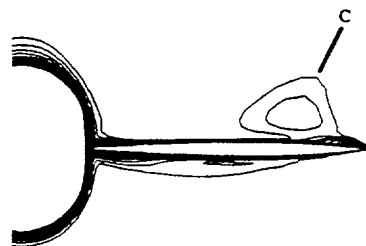
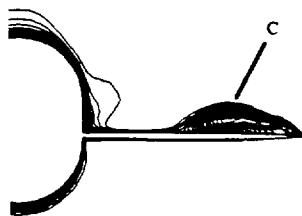
WING REGION ($x/c = 3.3$)



a) $t = 2.33$ deg

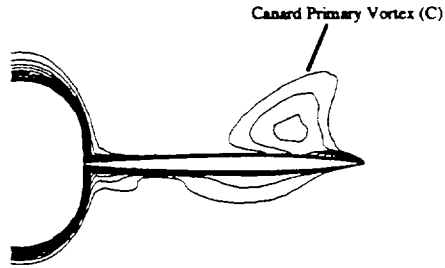


b) $t = 4.66$ deg

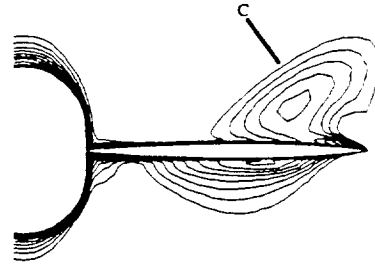


c) $t = 7.00$ deg

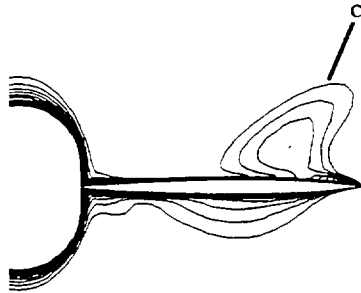
Figure 5.10. Crossflow total pressure contours over the canard ($x/\bar{c} = 2.0$) and wing ($x/\bar{c} = 3.3$) during the canard pitch-up ramp motion from $\delta_{c_i} = 0^\circ$ to $\delta_{c_f} = 9.25^\circ$. $M_\infty = 0.85$, $\alpha = 4.27^\circ$, $A_{pc} = 0.05$, $Re_{\bar{c}} = 2.82$ million.



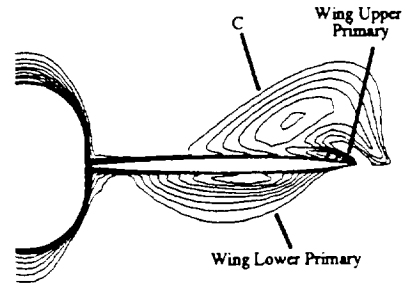
a) $t = 9.19$ deg



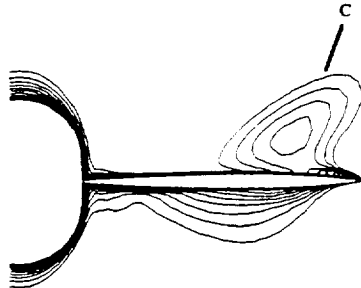
d) $t = 13.67$ deg. (Canard at 9.25 deg.)



b) $t = 10.59$ deg (Canard at 9.25 deg)



e) $t = 18.33$ deg. (Canard at 9.25 deg.)



c) $t = 12.00$ deg (Canard at 9.25 deg)

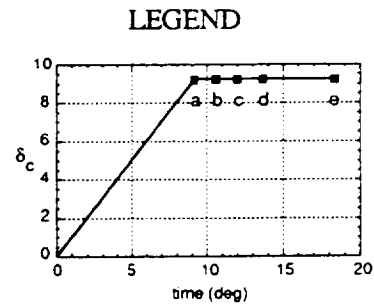
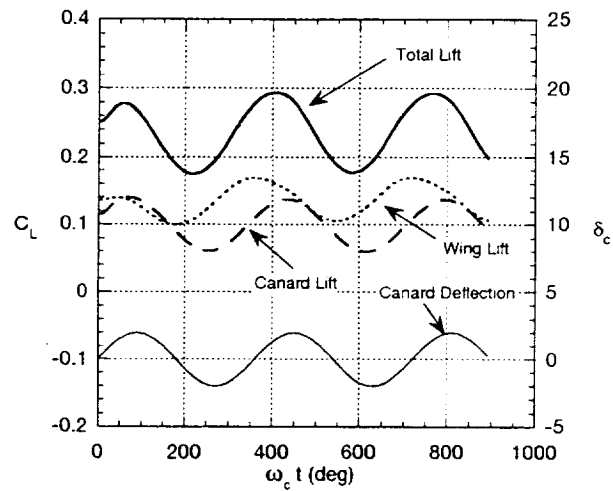
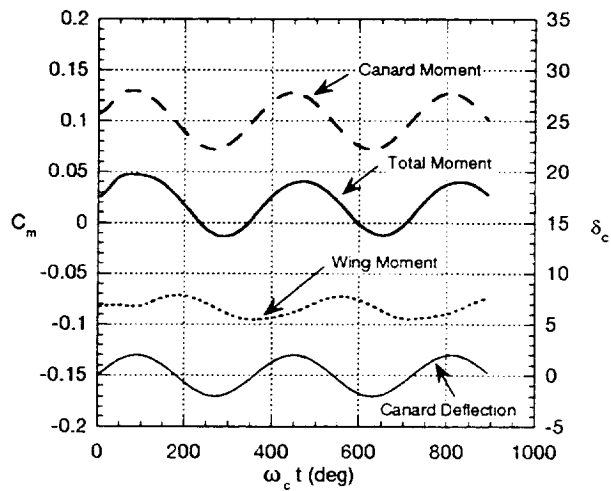


Figure 5.11. Crossflow total pressure contours over the wing ($x/\bar{c} = 3.3$) after the canard pitch-up ramp motion from $\delta_{c_i} = 0^\circ$ to $\delta_{c_f} = 9.25^\circ$. $M_\infty = 0.85$, $\alpha = 4.27^\circ$, $A_{pc} = 0.05$, $Re_{\bar{c}} = 2.82$ million.



a) Lift Coefficient



b) Pitching Moment Coefficient

Figure 5.12. Time history of unsteady lift and pitching-moment responses due to the canard pitch oscillation motion for the configuration at $\alpha = 4.27^\circ$. $M_\infty = 0.85$, $A_c = 2.0^\circ$, $k_c = 1.0$, $Re_{\bar{c}} = 2.82$ million.

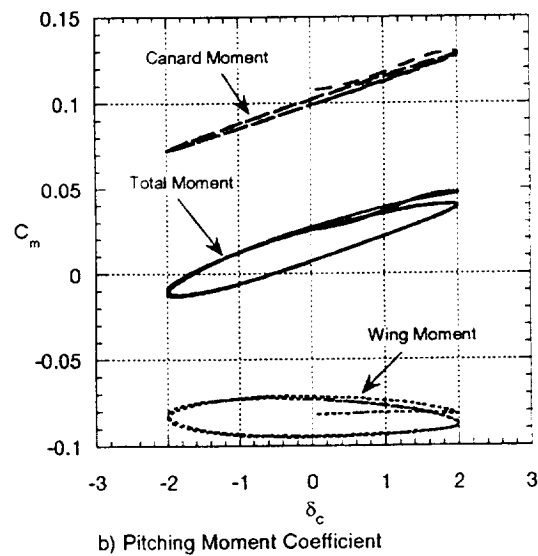
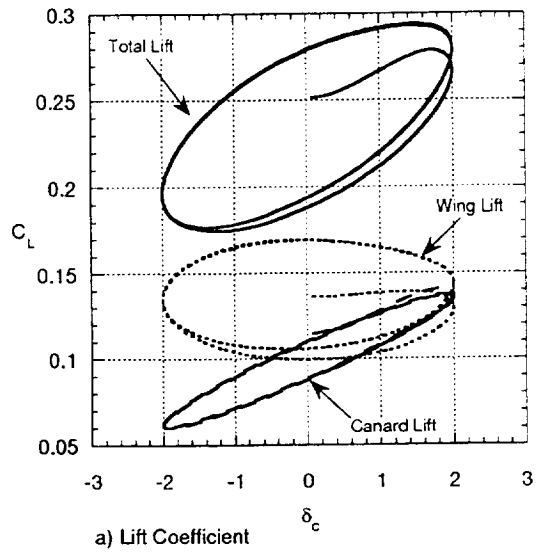
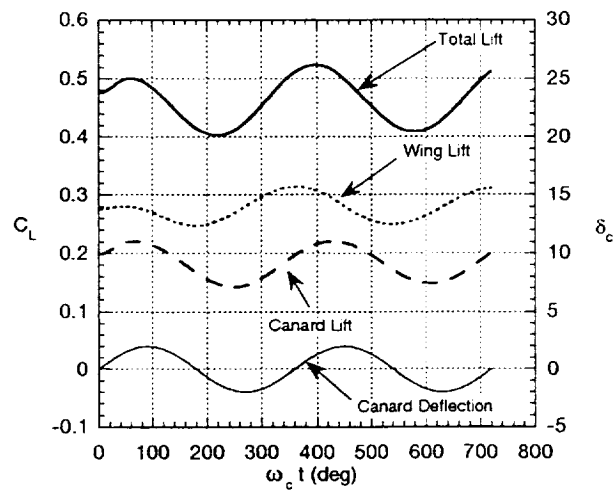
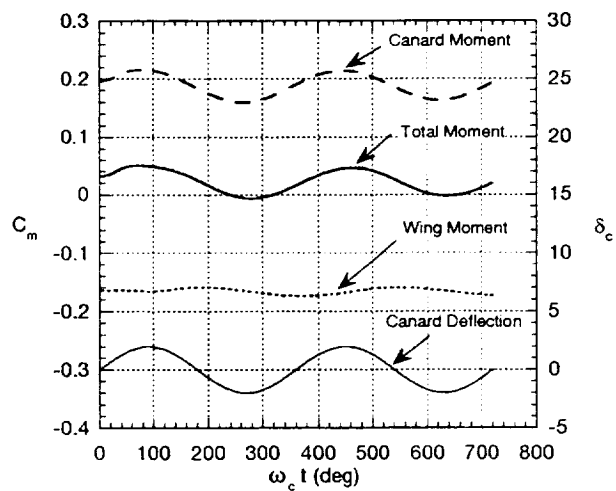


Figure 5.13. Lift and pitching-moment curves for the configuration undergoing canard pitch oscillation motion at $\alpha = 4.27^\circ$. $M_\infty = 0.85$, $A_c = 2.0^\circ$, $k_c = 1.0$, $Re_{\bar{c}} = 2.82$ million.



a) Lift Coefficient



b) Pitching Moment Coefficient

Figure 5.14. Time history of unsteady lift and pitching-moment responses due to the canard pitch oscillation motion for the configuration at $\alpha = 8.0^\circ$. $M_\infty = 0.85$, $A_c = 2.0^\circ$, $k_c = 1.0$, $Re_{\bar{c}} = 2.82$ million.

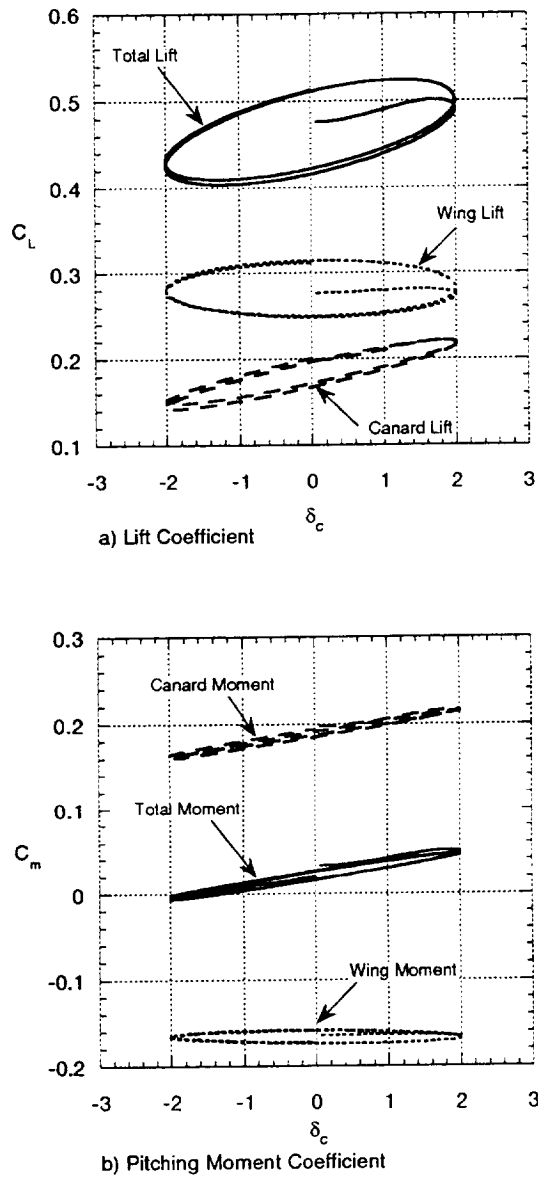


Figure 5.15. Lift and pitching-moment curves for the configuration undergoing canard pitch oscillation motion at $\alpha = 8.0^\circ$. $M_\infty = 0.85$, $A_c = 2.0^\circ$, $k_c = 1.0$, $Re_{\bar{c}} = 2.82$ million.

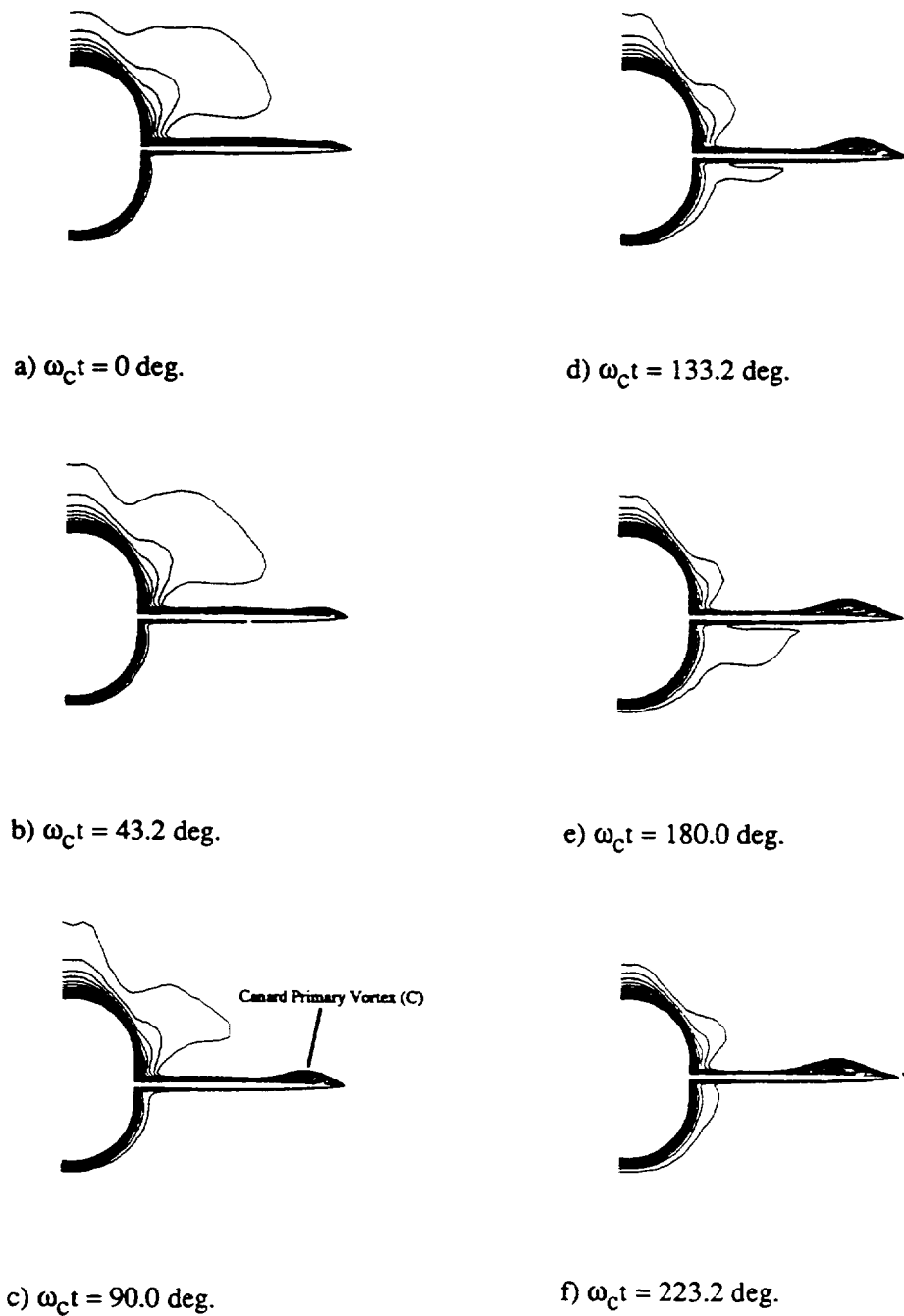
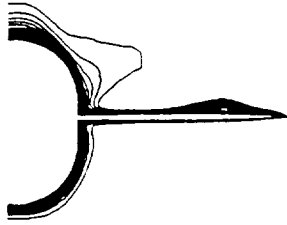
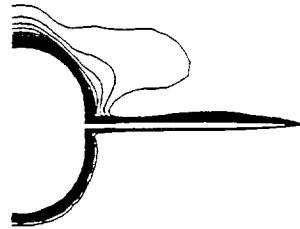


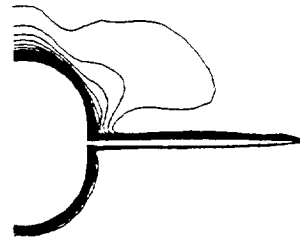
Figure 5.16. (Part-1) Crossflow total pressure contours over the canard ($x/\bar{c} = 2.0$) for the canard pitch oscillation motion at $\alpha = 4.27^\circ$. $M_\infty = 0.85$, $A_c = 2.0^\circ$, $k_c = 1.0$, $Re_{\bar{c}} = 2.82$ million.



g) $\omega_c t = 270.0$ deg.



h) $\omega_c t = 313.2$ deg.



i) $\omega_c t = 360.0$ deg.

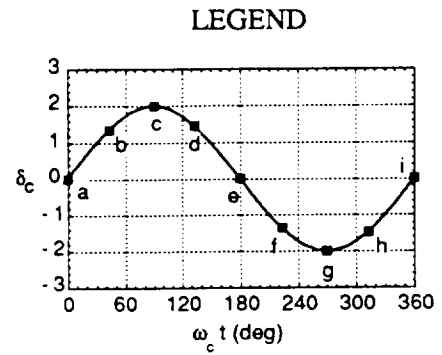


Figure 5.16. (Part-2) Crossflow total pressure contours over the canard ($x/\bar{c} = 2.0$) for the canard pitch oscillation motion at $\alpha = 4.27^\circ$. $M_\infty = 0.85$, $A_c = 2.0^\circ$, $k_c = 1.0$, $Re_{\bar{c}} = 2.82$ million.

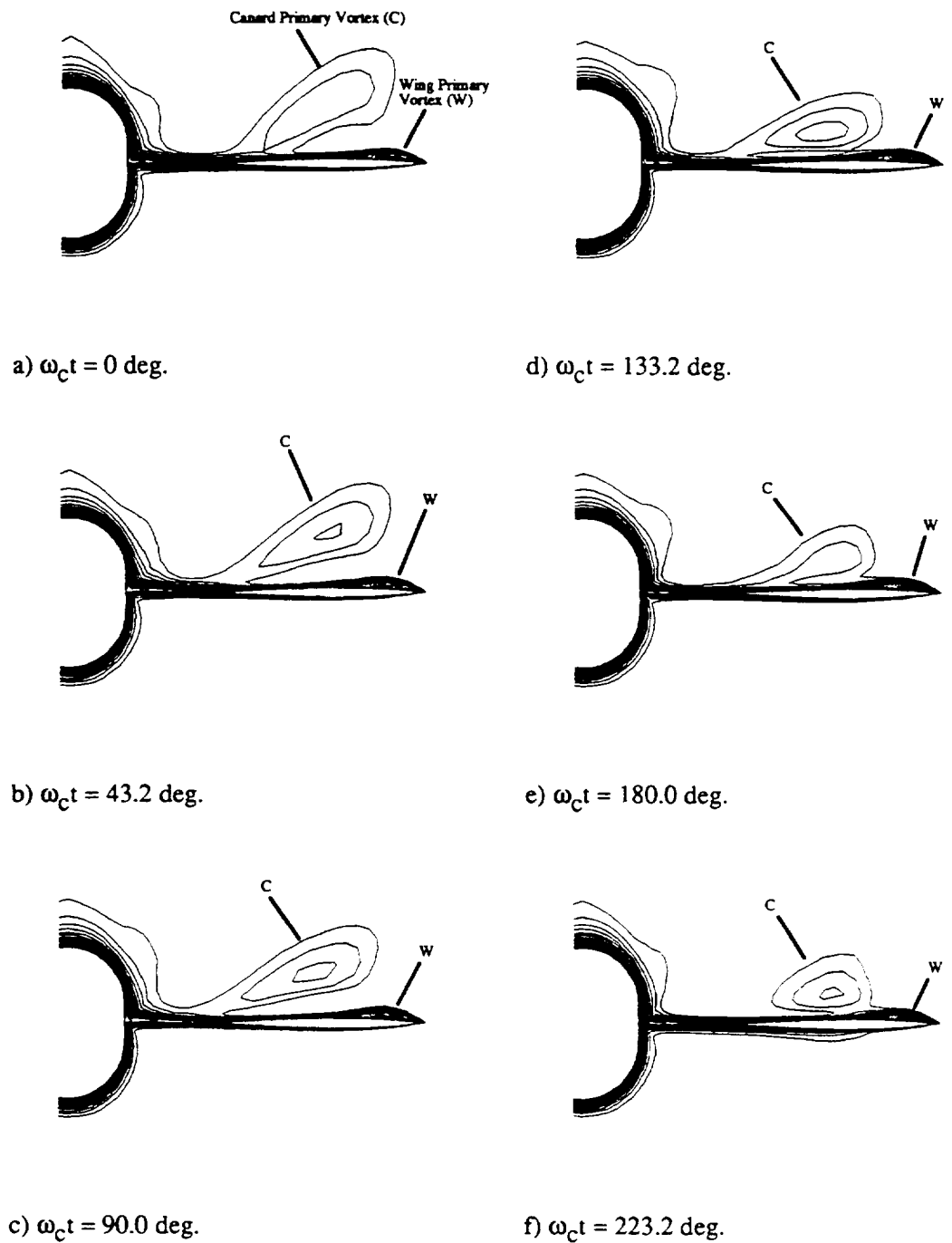
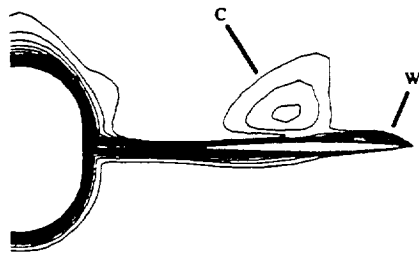
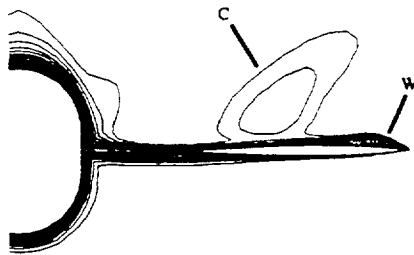


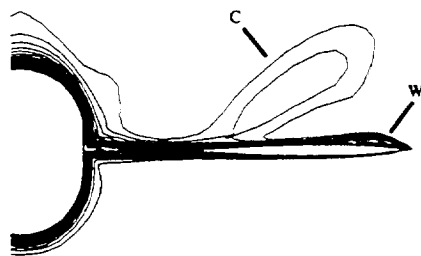
Figure 5.17. (Part-1) Crossflow total pressure contours over the wing ($x/\bar{c} = 3.5$) for the canard pitch oscillation motion at $\alpha = 4.27^\circ$. $M_\infty = 0.85$, $A_c = 2.0^\circ$, $k_c = 1.0$, $Re_{\bar{c}} = 2.82$ million.



g) $\omega_c t = 270.0$ deg.



h) $\omega_c t = 313.2$



i) $\omega_c t = 360.0$ deg.

LEGEND

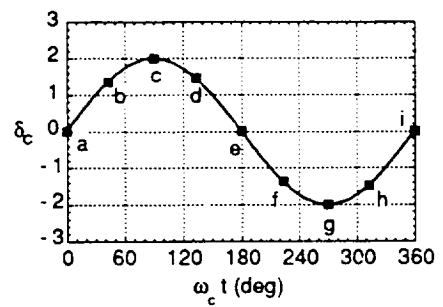
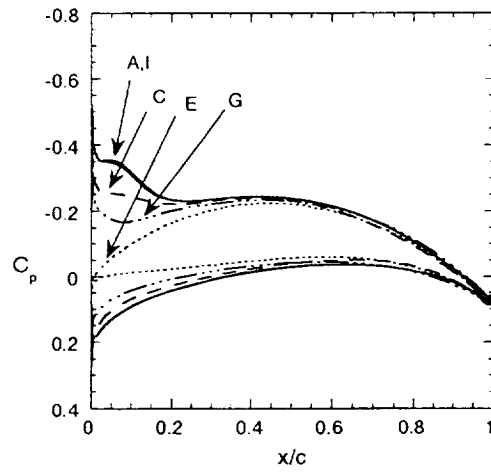
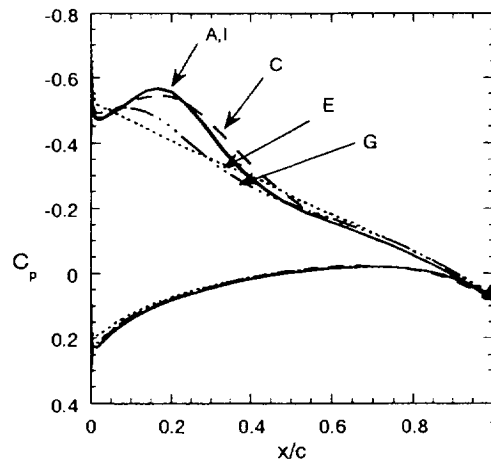


Figure 5.17. (Part-2) Crossflow total pressure contours over the wing ($x/\bar{c} = 3.5$) for the canard pitch oscillation motion at $\alpha = 4.27^\circ$. $M_\infty = 0.85$, $A_c = 2.0^\circ$, $k_c = 1.0$, $Re_{\bar{c}} = 2.82$ million.



a) 55% Span Station



b) 75% Span Station

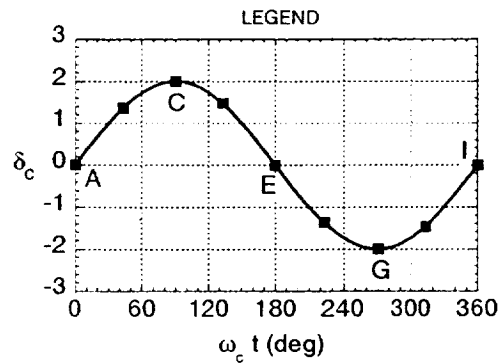
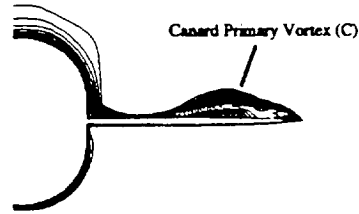
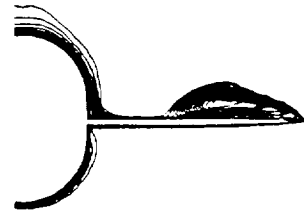


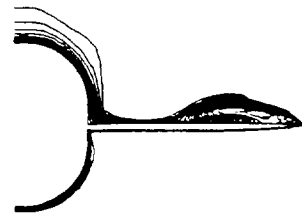
Figure 5.18. Effect of canard pitch oscillation motion on wing surface pressures at $\alpha = 4.27^\circ$. $M_\infty = 0.85$, $A_c = 2.0^\circ$, $k_c = 1.0$, $Re_{\bar{c}} = 2.82$ million.



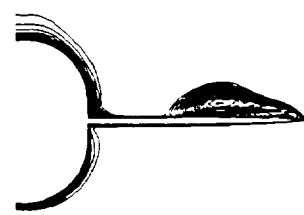
a) $\omega_c t = 0$ deg.



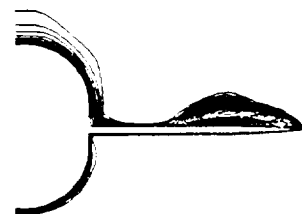
d) $\omega_c t = 133.2$ deg.



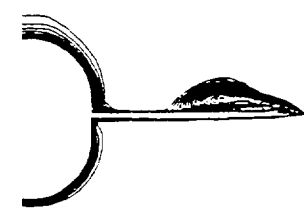
b) $\omega_c t = 43.2$ deg.



e) $\omega_c t = 180.0$ deg.

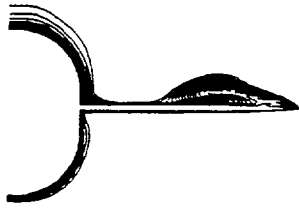


c) $\omega_c t = 90.0$ deg.

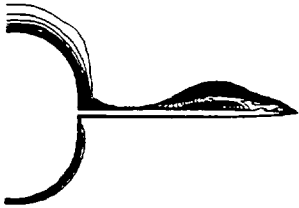


f) $\omega_c t = 223.2$ deg.

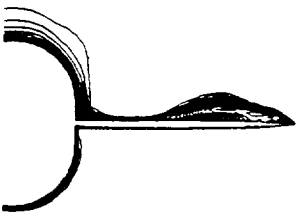
Figure 5.19. (Part-1) Crossflow total pressure contours over the canard ($x/\bar{c} = 2.0$) for the canard pitch oscillation motion at $\alpha = 8.0^\circ$. $M_\infty = 0.85$, $A_c = 2.0^\circ$, $k_c = 1.0$, $Re_{\bar{c}} = 2.82$ million.



g) $\omega_c t = 270.0$ deg.



h) $\omega_c t = 313.2$ deg.



i) $\omega_c t = 360.0$ deg.

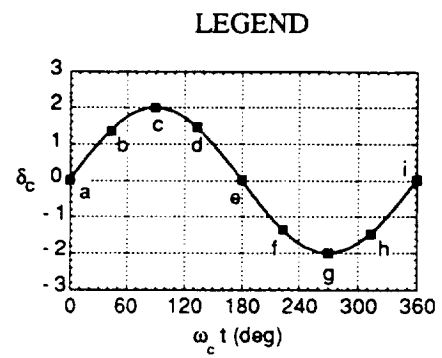


Figure 5.19. (Part-2) Crossflow total pressure contours over the canard ($x/\bar{c} = 2.0$) for the canard pitch oscillation motion at $\alpha = 8.0^\circ$. $M_\infty = 0.85$, $A_c = 2.0^\circ$, $k_c = 1.0$, $Re_{\bar{c}} = 2.82$ million.

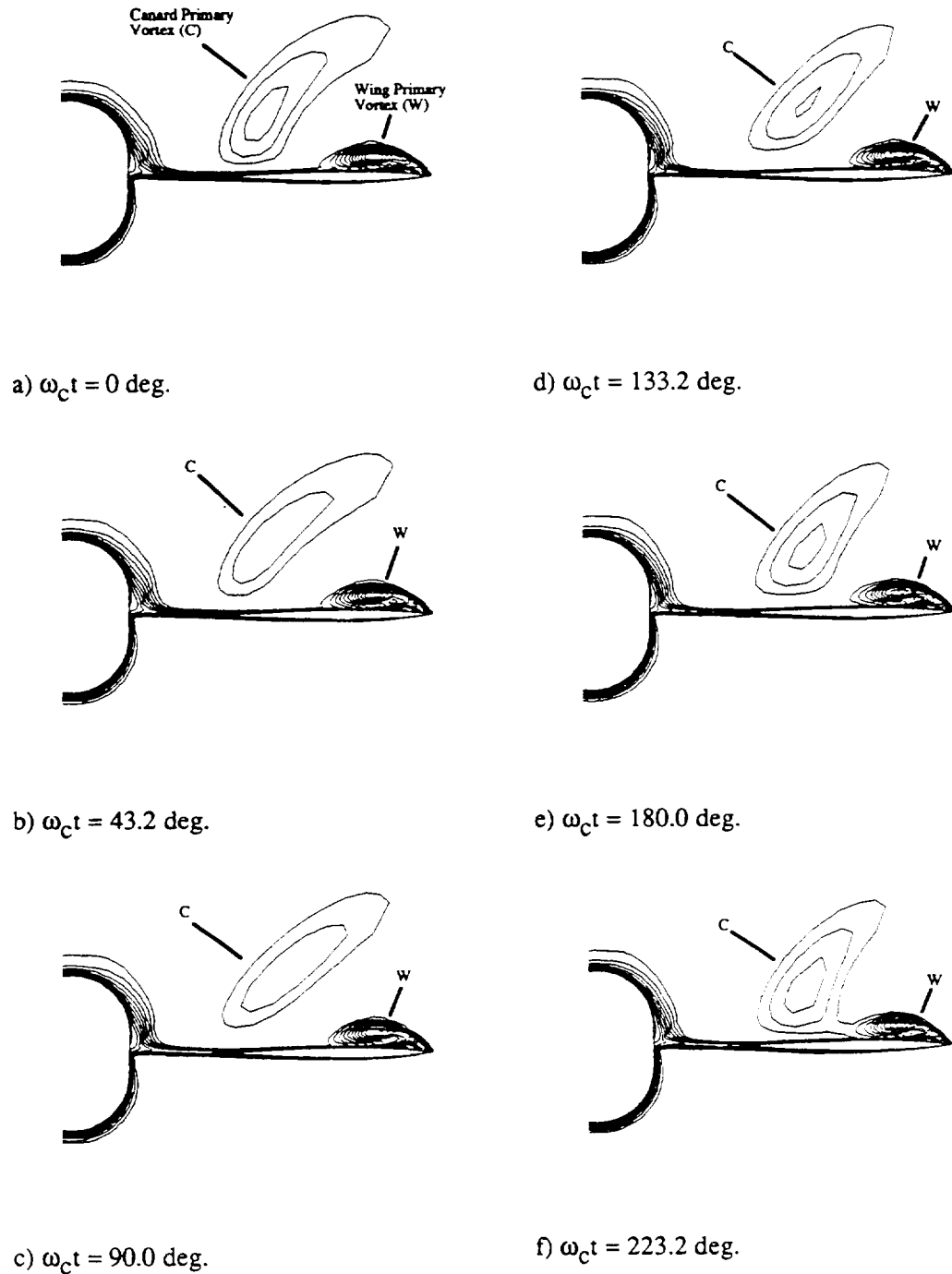
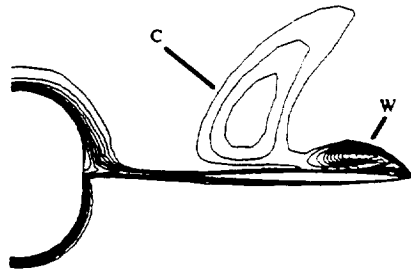
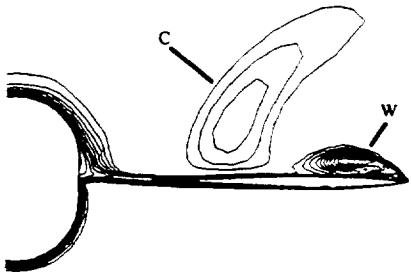


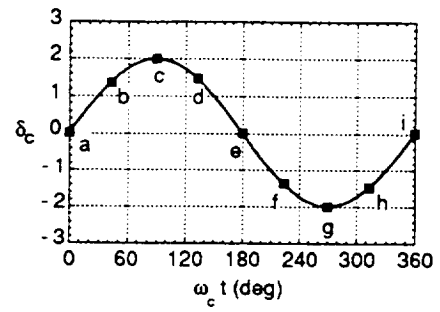
Figure 5.20. (Part-1) Crossflow total pressure contours over the wing ($x/\bar{c} = 3.5$) for the canard pitch oscillation motion at $\alpha = 8.0^\circ$. $M_\infty = 0.85$, $A_c = 2.0^\circ$, $k_c = 1.0$, $Re_{\bar{c}} = 2.82$ million.



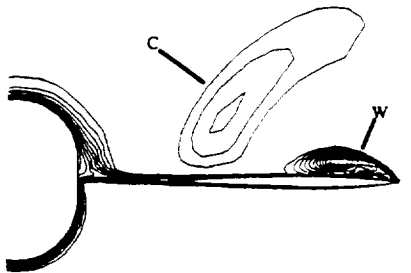
g) $\omega_c t = 270.0$ deg.



LEGEND

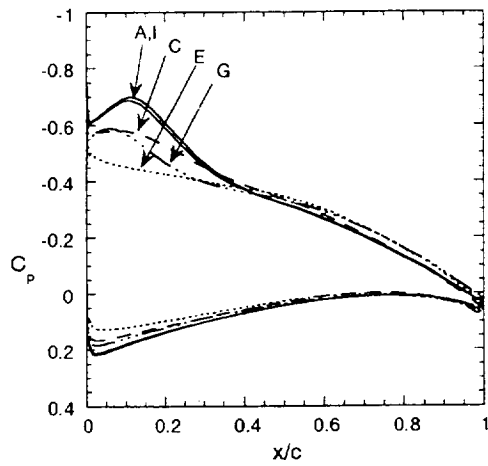


h) $\omega_c t = 313.2$ deg.

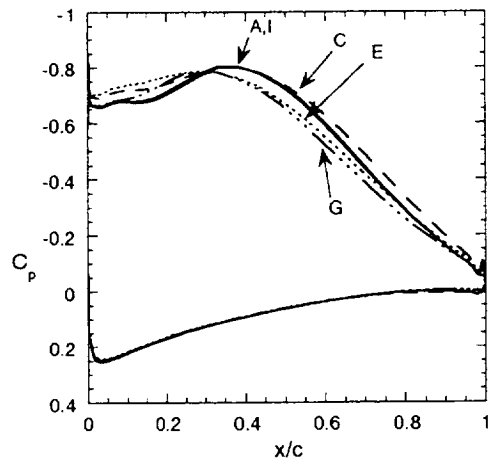


i) $\omega_c t = 360.0$ deg.

Figure 5.20. (Part-2) Crossflow total pressure contours over the wing ($x/\bar{c} = 3.5$) for the canard pitch oscillation motion at $\alpha = 8.0^\circ$. $M_\infty = 0.85$, $A_c = 2.0^\circ$, $k_c = 1.0$, $Re_{\bar{c}} = 2.82$ million.



a) 55% Span Station



b) 75% Span Station

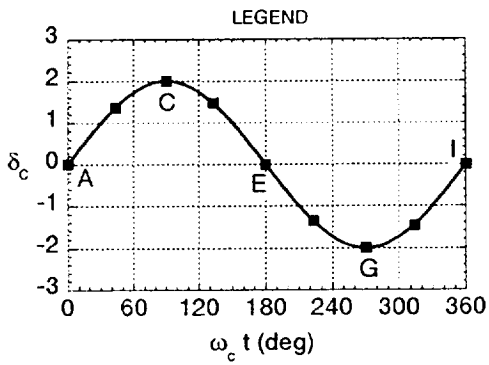


Figure 5.21. Effect of canard pitch oscillation motion on wing surface pressures at $\alpha = 8.0^\circ$. $M_\infty = 0.85$, $A_c = 2.0^\circ$, $k_c = 1.0$, $Re_{\bar{c}} = 2.82$ million.

Chapter 6

Conclusions

A detailed numerical investigation has been performed for the steady and unsteady flowfield about a static and dynamic canard-wing-body configuration. Computational technology has been developed and enhanced to perform a series of time-accurate Navier–Stokes simulations about the close-coupled canard configuration. The computational methods presented in this study are capable of accurately predicting the unsteady viscous flowfield for the canard-wing-body configuration with various fixed canard positions and with moving canards.

6.1 Validation of the Computational Method

The accuracy of the simulations is demonstrated by extensive comparisons with available steady and unsteady experimental data. Favorable comparisons with steady-state experimental surface pressures, forces, and moments for the configuration with various fixed canard positions verify that the present method is capable of accurately predicting the steady-state flowfield about such configurations. For low angles of attack (up to approximately 6 deg), a relatively coarse (baseline) grid was found to be effective in accurately computing surface pressures, forces and moments. However, a more refined grid was shown to be critical for higher angle-of-attack cases where boundary-layer separation, strong shocks, and vortex breakdown dominate the flow characteristics.

Comparisons of experimentally measured dynamic stability parameters with computations of the configuration undergoing pitch oscillations also demonstrate accurate predictions of the unsteady canard-wing-body flowfield. An analysis of the effect of reduced frequency was also performed and demonstrates the ability to accurately predict dynamic stability with considerably higher computational reduced frequencies. As a result, significant reductions in required computational resources allows the use of state-of-the-art computational fluid dynamics (CFD) for the prediction of dynamic stability about complex canard configurations. For those cases where experimental data was unavailable, a spatial and time-step refinement study was conducted to verify the convergence of the unsteady computations.

6.2 Canard-Wing-Body Steady Flowfield

For the steady-state mid-canard flowfield, the canard-induced downwash was found to weaken or delay formation of the wing leading-edge vortex. At $\alpha \approx 4$ deg, the formation of the wing leading-edge vortex is delayed to the canard-tip span-line of the wing. At $\alpha \approx 8$ deg and 12 deg, a weakened leading-edge vortex was observed on the inboard portion of the wing. The wing vortex on the outboard span was

shown to be influenced by both the canard vortex and the aforementioned canard downwash. The presence of the canard was also shown to eliminate the wing vortex breakdown which was evident in the canard-off case at $\alpha \approx 12$ deg. These results confirm and provide an explanation for the canard's potential for delaying wing vortex breakdown which has been observed in experimental studies.

At low to moderate angles of attack, the fixed high-canard configuration exhibits improved steady-state lift and drag over the mid-canard case. However, due to the interaction between the low-canard vortex and the wing surface, unfavorable lift and drag characteristics for the low-canard configuration are evident as angle of attack is increased. At low angles of attack, the low-canard vortex passes under the wing surface and can induce lower pressures on the wing lower surface. At higher angles of attack, the canard vortex is split by the wing surface into upper and lower vortices. Toward the outboard wing, the wing vortex induces a large inward movement of the canard upper-vortex.

When the fixed canard is positively deflected, a pronounced effect on aerodynamic performance parameters is observed, particularly for wing lift and configuration pitching moment. Visualization of the canard-wing-body flowfield shows a complex flow structure consisting of several interacting canard and wing vortices. Specifically, at significantly large canard deflection angles, effective wing angle of attack transitions from negative (inboard) to positive (outboard) values causing the formation of both lower and upper surface leading-edge vortices. Furthermore, due to the strength of these vortices, secondary vortices are present indicating strong viscous effects.

These findings both correlate with, and provide an explanation for, much of the experimental results presented in the literature. These results also suggest that detailed investigations are required to determine optimum canard positioning for given configurations. The accurate prediction of such steady-state effects are needed in the design and optimization of future close-coupled canard aircraft.

6.3 Canard-Wing-Body Unsteady Flowfield

To understand the predicted unsteady flowfield, an analysis of the unsteady canard-wing-body aerodynamics with emphasis on the canard-wing vortex interaction was performed. Dynamic conditions in this study included rigid-body pitch-up and pitch oscillation motions of both the entire configuration and the independent canard.

For the entire configuration undergoing pitch-up ramp motions, computations with and without the canard showed increased dynamic lift and improved lift-to-drag ratios for the configuration with the canard. Results also indicated the strong influence of the relative positioning of the canard and wing to the pitch axis. For the canard located forward of the pitch axis, the ramp motion at high pitch rates decreases the effective angle of attack of the canard and delays the formation of the canard vortex. However, as angle of attack increases and the ramp motion ends, the canard vortex and its interaction with the wing develops rapidly. As time increases, the configuration flowfield approaches a relatively steady solution.

During pitch oscillations, the fixed canard was found to have a pronounced effect on the unsteady aerodynamics associated with the wing-body configuration. Significant changes in amplitude and shifts in phase of the lifts and moments were observed with the addition of the canard. Using the results of the numerical pitch oscillation simulation, an analysis of the time histories of normal force and pitching moment coefficients led to the prediction of longitudinal dynamic stability parameters. These parameters were utilized to evaluate the effects of the canard on dynamic stability. The current study found that the presence of the canard increases the pitch damping of the configuration and decreases the oscillatory stability.

The current computational method has been further extended to investigate the unsteady aerodynamic effects of moving canards. Both canard pitch-up ramp and pitch oscillation motions were simulated using the developed dynamic gridding, zonal interfacing and boundary condition capabilities. The canard pitch-up ramp motion simulation showed that a transient increase in overall lift was the direct result of the time delay (or lag) in wing response from the convection of the canard effects. Furthermore, the vortex analyses illustrated the unsteady nature of the canard and wing vortex structures, particularly with respect to the formation of the upper- and lower-surface wing vortices.

The investigation of canard pitch oscillations demonstrated that high frequency, small amplitude oscillations can produce significant lift and moment responses of the wing. It was also observed that, similar to the canard ramp motion results, the canard responses were nearly in-phase with the canard motion while the wing responses showed significant phase shifts. Although the vortex visualizations indicated minimal changes in wing vortex characteristics, analyses of the wing surface pressures showed significant changes in the local angle of attack on the inboard wing and overall changes in wing vortex influences.

6.4 Recommendations for Future Studies

The current study has characterized the complex steady and unsteady aerodynamic flowfield of a canard configuration, including effects of both fixed canards at various positions and independently moving canards. Future studies should focus on utilizing the tools and findings which have been presented to optimize the use of canards for both cruise and maneuver aerodynamic performance. Such studies could include, but are not limited to:

1. Optimization of fixed canard positions (vertical, longitudinal, and deflection) for trimmed cruise performance;
2. Development of control-law based canard motions for enhanced maneuver performance;
3. Investigation of non-symmetric canard positions or motions for lateral stability and control;
4. Investigation of high-frequency canard oscillations for improved wing performance in pre- and post-stall environments;
5. Evaluation of complete static and dynamic stability characteristics of a canard configuration for stability and controls applications; and
6. Coupled controls-fluids simulation of a dynamic maneuver condition.

Appendix A

Governing Equations

Appendix A Governing Equations

(Note: For further details of the governing equations, numerical algorithm, and turbulence modeling, the reader is referred to ref. 43 and the appropriate original publications which are cited.)

The governing equations solved in this study are nondimensionalized by free-stream quantities and are transformed to the computational domain (ξ, η, ζ) so as to preserve the strong conservation form of the equations. The strong conservation law form of the Navier–Stokes equations are used for shock capturing purposes. The equations in Cartesian coordinates in non-dimensional form can be written as

$$\frac{\partial Q}{\partial t} + \frac{\partial E}{\partial x} + \frac{\partial F}{\partial y} + \frac{\partial G}{\partial z} = \frac{\partial E_\nu}{\partial x} + \frac{\partial F_\nu}{\partial y} + \frac{\partial G_\nu}{\partial z} \quad (\text{A} - 1)$$

where

$$Q = \begin{bmatrix} \rho \\ \rho u \\ \rho v \\ \rho w \\ e \end{bmatrix}$$

$$E = \begin{bmatrix} \rho u \\ \rho u^2 + p \\ \rho uv \\ \rho uw \\ u(e + p) \end{bmatrix}, \quad F = \begin{bmatrix} \rho v \\ \rho uv \\ \rho v^2 + p \\ \rho vw \\ v(e + p) \end{bmatrix}, \quad G = \begin{bmatrix} \rho w \\ \rho uw \\ \rho vw \\ \rho w^2 + p \\ w(e + p) \end{bmatrix}, \quad (\text{A} - 2)$$

$$E_\nu = Re^{-1} \begin{bmatrix} 0 \\ \tau_{xx} \\ \tau_{yx} \\ \tau_{zx} \\ \beta_x \end{bmatrix}, \quad F_\nu = Re^{-1} \begin{bmatrix} 0 \\ \tau_{xy} \\ \tau_{yy} \\ \tau_{zy} \\ \beta_y \end{bmatrix}, \quad G_\nu = Re^{-1} \begin{bmatrix} 0 \\ \tau_{xz} \\ \tau_{yz} \\ \tau_{zz} \\ \beta_z \end{bmatrix}$$

with

$$\begin{aligned} \tau_{xx} &= \lambda(u_x + v_y + w_z) + 2\mu u_x \\ \tau_{yy} &= \lambda(u_x + v_y + w_z) + 2\mu v_y \\ \tau_{zz} &= \lambda(u_x + v_y + w_z) + 2\mu w_z \\ \tau_{xy} &= \tau_{yx} = \mu(u_y + v_x) \\ \tau_{xz} &= \tau_{zx} = \mu(u_z + w_x) \\ \tau_{yz} &= \tau_{zy} = \mu(v_z + w_y) \\ \beta_x &= \gamma\kappa Pr^{-1} \partial_x e_I + u\tau_{xx} + v\tau_{xy} + w\tau_{xz} \\ \beta_y &= \gamma\kappa Pr^{-1} \partial_y e_I + u\tau_{yx} + v\tau_{yy} + w\tau_{yz} \\ \beta_z &= \gamma\kappa Pr^{-1} \partial_z e_I + u\tau_{zx} + v\tau_{zy} + w\tau_{zz} \\ e_I &= e\rho^{-1} - 0.5(u^2 + v^2 + w^2) \end{aligned} \quad (\text{A} - 3)$$

The Cartesian velocity components u , v , and w are nondimensionalized by a_∞ (the free-stream speed of sound), density ρ is nondimensionalized by ρ_∞ ; and the total energy per unit volume e is

nondimensionalized by $\rho_\infty a_\infty^2$. Pressure can be found from the ideal gas law as

$$p = (\gamma - 1)[e - 0.5\rho(u^2 + v^2 + w^2)] \quad (\text{A} - 4)$$

and throughout γ is the ratio of the specific heats. Also, κ is the coefficient of thermal conductivity, μ is the dynamic viscosity, and λ from the Stokes' hypothesis is $-2/3\mu$. The Reynolds number is Re and the Prandtl number is Pr .

To enhance numerical accuracy and efficiency and to handle boundary conditions more easily, the governing equations are transformed from the Cartesian coordinates to general curvilinear coordinates where

$$\begin{aligned} \tau &= t \\ \xi &= \xi(x, y, z, t) \\ \eta &= \eta(x, y, z, t) \\ \zeta &= \zeta(x, y, z, t) \end{aligned} \quad (\text{A} - 5)$$

The resulting transformed equations are not much more complicated than the original Cartesian set and can be written in nondimensional form as

$$\frac{\partial}{\partial \tau} \hat{Q} + \frac{\partial}{\partial \xi} (\hat{E} - \hat{E}_v) + \frac{\partial}{\partial \eta} (\hat{F} - \hat{F}_v) + \frac{\partial}{\partial \zeta} (\hat{G} - \hat{G}_v) = 0 \quad (\text{A} - 6)$$

where

$$\begin{aligned} \hat{Q} &= J^{-1} \begin{bmatrix} \rho \\ \rho u \\ \rho v \\ \rho w \\ e \end{bmatrix}, & \hat{E} &= J^{-1} \begin{bmatrix} \rho U \\ \rho u U + \xi_x p \\ \rho v U + \xi_y p \\ \rho w U + \xi_z p \\ (e + p)U - \xi_t p \end{bmatrix}, \\ \hat{F} &= J^{-1} \begin{bmatrix} \rho V \\ \rho u V + \eta_x p \\ \rho v V + \eta_y p \\ \rho w V + \eta_z p \\ (e + p)V - \eta_t p \end{bmatrix}, & \hat{G} &= J^{-1} \begin{bmatrix} \rho W \\ \rho u W + \zeta_x p \\ \rho v W + \zeta_y p \\ \rho w W + \zeta_z p \\ (e + p)W - \zeta_t p \end{bmatrix} \end{aligned} \quad (\text{A} - 7)$$

and

$$\begin{aligned} U &= \xi_t + \xi_x u + \xi_y v + \xi_z w \\ V &= \eta_t + \eta_x u + \eta_y v + \eta_z w \\ W &= \zeta_t + \zeta_x u + \zeta_y v + \zeta_z w \end{aligned} \quad (\text{A} - 8)$$

where U , V , and W are contravariant velocity components written without metric normalization. The viscous flux terms are given by

$$\begin{aligned}
\hat{E}_\nu &= J^{-1} Re^{-1} \begin{bmatrix} 0 \\ \xi_x \tau_{xx} + \xi_y \tau_{xy} + \xi_z \tau_{xz} \\ \xi_x \tau_{yx} + \xi_y \tau_{yy} + \xi_z \tau_{yz} \\ \xi_x \tau_{zx} + \xi_y \tau_{zy} + \xi_z \tau_{zz} \\ \xi_x \beta_x + \xi_y \beta_y + \xi_z \beta_z \end{bmatrix} \\
\hat{F}_\nu &= J^{-1} Re^{-1} \begin{bmatrix} 0 \\ \eta_x \tau_{xx} + \eta_y \tau_{xy} + \eta_z \tau_{xz} \\ \eta_x \tau_{yx} + \eta_y \tau_{yy} + \eta_z \tau_{yz} \\ \eta_x \tau_{zx} + \eta_y \tau_{zy} + \eta_z \tau_{zz} \\ \eta_x \beta_x + \eta_y \beta_y + \eta_z \beta_z \end{bmatrix} \\
\hat{G}_\nu &= J^{-1} Re^{-1} \begin{bmatrix} 0 \\ \zeta_x \tau_{xx} + \zeta_y \tau_{xy} + \zeta_z \tau_{xz} \\ \zeta_x \tau_{yx} + \zeta_y \tau_{yy} + \zeta_z \tau_{yz} \\ \zeta_x \tau_{zx} + \zeta_y \tau_{zy} + \zeta_z \tau_{zz} \\ \zeta_x \beta_x + \zeta_y \beta_y + \zeta_z \beta_z \end{bmatrix}
\end{aligned} \tag{A - 9}$$

where the components of the shear-stress tensor and heat-flux vector in nondimensional form were given in equation A-3. Here, the Cartesian derivatives are expanded in ξ , η , ζ space via chain-rule relations such as

$$u_x = \xi_x u_\xi + \eta_x u_\eta + \zeta_x u_\zeta$$

Finally, the metric terms are obtained from chain-rule expansion of x_ξ , y_η , etc., and solved for ξ_x , ξ_y , etc., to give

$$\begin{aligned}
\xi_x &= J(y_\eta z_\zeta - y_\zeta z_\eta) & \eta_x &= J(z_\xi y_\zeta - y_\xi z_\zeta) \\
\xi_y &= J(z_\eta x_\zeta - x_\eta z_\zeta) & \eta_y &= J(x_\xi z_\zeta - x_\zeta z_\xi) \\
\xi_z &= J(x_\eta y_\zeta - y_\eta x_\zeta) & \eta_z &= J(y_\xi x_\zeta - x_\xi y_\zeta) \\
\zeta_x &= J(y_\xi z_\eta - z_\xi y_\eta) & \xi_t &= -x_\tau \xi_x - y_\tau \xi_y - z_\tau \xi_z \\
\zeta_y &= J(x_\eta z_\xi - x_\xi z_\eta) & \eta_t &= -x_\tau \eta_x - y_\tau \eta_y - z_\tau \eta_z \\
\zeta_z &= J(x_\xi y_\eta - y_\xi x_\eta) & \zeta_t &= -x_\tau \zeta_x - y_\tau \zeta_y - z_\tau \zeta_z
\end{aligned} \tag{A - 10}$$

and

$$J^{-1} = x_\xi y_\eta z_\zeta + x_\zeta y_\xi z_\eta + x_\eta y_\zeta z_\xi - x_\xi y_\zeta z_\eta - x_\eta y_\xi z_\zeta - x_\zeta y_\eta z_\xi$$

In high Reynolds number flows, the viscous effects are confined to a thin layer near rigid boundaries. In most cases, there are only enough grid points to resolve the gradients normal to the body by clustering the grid in the normal direction, and resolution along the body is similar to what is needed in inviscid flow. As a result, even though the full derivatives are retained in the equations, the gradients along the body are not resolved unless the streamwise and circumferential grid spacings are sufficiently small. Hence, for many Navier–Stokes computations, the viscous derivatives along the body are dropped. This leads to the thin-layer Navier–Stokes equations.

The thin-layer model requires a boundary layer type coordinate system. For example, if ξ and η directions are along the body and the viscous derivatives associated with these directions are dropped, the terms in ζ only are retained and the body surface is mapped onto a constant ζ surface. As a result, equation A-6 simplifies to

$$\partial_\tau \hat{Q} + \partial_\xi \hat{E} + \partial_\eta \hat{F} + \partial_\zeta \hat{G} = Re^{-1} \partial_\zeta \hat{S} \tag{A - 11}$$

where

$$\hat{S} = J^{-1} = \begin{bmatrix} 0 \\ \mu(\zeta_x^2 + \zeta_y^2 + \zeta_z^2)u_\zeta + (\mu/3)(\zeta_x u_\zeta + \zeta_y v_\zeta + \zeta_z w_\zeta)\zeta_x \\ \mu(\zeta_x^2 + \zeta_y^2 + \zeta_z^2)v_\zeta + (\mu/3)(\zeta_x u_\zeta + \zeta_y v_\zeta + \zeta_z w_\zeta)\zeta_y \\ \mu(\zeta_x^2 + \zeta_y^2 + \zeta_z^2)w_\zeta + (\mu/3)(\zeta_x u_\zeta + \zeta_y v_\zeta + \zeta_z w_\zeta)\zeta_z \\ \{(\zeta_x^2 + \zeta_y^2 + \zeta_z^2)[0.5\mu(u^2 + v^2 + w^2)_\zeta \\ + \mu Pr^{-1}(\gamma - 1)^{-1}(a^2)_\zeta] + (\mu/3)(\zeta_x u + \zeta_y v + \zeta_z w) \\ \times (\zeta_x u_\zeta + \zeta_y v_\zeta + \zeta_z w_\zeta) \end{bmatrix} \quad (\text{A} - 12)$$

To generalize the coordinates of complex geometries, the thin-layer approximation can be made in all three coordinate directions and, as a result, only cross-derivative viscous terms are neglected. It should also be emphasized that the thin-layer approximation is valid only for high Reynolds number flows. Very large turbulent eddy viscosities would invalidate the thin-layer assumption.

Appendix B

Numerical Algorithm

Appendix B Numerical Algorithm

As mentioned in section 2.1, the algorithm used to solve the Reynolds-averaged Navier–Stokes equations is due to Beam-Warming. The basic Beam-Warming algorithm is first- or second-order accurate in time and second- or fourth-order accurate in space. The equations are approximately factored (spatially split) which, for a given time iteration, reduces the process to three one-dimensional problems. Due to the second-order central-difference operators employed, the algorithm produces block tridiagonal systems for each spatial dimension. The stability and accuracy of the numerical algorithm is described by Beam and Warming (ref. 40). According to the linear analysis, the numerical scheme is unconditionally stable in two dimensions but in actual practice time step limits are encountered because of the nonlinear nature of the equations. However, this limitation is much less stringent than comparable explicit schemes. In three dimensions the algorithm is unconditionally unstable, but stability is maintained by the addition of artificial dissipation terms.

The finite-difference algorithm due to Beam and Warming applied to equation A-11 results in the following approximate factorization:

$$\begin{aligned}
 & (I + h\delta_\xi \hat{A}^n + D_\xi^{(2)})(I + h\delta_\eta \hat{B}^n + D_\eta^{(2)}) \\
 & \times (I + h\delta_\zeta \hat{C}^n - hRe^{-1}\delta_\zeta J^{-1} \hat{M}^n J + D_\zeta^{(2)}) \Delta \hat{Q}^n = \hat{R}^n \\
 & = -\Delta\tau(\delta_\xi \hat{E}^n + \delta_\eta \hat{F}^n + \delta_\zeta \hat{G}^n - Re^{-1}\delta_\zeta \hat{S}^n) - D^{(4)} \hat{Q}^n
 \end{aligned} \tag{B - 1}$$

where δ is the central-difference operator and Δ and ∇ are forward and backward-difference operators, e.g.,

$$\begin{aligned}
 \delta_\xi \hat{Q} &= [\hat{Q}(\xi + \Delta\xi, \eta, \zeta) - \hat{Q}(\xi - \Delta\xi, \eta, \zeta)]/2\Delta\xi \\
 \Delta_\xi \hat{Q} &= [\hat{Q}(\xi + \Delta\xi, \eta, \zeta) - \hat{Q}(\xi, \eta, \zeta)]/\Delta\xi \\
 \nabla_\xi \hat{Q} &= [\hat{Q}(\xi, \eta, \zeta) - \hat{Q}(\xi - \Delta\xi, \eta, \zeta)]/\Delta\xi
 \end{aligned} \tag{B - 2}$$

Indices denoting spatial location are suppressed and $h = \Delta\tau$ corresponds to first-order time-accurate Euler Implicit and $h = \Delta\tau/2$ to second-order time-accurate Trapezoidal Rule. $D_\xi^{(2)}$, $D_\eta^{(2)}$, and $D_\zeta^{(2)}$ are the implicit and $D_\epsilon^{(4)}$ is the explicit smoothing operator which are given in detail in reference 43.

The Jacobian matrices \hat{A}^n , \hat{B}^n , and \hat{C}^n are obtained by linearizing the flux vectors \hat{E}^n , \hat{F}^n , and \hat{G}^n in time such that

$$\begin{aligned}
\hat{E}^{n+1} &= \hat{E}^n + \hat{A}^n(\hat{Q}^{n+1} - \hat{Q}^n) + O(\Delta\tau^2) \\
\hat{F}^{n+1} &= \hat{F}^n + \hat{B}^n(\hat{Q}^{n+1} - \hat{Q}^n) + O(\Delta\tau^2) \\
\hat{G}^{n+1} &= \hat{G}^n + \hat{C}^n(\hat{Q}^{n+1} - \hat{Q}^n) + O(\Delta\tau^2)
\end{aligned} \tag{B-3}$$

where indices denoting spatial location are suppressed again and

$$\hat{A} = \frac{\partial \hat{E}}{\partial \hat{Q}}, \quad \hat{B} = \frac{\partial \hat{F}}{\partial \hat{Q}}, \quad \hat{C} = \frac{\partial \hat{G}}{\partial \hat{Q}} \tag{B-4}$$

are the flux Jacobian matrices. These flux Jacobians and the viscous coefficient matrix \hat{M} , which comes from the time linearization of the viscous vector \hat{S}^{n+1} , are documented in reference 43.

Block tridiagonal-matrix inversions constitute the major portion of numerical work associated with the standard Beam-Warming algorithm. Equations A-6 are a coupled set of five equations and thereby produce a (5×5) block-tridiagonal structure for the implicit operators of equations B-1. The diagonal version of the standard algorithm due to Pulliam and Chaussee (ref. 41) overcomes this difficulty. In this algorithm, rather than inverting block-tridiagonal matrices in each direction, scalar pentadiagonal matrices are inverted. This is computationally more efficient.

The Jacobian matrices, \hat{A} , \hat{B} , and \hat{C} have a set of eigenvalues and a complete set of distinct eigenvectors. Similarity transformations can be used to diagonalize \hat{A} , \hat{B} , and \hat{C} ,

$$\hat{A} = T_\xi \hat{\Lambda}_\xi T_\xi^{-1}, \quad \hat{B} = T_\eta \hat{\Lambda}_\eta T_\eta^{-1}, \quad \hat{C} = T_\zeta \hat{\Lambda}_\zeta T_\zeta^{-1} \tag{B-5}$$

where

$$\begin{aligned}
\hat{\Lambda}_\xi &= D[U, U, U, U + c(\xi_x^2 + \xi_y^2 + \xi_z^2)^{1/2}, U - c(\xi_x^2 + \xi_y^2 + \xi_z^2)^{1/2}] \\
\hat{\Lambda}_\eta &= D[V, V, V, V + c(\eta_x^2 + \eta_y^2 + \eta_z^2)^{1/2}, V - c(\eta_x^2 + \eta_y^2 + \eta_z^2)^{1/2}] \\
\hat{\Lambda}_\zeta &= D[W, W, W, W + c(\zeta_x^2 + \zeta_y^2 + \zeta_z^2)^{1/2}, W - c(\zeta_x^2 + \zeta_y^2 + \zeta_z^2)^{1/2}]
\end{aligned} \tag{B-6}$$

where c is the speed of sound ($c^2 = \gamma p / \rho$), and for example $\hat{\Lambda}_\xi$ reads as

$$\hat{\Lambda}_\xi = \begin{bmatrix} U & 0 & 0 & 0 & 0 \\ 0 & U & 0 & 0 & 0 \\ 0 & 0 & U & 0 & 0 \\ 0 & 0 & 0 & U + c(\xi_x^2 + \xi_y^2 + \xi_z^2)^{1/2} & 0 \\ 0 & 0 & 0 & 0 & U - c(\xi_x^2 + \xi_y^2 + \xi_z^2)^{1/2} \end{bmatrix} \tag{B-7}$$

The similarity transformation matrices T_ξ , T_η , T_ζ and their inverse matrices are given in reference 43. Relations exist between T_ξ , T_η , and T_ζ of the form

$$\hat{N} = T_\xi^{-1} T_\eta, \quad \hat{N}^{-1} = T_\eta^{-1} T_\xi, \quad \hat{P} = T_\eta^{-1} T_\zeta, \quad \hat{P}^{-1} = T_\zeta^{-1} T_\eta \tag{B-8}$$

where

$$T_k^{-1}T_l = \begin{bmatrix} m_1 & m_2 & m_3 & -\mu m_4 & \mu m_4 \\ -m_2 & m_1 & m_4 & \mu m_3 & -\mu m_3 \\ -m_3 & -m_4 & m_1 & -\mu m_2 & \mu m_2 \\ \mu m_4 & -\mu m_3 & \mu m_2 & \mu^2(1+m_1) & \mu^2(1-m_1) \\ -\mu m_4 & \mu m_3 & -\mu m_2 & \mu^2(1-m_1) & \mu^2(1+m_1) \end{bmatrix} \quad (\text{B-9})$$

$$\begin{aligned} m_1 &= \tilde{k}_x \tilde{l}_x + \tilde{k}_y \tilde{l}_y + \tilde{k}_z \tilde{l}_z, & m_3 &= \tilde{k}_x \tilde{l}_z - \tilde{k}_z \tilde{l}_x, \\ m_2 &= \tilde{k}_x \tilde{l}_y - \tilde{k}_y \tilde{l}_x, & m_4 &= \tilde{k}_y \tilde{l}_z - \tilde{k}_z \tilde{l}_y, & \mu &= 1/\sqrt{2} \end{aligned}$$

After applying the similarity transformations of equation B-5 and identities given in equation B-8 into equation B-1 and exchanging the smoothing operators with new ones, the diagonal form of the standard algorithm reads

$$T_\xi(I + h\delta_\xi \hat{\Lambda}_\xi - hD_i|_\xi) \hat{N}(I + h\delta_\eta \hat{\Lambda}_\eta - hD_i|_\eta) \hat{P}(I + h\delta_\zeta \hat{\Lambda}_\zeta - hD_i|_\zeta) T_\zeta^{-1} \Delta \hat{Q}^n = R^n \quad (\text{B-10})$$

The spatial accuracy of the standard and diagonalized algorithms for steady-state problems (i.e., $\Delta \hat{Q}^n \rightarrow 0$ as $n \rightarrow \infty$) is determined by the type of differencing in forming \hat{R}^n . Since the modification that produces the diagonal algorithm does not effect \hat{R}^n , both schemes will have the same steady-state solution assuming that the steady-state solution is independent of the convergence path; i.e., that the steady state is unique. For unsteady simulations, care must be exercised in ensuring small enough time-step sizes for accuracy. When the diagonalized algorithm is used, the author strongly recommends time-step refinement studies to evaluate temporal accuracy of the unsteady simulations.

For constant coefficient matrices \hat{A} , \hat{B} , and \hat{C} , the diagonal algorithm reduces to the standard algorithm because the eigenvector matrices are also constant. Therefore, the linear stability analysis of Beam and Warming also holds for the diagonal algorithm.

Appendix C

Turbulence Modeling

Appendix C Turbulence Modeling

The apparent turbulent stresses in compressible flow can be written as

$$(\tau_{ij})_{turb} = -\rho \overline{u'_i u'_j} \quad (C-1)$$

and the apparent turbulent heat flux components as

$$-(\nabla \cdot \mathbf{q})_{turb} = -\frac{\partial}{\partial x_j} (\rho c_p \overline{T' u'_j}) \quad (C-2)$$

In order to predict turbulent flows by applying finite-difference methods to the Reynolds equations, it is necessary to make assumptions for the terms in equations C-1 and C-2. Boussinesq (1877) suggested that the apparent shearing stresses might be related to the rate of mean strain through an apparent turbulent or “eddy” viscosity given in incompressible flow by

$$-\rho \overline{u'_i u'_j} = \mu_T \left(\frac{\partial u_i}{\partial x_j} + \frac{\partial u_j}{\partial x_i} \right) \quad (C-3)$$

Closure for the Reynolds heat flux-term, $\rho c_p \overline{T' u'_j}$ is treated in algebraic models by a form of Reynolds analogy. The Reynolds analogy is based on the similarity between the transport of heat and momentum and applied to the apparent turbulent conductivity in the assumed Boussinesq form

$$\rho c_p \overline{T' u'_j} = -k_T \frac{\partial T}{\partial x_j} \quad (C-4)$$

Experiments reveal that the ratio of the diffusivities for the turbulent transport of heat and momentum which is called the turbulent Prandtl number, $Pr_T = \mu_T c_p / k_T$, is a well-behaved function across the flow and in algebraic models is generally taken to be 0.9. Using the turbulent Prandtl number, the turbulent heat flux is related to the turbulent viscosity and mean flow variables as

$$-\rho c_p \overline{T' u'_j} = \frac{c_p \mu_T}{Pr_T} \frac{\partial T}{\partial x_j} \quad (C-5)$$

In the Baldwin-Lomax model the effects of turbulence are simulated by replacing the molecular coefficient of viscosity μ_M with the effective viscosity $\mu_M + \mu_T$ in the stress terms of the laminar Navier-Stokes equations. In heat flux terms $k/c_p = \mu/Pr$ is replaced by $\mu/Pr + \mu_T/Pr_T$.

The Baldwin-Lomax model is a two-layer algebraic model in which μ_T is given by

$$\mu_T = \begin{cases} (\mu_T)_{inner}, & y \leq y_{crossover} \\ (\mu_T)_{outer}, & y \geq y_{crossover} \end{cases} \quad (C-6)$$

where y is the normal distance from the wall and $y_{crossover}$ is the smallest value of y at which values from the inner and outer formulas are equal. The eddy viscosity coefficient in the inner layer is based on the Prandtl mixing-length theory

$$(\mu_T)_{inner} = \rho \ell^2 |\omega| \quad (C-7)$$

The parameter ℓ is the mixing length corrected with the Van Driest damping factor to account for the laminar sublayer

$$\ell = k y [1 - \exp(-y^+ / A^+)] \quad (C-8)$$

where $k = 0.4$, $A^+ = 26$, and $|\omega|$ is the magnitude of the vorticity given by

$$|\omega| = \sqrt{(u_y - v_x)^2 + (v_z - w_y)^2 + (w_x - u_z)^2} \quad (\text{C} - 9)$$

and

$$y^+ = \frac{\rho_w u \tau y}{\mu_w} = \frac{\sqrt{\rho_w \tau_w y}}{\mu_w} \quad (\text{C} - 10)$$

The eddy viscosity coefficient in the outer layer is based on the distribution of vorticity which is used to determine the length scale and is given by

$$(\mu_T)_{outer} = K C_{CP} \rho F_{WAKE} F_{KLEB}(y) \quad (\text{C} - 11)$$

where $K = 0.0168$ is the Clauser constant and $C_{CP} = 1.6$ is an additional constant. F_{WAKE} is found via

$$F_{WAKE} = \min \left\{ \begin{array}{c} y_{max} F_{max} \\ \text{or} \\ C_{WK} y_{max} u_{DIF}^2 / F_{max} \end{array} \right\} \quad (\text{C} - 12)$$

where $C_{WK} = 0.25$ and

$$u_{DIF} = (\sqrt{u^2 + v^2 + w^2})_{max} - (\sqrt{u^2 + v^2 + w^2})_{min} \quad (\text{C} - 13)$$

In equation C-13 the second term is taken to be zero (except in wakes). The quantities y_{max} and F_{max} are determined from the function

$$F(y) = y |\omega| [1 - \exp(-y^+ / A^+)] \quad (\text{C} - 14)$$

In wakes the exponential term is set equal to zero. The quantity F_{max} is the maximum value of $F(y)$ that occurs in the profile and y_{max} is the value of y at which F_{max} occurs. The function F_{KLEB} is the Klebanoff intermittency factor given by

$$F_{KLEB}(y) = \left[1 + 5.5 \left(\frac{C_{KLEB} y}{y_{MAX}} \right)^6 \right]^{-1} \quad (\text{C} - 15)$$

and $C_{KLEB} = 0.3$.

Although not seen explicitly, the Reynolds number enters into the computation of eddy viscosity through the computation of y^+ . When the variables in equation C-10 are nondimensionalized, the following expression is obtained:

$$y^+ = \sqrt{\frac{Re \tilde{\rho}_w \tilde{\tau}_w}{\tilde{\mu}_w}} \tilde{y} \quad (\text{C} - 16)$$

In high Reynolds number flows, as $Re \rightarrow \infty$, the length scales l and $F(y)$ in the inner and outer layers go to zero, which result in vanishing values of μ_T . For more discussion on the Baldwin-Lomax turbulence model, the reader is referred to the original paper (ref. 44).

References

1. Yeh, D. T.; George, M.W.; Clever, W. C.; Tam, C. K.; and Woan, C. J.: Numerical Study of the X-31 High Angle-of-Attack Flow Characteristics. AIAA Paper 91-1630, June 1991.
2. Kehoe, M. W.; Bjarke, L. J.; and Laurie, E. J.: An In-Flight Interaction of the X-29A Canard and Flight Control System. NASA TM-101718, Apr. 1990.
3. Modin, K. E.; and Clareus, U.: Aerodynamic Design Evolution of the SAAB JAS 39 Gripen Aircraft. AIAA Paper 91-3195, Sept. 1991.
4. Behrbohm, H.: Basic Low Speed Aerodynamics of the Short-Coupled Canard Configuration of Small Aspect Ratio. SAAB Aircraft Co. TN-60, Linkoping, Sweden, July 1965.
5. Lacey, D. W.; and Chorney, S. J.: Subsonic Aerodynamic Characteristics of Close-Coupled Canards with Varying Area and Position Relative to a 50° Swept Wing. Naval Ship Research and Development Center, TN-AL-199, Mar. 1971.
6. McKinney, L. W.; and Dollyhigh, S. M.: Some Trim Drag Considerations for Maneuvering Aircraft. J. Aircraft, vol. 8, no. 8, Aug. 1971, pp. 623-629.
7. Dollyhigh, S. M.: Static Longitudinal Aerodynamic Characteristics of Close-Coupled Wing-Canard Configurations at Mach Numbers from 1.60 to 2.86. NASA TN-D-6597, Dec. 1971.
8. Gloss, B. B.; and McKinney, L. W.: Canard-Wing Lift Interference Related to Maneuvering Aircraft at Subsonic Speeds. NASA TM-X-2897, Dec. 1973.
9. Gloss, B. B.: The Effect of Canard Leading-Edge Sweep and Dihedral Angle on the Longitudinal and Lateral Aerodynamic Characteristics of a Close-Coupled Canard-Wing Configuration. NASA TN-D-7814, Dec. 1974.
10. Gloss, B. B.: Effect of Canard Location and Size on Canard-Wing Interference and Aerodynamic-Center Shift Related to Maneuvering Aircraft at Transonic Speeds. NASA TN-D-7505, June 1974.
11. Gloss, B. B.: Effect of Wing Planform and Canard Location and Geometry on the Longitudinal Aerodynamic Characteristics of a Close-Coupled Canard Wing Model at Subsonic Speeds. NASA TN-D-7910, June 1975.
12. Gloss, B. B.; Ray, E. J.; and Washburn, K. E.: Effect of Canard Vertical Location, Size, and Deflection on Canard-Wing Interference at Subsonic Speeds. NASA TM-78790, Dec. 1978.
13. Gloss, B. B.; and Washburn, K. E.: A Study of Canard-Wing Interference Using Experimental Pressure Data at Transonic Speeds. NASA TP-1355, Jan. 1979.
14. Lacey, D. W.: Aerodynamic Characteristics of the Close-Coupled Canard as Applied to Low-to-Moderate Swept Wings, vols. 1-4. David W. Taylor Naval Ship Research and Development Center Report DTNSWDC-79/001-004, Jan. 1979.
15. Ray, E. J.; and Henderson, W. P.: Low-Speed Aerodynamic Characteristics of a Highly Swept Supersonic Transport Model With Auxiliary Canard and High-Lift Devices. NASA TM-X-1694, Nov. 1968.
16. Re, R. J.; and Capone, F. J.: Longitudinal Aerodynamic Characteristics of a Fighter Model With a Close-Coupled Canard at Mach Numbers From 0.40 to 1.20. NASA TP-1206, July 1978.
17. Howard, R. M.; and Kersh, J. M., Jr.: Effect of Canard Deflection on Enhanced Lift for a Close-Coupled-Canard Configuration. AIAA Paper 91-3222-CP, Sept. 1991.
18. Ponton, A. J.; Lowson, M. V.; and Barrett, R. V.: The Evaluation of Canard Couplings at High Angles of Attack. AIAA Paper 92-0281, Jan. 1992.
19. Gloss, B. B.; and Washburn, K. E.: Load Distribution on a Close-Coupled Wing Canard at Transonic Speeds. J. Aircraft, vol. 15, no. 4, Apr. 1978, pp. 234-239.

20. Washburn, K. E.; and Gloss, B. B.: Aerodynamic Load Distributions at Transonic Speeds for a Close-Coupled Wing-Canard Configuration: Tabulated Pressure Data. NASA TM-78780, Oct. 1978.
21. Er-El, J.; and Seginer, A.: Vortex Trajectories and Breakdown on Wing-Canard Configurations. *J. Aircraft*, vol. 22, no. 8, Aug. 1985, pp. 641-648.
22. Calarese, W.: Vortex Interaction on a Canard-Wing Configuration. 1986, Air Force Wright Aeronautical Laboratories AFWAL-TR-86-3100 Oct.
23. Oelker, H.; and Hummel, D.: Investigations on the Vorticity Sheets of a Close-Coupled Delta-Canard Configuration. *J. Aircraft*, vol. 26, no. 7, July 1989, pp. 657-666.
24. Boyden, R. P.: Subsonic Dynamic Stability Characteristics of Two Close-Coupled Canard-Wing Configurations. NASA TP-1291, Oct. 1978.
25. O'Leary, J. F.: Flowfield Study of a Close-Coupled Canard Configuration. Master's thesis, Naval Postgraduate School, Monterey, Calif., June 1992.
26. Schmidt, D. C.: Lift Enhancement Using a Close-Coupled Oscillating Canard. Master's thesis, Naval Postgraduate School, Monterey, Calif., Sept. 1992.
27. Mc Bane, D. G.: Close-Coupled Oscillating Canard Effects on Post-Stall Lift Enhancement. Master's thesis, Naval Postgraduate School, Monterey, Calif., June 1993.
28. Mouch, T.; McLaughlin, T.; and Ashworth, J.: Unsteady Flows Produced by Small Amplitude Oscillations of the Canard. AIAA Paper 89-2229-CP, 1989.
29. Butler, G. F.: Effect of Downwash on the Induced Drag of Canard-Wing Combinations. *J. Aircraft*, vol. 19, no. 5, May 1982, pp. 410-411.
30. Kroo, I. M.; and McGeer, T.: Optimization of Canard Configurations - An Integrated Approach and Practical Drag Estimation Method. ICAS-82-6.8.1, Aug. 1982.
31. Kroo, I. M.: Minimum Induced Drag of Canard Configurations. *J. Aircraft*, vol. 19, no. 9, Sept. 1982, pp. 792-794.
32. McGeer, T.; and Kroo, I. M.: A Fundamental Comparison of Canard and Conventional Configurations. *J. Aircraft*, vol. 20, no. 11, Nov. 1983, pp. 983-992.
33. Kroo, I. M.: A General Approach to Multiple Lifting Surface Design and Analysis. AIAA Paper 84-2507, Nov. 1984.
34. Agrell, N.: Transonic Aerodynamic Computations for a Canard Configuration. AIAA Paper 84-2158, Aug. 1984.
35. Batina, J. T.: Unsteady Transonic Flow Calculations for Interfering Lifting Surface Configurations. AIAA Paper 85-1711, July 1985.
36. Rom, J.; and Gordon, R.: High Angle of Attack Non-Linear Vortex Lattice Calculations of Canard-Wing. AIAA Paper 88-0484, Jan. 1988.
37. Raj, P.; Keen, J. M.; and Singer, S. W.: Applications of an Euler Aerodynamic Method to Free-Vortex Flow Simulation. AIAA Paper 88-2517-CP, 1988.
38. Bandyopadhyay, G.: Low Speed Aerodynamics of Canard Configurations. *The Aeronautical J.*, vol. 93, no. 921, Jan. 1989.
39. Kroll, N.; Rossow, C.; Scherr, S.; and Schone, J.: Analysis of 3-D Aerospace Configurations Using the Euler Equations. AIAA Paper 89-0268, Jan. 1989.
40. Beam, R.; and Warming, R. F.: An Implicit Finite-Difference Algorithm for Hyperbolic Systems in Conservative-Law Form. *J. Computational Physics*, vol. 22, Sept. 1976, pp. 87-110.
41. Pulliam, T. H.; and Chaussee, D. S.: A Diagonal Form of an Implicit Approximate-Factorization Algorithm. *J. Computational Physics*, vol. 39, no. 2, Feb. 1981, pp. 347-363.

42. Flores, J.; and Holst, T. L.: Numerical Solution of the Navier–Stokes Equations for Complex Configurations. Lecture Series in Computational Fluid Dynamics, University of Tennessee Space Institute, Tullahoma, Tenn., Mar. 1988.
43. Kaynak, U.; Holst, T. L.; Cantwell, B. J.: Computation of Transonic Separated Wing Flows Using an Euler/Navier–Stokes Zonal Approach. NASA TM-88311, July 1986.
44. Baldwin, B. S.; and Lomax, H.: Thin Layer Approximation and Algebraic Model for Separated Turbulent Flows. AIAA Paper 78-257, Jan. 1978.
45. Degani, D.; and Schiff, L. B.: Computation of Turbulent Supersonic Flows Around Pointed Bodies Having Crossflow Separation. *J. Computational Physics*, vol. 66, 1986, pp. 173–196.
46. Luh, R. C.; Pierce, L.; and Yip, D.: Interactive Surface Grid Generation. AIAA Paper 91-0796, Jan. 1991.
47. Sorenson, R. L.: The 3DGRAPE Book: Theory, Users' Manual, Examples. NASA TM-102224, July 1989.
48. Steinbrenner, J. P.; Chawner, J. R.; and Fouts, C. L.: The Gridgen 3D Multiple Block Grid Generation System, Volumes I and II. WRDC-TR-90-3022, July 1990.
49. Anderson, D. A.; Tannehill, J. C.; and Pletcher, R. H.: *Computational Fluid Mechanics and Heat Transfer*. McGraw-Hill Book Company, New York, 1984.
50. Klopfer, G. H.; and Molvik, G. A.: Conservative Multizone Interface Algorithm for the 3-D Navier–Stokes Equations. AIAA Paper 91-1601, June 1991.
51. Klopfer, G. H.; and Obayashi, S.: Virtual Zone Navier–Stokes Computations for Oscillating Control Surfaces. AIAA Paper 93-3363, July 1993.
52. Srinivasan, G. R.; McCroskey, W. J.; Baeder, J. D.; and Edwards, T. A.: Numerical Simulation of Tip Vortices of Wings in Subsonic and Transonic Flows. *AIAA J.*, vol. 26, no. 10, Oct. 1988, pp. 1153–1162.
53. Bergmann, A.; Hummel, D.; and Oelker, H.-Chr.: Vortex Formation Over a Close-Coupled Canard-Wing-Body Configuration in Unsymmetrical Flow. Fluid Dynamics Panel Symposium on Vortex Flow Aerodynamics, Scheveningen, Netherlands, Oct. 1990.
54. Erickson, G. E.; Schreiner, J. A.; and Rogers, L. W.: Canard-Wing Vortex Interaction at Subsonic Through Supersonic Speeds. AIAA Paper 90-2814, Aug. 1990.
55. Longo, J. M. A.; and Das, A.: Numerical Simulation of Vortical Flows Over Close-Coupled Canard-Wing Configuration. AIAA Paper 90-0102, Jan. 1990.
56. Ekaterinaris, J. A.; and Schiff, L. B.: Vortical Flows over Delta Wings and Numerical Prediction of Vortex Breakdown. AIAA Paper 90-0102, Jan. 1990.
57. Jones, R. T.: *Wing Theory*. Princeton University, Princeton, N.J., 1990.
58. Chaderjian, N. M.: Navier–Stokes Prediction of Large-Amplitude Delta-Wing Roll Oscillations Characterizing Wing Rock. AIAA Paper 92-4428, Aug. 1992.

REPORT DOCUMENTATION PAGE

Form Approved
OMB No. 0704-0188

Public reporting burden for this collection of information is estimated to average 1 hour per response, including the time for reviewing instructions, searching existing data sources, gathering and maintaining the data needed, and completing and reviewing the collection of information. Send comments regarding this burden estimate or any other aspect of this collection of information, including suggestions for reducing this burden, to Washington Headquarters Services, Directorate for Information Operations and Reports, 1215 Jefferson Davis Highway, Suite 1204, Arlington, VA 22202-4302, and to the Office of Management and Budget, Paperwork Reduction Project (0704-0188), Washington, DC 20503.

1. AGENCY USE ONLY (Leave blank)		2. REPORT DATE August 1996	3. REPORT TYPE AND DATES COVERED Technical Memorandum	
4. TITLE AND SUBTITLE Numerical Study of Steady and Unsteady Canard-Wing-Body Aerodynamics			5. FUNDING NUMBERS 505-59-53	
6. AUTHOR(S) Eugene L. Tu				
7. PERFORMING ORGANIZATION NAME(S) AND ADDRESS(ES) Ames Research Center Moffett Field, CA 94035-1000			8. PERFORMING ORGANIZATION REPORT NUMBER A-961533	
9. SPONSORING/MONITORING AGENCY NAME(S) AND ADDRESS(ES) National Aeronautics and Space Administration Washington, DC 20546-0001			10. SPONSORING/MONITORING AGENCY REPORT NUMBER NASA TM-110394	
11. SUPPLEMENTARY NOTES Point of Contact: Eugene L. Tu, Ames Research Center, MS 258-1, Moffett Field, CA 94035-1000 (415) 604-4486				
12a. DISTRIBUTION/AVAILABILITY STATEMENT Unclassified-Unlimited Subject Category - 02 Available from the NASA Center for AeroSpace Information, 800 Elkridge Landing Road, Linthicum Heights, MD 21090; (301) 621-0390			12b. DISTRIBUTION CODE	
13. ABSTRACT (Maximum 200 words) The use of canards in advanced aircraft for control and improved aerodynamic performance is a topic of continued interest and research. In addition to providing maneuver control and trim, the influence of canards on wing aerodynamics can often result in increased maximum lift and decreased trim drag. In many canard-configured aircraft, the main benefits of canards are realized during maneuver or other dynamic conditions. Therefore, the detailed study and understanding of canards requires the accurate prediction of the non-linear unsteady aerodynamics of such configurations. For close-coupled canards, the unsteady aerodynamic performance associated with the canard-wing interaction is of particular interest. The presence of a canard in close proximity to the wing results in a highly coupled canard-wing aerodynamic flowfield which can include downwash/upwash effects, vortex-vortex interactions and vortex-surface interactions. For unsteady conditions, these complexities of the canard-wing flowfield are further increased. The development and integration of advanced computational technologies provide for the time-accurate Navier-Stokes simulations of the steady and unsteady canard-wing-body flowfields. Simulations are performed for non-linear flight regimes at transonic Mach numbers and for a wide range of angles of attack. For the static configurations, the effects of canard positioning and fixed deflection angles on aerodynamic performance and canard-wing vortex interactions are considered. For non-static configurations, the analyses of the canard-wing-body flowfield includes the unsteady aerodynamics associated with pitch-up ramp and pitch oscillatory motions of the entire geometry. The unsteady flowfield associated with moving canards, which are typically used as primary control surfaces, are considered as well. The steady and unsteady effects of the canard on surface pressures, integrated forces and moments, and canard-wing vortex interaction are presented in detail, including the effects of the canard on the static and dynamic stability characteristics. The current study provides an understanding of the steady and unsteady canard-wing-body flowfield. Emphasis is placed on the effects of the canard on aerodynamic performance as well as the detailed flow physics of the canard-wing flowfield interactions. The computational tools developed to accurately predict the time-accurate flowfield of moving canards provides for the capability of coupled fluids-controls simulations desired in the detailed design and analysis of advanced aircraft.				
14. SUBJECT TERMS Canard aerodynamics, Unsteady aerodynamics, Moving canard, Dynamic stability			15. NUMBER OF PAGES 154	
			16. PRICE CODE A08	
17. SECURITY CLASSIFICATION OF REPORT Unclassified	18. SECURITY CLASSIFICATION OF THIS PAGE Unclassified	19. SECURITY CLASSIFICATION OF ABSTRACT -	20. LIMITATION OF ABSTRACT	